2013

Structural Health Monitoring and Application of Wireless Sensor Networks

Siavash Dorvash
Lehigh University

Structural Health Monitoring and Application of Wireless Sensor Networks

By

Siavash Dorvash

Presented to the Graduate and Research Committee

of Lehigh University

in Candidacy for the Degree of

Doctor of Philosophy

in

Structural Engineering

Lehigh University

May 2013

Acknowledgements

The research presented in this dissertation was conducted at the Research Center for Advanced Technology for Large Structural Systems (ATLSS), Department of Civil and Environmental Engineering, Lehigh University, Bethlehem, Pennsylvania. During the study, the chairmanship of the department was held by Dr. Stephen P. Pessiki and Dr. Sibel Pamukcu. Funding for this research was provided by National Science Foundation, through Sensors Sensing and Systems Program, and also PITA.

The author would like to thank his research advisor, Dr. Shamim Pakzad, for his guidance, and advice. The author would also like to thank Dr. John L. Wilson, the chair of his research committee, for his advice and input. The author appreciates the time and contributions of his other committee members, Dr. Liang Cheng, Dr. Dan Frangopol, and Dr. James Ricles. Also, the author would like to thank Dr. Clay Naito, Dr. Richard Sause, Dr. Ben Yen, and Mr. Ian Hodgson for their advice and input through this doctoral research. The author would like to thank the following people for their support during his research: the laboratory staff, particularly John Hoffner, Carl Bowman, and Edward A Tomlinson; the ATLSS staff, particularly Peter Bryan and Betty MacAdam; and fellow researchers.

The author would like to extend his deepest thanks to his family and friends who have offered support. The author extends special thanks to his parents, who have been his supporters since the first day of school. Most of all, the author is extremely thankful for the help, support, patience, and love of his wonderful wife, Zharfa.

Table of Contents

Table of Figures

Abstract

Different elements of structural health monitoring (SHM) can benefit from the application of wireless sensor Networks (WSNs), as advanced sensing systems. While WSNs can significantly enhance the SHM by facilitating deployment of scalable and dense monitoring systems, challenges in the power consumption and data communication, and concerns regarding the possible impacts of their associated quality on the results have restricted their broad application. This research contributes in addressing the limitation associated with the prohibitive data communication delay and power consumption by introducing a novel time- and energy-efficient distributed algorithm for modal identification, and also addressing the concerns regarding the possible effects of their sensing quality by development of quality assessment approaches for modal identification and damage detection practices.

The onboard processing techniques attempt to reduce the communication and power consumption by pushing the computation into the network. Efforts in developing onboard processing algorithms are restricted by the topology and algorithms, and their efficiency is not high enough to alleviate the challenge. A novel approach for modal identification of structural systems in a distributed scheme is developed which assigns the entire computational task of modal identification to remote nodes and limits the communication to transmission of only system's parameters. The algorithm is based on estimation-updating steps at remote nodes and iterations by passing the results through the network

for convergence of estimation. The algorithm is first developed for input-output scenarios and then is further expanded to address output-only systems as well. Development of approaches such as Cumulative System Formation for providing initial estimates of the system (as starting point of iteration) and also a novel AR-ARX approach for expediting the convergence also further enhanced the developed algorithm. Experiments and implementations have proved the functionality and performance of the algorithm.

While the focus of the research is on development of algorithms for enhancing the application of wireless sensors in modal identification, other aspects of data-driven SHM such as damage detection, and performance evaluation through field-testing of real-life structures are also studied. A framework for damage detection algorithm including accuracy indicators and statistical approaches for change point detection is developed and validated through implementation on different experimental models. Moreover, the state of the art in structural monitoring and vibration evaluation is presented in two field deployments.

Chapter 1

Introduction

1. Introduction

Civil structures and infrastructure are fundamental assets of a nation, needed for operation of the society and integral for the safety of people living in the society. These national assets, as of their role, withstand a number of loading scenarios on a daily basis ranging from typical ambient loads to more extreme wind and earthquake loads. Due to the uncertain nature of loading scenarios and environmental conditions the health state of infrastructure is undetermined. Moreover, infrastructure systems experience long term deterioration during their life time due to aging of elements and components. It is evident that the deteriorating and uncertain state of the nation's infrastructure without adequate attention can reach to a detrimental point which, in turn, threats the safety of people in the society.

In a Report Card for American Infrastructure, the American Society of Civil Engineers stated that "more than 26%, or one in four, of the nation's bridges are either structurally deficient or functionally obsolete," and estimated a need for a $2.2 trillion dollar investment to bring the nation's infrastructure up to an acceptable conditions (ASCE 2010). While the "structurally deficient" or "functionally obsolete" designations do not necessarily indicate that a bridge is unsafe, it points that these structures require significant maintenance and repair to remain in service (FHWA 2010). It is well understood that the deficiency of these structures can easily turn to occurrence of catastrophic failure events such as the collapse of I-35W Bridge in Minneapolis.

Concerns regarding the sub-standard functionality of a large portion of existing infrastructure motivated civil engineers to seek effective approaches to ensure safety and healthy performance of existing structures. As an intuitive solution, community of civil engineers developed the concept of structural health monitoring (SHM) which included a large variety of practices and algorithms, such as inspection, measurement and analysis, intended to assess the state of structures.

One of the applicable approaches for monitoring of in-service structural system is non-destructive testing and evaluation (NDT & E) techniques. Some of the traditional non-destructive evaluation (NDE) techniques, listed in ASM Handbook (Anon. 1992) include but are not limited to visual inspection, liquid penetrant (Deutsch 1979), eddy currents (Banks et al. 2002; Ziberstein et al. 2003), ultrasonic waves (Mallet et al. 2004), acoustic emission, and infrared thermography (Trimm 2003, Ball and Almond 1998). While these methods are proven to be useful tools for indication of structural malfunctioning without inducing to structure, there are certain limitations in their application. For example, to implement these techniques one must have direct access to the locations of potential damages, which may be difficult to reach, especially after an event such as an earthquake. Also, some problems such as overloading, settlement, fatigue damage, and locked bearings are hard to be visually identified until they are in extreme situations. The FHWA admits that assessment ratings presented in the National Bridge Inventory (NBI) by visual inspections do not provide adequate detail for managing maintenance programs and

planning rehabilitations (Chase, 2005). Furthermore, NDE techniques are costly, difficult to use with complex equipment, and provide only a temporary means of SHM.

While the NDT&E techniques lack the ability to address all the needs for health monitoring and performance evaluation of structural systems, advances in sensing technology and data processing algorithms provide a more intelligent approach, called *data-driven SHM*, as a substitute or, at least, a complement to the traditional techniques. The main concept in data-driven SHM is to estimate the state of a structural system from its measured response to the applied loads. Some common tasks in data-driven SHM approach are: response measurement, preprocessing (e.g. data cleansing and filtering), data interpretation, feature extraction, model updating, and performance evaluation. Two fundamental categories of testing and response measurement are static testing and dynamic testing, and also some basic data-driven SHM practices are modal parameter identification, finite element model updating, and damage detection.

Static Load Testing versus Dynamic Testing

One of the commonly used testing in data-driven SHM is static load testing which aims performance evaluation of the instrumented structure by means of measuring the response to controlled static loads. Results of static load testing of a structure help developing accurate numerical models of structures (or updating the existing models) which represent their real behavior under different loading scenarios, i.e. finite element model updating. These models enable estimation of structure's performance under future load effects (e.g. increased traffic load on a bridge structure) and thus, help with making

more realistic decision and management. This technique can also assist with realizing and detecting abnormal behaviors of the system. Although the static load testing results in an accurate evaluation of structure's performance, its implementation is usually very expensive and need a significant preparation. For example, the first requirement for static load testing of a bridge structure is closing the traffic lane which is not a simple and practical task for many traffic networks.

An alternative to static tests is vibration monitoring or dynamic testing. In this approach the objective is to collect the vibration response of the structure under the effects of its daily ambient loads. Unlike static load testing, dynamic testing does not require operation interruption as it can be conducted as the structure is in service. This characteristic makes the approach significantly simpler and more applicable. The data collected during dynamic testing provides fundamental dynamic characteristics of the structure by means of modal parameter identification and can be used for finite element model updating and damage detection. Since in dynamic testing the input loads are not controllable and are usually random, the results of this technique encompass more uncertainty. However, considering the relatively easier implementation, this approach is more popular in many circumstances. Dynamic and static testing can be also considered as complementary tasks as they can extract different parameters of the instrumented structure.

Modal Parameter Identification

As mentioned above, the dynamic testing provides the data for identification of the dynamic characteristics of the structure. The identified parameters can be used for different applications such as finite element model updating, performance evaluation and damage detection. An approach which provides the dynamic parameters of the monitored structure from the measured response is called system identification. The goal in the system identification is to extract a mathematical model for a system based on its measured response. In the context of civil engineering, system identification is mostly referred to as identification of modal parameters of the structure (i.e. modal parameter identification). Realizing the importance of this concept, researcher have devoted significant effort into this topic and developed and improved many approaches specifically useful for civil structures. Some examples of time domain approaches for system identification are: Eigensystem realization algorithm (ERA) (Juang and Papa, 1985); Q-Markov algorithm (Anderson et al., 1988); ERA using data correlation (ERA/DC) (Juang et al., 1988); ERA-NExT (James et al. 1992, 1993, 1996; Farrar and James 1997); Auto-Regressive model with Moving Average (ARMA), (Pandit 1991, Roeck et al. 1994) and subspace identification (SSI) algorithms, (Van Overschee 1991, 1995). As well, some examples of frequency domain approaches are: Poly-reference frequency domain algorithm (Zhang et al., 1985), orthogonal polynomial algorithm (Rechardson et al. 1982, Vold, 1986 and Auweraer et al., 1987), Modal parameter

identification using Complex Mode Indication Function (Shih et al. 1988) and multivariate mode indication function (MvMIF) (Williams et al. 1985).

Finite-Element Model Updating

Extracting the structural (dynamic) characteristics of the monitored structure, the finite element model can be tuned (i.e. updated). This practice in data-driven SHM is called finite element model updating. As the name suggests, this task updates the finite element model such that the simulated responses of the model matches the real structure's response measured during the experiment. Finite element model updating is a very important practice in SHM as it provides the owner and correspondences of structure with reliable analytical models and an accurate estimate of the structure's reserved capacity.

While the concept is the same, the methods in which finite element model updating is implemented can be very different. When static load testing is conducted on the structure the finite element is tuned to match the structure's static response (e.g. displacements and stresses) and thus, the parameters such as mass and damping which do not contribute in static response will not be updated. On the other hand, updating based on dynamic response will tune the structure such that dynamic characteristics of the analytical model agree with parameters extracted from dynamic testing (e.g. natural frequencies, natural damping ratios, and mode shapes). Each of the aforementioned methods has certain advantages and weaknesses. While updating based on dynamic testing focuses on more general characteristics of the structure (i.e. dynamic characteristics), this approach is

more prone to uncertainties because dynamic testing and vibration monitoring are more sensitive to operational and environmental condition than static load testing. However, vibration monitoring is a lot simpler in terms of implementation and testing, as explained earlier. Beside the classification based on testing method, there is also a broad range of algorithms for implementation of model updating. Direct method, iterative sensitivity based method, frequency domain method, and response surface method are some categories of such algorithms.

Damage Detection

Another application of the response measurement and structural identification is in structural damage detection. Damage detection using structural vibration measurements has been actively investigated by the civil engineering research community in the past few decades (Yao and Pakzad, 2012). Methods of damage detection can be classified in different ways. One common classification is as physics-based (model-based) methods and non-physics-based (model free) methods (ASCE 2011). In the physics-based methods, a structural model is formed using the measured vibration. From comparison of different estimated models (as results of different measurements through the time), together with using some statistical frameworks, the damage (if any) can be detected. The advantage of this model is that it provides a physical interpretation of the measured vibration and correlates the collected data to the behavior of the structural model and helps in making reasonable conclusions. However, creating structural models for civil infrastructure is not always easy and complexity of models may bring some uncertainties

into the problem. One of the basic damage detection approaches, classified as model-based methods, is to estimate modal property from system identification and detect their changes throughout the structure's life-time. This approach is valid as modal parameters are directly related to the physics of the structure according to classical dynamics theory. However, the effectiveness of modal property as damage indicator varies depending on the structural layout and damage type (Yao and Pakzad, 2012). It is shown in many studies that modal parameters can be insensitive to some local damages (Doebling et al. 1996). The performance of this approach can be improved by considering the modal property in the finite element model updating. However, this will increase the algorithm complexity. Thus, more efficient alternatives are needed. The non-physics-based algorithms, on the other hand, do not need structural models as these algorithms only interpret the measured responses without consideration of material and geometrical information. These approaches detect and localize the damage based on investigating the collected signal and despite the absence of physical model, they are sometimes more successful in identifying the damage.

Sensing Systems

As can be realized from each of above-mentioned practices, a fundamental task in data-driven SHM is monitoring and data collection. The reliability of all these approaches is highly dependent on the quality of the collected data. Higher the quality of the data is, more accurate the results will be. Besides, to draw reliable conclusions, temporal and spatial resolution of the sensing system is crucial. Capturing the response with dense

array of sensors for a long term period provides much information regarding the state of the structure and the results of that study would be significantly more accurate than when the response is measured at only limited number of locations, and in short period of time.

In general, reliability of data and sensor network, temporal and spatial resolution of measurement, sensitivity and the level of sensor noise, and agility of the sensor network in communication and response to commands are major quality aspects of a sensing network. Many sensing protocols have been developed in past decades and numerous structures around the world are already instrumented by these systems for SHM (Bolton et al., 2002; Masri et al., 2004; Wahbeh et al., 2005; Ko and Ni, 2005; Guan et al., 2006; Fraser et al., 2009). Also, during the past few decades, many different technologies have been established with variety of features. These achievements are ranged from development of new material and technologies for sensing to advancements in data transmission and acquisition systems (e.g. piezoelectric sensors, capacitive sensors, micro-electro-mechanical systems, non-contact laser vibrometry, electro-optical accelerometer, fiber optics, photogrammetry sensors, global positioning sensors, etc.). The challenge in application of mentioned sensing systems, however, is their preventive cost. The expense of instrumentation of structures with a dense and high quality sensing network has been extremely high such that their application has been limited to only eminent structures and infrastructure. Considering the cost, the challenge in the application of sensing systems for health monitoring of structures is the trade-off between the quality of the measurement and the expenses of instrumentations. Higher quality

results in a more accurate estimate of the structure's state and consequently more reliable health monitoring. On the other hand, as the quality increases, the costs of the monitoring system also increases which may prevent the wide-spread use of SHM. In the past decade, this trade-off has become as a motivation to researchers to pursue efficient ways of sensing to decrease the health monitoring costs.

One of the important developments in the area of sensing and monitoring system is incorporation of wireless technology for data transmission in the sensing networks. For many years sensing systems in SHM used wires for transmitting power and data from the sensors to the data acquisition system (i.e. base station). This type of transmission and communication between sensors and base station has been the most commonly used approach in many commercial and somewhat research projects and thus, these wired sensors are very well established and reliable. Although the wired sensor networks are reliable, the installation is costly and labor-intensive (Lynch et al. 2006). A significant portion of the time and money spent on installation of sensor networks is associated with the wiring process. Additionally, installing cable in some in-service structures may introduce some challenges which make a new limitation to the dimension of the sensing network and its spatial resolution.

Considering the difficulties in the instrumentation with wired sensor networks, the application of wireless technology attracted the interest of many researchers in SHM area. The earliest application of wireless technology in the field of SHM goes back to late 1990^{th} conducted by Kirmijian et al (1998). Soon after revealing the functionality and

performance of wireless sensors, many researchers focused on developing new wireless sensor platforms and improving their performances. A complementary advantage of WSNs is possession of computation capability on-board. This capability helps the sensing network to conduct a portion of data processing right after the data is collected. This ability is crucial for data management, preventing data overwhelming, and having a responsive sensing system. A detailed development history of wireless sensors is presented in the next chapter.

While WSN makes the deployment of SHM more convenient, a few challenges have restricted its application in large scale and for long term health monitoring of structural systems. Due to these challenges, the use of wireless sensors is still mostly limited to research projects and not commercial projects. The most important drawbacks in application of WSN are the latency in the process due to the low data communication bandwidth and the difficulties in providing operational power of sensors for long term monitoring. Particularly in the event of an earthquake, WSNs need to be responsive in capturing and processing the data. Thus, new approaches are required to address these challenges and make the existing WSN technology suitable for a wide variety of applications. Possible solutions to these challenges rely on either a new technology (e.g. use of wireless power transmission or energy harvesting) or a new processing strategy which minimizes the need for communication energy. Although technological solutions, such as energy harvesting (Casciati et al., 2007) and wireless power transmission (Das et al., 1998), are promising and necessary in the future application of WSNs, they do not

eliminate the entire challenges and it is still necessary to develop new approaches to manage and minimize their power consumption. An idea which attracted many researchers after early application of WSN in SHM was incorporating on-board computational capability of wireless sensors in data processing and management of limited wireless power. It is shown that the power consumption of the communication task is significantly higher than that of on-board computation. Hence, the logical goal in using on-board computational capability is to assign a portion of data processing to on-board processors (so called distributed data processing) and minimize the data transmission which is the more power consuming task. During the past few years, many different algorithms for distributed data processing are proposed and implemented on experimental monitoring systems, including this doctoral research.

Scope of the Research

This doctoral research while demonstrates the advantages of wireless sensors as a more cost-effective and potentially superior alternative over the traditional monitoring systems, contributes in addressing challenges in their application in structural health monitoring. An algorithm is developed for distributed modal identification to eliminate the need for the in-network transmission of the time-history data and as a result, minimize the required energy for communication and the delay in network's response. Besides, as the low cost characteristic of these sensors may introduce some limitation on the quality of sensing and the level of the noise associated with the measurements, this research also investigates the effect of measurement noise on the modal identification

through development of parameters which quantify the quality of the estimated modal parameters from response measurements.

While the focus of the research is on development of algorithms for application of wireless sensors in modal identification, a significant effort is also spent on other aspects of data-driven SHM such as damage detection, and deployment and field-testing of real-life structures. This research has contributed in development and validation of a statistic-based damage detection algorithm which identifies the changes in the behavior of structural system using the measured response. The damage detection algorithm is validated through the use of wireless sensors as well as traditional wired sensors and implementation on different experimental specimens. Moreover, this research presents implementation of state-of-the-art sensing system on two in-service infrastructure systems: a tall building and a cantilevered truss bridge. These works include instrumentation of the structures together with the extensive data processing for extraction of structural characteristics and performance evaluation.

Organization of the Dissertation

Chapter 2 presents the background information on the development of WSNs and their application in SHM and also provides the necessary background knowledge on system identification which will be used in the later chapters of this dissertation.

Chapter 3 presents a distributed modal identification approach which is developed to enhance the efficiency in application of wireless sensor networks (WSNs) for modal

identification of structural systems. In this approach the computational task is distributed among remote nodes to reduce the communication burden of the network and as a result, optimize the time and the energy consumption of the monitoring system. The algorithm relies on a class of estimation method, called Expectation-Maximization (EM), which estimates unknown parameters, given the measurement data in the absence of access to complete information about the system. The adoption of EM for modal identification is such that each node of the network estimates modal parameters using the local measurement and the estimated parameters received from the neighbor node. The estimation results are updated recursively by passing the results through the network in an iterative manner. The formulation of the approach, called Iterative Modal Identification (IMID), is presented in Chapter 3 and its performance is validated through the implementation of the algorithm on numerically simulated and experimental data. This algorithm is further improved to be applicable for output-only systems and eliminate the need for availability of excitation load and initial estimate of the system parameters. Furthermore, the performance of the algorithm is evaluated using data from an ambient vibration test of Golden Gate Bridge. Results of these implementations verify the functionality of the algorithm in monitoring of real-life structural systems.

Chapter 4 presents an effort towards understanding the effects of measurement noise on the modal identification. One challenge associated with the design of wireless sensor platforms is the trade-off between the functionality and the power consumption and attempts for minimizing the cost. These considerations usually cause limitations in the architecture and quality of wireless sensors which do not necessarily exist in the design of

wired systems. Thus, it is important to carefully investigate the impact of sensor quality on the results obtained from data-driven SHM applications. This study develops parameters that quantify the quality of estimated modal parameters and determine the influence of noise on accuracy of results. The performance of these parameters is validated by a numerically simulated example and then, they are used to investigate the accuracy of identified modal properties of Golden Gate Bridge using ambient data, collected by wireless sensors. The vibration monitoring tests of Golden Gate Bridge provided two synchronized data sets collected by two different sensor types. The influence of sensor's noise level on the accuracy of results is investigated throughout this work and it is shown that the high quality sensors provide more accurate results as the physical contribution of response in their measured data is significantly higher. The developed quality metric and the implementation on numerical and real-life data are presented in Chapter 4.

Chapter 5 presents contribution of this research in development and validation of a damage detection algorithm. A damage detection algorithm is validated through experimental implementation on different experimental specimens constructed in ATLSS research center. A scaled steel beam-column connection is densely instrumented by synchronized sensor networks of both traditional wired piezoelectric and wireless sensors. The collected response data from the experimental model are used to estimate the two sets of influence coefficients with the wired one as the reference baseline. The functionality of the algorithm is validated and in addition, the effect of sensor quality on

its performance is evaluated by comparing the resulted quality metrics from two sensor networks. The algorithm is also implemented on the strain data collected from a large scale beam-column connection under cyclic loading. The results of these works on damage detection are presented in Chapter 5.

Chapter 6 presents an example of application of sensing in structural monitoring and performance evaluation of a building structure. A state-of-the-art sensing system, consist of both wired and wireless sensors, together with different data processing techniques is utilized for forensic quantification of the building. The performance of the building is evaluated in terms of serviceability and strength demand. Time- and frequency-domain analysis of response and wind spectrum analysis are some data processing tasks performed in this work.

Chapter 7 also presents another field implementation which is deployment of a network of wireless sensors for vibration monitoring of a steel bridge structure. The monitoring task is performed in a one-year period during multiple tests (more than 50 tests) in different seasons as to not only identify the dynamic characteristics of the bridge, but also find the uncertainty introduced to the results due to the changes in environmental and operational condition of different tests. The parameters which their effects are studied in this work are temperature gradient and the volume of traffic load. Variation of results due to variation of each of these factors and a general conclusion is presented in Chapter 7.

Chapter 8 provides a summary of the research presented in this dissertation and discusses the original contribution and the broader impact of the research and finally the potential future studies to continue the advancement in data-driven SHM.

Chapter 2

Background and Literature Review

2. Background and Literature Review

This chapter presents development history and a summary review of some of the fundamental topics of this research including WSNs and their application for SHM, advantages and challenges of wireless sensors for SHM, and modal identification of structural systems as a basic practice in SHM. The terminology and methodologies explained in this chapter will be used later in other chapters of this dissertation.

2.1. Wireless Sensors for Structural Health Monitoring

A wireless sensor network is defined as a set of integrated elements which work together to measure a physical quantity, and interrogate and wirelessly transmit the measurements to a receiver, called base station, for repository. To achieve these capabilities, each unit in a WSN needs to encompass four fundamental subsystems: sensing interface, processing core, wireless transceiver and power supplier.

(i) Sensing interface is designed to measure the physical quantity of interest (e.g. acceleration, displacement, strain, temperature, etc.) and convert the measured analog data into the digital data. This part usually includes sensors for measurement and other supplemental components such as Analog to Digital Convertor (ADC), Signal Conditioner and amplifier, for conditioning and converting the data.

(ii) The processing subsystem is integrated to save, process, and interrogate the measured data. This part includes processor, random access memory (RAM) and read only memory (ROM), as the fundamental components.

(iii) Wireless transceiver enables the wireless units to communicate with other units and the base station to send/receive data through radio signals. The wireless transceiver is usually embedded on the processing board.

(iv) Power supplier is a simple part of a wireless sensor unit which provides the required power for all subsystems. This component usually consists of a battery board interfaced with processing board. Energy harvesting techniques can also be integrated for supplying the required power, as well.

Wireless sensor prototypes may differ from each other based on their computational power, the type of physical quantity which is measured, the power consumption, the communication capability and associated cost. Over the past decade, numerous WSN prototypes have been developed and deployed on experimental and real-life structures. Each prototype introduced an improvement over the earlier versions and a solution to a challenge in WSN. Some of these WSN designs were deployed in large-scale structural monitoring projects and their performance were evaluated under realistic conditions.

Based on available summary reviews (Spencer et al. 2004 and Lynch et al. 2006), WSN platforms can be divided into two broad categories of academic and commercial WSN prototypes. Academic prototypes generally incorporate commercial out-of-the-shelf components based on the specific requirements of users. While academic platforms are well suited for specified requirements of SHM, their limited number of users prevents the technical contribution of other communities and therefore restricts their access to technology advancements (Rice, 2008). In contrast, commercial platforms are developed

based on open source hardware and software which allows the access by broader community and makes them a better choice for large variety of industrial applications. However, both academic and commercial platforms have played important roles in the development of WSN application in SHM.

As the first WSN platform for SHM application, Straser and Kiremidjian (1998) proposed the design of a wireless modular monitoring system (WiMMS). This low-cost sensing unit was built around a Motorola 68HC11 microprocessor, micros prototyping board NMIT-0022 and 64 kB address space for data and program storage. In order to store embedded software for local data processing, 32 kB of additional RAM and 16 kB of additional ROM were included in the design. An eight-channel, 16- bit, 240 Hz Harris H17188IP sigma-delta ADC was used to convert analog signals to digital forms. The sampling rate of this ADC was fixed 240 Hz and no anti-aliasing filter was utilized. This prototype is considered as the first step toward application of WSN in SHM (Lynch et al 2006).

Later in early 21st many researchers developed new wireless sensor platform by selection of different components and improving the hardware and software architecture to address particular challenges. Mitchell et al. (2002) proposed a new architecture of WSN in SHM which was based on distribution of monitoring procedure among wireless sensors. In this design, the network consists of several clusters each has a separate server which is called cluster node. Each of the cluster nodes was designed to have both short and long-range radio for communication with nodes in its cluster and other cluster nodes

in the network. A powerful Cygnal 8051F006 microcontroller is integrated on the platform of sensing nodes. Similar to the idea of two-tiered wireless SHM system proposed by Mitchell et al. (2002), Kottapalli et al. (2003) developed a prototype which separated sensing units in different groups and put a site master on the top of each group. This prototype aimed to overcome challenges associated with power consumption and time synchronization. In this design, the hardware platforms of sensing units were different from site masters. Since the power consumption of the site master is relatively high, the site master node is considered to be connected to an outlet power. This issue limits the application of this architecture design of WSN. Power consumption of microprocessors with high computational throughput motivated Lynch et al. (2003a, 2004a, 2004e) to focus on the design of a low-power but computationally powerful wireless sensing unit. This unit integrated a dual-processor computational core which one of them was designated for overall operation and real-time data collection and the other one was utilized for the local processing of data. Using two types of processor, each appropriate for specific purpose, the power consumption would be optimum. Later, Swartz et al. (2005) presented the design of a wireless sensor platform called Narada, which was designed for both monitoring and feedback control of civil structures. The distinguishing feature of the Narada wireless sensor node was the inclusion of an actuation interface for high speed feedback control of actuators. The Atmega128 is a low-power, 8-bit microcontroller with 128 kB of flash memory, 4 kB of electrically erasable programmable read-only memory (EPROM), 4 kB of static random access memory and an additional 128 kB of external static RAM are integrated on this wireless sensor

platform. For wireless communications, the Texas Instruments CC2420 IEEE 802.15.4 transceiver is selected. The CC2420 operates on the 2.4 GHz band at 250 kbps using direct sequence spread spectrum (DSSS) radio frequency modulation techniques. The CC2420 transceiver enables the user to adjust the signal strength from weak to strong. This feature is particularly useful since it allows balancing the communication range and the power consumption of the radio.

Because of the out of-the-box operation of the commercial platforms and also their low cost and technical supports from the manufacturers, this class of WSN platforms became more attractive for many researchers (Rice, 2008). Mote wireless sensor platform was one of the first wireless sensor platforms which attracted researchers in different disciplines. The goal of creation of this family of platforms was development of a "smart dust" which was tiny, autonomous, low-power and low cost for use in dense sensor arrays (Hollar 2000). Mote platform later became commercialized by Crossbow (http://www.xbow.com) and available to the public. Rene Mote (1999) was the first commercialized prototype of this family. The software platform for Mote was TinyOS and nesC programming language. To employ Mote wireless sensors in structural monitoring systems, Tanner et al. (2002, 2003) presented the application of Crossbow Rene2 Mote in a SHM system. Two types of Micro Electric Members (MEM) were integrated in this platform: the Analog Devices ADXL202 and Silicon Devices SD-1221 with a 10-bit ADC. Small amount of on-board RAM and sampling of only one channel at each time instant were two limitations of Rene2 Mote.

In early 2002, Crossbow released MICA Mote wireless sensor which incorporated 8-bit Atmel ATmega103L microcontroller with 128 kB flash ROM, 4 kB RAM for installation of embedded programs (Tiny OS) and 512 kb of non-volatile, off-chip memory. The single-channel amplitude modulation TR1000 wireless transceiver was selected for wireless communications. Upgrading the radio transceiver, Crossbow introduced MICA2 (2003). This platform, offered a greater reliability of communication with using Chipcon CC1000 wireless transceiver. The Chipcon CC1000 operates on the 900 MHz radio band and is capable of 38.4 kbps data transmission rate. Upgrading this platform, Crossbow introduced MICAz in 2004 which incorporates 2.4 GHz IEEE802.15.4 wireless transceiver which is more improved compared to Chipcon CC1000.

Tmote Sky (2006) is another mote platform suitable for extremely low power, high data-rate sensor network applications. The low power operation of the Tmote Sky module is relied on the ultra-low-power TI MSP430 F1611 microcontroller. The 16-bit RISC processor features extremely low active and sleep current consumption. The microcontroller is coupled with 10 kB of RAM and 48 kB of flash memory. It also uses a USB controller from FTDI to communicate with the host computer. The MSP430 microcontroller has eight external 12-bit ADC ports of which six are accessible on a pin header on the Tmote.

Realizing the popularity of Mote platforms, Intel Research Berkeley Laboratory cooperated with UC Berkeley and introduced a new platform called Imote (Kling et al.

2005). This new platform integrated only the computation core and radio transceiver. Based on the choice of user, any sensor board can be designed to be attached onto the Imote circuit. This platform employs the 32-bit ARM7TDMI microcontroller operating at 12 MHz which its significant computational power makes Imote distinguished from other platforms. As an upgraded version of Imote, Intel released the most recent generation of Mote wireless sensor platforms, called Imote2 (2007). This platform integrates a low-power PXA271 XScale CPU. The processor operates in a low-voltage, low-frequency mode, and enables low-power operation. The frequency of processor can be scaled from 13MHz to 416 MHz with dynamic voltage scaling, which is a key feature for optimizing the power consumption. This platform contains 256 kB SRAM, 32 MB SDRAM, and 32 MB of FLASH memory, which makes it even more popular than other smart sensor platforms. For communication purposes, Imote2 integrates the CC2420 IEEE 802.15.4 radio transceiver from Texas Instruments, which supports a 250 kb/s data rate with 16 channels in the 2.4 GHz band. A 2.4 GHz surface mount antenna is provided on the Imote2 platform. Additional external antennas, like Antenova Titanis 2.4 GHz Swivel SMA, can be also used in conjunction with Imote2's onboard antenna (Linderman et al., 2008).

Figure 2.1 and Figure 2.2 show several examples of academic and commercial wireless sensor platforms developed since 1998, respectively.

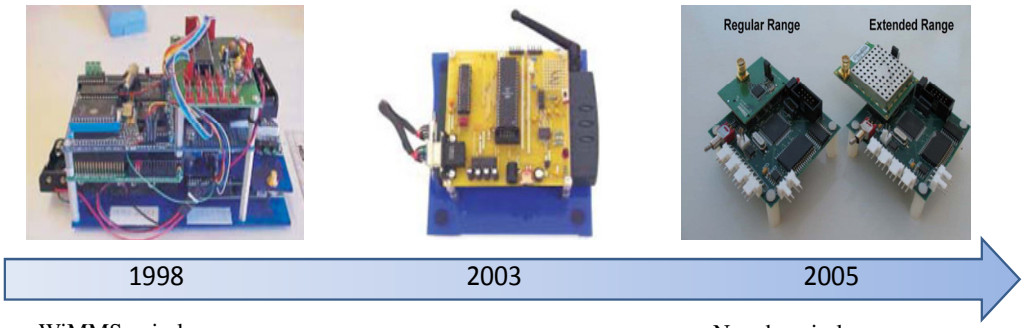

Figure 2.1. Examples of academic wireless sensor prototypes

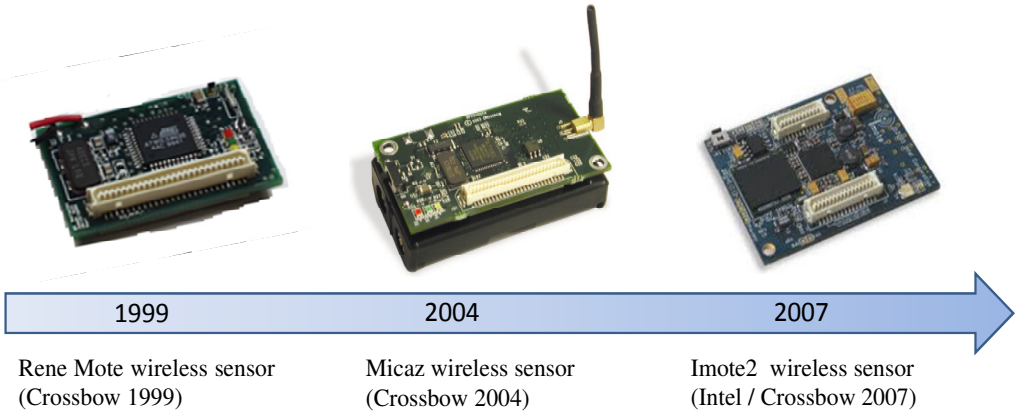

Figure 2.2. Examples of commercially developed wireless sensor prototypes

2.2. Application of WSN in SHM

Over the past decade, WSNs have been used as the primary data acquisition system in numbers of structural monitoring projects. Deployment of developed prototypes of WSN provides the opportunity to evaluate their performance in realistic scenarios and paves the road towards a broader application of this technology. A review of several prominent WSN deployments in the SHM field is presented in this section.

As the first application of WSN in SHM, Straser and Kiremidjian (1998) instrumented the Alamosa Canyon Bridge with the developed wireless sensor platforms to validate their performance. Researchers from Los Alamos National Laboratory had previously instrumented the bridge with traditional sensor networks for system identification purpose and the modal properties of the structure were documented. In this work, totally five wireless sensing units with EG&IC 3145 MEMS accelerometers were mounted to the girder along one of the spans. The response of the bridge under ambient and impulse loading was recorded by both wired and wireless systems. The modal parameters obtained from wireless network data were perfectly consistent with the results of the wired sensor system.

This implementation was particularly important as it was the first application of WSN in monitoring of structural systems. Following this work, many other platforms are deployed for monitoring of bridge and building structures. These implementations are conducted to either verify the performance of the platforms, through cross-verification (using traditional wired sensors), and/or to extract the structural and dynamic characteristics of the instrumented structures. A few of the largest and the most up-to-date deployments are briefly presented in the following paragraphs.

Pakzad et al. (2008) at University of California-Berkeley designed and implemented a wireless sensor platform for monitoring of the Golden Gate suspension bridge. In this platform two commercially available MEMS accelerometers, ADXL202 and Analog Devices (SD 1221), were used to measure the high-level and low-level accelerations

respectively. This combination of two accelerometer types was a cost-effective way in design of sensor units. The ADXL202 has ±2 g range and the sensitivity of 1 mg at 25 Hz which makes this accelerometer suitable for measuring the high-level accelerations (Analog Devices 1999). In conjugate with ADXL202, the Silicon Design 1221L, with noise ceiling of 10 μg, was used to measure the low-level accelerations. The processing board of this platform was Micaz. The network included 64 wireless sensors collecting data simultaneously and is considered as the largest deployment of WSN up to the date of implementation. Wireless sensors were installed along the long-span and the tower of the bridge (54 sensing units on the main span and 8 units on the south tower). The sampling rate during this test was 1 KHz and the data were down-sampled into 50 and 200 Hz. This large spatial resolution of the network and high sampling rate of 1 kHz resulted in about 20 MB of data at each cycle of measurement and collection which took about 9 hour of transmission to the base station. Because of the long linear topology of the structure, multi-hop/pipelining data communication routing was used for transmission of data in the network. In the multi-hop routing the data is transferred to the base station using the intermediary nodes. Finally, the collected data were used to extract the modal properties of the main span and the south tower of Golden Gate Bridge.

Whelan et al. (2009a) at Clarkson University's Laboratory for Intelligent Infrastructure and Transportation Technologies (LIITT) developed a wireless sensor platform and deployed this platform in a network of 40 channels for monitoring of a single-span bridge in St. Lawrence County, NY. The presented platform incorporated the Tmote Sky

wireless sensor network platform together with single-ended and differential analog signal conditioning for increasing the quality of collected data. Totally 29 low-noise, low-power LIS2L02AL MEMS accelerometers together with 11 strain transducers were installed on the bridge. In this work, real-time data transmission is used which made it different from other similar works. The sampling rate for measurement was 512 Hz which after passing through a low-pass filter it was down-sampled to 128 Hz. Because of the real-time data transmission, the low sampling rate was necessary. Less than 0.1% data loss during real-time transmission was reported in this work which is acceptable for the SHM applications. Modal properties of the instrumented bridge were extracted using the measured data. Using the same platform and configuration, Gangone et al. (2009) performed several other field experiments on Wright Road, Route 56 Colton and Route 345 Waddington Bridge.

Finally, as the largest WSN deployments, Jang et al. (2010) and Cho et al. (2010) presented deployment of a network of 70 wireless sensor nodes on Jindo, Bridge in Korea. In the data collection phase, the network was divided into two sub-networks, one with 33 nodes and one with 37 nodes, on two sides of the bridge. The reason for dividing the network in two separate sub-networks is the use of single-hop data transmission. In this deployment Imote2 together with SHM-A multi-scale sensor board are used. To monitor the wind, the SHM-A is modified with adding an anemometer and is named SHM-W. This sensor board has three external channels for wind speed in three directions and one channel for acceleration. As a solution to power consumption problem in long-

term monitoring, energy harvesting with solar panels are used for some of wireless sensor nodes. The software platform which is employed during this deployment is ISHMP service tool-suite, developed in Open Systems Laboratory & Smart Structures Technology Laboratory at University of Illinois at Urbana Champaign. The network is programmed by an autonomous SHM network management application, called Auto-Monitor, which combines Remote-Sensing, Decentralized-Data-Aggregation, Threshold-Sentry and Snooze-Alarm applications (Rice and Spencer 2009). Installing Auto-Monitor application on the base station, the user can decide whether raw acceleration data or the correlation functions from the local sensor nodes of the network are returned to the base station by selecting one of the Remote-Sensing or Decentralized-Data-Aggregation applications respectively. The network was programmed to perform data collection 4 times per day for a period of 4 months. At each run, 10,000 samples of acceleration data were collected and transmitted to the base station. Threshold-Sentry application was installed to make additional measurement in the case of vibrations more than 50 *mg* which was the triggering threshold. The performance of the network is evaluated after 4 months of monitoring. Stable and reliable performance of the network is reported. As a limitation in this deployment, single-hop routing of this network has significantly restricted the length of the radio coverage and imposed the division of network to two sub-networks. As a result the collected data from two sub-networks are not synchronized.

2.3. Advantages, challenges and solutions in WSN

Due to the advantages of WSN, researchers are interested in using this technology for SHM. Relative low-cost, ease of implementation and the capability of data management via on-board processing are the main advantageous features of WSN.

The *low-cost*: this characteristic becomes evident when considering a simple comparison of different instrumentation costs. Celebi et al. 2002 reported an average of $15,000 per sensing channel on instrumentation of Emerson Memorial Bridge with cable-based data acquisition system while in the vibration monitoring of Jindo Bridge, Jang et al. (2010) reported an average of less than $500 per each wireless sensor unit. Such a significant difference between the cost of wireless and wired sensor networks in SHM clearly attracts engineers to application of WSN.

The *ease of installation*: using wireless sensors eliminates the time of installation of wires and results in the rapid deployment of WSNs. Straser and Kiremidjian (1998) reported 30 minute time for the installation of each wireless sensor, whereas for a similar project but cable-based monitoring system, this time is about 150 min. in average (Lynch et al. 2006). Additionally, due to the elimination of wiring, modification of network geometry is easy, such that additional sensors can be easily added to a network as it is required or the sensor locations can be effortlessly changed.

The *capability of on-board computation*: this feature is used for on-board digital signal processing, data aggregation and self-operative functions. Using the capability of on-

board computation, the collected data can be processed and transformed into a more efficient format and then transmitted to the base station. This strategy eliminates the transmission of a large volume of raw data and consequently preserves the limited battery power.

Considering these advantages, the question which remains is that why despite all the advantages of WSNs, this approach has not still achieved its wide-spread deployment in health monitoring of structural systems and is not the preferred tool for commercial projects in the industry yet. The reason is perhaps attributed to the existence of a few challenges in the way of broad acceptance of the WSN technology. These challenging drawbacks can be categorized as: (i) the need for time synchronization of sensor nodes in the network, (ii) the uncertainty in wireless communication (i.e. data transmission reliability), (iii) the limitation in wireless data transmission bandwidth, and (iv) the prohibitive power consumption.

2.3.1 Time synchronization

Time synchronization of the wireless networks has been one of the challenges in the wireless technology which has been the focus of researchers for several years since their early applications. The situation in wireless communication is such that when a simple command/data is sent to a cluster of receivers, in a network, it is not always feasible to have all the nodes receive it at the exact same time and start performing the requested task all together. Therefore, in a scenario which sensors collect vibration data, the captured response at different locations do not correspond to the exact same time and as a

result, the obtained results will experience an erroneous phase shift. For instance, the result of non-synchronized network in system identification will be extraction of structure's natural modeshapes with phase lags and estimation of non-symmetric stiffness matrices. The approach that addresses this problem is called network time synchronization. Fortunately, extensive research have been conducted on this topic over the past several years and these studies have resulted in many advanced approaches. Currently, time synchronization protocols are perfectly reliable and necessarily included as a part of wireless sensor applications. Maróti et al. (2004) and Ying et al. (2005) are examples of a broad collection of studies on this area.

2.3.2 Data transmission reliability

Another primary challenge in the wireless technology is the radio miss-connectivity which may result in data loses during transmission. The low signal power, absence of the line-of-site in communication, signals collision and physical interference between the wireless communication lines are major reasons of this issue. To overcome the data loss during wireless communication, researchers have developed protocols, called reliable data transfer protocols. These approaches ensure the transmission of the entire data packets when the communication is physically feasible. One example of such protocols is the Scalable Thin and Rapid Amassment Without loss (Straw) which is a selective negative-acknowledgement (NACK) collection protocol. In this transmission scheme, the data is sent to the receiver upon a request and then, the receiver identifies and sends back a list of missing packets asking for retransmission (Pakzad et al. 2008). This task

continues until transmission of all the data. During the past decade, many advanced algorithms have been developed for addressing challenges and enhancing the communication reliability of the wireless networks and thus, this is no longer a critical issue in the application of WSNs in SHM.

2.3.3 Data transmission bandwidth

The limited bandwidth in wireless communication is another challenge in application of WSNs. This issue is particularly important when a large amount of data is required to be transferred timely, as a following action is waiting for the completion of the communication. This scenario is a possible situation in the long-term monitoring of structural systems (e.g. when the sensor network is required to capture the response to drastic events, such as earthquake, and a follow up conclusions are necessary to be made immediately).

One effective solution to this issue is to minimize the communication burden, using the on-board computation. This approach is called optimal data communication and targets minimizing the required in-network data transmission. The basic idea in the optimal data communication is utilizing the on-board computational capability of wireless sensors, aiming to minimize the required time and energy for estimating the state of the structure from the measured data. In a majority of WSN deployments for SHM, the network architecture is designed such that all data is sent to a central station for further data processing. In such a central data processing scheme, a long time and large portion of the finite power resource is spent on wireless communication for transmission of

collected data. However, through the use of an optimal usage strategy, a system can be designed such that it incorporates the on-board computation for data conversion or data processing and preserves time and power by avoiding the communication of the entire collected data.

One example of such algorithms is Distributed Computing Strategy (DCS) which is a hierarchical approach of data processing. This approach takes the advantage of wireless sensor's computational capacity and involves sensor nodes in the data processing task. In this scheme, the sensor network is divided into hierarchical communities, in which each community communicate inside their own network, perform system identification among their local community and send the outcomes to the higher level cluster heads. The DCS was initially developed for implementation of Natural Excitation Technique (NExT, James et al. 1993) in conjunction with ERA (Juang and Pappa 1985) for system identification. Later, the flexibility-based Damage Locating Vector (DLV) method (Bernal 2002) also adopted for DCS. This distributed approach reduces the amount of required communication and therefore conserves energy and transmission bandwidth. Figure 2.3 shows a schematic transmission routing in the hierarchical topology. The deficiency of these approaches is that they are not completely distributed, but partially distributed. Thus, significant portion of processing is still left for the centralized processing. Also, they are restricted by the topology of the network and the utilized algorithm, and more importantly, their efficiency is not high enough to alleviate the problem. Chapter 3 presents a novel distributed data processing technique which is

developed to estimates the parameters of the instrumented system through an onboard iterative estimation approach. The efficiency of the developed approach is significantly higher than the available algorithms and it does not leave any portion of processing to the central processing. Details of the algorithm and the implementation examples are presented comprehensively in Chapter 3.

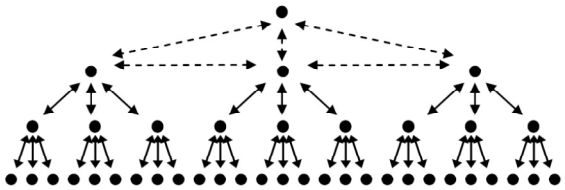

Figure 2.3. Hierarchical topology of a wireless network

Another solution to the limited bandwidth of the network is to use different transmission routings, such as multi-hop data communication, instead of simple one-hope transmission between each node to the base station. Multi-hop communication is defined as transmission of data between two nodes that are not in the direct radio range, using intermediary nodes (Pakzad et al. 2008). This routing is useful in linear network topologies. To make an effective use of the available bandwidth during the data transmission in multi-hop scheme, data pipelining is also proposed. The basic idea of pipelining is to schedule the data transmission of the nodes along the multi-hop communication path, such that it maximizes the channel usage and minimizes the energy and time (Li et al. 2010). Figure 2.4 graphically shows the pipelining approach in multi-hop data transmission scheme.

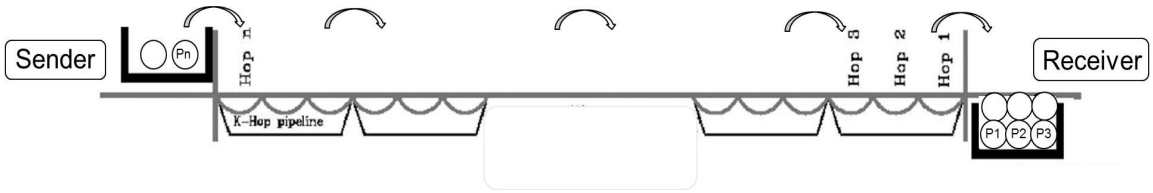

Figure 2.4. Multihop/Pipelining data transfer

2.3.4 Power consumption

In absence of wires in a sensor network, maintenance of power for different components of a sensor unit is considered as a critical issue. Although using battery as a ready-to-use power resource is a convenient option, the regular replacement, required for long-term monitoring, makes it a challenging drawback. One solution to this challenge is using energy harvesting approach which is transformation of available environmental energy such as wind, solar power, vibration and thermal, to the electrical energy. Over the past decade, many researchers have been working on this topic. Meninger et al. (1999, 2001), Elvin et al. (2001), Casciati et al. (2003d), Churchill et al. (2003), Sodano et al. (2003, 2004) and Wang et al. (2003b) are few examples of studies on this area. In a comparison work, Roundy et al. (2004) compared the potential power densities from different environmental energy sources and showed that the solar energy is the largest energy source available and proper for the field deployments. Table 2.1 shows the power densities that can be obtained from different sources. Jang et al. (2010) and Hoult et al. (2010) are two examples of recent WSN deployments which have used energy harvesting with solar panels as one of the power sources. Although this approach is an effective solution, the associated expenses are still relatively high.

Table 2.1. Comparison of energy sources (Roundy et al. 2004)

Source	Power density ($\mu W/cm^3$)
Solar (outdoors)	15000 (direct sun) 150 (cloudy day)
Solar (indoors)	5 (office desk)
Vibrations	200
Acoustic noise	0.003 at 75 dB 0.96 at 100 dB
Daily temp. variation	10
Temperature gradient	15 at 10^oC gradient
Shoe inserts	330

Optimal usage of the energy is another approach which can increase the life-time of batteries of a wireless monitoring system. When the power resource is strictly limited, careful consideration needs to be given to the consumption of different components of a wireless sensor unit. Sensing unit, processor and the transmission unit are different power consumers of a wireless sensor unit. Among these components, the radio transceiver is the major power consumer which consumes significantly more energy in comparison with other components. As an example, Whelan et al. (2009) reported that the power consumption of the CC2420 transceiver is 59 mW, whereas the MSP430F1611 microcontroller and LIS2L02AL accelerometer consumes 2.5 and 2.4 mW (both in the active mode) respectively. This comparison shows noticeable higher power consumption of transmission task in a wireless sensing unit. Therefore, it is an effective approach to optimize the power consumption of communication and minimize the volume of the data for transmission.

Considering the transmission of the raw data as a time consuming task and a wasteful use of energy resources, data compression (Lynch et al. 2003) and data conversion approaches, such as the use of frequency responses (Caffrey et al. 2004, Lynch et al. 2004a, Lynch et al. 2004b, and Nitta et al., 2005), have been developed to reduce the volume of communication. Research has also been focused on distributing damage detection algorithms to make them suitable for implementation on WSN (Lynch et al. 2004, Gao et al. 2006, and Hackmann et al. 2008). More recently, further progress is made towards the concept of local data processing for modal identification such that just an informative and condensed format of the data is communicated through the network.

Swartz et al. (2009) proposed a decentralized damage detection algorithm using transfer function. In this algorithm, the collected data in each sensor is used to fit a time-series model and then associated coefficients are estimated using Auto Regressive Exogenous (ARX) algorithm. Employing these coefficients, the transfer function of the structural system is estimated. The migrations of poles of the system in different experiments are used to construct a parametric feature representing the occurrence and severity of the damage. For validation purposes, this algorithm was implemented on a laboratory specimen and the reliability of the algorithm was reported. In another work, Castaneda et al. (2008) employed the on-board processing capability of wireless sensors to calculate the power spectrum density and corresponding parameters of curve fitting of the response at each separate node. Afterward, the estimated parameters are sent to the base station for implementation of a correlation based damage detection algorithm. The

described DCS approach, proposed by Gao and Spencer (2008), is also another example of effective works on this area.

Compared to the damage detection, less attention is paid to development of onboard modal identification algorithms. An example of such approaches is Coordinated Computing Strategy (Nagayama and Spencer 2007) which divides the network into a number of sub-networks with cluster heads in a hierarchical topology. In this design, all the leaf nodes in each sub-network receive the data from cluster heads and estimate and broadcast the correlation functions (under the assumption of ambient excitation) for implementation of Eigensystem Realization Algorithm (ERA). Further improvement of the approach is the use of decentralized Random Decrement Technique (Sim, et al. 2010) in which instead of transmission of raw data from cluster head to leaf nodes, the trigger crossing information is sent for estimation of correlation functions. Although these approaches reduce the amount of communicated data, they are partially distributed, restricted by the network topology and the underlying identification algorithms and their efficiency is not high enough for this problem. Additionally, more algorithm improvement is still required to remedy the latency and power consumption issue which exist in the current WSN deployments.

Chapter 3 presents an approach which is developed in this research and aims to distribute the modal identification process in network such that the modal parameters of the structural system are identified without need for transmission of raw data from sensors to a central computation station. This approach utilizes an iterative estimation

which is similar to Estimation-Maximization (EM) algorithm. The developed approach is flexible in the type of underlying algorithms and can be adopted to use different standard system identification and simulation techniques. To provide a background on the concept of modal identification, the next section provides the necessary terminology and a summary review of some commonly used algorithms.

2.4. A review on system identification algorithms

Health monitoring of civil infrastructure may be classified into two general terms of "local" and "global" monitoring. The local health monitoring seeks the local deficiencies and malfunctioning of the system's components which is usually based on physical evaluation or visual inspection. On the other hand, the global term monitors the general behavior of the system over its designed life-time. One of the most effective classes of global health monitoring is vibration-based monitoring which estimates the state of the structure using its dynamic response. The approach in which a mathematical model is estimated for a system using the experimental observations (i.e. its response) is called system identification. In other words, system identification is defined as the process of developing a mathematical model for a physical system by using experimental data (Juang and Phan 2001). Generally, in any system identification algorithm, the objective is to estimate the dynamic characteristics of the system (e.g. modal properties), using the output response of the system with or without the input load. Figure 2.5 illustrates the general idea of the System Identification for a Multi Input Multi Output (MIMO) system.

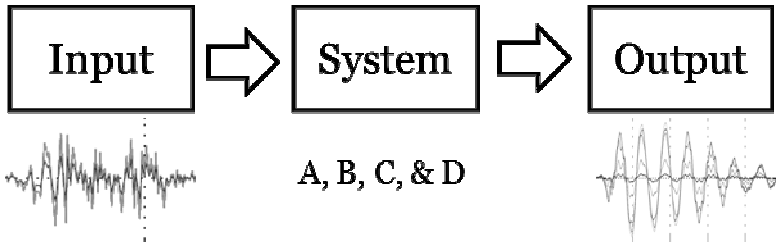

Figure 2.5. System Identification

System identification has been an active research area for a few decades in many engineering fields such as electrical, control, mechanical and civil engineering. Because of its broad application, a large variety of system identification algorithms have been developed to date. The concept was first introduced to civil engineering researchers by Liu and Yao (1978) and since then, it has been attracting attentions due to its application in damage detection of aged structures, finite element model updating, and verification of the finite element models of newly constructed structures.

System identification techniques in civil and mechanical engineering are generally classified in two categories: "input-output" and "output-only" identification algorithms (Yi and Yun 2004). Input-output class is developed based on the availability of information about the excitation of the structure and therefore they can be carried out when the input loads are controllable and/or measurable. In contrary, output-only algorithms are independent of exact excitation function and can be applied when the excitation is random ambient loads such as traffic and wind loadings. In output-only algorithms, the ambient excitation is considered to be stationary stochastic process.

The need to perform ambient vibration tests emerged in structures where controlled excitation is very expensive, difficult and even impractical. Civil infrastructure such as bridges and buildings are examples of this class of structures. While testing under ambient loads is simple and practical for civil structures, it adds some uncertainties into the identification problem. One common uncertainty regarding ambient vibration tests is the non-stationary assumption of excitation. Although ambient vibrations are considered as random inputs, they are not perfectly stationary functions and thus the results obtained upon this assumption contain some uncertainties. A solution to minimize this issue is collection of sufficiently long data from the response of the structure.

In the past few decades, many algorithms are proposed on both input-output and output-only modal identification which some more important ones are discussed as follows:

Ibrahim et al. (1977) developed an algorithm, called Ibrahim Time Domain (ITD) algorithm, which provides the modal properties of the structure using its free vibration response (Ibrahim and Mikulcik 1977, Ibrahim and Pappa 1982). When the excitation is ambient, the free vibration response can be extracted using Random Decrement Technique (RDT) (Ibrahim, 1977, Yang et al., 1984). Juang and Pappa (1985) introduced an algorithm called Eigen Realization Algorithm (ERA). ERA uses Markov parameters to construct the Hankel matrix which from its singular value decomposition (SVD), state space matrices can be extracted. Similar to ITD method, ERA works with the free vibration response of the structure (Markov parameters are formed based on the free

vibration response of the structure). Later, Natural Excitation Technique (NExT) (James et al. 1992) was developed to estimate the free vibration response of the structure using ambient response. NExT uses the white-noise property, in which there is no correlation between the inputs in different time steps, and shows that the cross correlation function between responses of structure to white-noise at two DOFs (y_1 and y_2) is the same as the impulse response at y_2 due to a unit impulse, u_1, multiplied by a factor. Implementation of NExT in identification of modal parameters of various types of civil structures under ambient vibration demonstrated the effectiveness of this algorithm. Researchers employed NExT for the system identification in both analytical and experimental studies. James et al. (1993) identified modal parameters of the Department of Energy/Sandia vertical axis wind turbine using NExT, in combination with the Poly-reference Technique and the ERA. Results of this work showed an agreement between the modal parameters from identification and analytical model. Beck et al. (1994b) also applied NExT to identify modal parameters of the Robert A. Millikan Library located at the California Institute of Technology. In another work, Farrar and James (1997) used NExT to determine natural frequencies and mode shapes of a portion of a bridge which once spanned the Rio Grande in Albuquerque, New Mexico along the I-40 highway.

Anderson (1997) proposed application of Auto-Regressive and Moving-Average with Exogenous terms (ARMAX) models for system identification. ARMAX uses stochastic relationships between input and output data and forms the state space matrices of the

system using ARMA parameters in different forms of controller, observer or modal forms.

Van Overschee and De Moor (1994) proposed numerical algorithms for subspace state-space identification (SSI) which similar to ERA utilizes the SVD of block Hankel matrix with cross correlation matrix of the response. The basis of SSI is the stochastic state space equation which considers the dynamics of the system under stochastic random excitation and random noise. This method decomposes the Hankel matrix into observability and controllability matrixes and from there, the system matrices can be extracted from observability matrix.

Another class of system identifications is frequency domain algorithms. As well as the time domain algorithms, a broad variety of frequency domain approaches are developed in past few decades. Power Spectral method (also known as peak picking) is one of the most popular methods in which the modal properties of the structure can be extracted by reading the peak frequencies and amplitudes of Power Spectral Density (PSD) function (Newland 1984, Bendat and Piersol 1993). Frequency Domain Decomposition (FDD) (Otee et al. 1990, Brinker et al. 2000) is another algorithm which uses the singular value decomposition of PSD function to estimate the modal properties of the system. In this method, natural frequencies are estimated based on the peaks of the first singular values and mode shapes are estimated from the first singular vectors at frequencies corresponding to peaks of the singular values. Poly-reference frequency domain algorithm (Zhang et al., 1985), orthogonal polynomial algorithm (Rechardson et al. 1982,

Vold, 1986 and Auweraer et al., 1987), Complex Mode Indication Function (Shih et al. 1988) and multivariate mode indication function (MvMIF) (Williams et al. 1985) are some other examples of frequency domain modal identification.

Discussion about the details of all developed system identification algorithm is not the scope of this research. However, in this section, a brief description on a few commonly used time domain identification algorithms, ERA, Stochastic Subspace Identification (SSI) and Auto Regressive with exogenous (ARX) model, is presented to provide the background and the terminology for other chapters.

Considering the dynamics of a mechanical system consisting of n masses connected through springs and dampers, the equation of motion can be written as following matrix differential equation:

$$M\ddot{q}(t) + C_d\dot{q}(t) + Kq(t) = u(t) \tag{2.1}$$

where M, C_d and K are n by n mass, damping and stiffness matrices, $u(t)$ is the input of the system which can be an external excitation or ground motion, and $\ddot{q}(t)$, $\dot{q}(t)$ and $q(t)$ are the acceleration, velocity and displacement vectors at time t.

Although the physical model of Equation 2.1 is a good representation of the dynamics of a structure, it is not a proper model in an experimental modeling context (Peeter et al. 2001). First, in most of the practical problems, it is not possible to measure the response of all DOFs of the FE model. Second, while there are many additional unknown excitations, the presence of noise in the experimental modeling should be also

considered. These two issues of FE model can be resolved by the use of State-Space representation.

The state space model in continues domain is presented as follow:

$$\begin{aligned} \dot{x}(t) &= A_c x(t) + B_c u(t) \\ y(t) &= Cx(t) + Du(t) \end{aligned} \qquad \text{(2.2a \& 2.2b)}$$

where $x(t)$ is defined as the state vector at time t, $y(t)$ is the observation vector at time t, $u(t)$ is the input vector, A_c is the state matrix, B_c is input matrix, C is the observation matrix (also called influence matrix) and D is transmission matrix. All these variables are in continues domain.

The state of the system, $x(t)$, can include any variables representing the system. One conventional chooses of structural systems is as follow:

$$x(t) = \begin{bmatrix} q(t) \\ \dot{q}(t) \end{bmatrix} \qquad (2.3)$$

For such state variables, the state and input matrices would be:

$$A_c = \begin{bmatrix} 0 & I \\ -M^{-1}K & -M^{-1}C_d \end{bmatrix} \qquad (2.4)$$

$$B_c = \begin{bmatrix} 0 \\ M^{-1} \end{bmatrix} \qquad (2.5)$$

M, K and C are mass, stiffness and damping matrices of the structure. $y(t)$ in Equation (2.2) is the observation vector at time t which is defined based on the observed response

at specified DOFs. The definition of matrices *C* and *D* depend on the vector of observations. For example if *y*(*t*) is defined as the accelerations at all DOFs, the corresponding *C* and *D* matrices would be as follow:

$$C = [-M^{-1}K \quad -M^{-1}C_d] \tag{2.6}$$

$$D = M^{-1} \tag{2.7}$$

In practice, continues models need to be transformed into the discrete domain.

$$x(t) = e^{A(t-t_0)}x(t_0) + \int_{t_0}^{t} e^{A(t-\tau)}\,Bu(\tau)d\tau \tag{2.8}$$

$$y(t) = Ce^{A(t-t_0)}x(t_0) + \int_{t_0}^{t} Ce^{A(t-\tau)}\,Bu(\tau)d\tau + Du(t) \tag{2.9}$$

Considering zero-order-hold input and discretization as $t = (n+1)\Delta t$ and $t_0 = n\Delta t$, Equation 2.2a (state equation) can be written as:

$$x[(k+1)\,\Delta t] = e^{A(k\Delta t)}x(k\Delta t) + \int_{k\Delta t}^{(k+1)\Delta t} e^{A[(k+1)\,\Delta t-\tau]}\,Bu(\tau)d\tau \tag{2.10}$$

$$x[(k+1)\,\Delta t] = e^{A(k\Delta t)}x(k\Delta t) + \int_{0}^{k\Delta t} e^{A\tau'}\,Bu(\tau)d\tau' \tag{2.11}$$

Thus, the state-space model in discrete time can be shown as:

$$\begin{aligned} x(n+1) &= A_d\,x(n) + B_d\,u(n) \\ y(n) &= Cx(n) + Du(n) \end{aligned} \tag{2.12a \& 2.12b}$$

where n is the time index ($t = n \times \Delta t$) and A_d and B_d are discrete versions of state and input matrices. The following relation between continues and discrete state space matrices can be obtained from the solution of matrix differential equation:

$$A_d = e^{A_c(\Delta t)} \qquad \text{and} \qquad B_d = (\int_0^{\Delta t} e^{A_c \tau} d\tau).B_c \qquad (2.13)\ \&$$

and

$$B_d = \int_0^{k\Delta t} e^{A\tau'} Bu(\tau) d\tau' = A_c^{-1}(A - I)B_c \qquad (2.14)$$

where Δt is the time step. Observation and transmission matrices (C and D) in discrete and continues time models are the same.

State space representation of the dynamics of a system results in the advantage of using theories of first-order matrix differential equations. Additionally, in this form, the observation vector is separated from the system's state vector which is consistent with real situation where the measurement differs from the real state of the structure.

In most civil structures the excitation is not measurable and as a result, considering the Input-Output models is not practical. However, when the vibration source is only ambient load, it is assumed that the excitation is a white noise function and thus, output-only approaches are applicable. The state-space equation for output-only systems is modified by replacing the excitation terms in the state and observation equations [$B_d(u)$ & $D(u)$] with noise functions such that:

$$x(n+1) = Ax(n) + w(n)$$
$$y(n) = Cx(n) + v(n) \qquad \text{(2.15a \& 2.15b)}$$

where $w(n)$ is the process noise and $v(n)$ is the measurement noise.

In this formulation, the identification problem is to determine the system's state and observation matrix (A & C), having the measurement data (observation vector) and assumed errors. NExT (James et al. 1992) is an effective algorithms for solving output-only system identification which estimates the free vibration response of the structure using the cross-correlation functions of outputs when the input is stochastic Gaussian white noise. It should be noted that given the free vibration response of the system, there are several methods for identification of system's state-space model.

To clarify the theory of NExT, consider the equation of motion for a multi-degree-of-freedom, linear time invariant system (Equation 2.1) and assume that the excitation and responses are stationary random processes. Post multiplying the equation by a reference response process $q_i(s)$ and taking the expected value of both sides of the equation yield:

$$ME[\ddot{q}(t)q_i(s)] + C_d E[\dot{q}(t)q_i(s)] + KE[q(t)q_i(s)] = E[u(t)q_i(s)] \qquad (2.16)$$

Note that structural parameters (M, C_d and K) are assumed to be deterministic. E[.] in Equation (2.12) denotes the expectation. Based on definition of cross correlation, Equation 2.12 can be written as:

$$MR_{\ddot{q}q_i} + C_d R_{\dot{q}q_i} + KR_{qq_i} = R_{uq_i} \qquad (2.17)$$

where $R(.)$ denotes the correlation function. It can be easily shown that for a weakly stationary process (D. E. Newland 1975):

$$E[\dot{q}(t)q(t+\tau)] = \frac{d}{d\tau}R_q(\tau) \tag{2.18}$$

Also, based on the assumption of white noise excitation, the response is uncorrelated to the excitation for positive time lags. In other word, the response at time t_n is uncorrelated to the excitation at any time after t_n. Thus, Equation (2.13) can be written as:

$$M\ddot{R}_{qq_i} + C\dot{R}_{qq_i} + KR_{qq_i} = 0 \tag{2.19}$$

This equation shows that the correlation function of displacement processes satisfy the homogeneous differential equation of motion. Therefore, in structural systems under white noise disturbances, the free decay response can be estimated by correlation function of their responses. Next sections present the three mentioned system identification algorithms.

2.4.5 Eigen Realization Algorithm (ERA)

As mentioned earlier, there are a few system identification algorithms which estimate the dynamics of the structure based on the impulse (or free decaying) response. One of the widely-used algorithms, applicable for input/output systems, is Eigen Realization Algorithm (ERA) (Juang and Papa 1985). In ERA, using the Markov parameters, the Hankel block matrix is formed as:

$$H(n-1)=\begin{bmatrix} Y(n) & Y(n+1) & . & . & Y(n+p) \\ Y(n+1) & Y(n+2) & . & . & . \\ . & . & . & . & . \\ . & . & . & . & . \\ Y(n+q) & . & . & . & Y(n+p+q) \end{bmatrix} \tag{2.20}$$

where $Y(n)$ is $m \times r$ (m is the number of outputs and r is the number of inputs) impulse response matrix at n^{th} time step; i.e., $Y_{ij}(n)$ is the i^{th} output due to an impulse at j^{th} input. p and q are also corresponded to the order of Hankel matrix which can be determined using stabilization diagram (Peeters and de Roeck 2001a) or other approaches presented in literature. It is stated that for an acceptable result, p is better to be approximately ten times the number of modes and q should be selected to be 2-3 times p (Caicedo et al., 2004, Juang and Pappa 1985). Singular value decomposition is performed on Hankel matrix at initial time step, $H(0)$:

$$H(0) = P\Sigma Q^T \tag{2.21}$$

where P and Q are matrices of left and right singular vectors of $H(0)$ respectively and $\sum$ is the diagonal matrix of singular values. Small singular values along the diagonal of $\sum$ correspond to computational or noise modes (non-physical modes). Therefore, the row and columns associated with nonphysical mode are eliminated from the singular-vectors and singular-values matrices. The truncated matrices, $\sum_n$, P_n and Q_n are used to estimate the sate-space matrices (A, B and C) for the discrete-time structural model as follow (Juang and Pappa 1985):

$$\hat{A} = \Sigma_n^{-1/2} P_n^T H(1) Q_n \Sigma_n^{-1/2} \tag{2.22}$$

$$\hat{B} = \Sigma_n^{-1/2} Q_n^T E_m \tag{2.23}$$

$$\hat{C} = E_r^T P_n \Sigma_n^{-1/2} \tag{2.24}$$

where E_m and E_r are matrices containing 1 and 0 with appropriate dimensions ([I 0]).

Estimated state matrix can be used to extract the modal frequencies ω_i and damping ratios ζ_i of the system. Eigenvalue decomposition of the state matrix results in the diagonal matrix of eigenvalues (Λ) and the matrix of eigenvectors (ψ) which are in relationship with the system's frequencies, damping ratios and mode shapes via following equation:

$$\lambda_{c_i}, \lambda_{c_i}^* = -\zeta_i \omega_i \pm j\omega_i \sqrt{1-\zeta_i^2} \tag{2.25}$$

where (*) denotes complex conjugate and λ_c is the i^{th} eigenvalue of the continues system which is obtained from the transformation of the discrete model to the continues model:

$$\lambda_{c_i} = \frac{\ln(\lambda_i)}{\Delta t} \tag{2.26}$$

and λ_i is the i^{th} eigenvalue of the estimated discrete state matrix , i.e. $\lambda_i = diag(\Lambda)$; Δt is also the sampling time which is used in data collection.

Equation (2.21) results in:

$$\omega_i = \sqrt{\lambda_{c_i} \lambda_{c_i}^*} \quad \text{and} \quad \zeta_i = \frac{\mathrm{Re}al(\lambda_{c_i})}{\omega_i} \tag{2.27}$$

The observation matrix, C, is used to transform the computed eigen-vector to the matrix of mode shapes as follow:

$$\phi_i = C\psi_i \tag{2.28}$$

where ψ_i is the i^{th} eigenvector of the discrete state matrix and ϕ_i is the i^{th} estimated mode shape of the system.

2.4.6 Stochastic Subspace Identification (SSI) algorithm

Stochastic subspace identification is another popular time domain algorithm which can be applied on both input-output and output-only problems. This algorithm relies on the property of the stochastic state-space systems (Equation 2.11) which relates the output covariance (R) to the next state-output covariance matrix (G). R and G are defined as follow:

$$R_i = E[y_{k+i} y_k^T] \tag{2.29}$$

$$G_k = E[x_{k+1} y_k^T] \tag{2.30}$$

where x and y are state and output respectively. The relation between these covariance matrices is:

$$R_i = CA^{i-1}G_k \tag{2.31}$$

where again, A and C are state and observation matrices respectively. The output covariance function can be obtained, having measured response. To obtain C, A and G matrices, the block Hankel matrix is formed and decomposed as follow:

$$H_i = \begin{bmatrix} R_i & R_{i-1} & \dots & R_1 \\ R_{i+1} & R_i & \dots & R_2 \\ \dots & \dots & \dots & \dots \\ R_{2i-1} & R_{2i-2} & \dots & R_i \end{bmatrix} = \begin{pmatrix} C \\ CA \\ \dots \\ CA^{i-1} \end{pmatrix} \begin{pmatrix} A^{i-1}G & \dots & AG & G \end{pmatrix} = \mathrm{O}_i \Gamma_i \tag{2.32}$$

where O_i and Γ_i are extended observability and stochastic controllability matrices. SVD can be applied for this decomposition similar to Equation 2.17 and from there:

$$\mathrm{O}_{i1} = P\Sigma^{-1/2} = \begin{pmatrix} C \\ CA \\ \dots \\ CA^{i-1} \end{pmatrix} \tag{2.33}$$

A and C can be obtained from observability matrix and modal properties can be extracted based on a similar relationships explained for ERA algorithm.

2.4.7 Auto Regressive and Exogenous (ARX) algorithm

Another useful method for system identification of a linear time-invariant system is Autoregressive method. For an output-only system under white noise excitation, Auto Regressive (AR) model suffices to provide a reliable and accurate estimate of modal parameters (Pandit, 1991 and De Roeck et al., 1995). However, addition of Exogenous term (ARX) to the model results in an improvement of the accuracy. The ARX model can be written as:

$$\sum_{i=0}^{p} \alpha_i \bar{y}(n-i) = \sum_{i=1}^{q} \beta_i \bar{x}(n-i) + \bar{e}(n) \tag{2.34}$$

where $\bar{y}(n) = [y_1(n) \quad y_2(n) \quad ... \quad y_m(n)]$ and $\bar{x}(n) = [x_1(n) \quad x_2(n) \quad ... \quad x_r(n)]$ are matrices including output and input vectors respectively; α_i 's and β_i 's are ARX coefficients; $\bar{e}(n)$ represents the noise and measurement error; and finally, p and q are the orders of Auto-Regressive and Exogenous terms and are usually assumed to be identical.

When the input is white noise and is not distinguishable from measurement noise, the system can be modeled by:

$$\sum_{i=0}^{p} \alpha_i \bar{y}(n-i) = \sum_{i=1}^{q} \beta_i \bar{e}(n-i) + \bar{e}(n) \tag{2.35}$$

ARX coefficients can be directly obtained, using the output data. It can be shown that the system's state matrix can be expressed as:

$$\hat{A} = \begin{bmatrix} 0 & I & . & . & 0 & 0 \\ 0 & 0 & . & . & 0 & 0 \\ . & . & . & . & . & . \\ . & . & . & . & . & . \\ 0 & 0 & . & . & 0 & I \\ -\alpha_p & -\alpha_{p-1} & . & . & . & -\alpha_1 \end{bmatrix} \tag{2.36}$$

and the observation matrix is considered as:

$$C = \begin{bmatrix} I & 0 & . & . & 0 & 0 \end{bmatrix} \tag{2.37}$$

Therefore, the modal parameters of the system (modal frequencies, damping ratios and mode shapes) will be computed by the eigenvalue decomposition of the system's matrix and transformation of parameters of discrete system to continues system as it is explained in ERA algorithm.

2.4.8 Frequency Domain Decomposition (FDD) Algorithm:

FDD is another algorithm which provides modal properties of the system. This algorithm uses the Cross Power Spectral Density (CPSD) of the output signals to estimate the poles and eigen-vectors of the system by its singular value decomposition. Considering the CPSD matrix of the outputs *(y)*, which is defined as a function of frequency, the SVD can be applied as:

$$\hat{G}_{yy}(\omega) = U(\omega)S(\omega)V^T(\omega) \tag{2.38}$$

where $S(\omega)$ is the diagonal matrix of singular values and U and V are matrices of singular vectors. It can be shown that the peaks in vector of first singular values, $S_{11}(\omega)$, represents the poles of the system and the first singular vector, $U_1(\omega)$, at the frequencies of poles, would be an estimate for the mode shapes of the structure.

Summary of the process is: (i) pre-processing the data: the measured data is passed through a filter to clean the signals from noises, (ii) calculating the Cross Power Spectral Density as a function of frequency (iii) Singular Value Decomposition of the CPSD, and (iv) finding the frequencies at which the first component of singular value matrix is

maximized (as natural frequency of the structure) and also to find the corresponding first singular vector (as the mode shape of the structure).

2.4.9 Stabilization Diagram for Optimum Model Order

One of the difficulties in most of the system identification algorithms is selection of adequate system's order. An effective method for this problem is using stabilization diagram This diagram shows the stable modes as a function of increasing system's order. As the order increases, the deviation of the modal parameters is assessed and an optimum order is selected. An example criterion for optimum order, proposed by Yi and Yun (2004), determines a stable order in which the deviation of natural frequency and damping ratio in order p from the order $p-1$ is less than 0.05 and 0.2 respectively. As well, the modal assurance criterion (MAC) value (Allemang and Brown 1982) between two extracted mode shapes from orders p and $p-1$ is greater than 0.95.

2.4.10 Summary of the Development History and Literature Review

The development history of wireless sensors and their application in structural monitoring and modal identification is presented in this chapter. Advantages and challenges in application of wireless sensors for SHM, and modal identification of structural systems, as a basic practice in SHM, are discussed. The concept of modal identification and the available time and frequency-domain approaches are presented and the necessary background and terminology are provided to be used later in other chapters of this dissertation.

Chapter 3

Distributed Data Processing

3. Distributed Modal Identification

3.1. Background

While WSN facilitates the deployment of SHM, a few challenges have restricted its application in large scale and for long term health monitoring of structural systems. Challenges in application of WSN are explained in Chapter 2. Among those, the latency in the process due to the low data bandwidth and the difficulties in providing operational power of sensors for long term monitoring are more important issues, because less research effort has been devoted to address them in the literature. In particular, for monitoring of structural response due to drastic loads (e.g. earthquake) WSNs need to be responsive in capturing and processing the data. Thus, new approaches are required to address these challenges and make the existing WSN technology suitable for a wide variety of applications.

To address the power consumption issue, different approaches have been developed in recent years. Energy harvesting (Grisso et al., 2005), wireless power transmission (Das et al. 1998), and optimal power usage strategy are some examples of such approaches. While these methods rely on technological developments, the optimal usage strategy offers an efficient and integral way of preserving energy just by applying smart local algorithms on wireless units. In addition, even with the use of energy harvesting or wireless power, it is still necessary to manage the power consumption and therefore, optimal usage strategies are crucial.

In Chapter 2, it was discussed that the available efforts in utilization of onboard processing capability for modal identification are very limited. A few available works on this topic are presented. As explained, the developed approaches are partially distributed, limited by network topology and the identification algorithm, and their performances are not significant enough. This chapter, however, presents a novel distributed modal identification approach for application of WSN in SHM which is completely onboard and flexible to be used with a broad range of identification algorithms and different network topologies. The proposed algorithm, called Iterative Modal Identification (IMID), assigns a computational task of modal identification to each remote node and limits the data communication to transmission of only modal analysis results. An iterative algorithm is developed such that each sensing node in the network sufficiently influences on the final estimated results. The necessary requirement for the implementation of the proposed algorithm is an initial estimate of the structural modal properties which can be available for many structural systems. In this chapter, the formulation of this method is presented, and as a proof of concept, the algorithm is implemented on numerically simulated shear structures and experimental models. Then, the limitations of the algorithms are discussed and the solutions are presented accordingly. For discussed limitations, separate approaches are proposed and each approach is then validated through additional numerical and experimental examples.

3.2. Significance of the Distributed Modal Identification Algorithms

Latency in the data collection and prohibitive power consumption, as major drawbacks in application of WSN in SHM, need special considerations in design of WSN architecture. In a long term SHM scenario, the monitoring system is expected to be prepared for collecting data and also responsive for processing the data and extracting important information about the state of the structure. Due to the limited bandwidth in wireless networks, transmitting large volumes of data can take a prohibitively long time. In a large scale deployment, tens of megabytes (MBs) data need to be transferred through the network while the network bandwidth is strictly limited. In one of the large scale deployments of WSN, Pakzad et al. (2008) reported the average bandwidth of 550 bytes/s in multi-hop data transmission, which resulted in about 9 hours for transferring 20 MB of data from 64 sensor nodes to the base station. Such a delay in the procedure prevents the monitoring system from prompt response which is particularly required in the event of an earthquake.

In addition to the latency, caused by the data transmission, power consumption also limits the performance of WSNs in long term monitoring. Different components of a wireless sensor unit for vibration monitoring (e.g. accelerometer, processor, and transceiver) consume different amounts of energy when performing different tasks. Figure 3.1 shows a unit of wireless sensor platform with its different components: SHM-A sensor board (Rice et al., 2008) and Imote2 processing board (Crossbow, 2007). Figure 3.2 also presents a graph that shows the results of the power consumption measurement

on this wireless sensor unit during the following tasks: standby, temperature sensing, acceleration sensing (25, 50, 100, and 280 Hz sampling rates), data interrogation, and data transmission. It is observed that the sampling rate in acceleration sensing has no effect on power consumption since it only depends on whether the sensor and ADC chips are powered on, and not what task they are performing. This figure shows that the highest energy consumption rate corresponds to acceleration sensing task and then, the communication task. Considering the limited capacity of standard batteries and the fact that the battery voltage does not remain constant throughout usage, it is evident that a wireless node cannot last for a long time (with regular batteries they last just a few hours depending on the ongoing tasks) on its battery power.

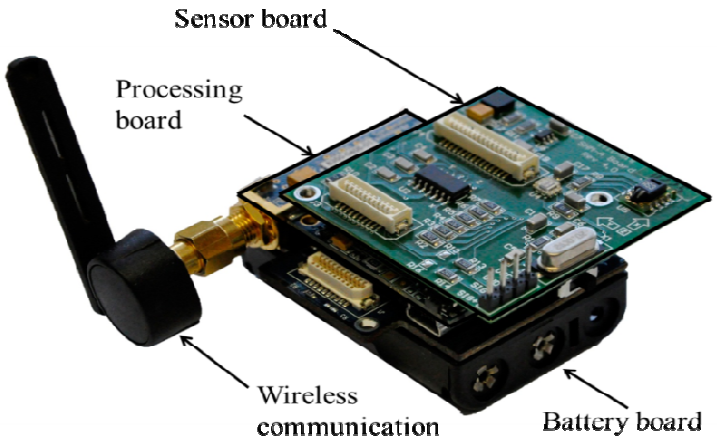

Figure 3.1. A wireless sensor platform (Imote2 and SHM-A)

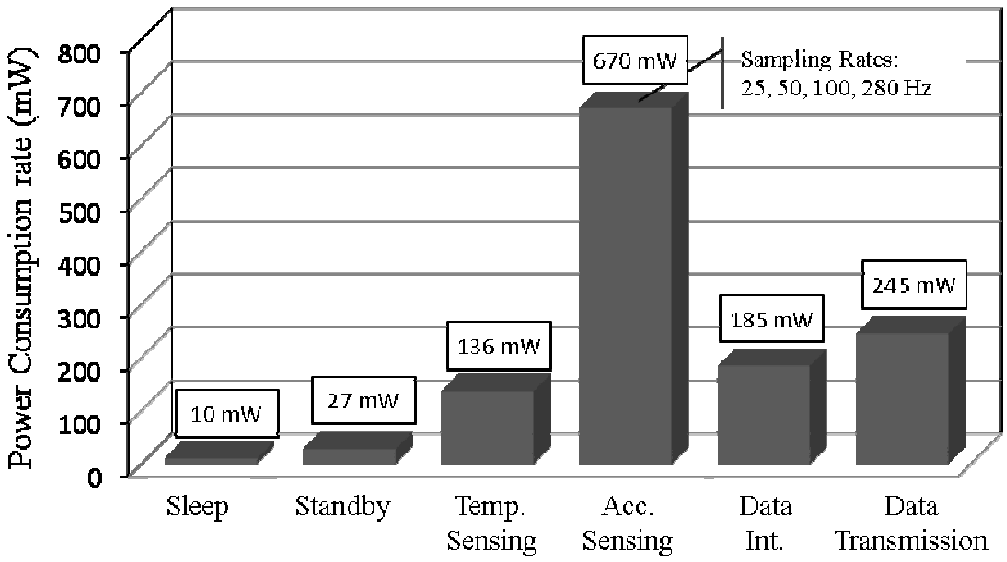

Figure 3.2. Power consumption rate during different tasks

Comparing the power consumption of different integrated components of a wireless sensor is important in managing the limited power resource. In an inclusive power consumption measurement, Whelan et al. (2009) reported the power consumption rate of 79.4 mW from all components of acceleration monitoring (for a specific wireless sensor platform) where 59 mW of that was from the CC2420 transceiver. Considering the communication time and the result of this power measurement, it can be realized that the radio transceiver is the major power consumer in the entire unit.

A distributed modal identification method incorporates the on-board processing capability to reduce the communication in the network. The importance of this approach is because transmitting data over a wireless network not only takes a long time but also consumes significantly more energy than performing a local computation. An

approximation of the required energy for performing a simple computation on one kB data and also for transmission of the same data through the radio signal can be obtained as:

$$E_{computation}=[Number\ of\ cycles\ for\ computation\ (ALU)]\times[1/Clock\ speed(Hz)]\times[power\ consumption\ rate(mW)] \quad (3.1)$$

$$E_{trsmission}=[1/transmission\ rate(Kbps)]\times[power\ consumption\ rate(mW)] \quad (3.2)$$

where transmission rate, power consumption rate and clock speed are specifications of the transceiver and the processor. The number of required cycles for computation depends on the algorithm which is used in the specific type of processor. ALU refers to Arithmetic Logic Unit which is a fundamental building block of the CPU of a computer.

Considering the specifications of CC2420 transceiver (Chipcon AS SmartRF, 2004) and PXA27x Processor (Intel, 2004), which are integrated in Imote2 platform (Crossbow, 2007), the estimated consumed energy for transmission of one kB data is 0.24 mW-sec, whereas the estimated required energy for a simple computation on one kB data is 2.25×10^{-5} mW-sec. This result evidently shows the noticeable higher power consumption of the transmission task and highlights the importance of developing and incorporating distributed modal identification algorithms to reduce the communication load and to preserve the limited energy.

3.3. Iterative Modal Identification, Theory and Methodology

A basic requirement for most of the existing modal identification algorithms is the access to the entire measured data for computation of the full cross-correlation matrix. This restriction requires the sensor network to transmit all the collected data from each sensor to a base station. The proposed algorithm, called IMID, estimates the modal parameters of the system without requiring simultaneous access to the entire data.

IMID relies on a class of estimation algorithm, called Expectation-Maximization (EM). EM estimates unknown parameter (Θ), given the measurement data (Y) in the presence of some hidden variables ($\hat{Y}$) (Dempster, 1977). This algorithm is in fact a generalized form of maximum-likelihood estimation, which is applicable when the data is incomplete. Considering the log-likelihood function of unknown parameters Θ as:

$$L(\theta) = \log[p(Y / \theta)] \tag{3.3}$$

the estimation of unknowns (Θ) is given by maximizing the function, $L(\Theta)$, over Θ:

$$\theta = Arg.\max[L(\theta)] \tag{3.4}$$

where Y is the available data (complete measured data).

When the entire data for estimation is not available (data is incomplete), an iterative method such as EM is applicable. EM first estimates the complete data using initially assumed parameters, Θ^p (expectation phase), then maximizes the likelihood function over

system's parameter to find Θ^{p+1} (maximization step) and continues until the convergence for the parameters is achieved. EM can be formally expressed as:

Expectation step:

$$Q(\theta, \theta^p) = E[\log(p(X/\theta)/Y, \theta^p] \tag{3.5}$$

Maximization step:

$$\theta^{p+1} \in \arg.\max Q(\theta, \theta^p) \tag{3.6}$$

where Θ^p denotes the value of the system's parameter obtained at the p^{th} iteration. The concept of EM is also illustrated in Figure 3.3.

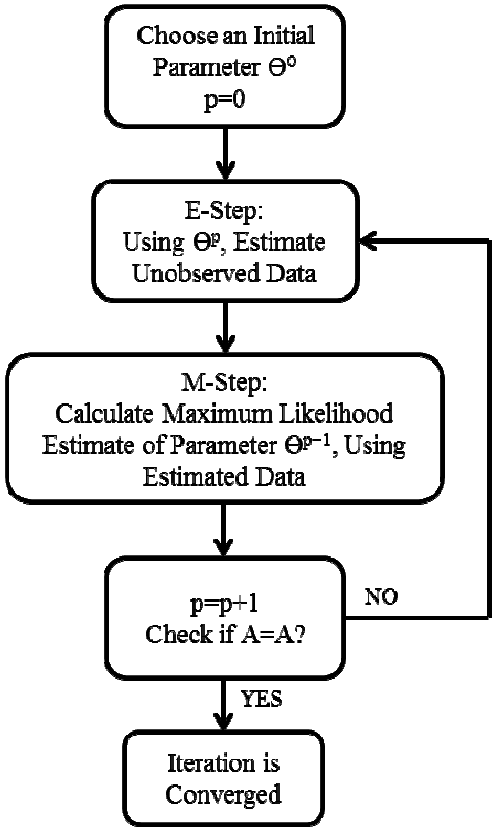

Figure 3.3. **The block chart presenting the Expectation Maximization algorithm**

The similarity of the proposed identification algorithm (IMID) and EM is that in IMID, each node separately estimates the system's parameter (Θ) based on the measured data at the node (available observation, Y) plus the assumed responses in the other nodes, $\hat{Y}$. In other words, each node estimates the system's parameter, having incomplete data.

Considering a structure instrumented by N sensor nodes, the first node uses the initial value of the parameters and makes a numerical simulation to obtain the response on other nodes (this step corresponds to the expectation step in EM algorithm). The simulated response and the measured data at this node are used to make an estimate on system's

modal parameters (this is the maximization step in EM algorithm). Then this node sends the system's parameters to the second node in the network for a similar local processing. These steps are taken in all of the nodes of the network one-by-one. However, for simulation of the response at other nodes, each node uses the system's parameter estimated at its previous node. Therefore, each node updates the estimation by the measured data at its location. This procedure is continued inside the network until the estimated parameters are stabilized and converged. Note that the algorithm with this configuration is applicable to input-output systems and assumes that the excitation signal was measured and communicated through the network so all of the nodes have access to it. The modifications for output-only systems will be presented later in this chapter. A possible scenario for application of input-output vibration testing is in the controlled load tests or in the impact test where the excitation is known to all the sensing nodes, as well as in earthquake events where the ground motion is also measured. Figure 3.4, shows a step-by-step block chart, illustrating IMID.

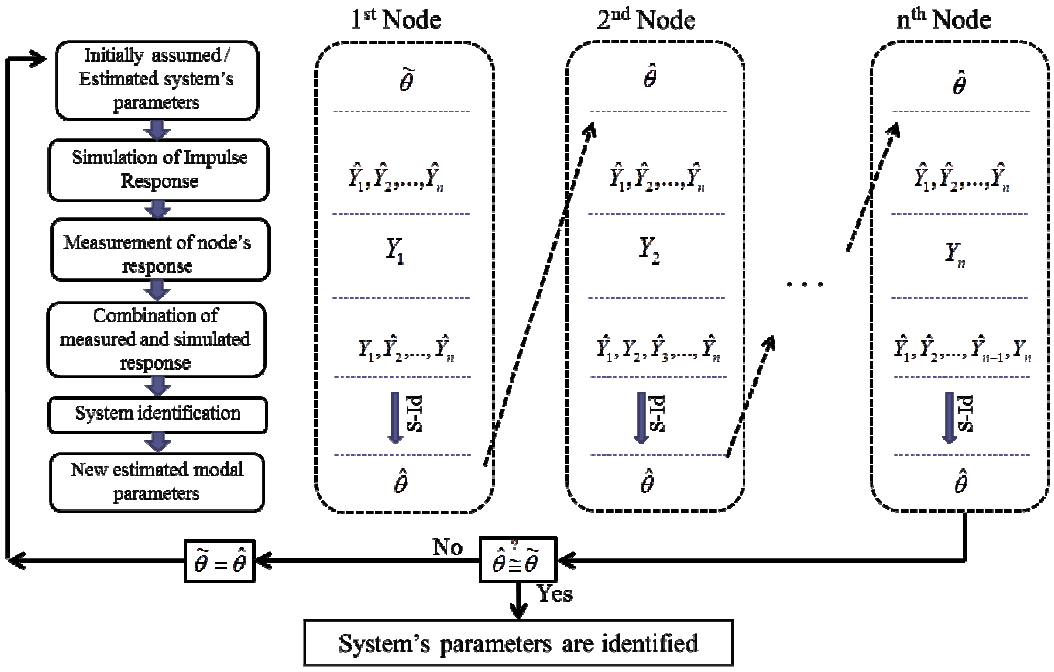

Figure 3.4. The block chart presenting the iterative modal identification (IMID) algorithm

Considering the fact that the transmission volume for the estimated parameters is very small compared to the time history data, IMID can significantly reduce the data traffic flowing through the network. As a result, it saves a considerable amount of time and energy in communication task. It should be noted that this implementation of the algorithm, an initial estimate of system's parameters are required. This initial estimate can be achieved either from the Finite Element model of the structure or, in long term vibration monitoring, from an initial data collection and performing a centralized data processing. However, an approach which addresses this requirement is also developed, called cumulative system formation, and is presented later in this chapter.

Fundamental iterative steps in IMID are (i): simulation of the response using the estimated parameters, and (ii): modal identification using the collected data and simulated response. Several system identification models are available for both simulation of the response (e.g. Newmark numerical method and the use of Auto Regressive with Exogenous (ARX) model) and modal realization (e.g. Eigensystem Realization Algorithm (ERA), Stochastic Subspace Identification (SSI), ARX and Least Square algorithm). Selection of the best algorithm for each of these steps is one of the critical tasks in developing IMID. The performance of simulation and identification techniques, in terms of accuracy and efficiency, is the factor that needs to be considered in selection of algorithms for IMID. Additionally, since the objective of IMID is to utilize the on-board processors of the wireless sensors, it is also important to find a computationally efficient algorithm for implementation of IMID.

In summary, different steps in IMID are:

(i) All sensing nodes in the network perform the measurement

(ii) First node estimates the system and transmits to the second node

(iii) Second node receives parameters from the first node, simulate the first node's response, together with its measurement, updates the system parameter and passes it to the next node

(iv) Process continues up to the last node

(v) If the convergence has not happened in the first cycle, the iteration starts the next cycle

(vi) Iteration continues until the system parameters are converged

The following section describes some implementation aspects of IMID algorithm.

3.4. Implementation of IMID

As previously mentioned, in IMID all the nodes in the network contribute in modal identification process. In order to explain the implementation details of the algorithm, different tasks that need to be done in each node are discussed in this section. Figure 3.5 shows the necessary tasks that are assigned to each node in every iteration cycles.

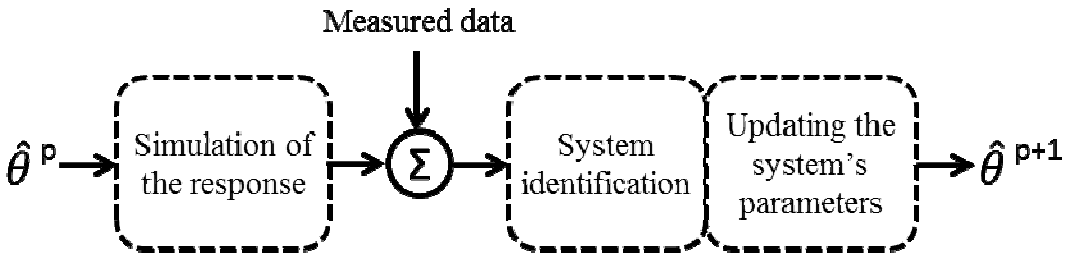

Figure 3.5. The block chart presenting the tasks assigned to each node

Simulation of the response:

The first step in IMID is simulation of the dynamic response of the structure under the applied excitation. As long as the dynamic properties of the structure are available, this task can be done using any numerical methods. However, the selection of simulation method is related to the selected parameters for communication. For example, to apply numerical methods such as Newmark's method or Central Difference, the structural properties of the structure (i.e. mass, damping and stiffness matrices) are required.

As an alternative method for simulation of response, the ARX model of the system can be used. In this approach, the response at current time can be estimated using ARX parameters, past response, and current and past inputs of the system. It is evident that utilizing ARX for simulation of the response requires ARX parameters to be transferred in the network.

Modal Identification:

After the dynamic response of the system is simulated at a remote node, the measured response is replaced with the corresponding simulated response at that point and, together with the simulated responses for other nodes, is fed into modal identification algorithm. The modal identification can be performed using any algorithm such as those explained in Chapter 2.

Selection and assessment of the system's parameters for transmission:

Estimation of system's parameters in IMID is not only the final objective, but a step which is taken at each node in every iteration cycles. In fact, estimated parameters at each node are transmitted through the network to be updated node-by-node. Additionally, these parameters are checked for convergence, at each cycle. Therefore, it is important to select the most informative parameters representing the system. Several alternatives for system's parameters are: ARX parameters, state space matrices, and modal properties of the structure.

The ARX parameters and state-space matrices can be the direct result of system identification step and no further assessment is needed before transmission of the parameters. However, extraction of structural properties (mass, damping and stiffness matrices) from the result of system identification step needs some considerations. It should be noted that the advantage of selecting these properties, compared to other alternatives, is their compact transmission volume.

Another challenge in the procedure of extraction of modal properties or dynamic properties of structural system from the results of identification algorithms is existence of complex eigenvectors. Since the damping is involved in construction of the state matrix A, the eigenvectors and eigenvalues are reasonable to be complex. The natural frequencies and damping ratios can be simply obtained from Equation (2.23). But from the complex components of the eigenvectors, there is no such exact solution to derive the normal real mode shapes. In fact, mode shape components contain both amplitude and phase. Figure 3.6 shows an example of such mode shape for an exaggerated case.

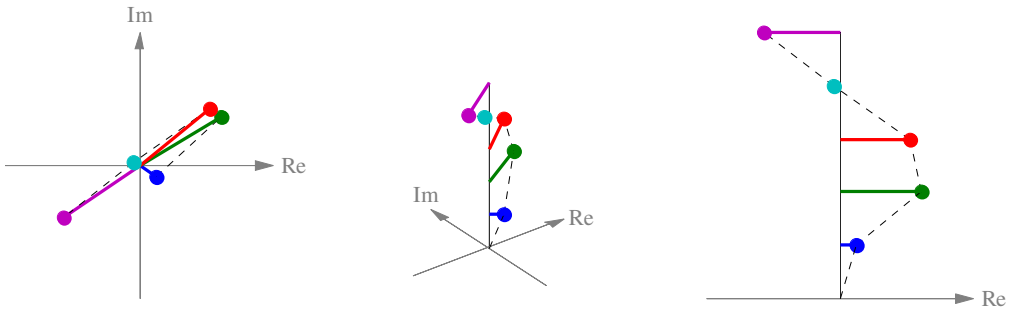

Figure 3.6. Example of a complex mode for a 5 story shear building

In many practical cases that the damping is nearly proportional and there is no significant error, eigenvectors can be scaled in a way that imaginary parts of the components become negligible and real parts of the eigenvectors contain sufficient information about the mode shapes. But when the complexity is high this approximation is not acceptable and both the amplitude and the phase of eigenvectors should contribute in the extraction of modal properties.

One approach to address the complexity of mode shapes is to derive the dynamic properties directly from complex eigenvectors. Rewrite the FE equation of motion for free vibration:

$$M\ddot{q}(t) + C_d\dot{q}(t) + Kq(t) = 0 \tag{3.7}$$

the solution will be:

$$q(t) = e^{\lambda_n t}\psi_n \tag{3.8}$$

Substitution of Eq. (3.8) into (3.7) results in:

$$(\lambda_n^2 m + \lambda_n c + k)\psi_n = 0 \tag{3.9}$$

where λ_n and ψ_n are the n^{th} complex eigenvalue and eigenvector of the dynamic system. Pre-multiplying this equation by m^{-1}, it can be rewritten as:

$$\begin{bmatrix} m^{-1}k & m^{-1}c \end{bmatrix} \begin{Bmatrix} \psi_n \\ \lambda_n\psi_n \end{Bmatrix} = -\lambda_n^2\psi_n \tag{3.10}$$

which holds for each eigenvalue and eigenvector. Expanding the equation to include all n modes of the system, it becomes:

$$\begin{bmatrix} m^{-1}k & m^{-1}c \end{bmatrix} \begin{bmatrix} \psi_1 & \psi_2 & \cdots & \psi_n \\ \lambda_1\psi_1 & \lambda_2\psi_2 & \cdots & \lambda_n\psi_n \end{bmatrix} = -\begin{bmatrix} \lambda_1^2\psi_1 & \lambda_2^2\psi_2 & \cdots & \lambda_n^2\psi_n \end{bmatrix} \tag{3.11}$$

or

$$\begin{bmatrix} m^{-1}k & m^{-1}c \end{bmatrix} = -\begin{bmatrix} \lambda_1^2\psi_1 & \lambda_2^2\psi_2 & \cdots & \lambda_n^2\psi_n \end{bmatrix} \begin{bmatrix} \psi_1 & \psi_2 & \cdots & \psi_n \\ \lambda_1\psi_1 & \lambda_2\psi_2 & \cdots & \lambda_n\psi_n \end{bmatrix}^* \tag{3.12}$$

where "*" denotes the pseudo-inverse of a matrix. From this equation, $[m^{-1}k]$ and $[m^{-1}c]$ can be easily extracted with the minimum least square error. Having an estimate on the mass of the system, stiffness and damping can be obtained.

The remaining issue is determination of eigenvalues and eigenvectors associated with the physical system from those generated by noise. During the system identification process, it is common to identify some modes that are not from the underlying physical system, but are due to the noise in the data and over-parameterization of the problem (computational and spurious modes). Constructing stability diagram (Peeters and Roeck 2001) is an approach that addresses this difficulty based on the fact that structural modes stabilize through the process of increasing the model order whereas the spurious modes will not converge. Another available approach is determination of confidence interval for modes through the Consistent Mode Indicator (CMI) (Papa et al. 1998). In

implementation of IMID, having an initial estimate of the system is also an advantage which can assists with determination of structural modes from all identified modes.

3.5. Validation through Numerical Simulation

To validate the performance of IMID, it is implemented in identification of two numerically simulated models. The models are a 5 degree of freedom (DOF) shear structure, shown in Figure 3.7-(a), and a 10 DOF mass-spring-damping model, shown in Figure 3.7-(b). The objective is to use IMID for identification of the modal properties of these systems. The simulation of the model and the steps of IMID are carried out in MATLAB (The Math Works, Inc. Natick, Mass., 1997).

As the starting point for the iteration process, stiffness matrices are perturbed in each case to form an initial estimate of the system. For perturbation, up to 20 percent random changes are applied to the stiffness coefficients and the perturbed coefficients are used as the initial estimate for the algorithm. Considering application of IMID in long term monitoring scenario, where the initial estimates can be obtained through an initial data collection and a centralized data processing, 20% deviation of the initial estimate from the real values is substantial and larger than the deviation reported in long term monitoring studies in literature as a result of environmental variation, measurement noise or even small structural damage (for example, statistical study performed on the 174 data sets, collected during 3 months from Golden Gate Bridge [Pakzad et al. 2009], concluded that the deviation in the estimated frequencies is at most 1.2% due to measurement noise and environmental effects). Also, considering the use of finite element models for

obtaining the initial estimate, the level of perturbation is consistent with practical scenarios, presented in the literature in the Finite Element Model Updating field (Zhang et al. 2001; Brownjohn et al. 2000).

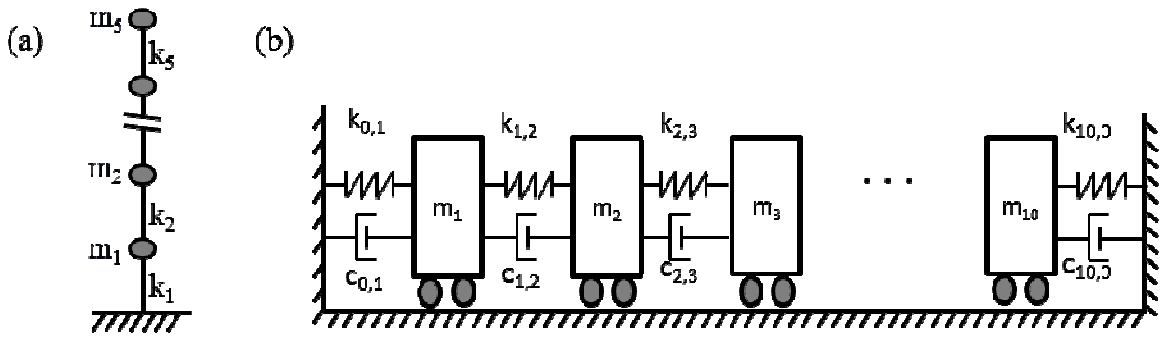

Figure 3.7. The 5 DOF (a) and 10 DOF (b) numerically simulated models

The 5 DOF model is assumed to have mass and stiffness matrices as follow:

$$k\_true = \begin{bmatrix} k_1+k_2 & -k_2 & 0 & 0 & 0 \\ -k_2 & k_2+k_3 & -k_3 & 0 & 0 \\ 0 & -k_3 & k_3+k_4 & -k_4 & 0 \\ 0 & 0 & -k_4 & k_4+k_5 & -k_5 \\ 0 & 0 & 0 & -k_5 & k_5 \end{bmatrix} \qquad m = \begin{bmatrix} m_1 & 0 & 0 & 0 & 0 \\ 0 & m_2 & 0 & 0 & 0 \\ 0 & 0 & m_3 & 0 & 0 \\ 0 & 0 & 0 & m_4 & 0 \\ 0 & 0 & 0 & 0 & m_5 \end{bmatrix}$$

Damping ratio is assumed to be 5% in all modes. This system is considered as the true system which represents the real existing system. Thus, it is used to simulate the measurements or observations.

The goal of the algorithm is identification of modal properties of the true system, having an initial estimate of the system. An important assumption at this stage is the availability of some information about the system. For example, it is assumed that the

mass matrix is known. To simulate the real condition, an initial estimate on the system should be made. For this implementation, the initially estimated parameters are considered to be a perturbed version of the true stiffness matrix together with the same mass matrix and damping ratios as the true system.

Perturbation is performed by multiplying the stiffness matrix by factors between 0.8 to 1.2 (i.e. $0.8 < \alpha < 1.2$):

$$k\_perturbed = \begin{bmatrix} \alpha_1 k_1 + \alpha_2 k_2 & -\alpha_2 k_2 & 0 & 0 & 0 \\ -\alpha_2 k_2 & \alpha_2 k_2 + \alpha_3 k_3 & -\alpha_3 k_3 & 0 & 0 \\ 0 & -\alpha_3 k_3 & \alpha_3 k_3 + \alpha_4 k_4 & -\alpha_4 k_4 & 0 \\ 0 & 0 & -\alpha_4 k_4 & \alpha_4 k_4 + \alpha_5 k_5 & -\alpha_5 k_5 \\ 0 & 0 & 0 & -\alpha_5 k_5 & \alpha_5 k_5 \end{bmatrix}$$

Now, the perturbed system is used as an initial estimate of the system for the beginning of the iteration algorithm. Mass, damping ratio, and stiffness components for the 10 DOF system are similarly modeled.

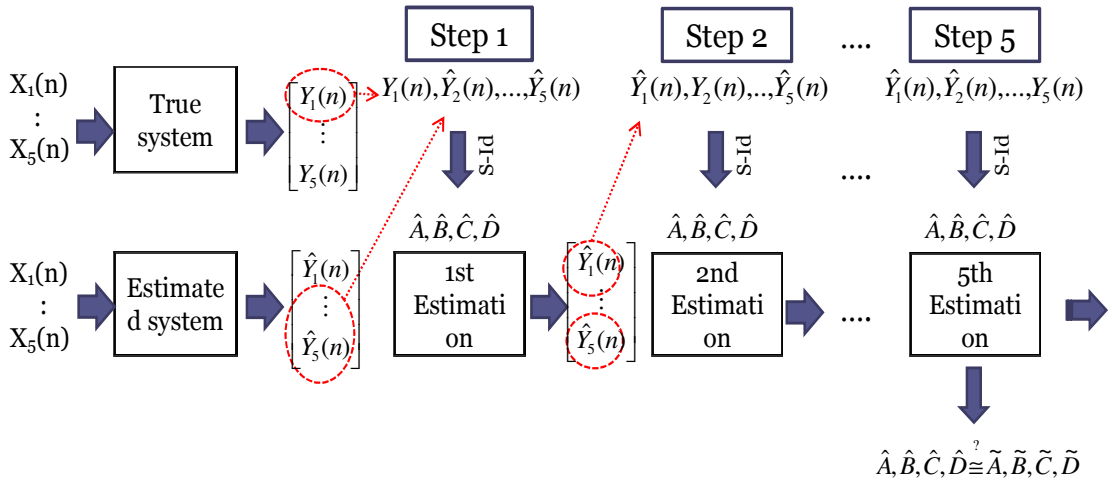

Figure 3.8. Implementation schematic of algorithm on the 5 DOF shear model

In these numerically simulated examples, measurement noise is also added to the responses to verify the functionality of the algorithm in the presence of noises. The noise signals have a Root Mean Square (RMS) equal to 10% of the response signal's RMS. The mass and damping ratios are assumed to be constant throughout the iterations and stiffness coefficients are selected for updating and transmission through the network. Schematic of the algorithm for the 5 DOF model is shown in Figure 3.8.

Simulation step:

For simulation of the response, Newmark's numerical method is used. This numerical time-stepping method calculates the response of a structural system under any arbitrary excitation. Through the use of Newmark's method, the response at any time step is calculated based on the response at previous time step and the applied force.

For simulation of the response, Newmark's numerical method is used. Considering the second order equation of motion at time step i+1 as:

$$m\ddot{y}_{i+1} + c\dot{y}_{i+1} + ky_{i+1} = p_{i+1} \tag{3.13}$$

where y is the response, p is the excitation, and m, c, k are mass, damping and stiffness matrices respectively, Newmark's method is developed based on following equations:

$$\dot{y}_{i+1} = \dot{y}_i + [(1-\gamma)\Delta t]\ddot{y}_i + (\gamma\Delta t)\ddot{y}_{i+1} \tag{3.14}$$

$$y_{i+1} = y_i + (\Delta t)\dot{y}_i + [(0.5-\beta)(\Delta t)^2]\ddot{y}_i + [\beta(\Delta t)^2]\ddot{y}_{i+1} \tag{3.15}$$

which incorporates the estimation of stiffness matrix at each step. Although the considered system is a model of a shear structure, the estimated stiffness matrix does not necessarily follow the expected format of a shear building structure. To address this issue, least square approach is used which estimates the best stiffness coefficient for constructing the stiffness matrix with the format of shear building stiffness.

Identification step:

In order to estimate the system's parameters, ARX algorithm (Pandit, 1991 and Roeck et al., 1995) is used. The ARX algorithm is explained in Chapter 2.

Results of the implementation:

To check the convergence of the results, stiffness coefficients of the structure, identified frequencies, and mode shapes are assessed after each iteration cycle. The criterion for convergence of modal properties is defined by a predetermined threshold for

the estimated parameters of the system at the end of each cycle. Modal Accuracy Criterion (MAC) value is used for comparison of mode shapes in consecutive cycles. This criterion is defined as:

$$MAC = \frac{(\phi_p^T \times \phi_{p+1})^2}{(\phi_p^T \times \phi_p) \times (\phi_{p+1}^T \times \phi_{p+1})} \tag{3.16}$$

where ϕ_p and ϕ_{p+1} are the estimated mode shapes at iteration cycles p and p+1.

The error percentages of stiffness coefficients, natural frequencies and mode shapes, in the initial estimates and during the iterations are presented in the Figures 3.9 and 3.10 for 5 and 10 DOF models, respectively. Depending on the desired level of accuracy, consistent results are achieved in all of the cases presented in the simulated examples. The identified modal properties of the two models (5 and 10 DOF), from Finite Element model, IMID, and centralized ARX technique, are also presented in Tables 3.1 and 3.2.

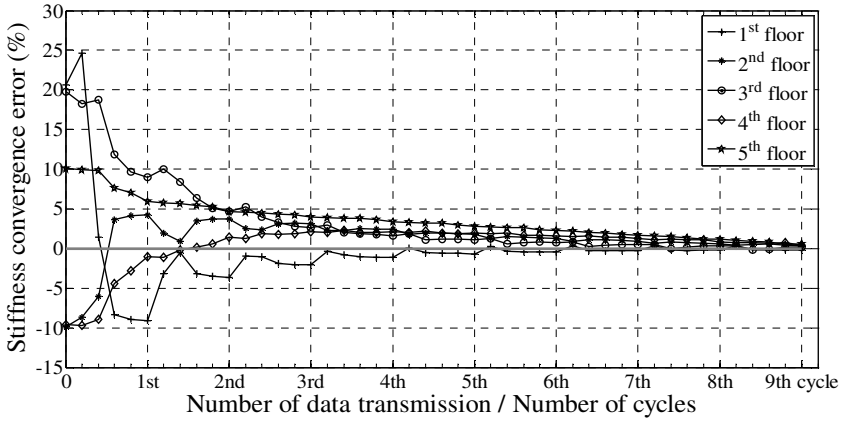

(a)

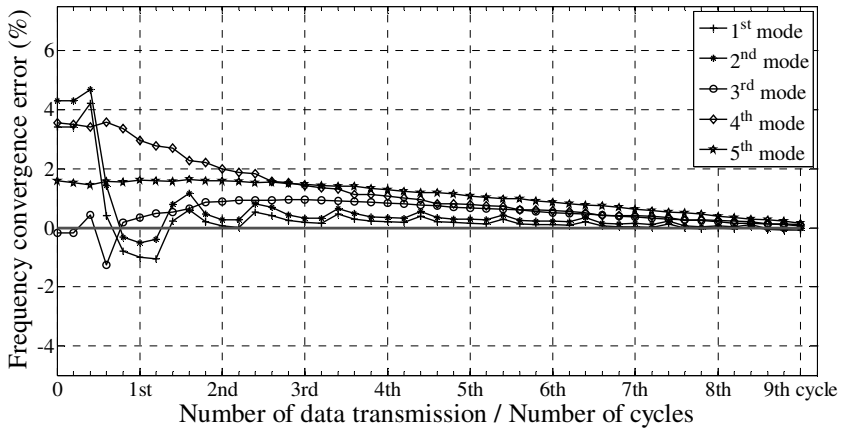

(b)

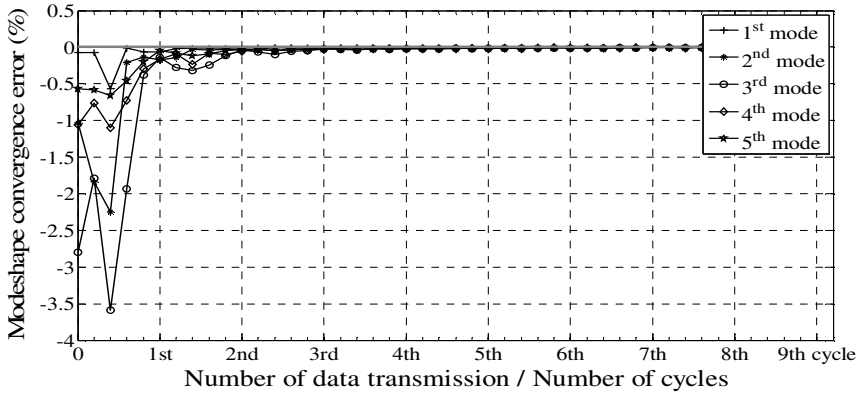

(c)

Figure 3.9. (a) to (c), the convergence of stiffness coefficients and modal properties of the 5 DOF model

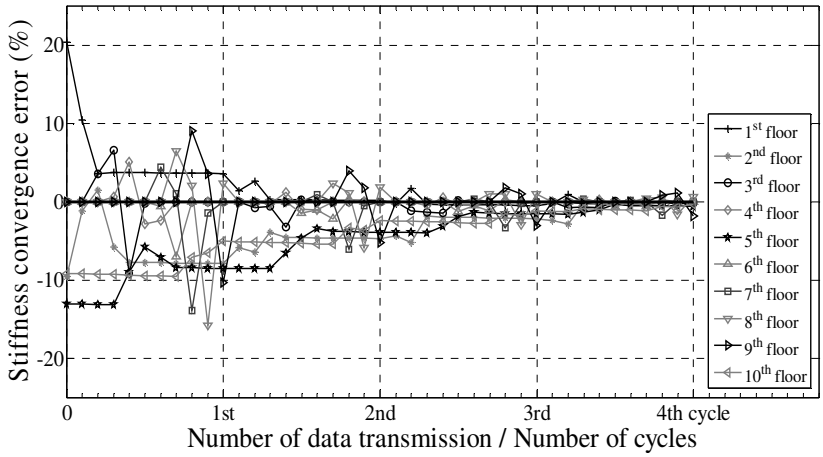

(a)

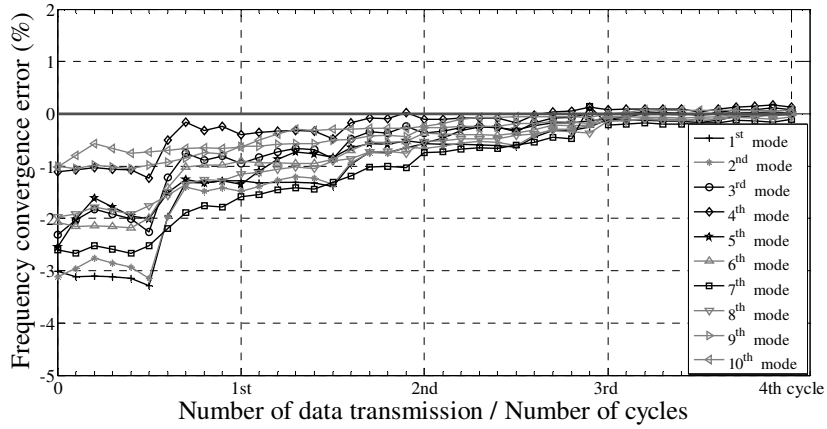

(b)

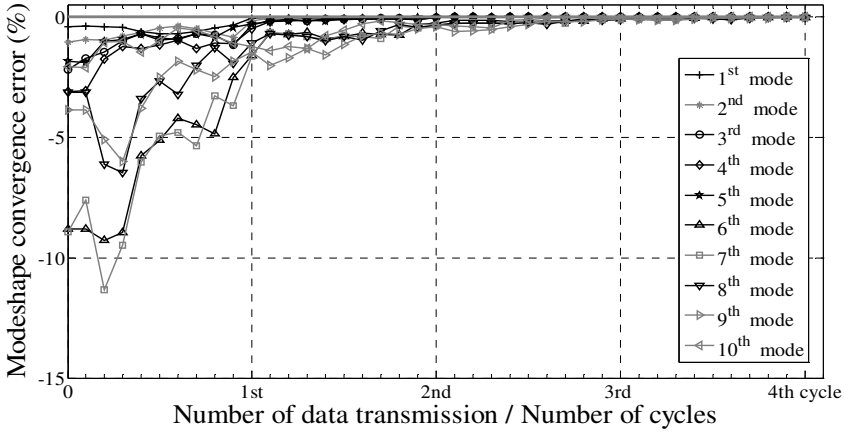

(c)

Figure 3.10. (a) to (c), the convergence of stiffness coefficients and modal properties of the 10 DOF model

Table 3.1. Comparison of identified modal properties of 5 DOF model, using different algorithms

Frequencies (Hz)			MAC value		Damping ratio (%)		
True value (FE model)	Centralized ARX	IMID after 7 cycles	FE vs. ARX (Centralized)	FE vs. IMID after 7 cycles	True value (FE model)	Centralized ARX	IMID after 7 cycles
0.4158	0.4165	0.4153	1.0000	1.0000	5.000	5.000	5.042
1.0197	1.0249	1.0184	1.0000	1.0000	5.000	5.000	5.031
1.5724	1.5878	1.5715	1.0000	0.9996	5.000	4.990	4.985
1.9449	1.9598	1.9444	1.0000	0.9996	5.000	4.980	4.966
2.4391	2.4495	2.4385	1.0000	0.9997	5.000	4.970	4.964

Table 3.2. Comparison of identified modal properties of 10 DOF model, using different algorithms

Frequencies (Hz)			MAC value		Damping ratio (%)		
True value (FE model)	Centralized ARX	IMID after 4 cycles	FE vs. ARX (Centralized)	FE vs. IMID after 4 cycles	True value (FE model)	Centralized ARX	IMID after 4 cycles
0.3141	0.3152	0.3132	1.0000	1.0000	5.0000	5.0153	5.0194
0.5386	0.5428	0.5369	1.0000	1.0000	5.0000	5.0154	5.0288
0.8206	0.8258	0.8190	1.0000	0.9999	5.0000	5.0090	5.0120
1.0314	1.0436	1.0302	1.0000	0.9994	5.0000	5.0045	5.0110
1.2685	1.2846	1.2653	1.0000	0.9994	5.0000	5.0108	5.0122
1.5202	1.5395	1.5165	0.9998	0.9986	5.0000	5.0094	5.0109
1.6378	1.6725	1.6316	0.9997	0.9932	5.0000	5.0160	5.0175
1.7819	1.7612	1.7765	0.9997	0.9918	5.0000	5.0114	5.0224
1.8672	1.8607	1.8633	0.9996	0.9973	5.0000	5.0060	5.0255
1.9262	1.9259	1.9229	0.9998	0.9981	5.0000	5.0039	5.0124

To identify the sensitivity of the convergence to the level of initial estimate error, a large set of simulations are performed with different levels of initial perturbations for the 5 DOF shear model. The initial estimates of stiffness components are selected to be ranged from 50% to 150% of the actual values, with a 5% increment. The results showed that, when the initial estimate error is from 5 to 25% (initial values are from 75% to 125% of the actual values), the convergence, with less than 1% error, happens in less than 8 cycles (increasing by the increase of initial estimate error). Also for initial estimate errors of 25% to 35%, the convergence eventually happened after a maximum of 15 cycles. However, for initial estimate errors, beyond 35%, in some cases, the algorithm did not converge. It should be noted that this level of error is beyond what is expected in application scenarios, discussed in the beginning of this section.

3.6. Experimental Validation of IMID

The simulation results in section 3.5 showed the robustness of IMID. The next step is experimental validation of the algorithm. For this purpose, a series of dynamic tests were performed on two experimental structures in the laboratory. The first one is a 5-story model structure excited with a shaking table (Figure 3.11), and the second one is a truss structure which is excited by impulsive load, using a hammer test (Figure 3.17).

3.6.1 The 5-story model structure

The structure is a 5 story laboratory model with 5 degrees-of-freedom and is subjected to earthquake ground excitation. The excitation is El Centro earthquake record

(California, 1940 – S00E), and the response is recorded via 5 Imote2 wireless sensors with SHM-A sensor boards using 280 Hz sampling rate. The framework for programming Imote2 is TinyOS operating system. For collecting data, a software package which is developed by Illinois Structural Health Monitoring Project (ISHMP, 2009) is used. As an essential requirement in vibration monitoring using wireless sensors, time synchronization is utilized in acceleration sensing application of ISHMP tool-suit. Time synchronization of sensing nodes is a relatively short task (less than 30 seconds in this experiment) which is necessary in extraction of accurate modeshapes from modal identification of structural systems. The utilized time synchronization protocol in this application is TPSN (Ganeriwal et al. 2003).

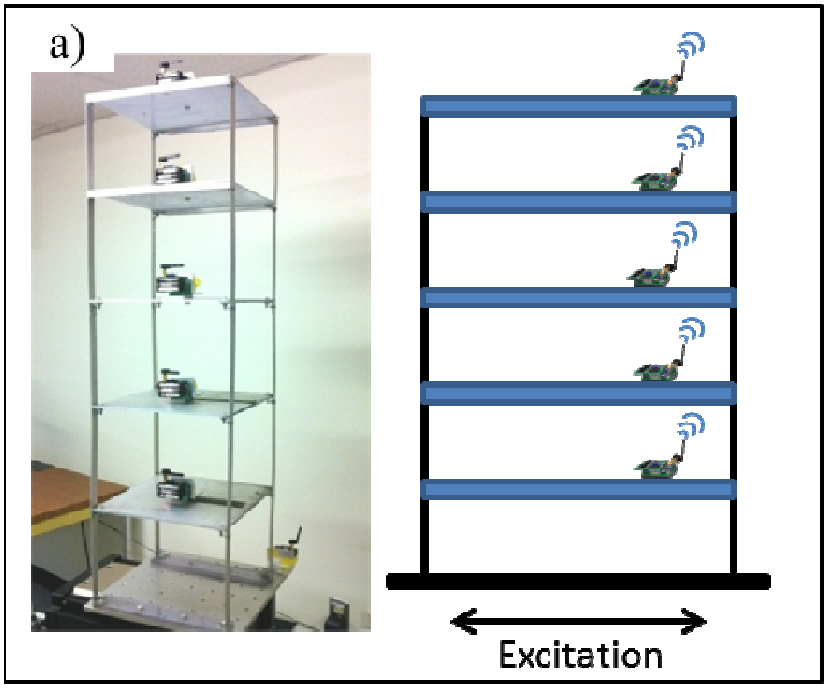

Figure 3.11. The experimental model on shaking table

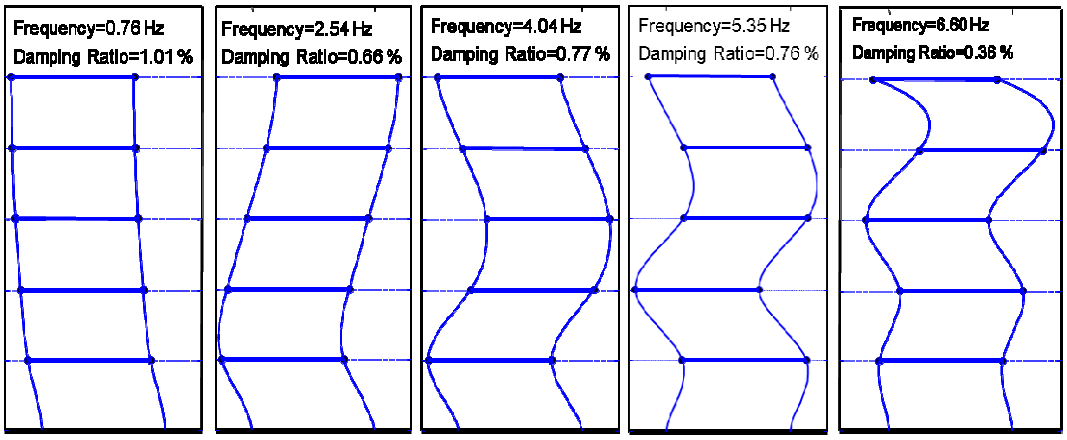

Figure 3.12. The identified modal properties of the experimental model

The objective of the test is to use IMID to find the modal properties of the model. To have a basis for comparison of the results, the modal properties are identified using Stochastic Subspace System Identification (SSI) method (Overschee et al., 1994, as explained in chapter 2) with centralized data collection scheme. The estimated modal properties are presented in Figure 3.12. To begin the iteration, an initial estimate of the structural model is required as the starting point for the iterative process. For this example, masses are added to different floors, a separate modal analysis is conducted, and the identified parameters of the altered model are used as the initial estimates for the algorithm. This is similar to the perturbation of stiffness matrix which was used in the simulation examples.

Due to the contribution of disturbances in the measured data (e.g. measurement noise and nonlinearities in the response), careful considerations should be given to the selection of the model representing the structure. In contrast to the noise free data where the structural properties (m, c, and k) are sufficient to describe the system, in the

experimental data more informative parameters are required to accurately characterize the underlying system. As an alternative to the structural properties, ARX parameters (α_i's and β_i's) can be used to represent the structural system in simulation. In this case, ARX parameters are considered to be transmitted through the network as the system's parameters. In comparison with structural properties, these parameters can carry a larger amount of information about the system. For example, a 5 DOF structure can be characterized by stiffness, mass and damping matrices of size 5 by 5. However, the ARX model with order 5 (for instance) describes the same system by 10 matrices of size 5 by 5 (5 autoregressive and 5 exogenous matrices). In the absence of noise, the larger size of these parameters does not provide any additional information for simulation. However in practical problems, these parameters provide more accurate results. It should be noted that as the order of the assumed model increases, the size of the transmitted data increases and consequently, the communication burden of the network also increases. Therefore optimizing the selected model and the corresponding order is important. Additionally, high model order may result in an over-parameterized model for the system and result in even less accurate estimation. In literature, there are established criteria which assist with finding the best order for systems (e.g. Akaike's Information Criterion (AIC), Brockwell et al. 2002).

To illustrate the effect of model order in the accuracy of the simulation, the measured responses are compared to the simulation results, in different ARX model orders. Figure 3.13, shows the changes in the ratio of residual-to-response RMS, versus the model

orders. Residuals are defined as the difference of the simulated response and the measurement data. This ratio reflects the accuracy of the estimated model in terms of predicting the outputs. The results show that the optimum model order, for this specific model, is 13. This optimum order is, of course, system and algorithm dependent which means for any different system, the best order should be obtained through a pre-processing. Figure 3.14 also shows the two simulated and measured responses when using the fitted model with selected order. Although the two signals are not perfectly identical, the differences are minimal when the proper model order is selected.

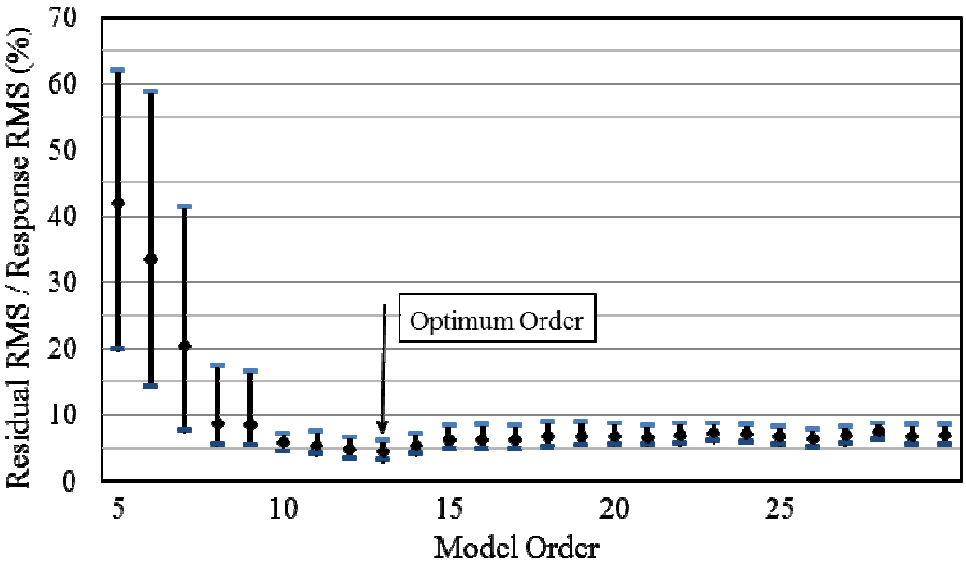

Figure 3.13. The residual-response ratio (max., min., and avg. of different nodes) versus model order

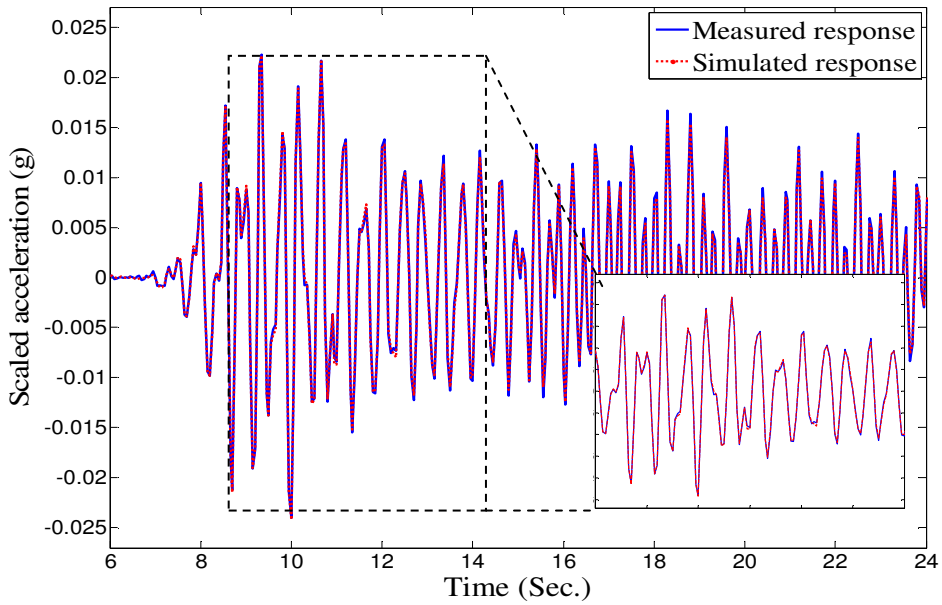

Figure 3.14. Measured response and simulated response from estimated model with optimal order

Once the order is selected, IMID starts iteration from an initial estimate using the ARX model for both simulation and identification. To track the convergence, the changes in the estimated modal properties are assessed at the end of each cycle. Figures 3.15-(a) and 3.15-(b) show the error percentage in estimated natural frequencies and mode shapes versus the number of iteration cycles. It is shown that after a few cycles, modal properties converge with less than 1% error. The results are also compared to the modal properties which are extracted from centralized modal identification with ARX and Stochastic Subspace Identification (SSI) methods. Table 3.3 summarizes the results obtained from different algorithms. This table shows the accuracy of the obtained results from IMID, based on the estimated results from centrally processed data.

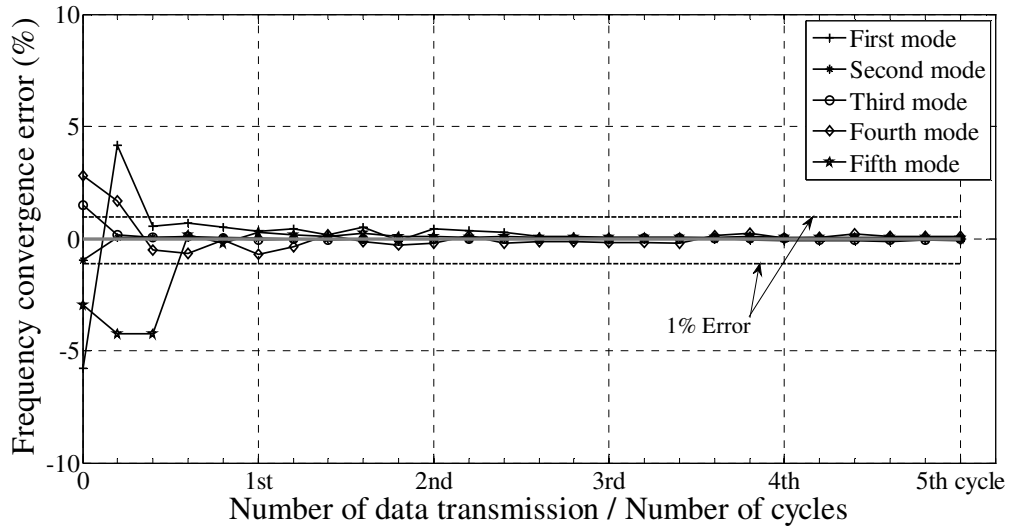

(a)

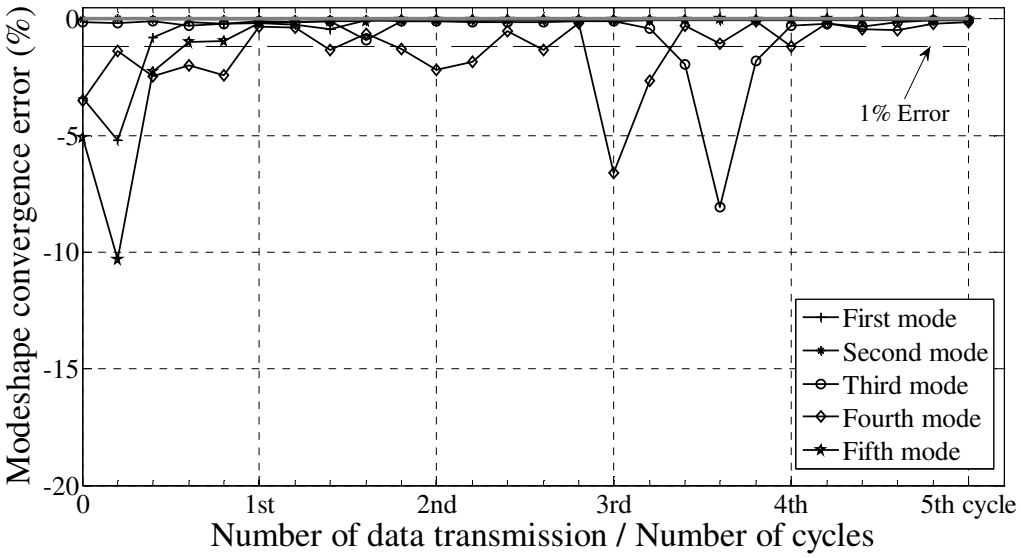

(b)

Figure 3.15. (a) and (b), the convergence of natural frequencies and mode shapes of 5 story experimental model versus iteration cycles

Table 3.3. Comparison of identified modal properties of the experimental model, using different algorithms

Frequencies (Hz)			Damping Ratios (%)			MAC
Centralized SSI	Centralized ARX	IMID after 4 cycles	Centralized SSI	Centralized ARX	IMID after 4 cycles	IMID vs. SSI after 4 cycles
0.7598	0.7590	0.7601	1.0049	0.9401	1.0620	0.9996
2.5426	2.5425	2.5423	0.6569	0.6580	0.6385	1.0000
4.0427	4.0428	4.0413	0.7741	0.7907	0.8385	0.9993
5.3453	5.3311	5.3447	0.7568	0.8284	1.0952	0.9925
6.6048	6.6076	6.6084	0.3574	0.3628	0.3738	0.9999

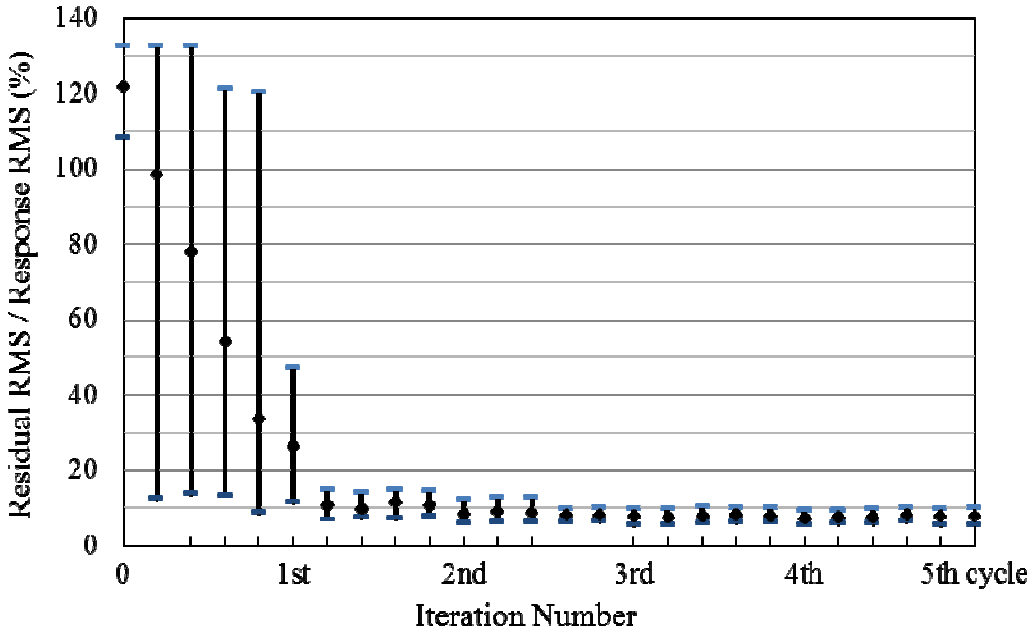

Figure 3.16. The residual-response ratio (max., min., and avg. of different nodes) versus iteration number

Figure 3.16 also shows the changes in the ratio of residual-to-response RMS over the iteration cycles. This result supports the fact that the assumed model at different nodes of the network converges to the real system after a few cycles of iteration.

3.6.2 Experimental Truss Structure

To further validate the IMID, the algorithm is used for modal identification of a three dimensional steel truss structure. The truss 27.5 feet long and has 6 panels as shown in Figure 3.17. A network of 10 wireless sensors is installed on lower chord of the truss to collect the acceleration data in lateral and vertical directions (Figure 3.18). The accelerometers are LIS3L02AS4 [17] with 50 μg/√Hz noise density in X and Y direction and resolution of 0.66 V/g, capturing acceleration in ±2g range. The structure is excited by impulsive load, using a hammer test.

Having a relatively stiff structure with natural frequencies all above 10 Hz, a relatively long response measurement with a high sampling rate is required for obtaining fundamental natural modes. For the experiments, the impacts were applied on location 2 in both vertical and lateral directions. It takes about 30 to 40 seconds to have the impulse response with a peak of 0.6 g fully attenuated. The sampling rate was 280 Hz and the length of the data used for the algorithm was 10000 points. Figure 3.19 shows the collected response from sensor number 3 at the mid-span and its power spectrum. Using AR algorithm, the modal frequencies, damping ratios and mode shapes of the truss are identified to be used as a reference for validation of the results, obtained from IMID implementation. Figure 3.20 shows the identified modal properties.

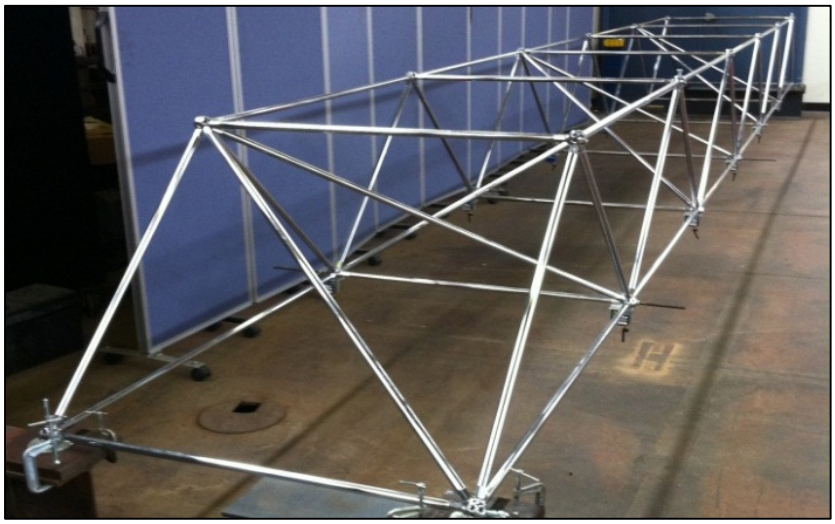

Figure 3.17. The experimental truss structure

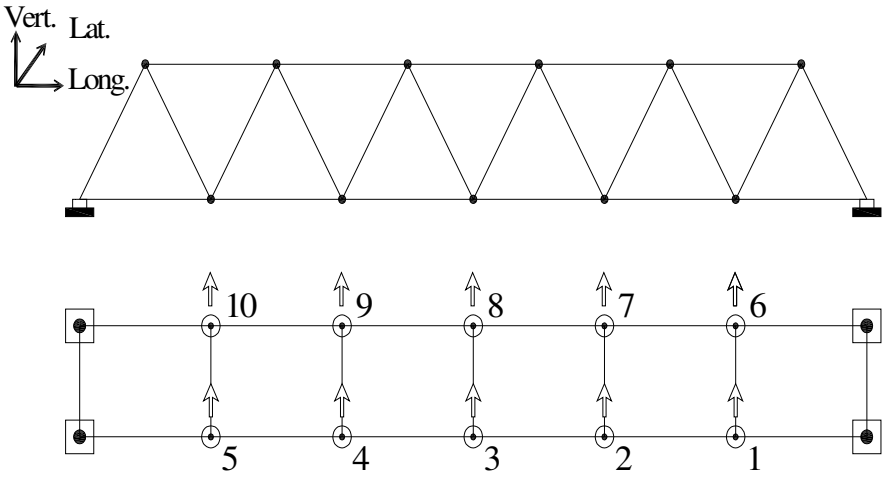

Figure 3.18. Location of sensors on the truss

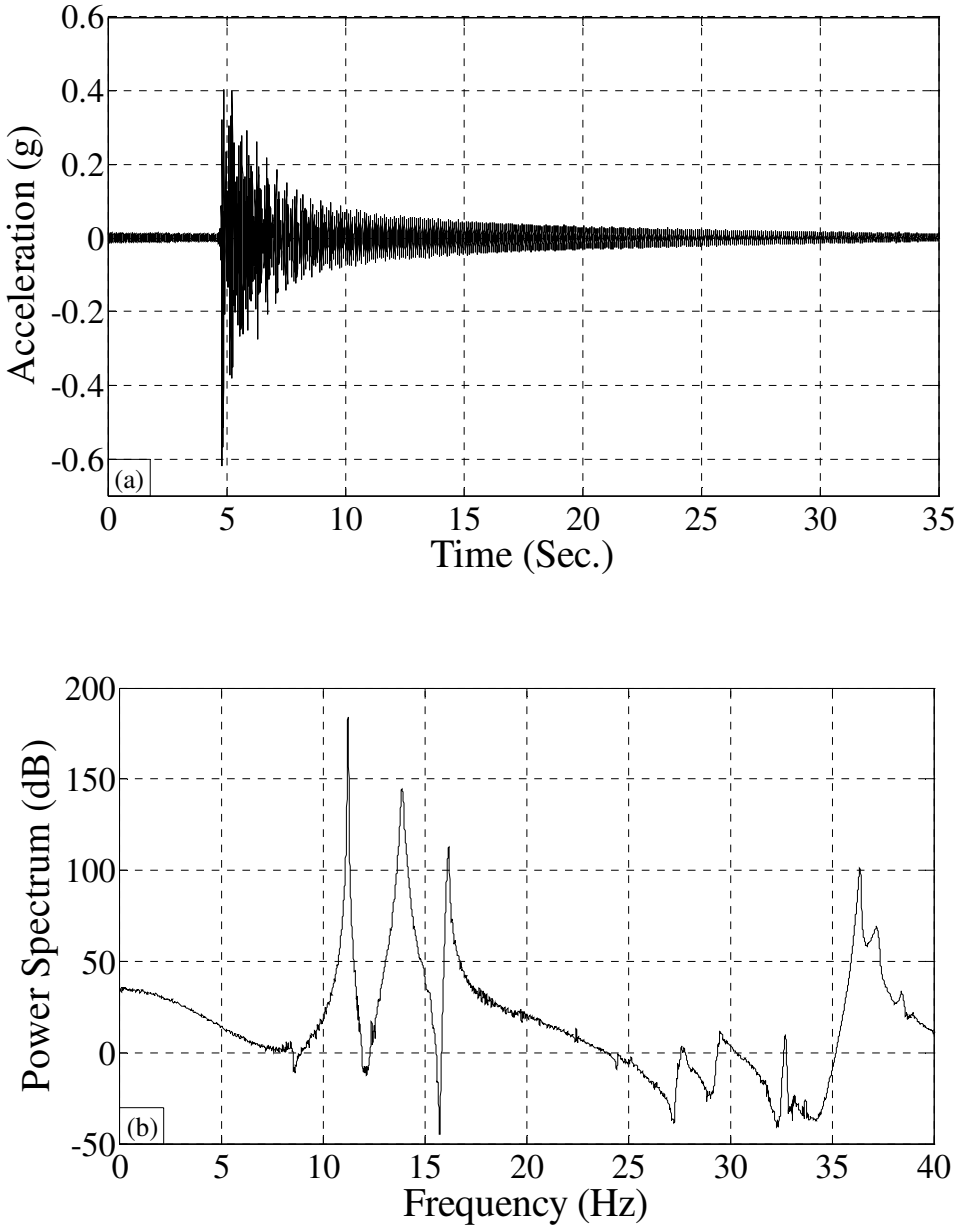

Figure 3.19. (a) The impulse response in a node at mid-span, (b) the power spectrum of the response

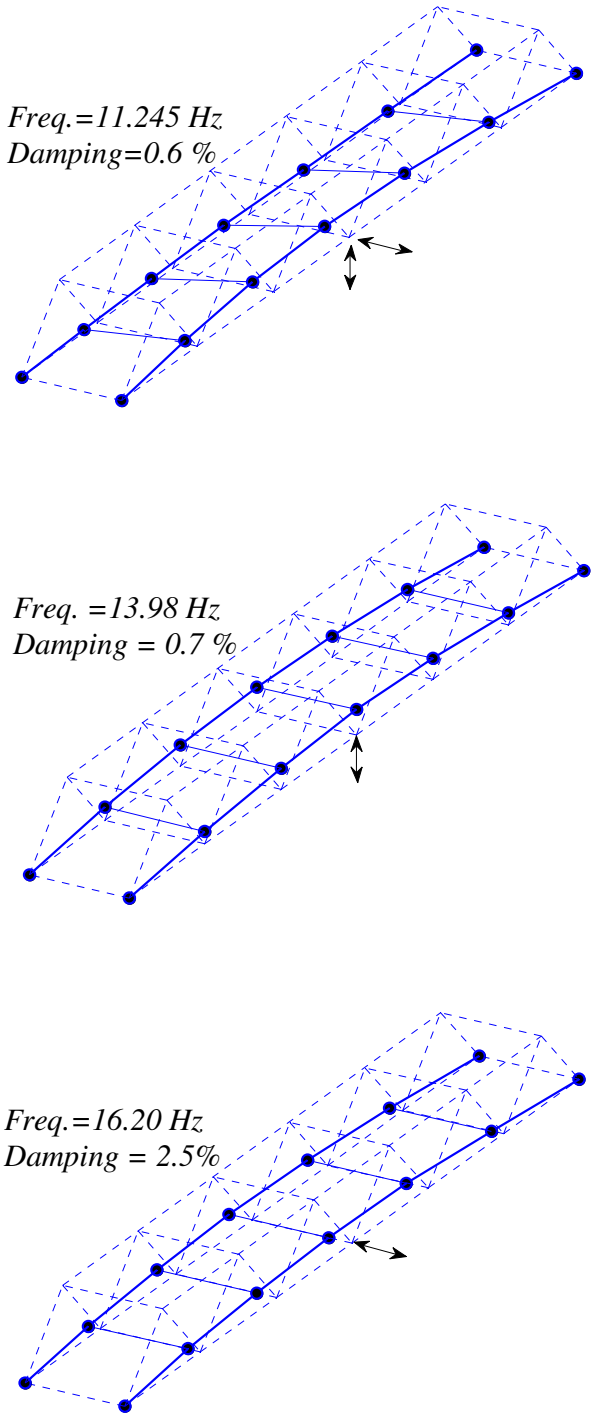

Figure 3.20. Identified mode shapes of the experimental truss structure

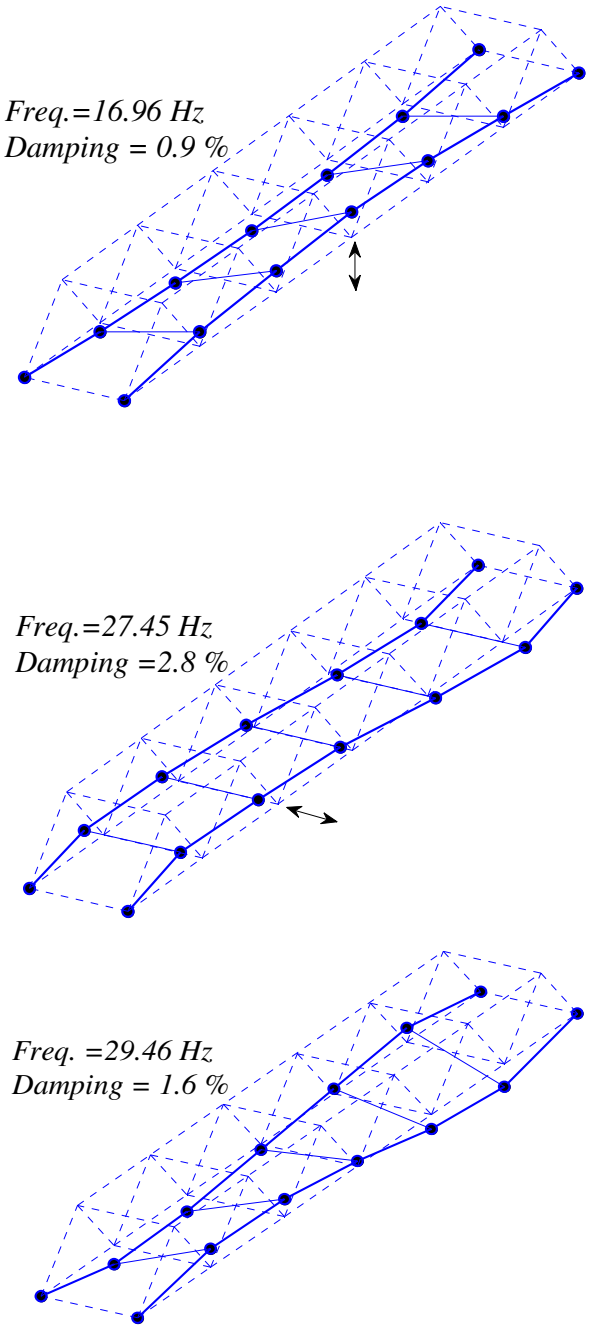

Figure 3.21 (Cont'd). Identified mode shapes of the experimental truss structure

For simulation of the response in this implementation, ARX algorithm is applied. Using this algorithm, response at any time step can be estimated based on the past inputs and outputs and the current input. Considering the noise with zero mean, ARX model can be rewritten to estimate for the response at time step *n*:

$$\bar{y}(n) = -\sum_{i=1}^{p} \alpha_i y(n-i) + \sum_{i=0}^{q} \beta_i x(n-i) \tag{3.17}$$

When the input is an impulse, for $n > p+1$, Equation (3.17) will be simplified to:

$$\bar{y}(n) = -\sum_{i=1}^{p} \alpha_i y(n-i) \tag{3.18}$$

This equation can be used for one-step output prediction. For multi-step output prediction, the vector of *s* steps responses can be obtained directly by the following equation (Juang and Phan, 2001):

$$\begin{bmatrix} y(n) \\ y(n+1) \\ \vdots \\ y(n+s-1) \end{bmatrix} = -\begin{bmatrix} \alpha_p & \alpha_{p-1} & \cdots & \alpha_1 \\ \alpha_p^{(1)} & \alpha_{p-1}^{(1)} & \cdots & \alpha_1^{(1)} \\ \vdots & \vdots & \ddots & \vdots \\ \alpha_p^{(s-1)} & \alpha_{p-1}^{(s-1)} & \cdots & \alpha_1^{(s-1)} \end{bmatrix} \cdot \begin{bmatrix} y(n-p) \\ y(n-p+1) \\ \vdots \\ y(n-1) \end{bmatrix} \tag{3.19}$$

where:

$$\alpha_1^{(0)} = \alpha_1$$

$$\alpha_1^{(k)} = \alpha_{k+1} - \sum_{i=1}^{k} \alpha_i \alpha_1^{(k-i)} \quad for\ k < p$$

$$\alpha_1^{(k)} = \alpha_{k+1} - \sum_{i=1}^{k} \alpha_i \alpha_1^{(k-i)} \quad for\ k \geq p$$

Therefore, to predict the output response, a sensor only needs AR parameters of the system which is estimated in previous sensor and is passed through the network.

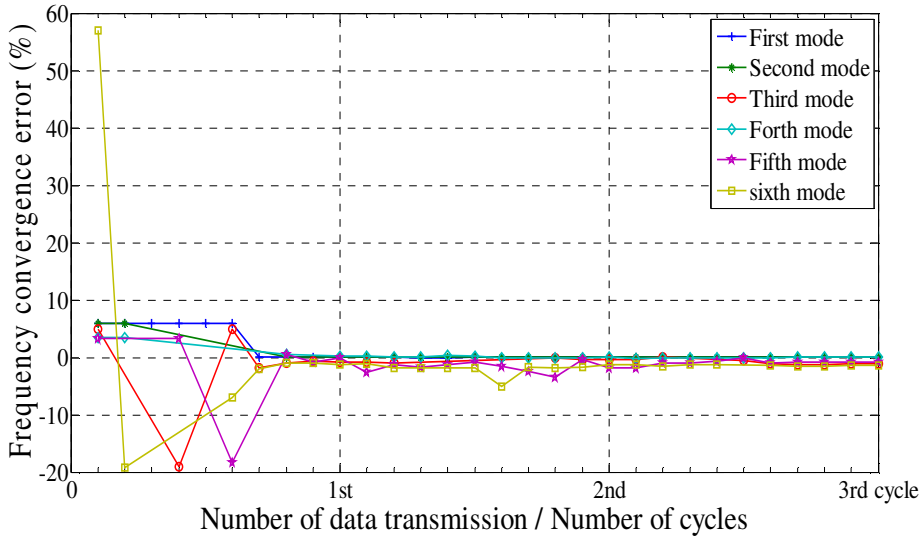

(a)

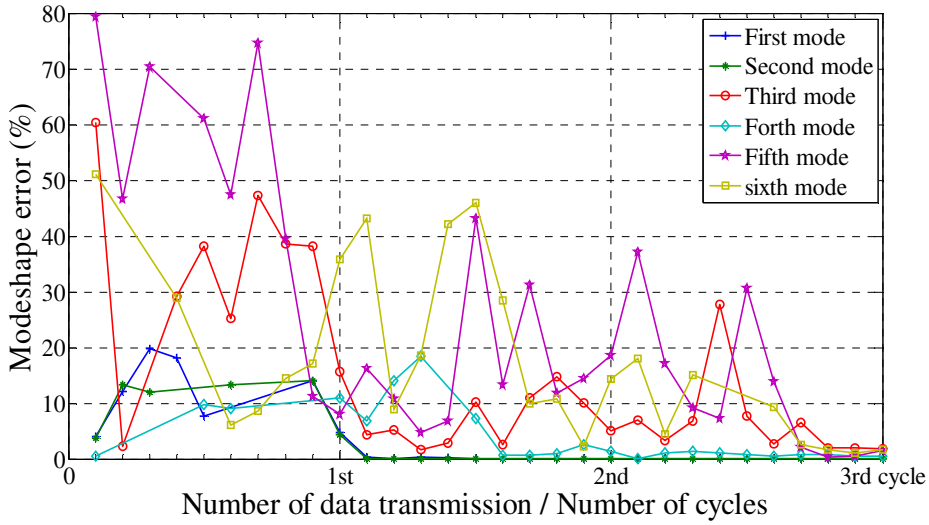

(b)

Figure 3.22. (a) and (b), the convergence of natural frequencies and mode shapes of the 6 identified modes of the experimental truss structure versus iteration cycles

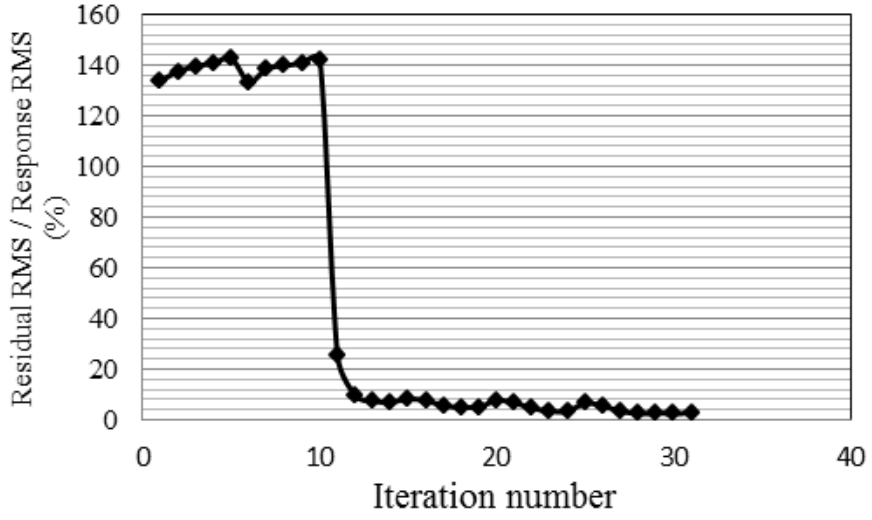

(a)

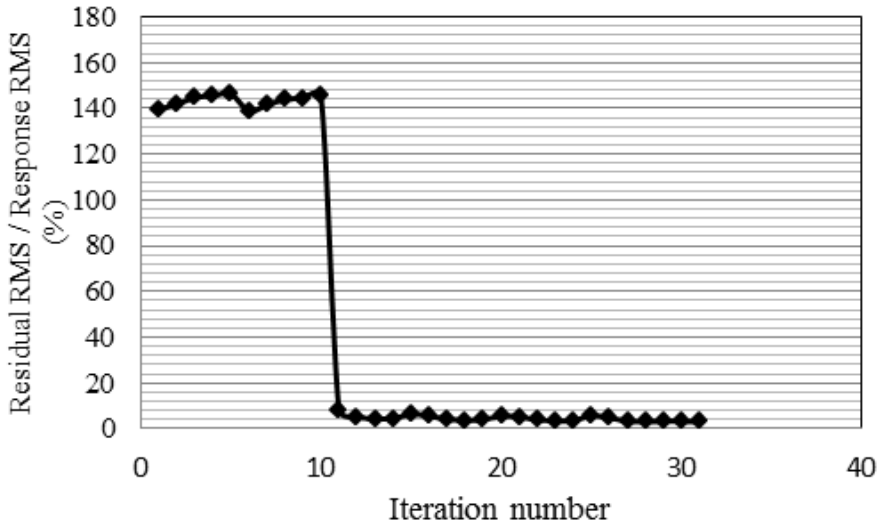

(b)

Figure 3.23. Residual to response ratio during iteration at different nodes, (a) lateral direction (b) vertical direction

To begin the iteration process, an initial estimation of the structural model is required as the starting point of the iterative process. For this purpose, random masses are added to different nodes such that the additional masses make about 10 percent changes in the natural frequencies of the system. An AR model is fitted to the response of the altered truss to represent the initial estimate of the structure.

An important parameter in IMID is the order of the AR model. Usually, higher model order result in better representation of the fitted model which particularly enhance the accuracy in simulation step. However since the AR parameters should be transmitted through the network, increasing the model order increases the size of communication burden in the network. The selected model order for this implementation is 10 which results in 10 matrices of AR parameters, communicated among the nodes of the network.

To check the convergence of the results, identified frequencies and mode shapes at each step are compared to those identified in previous step and the error is calculated .Figures 3.21- (a) and 3.21-(b) show the error percentage in estimated natural frequencies and mode shapes, versus the iteration cycles. These figure show that before 3 cycles, the natural frequencies and mode shape errors are less than 2 percent.

Another parameter which shows the convergence of the procedure is the residual to response ratio. Available at each node are the measured response and the simulated response at the node location. The difference of these two signals defines the residual signal. The ratio of the residual-to-response RMS can be also considered as a parameter for assessing the convergence status. Figure 3.22-(a) and 3.22-(b) present this ratio for

lateral and vertical directions over the iteration cycles. It can be seen that this ratio drops after one full cycle (passed through all 10 nodes) and becomes relatively small before the third full cycle.

3.7. Efficiency investigation of IMID

The enhancement in efficiency in modal identification, using the proposed algorithm, is evaluated in this section. The basis for this assessment is the reduction in the total communicated data points and also the total required energy that is required for the estimation of structural modal properties. These parameters are selected since they reflect the improvement of modal identification in terms of minimizing both latency and energy usage. The results of numerical examples and the experimental 5-story model are used to evaluate the efficiency of IMID.

For the numerical example, the coefficients of stiffness matrix are transmitted through the network and therefore, the total number of transmitted data points can be obtained from:

$$N_{total}=(number\ of\ cycles \times number\ of\ nodes) \times (number\ of\ stiffness\ matrix\ coefficients) \quad (3.20)$$

Considering less than 1% error in convergence of modal parameters, the total number of transmitted data is:

$$N_{total}=(7\times5)\times5=175 \quad (for\ 5\ DOF\ model)$$

$$N_{total}=(4\times10)\times10=400 \quad (for\ 10\ DOF\ model)$$

For the experimental validation, the ARX parameters were sent through the network. In this case, based on the cycles of iteration and the selected ARX model, the total number of transmitted data points can be obtained as:

$$N_{total}=(number\ of\ cycles \times number\ of\ nodes) \times (ARX\ order \times size\ of\ ARX\ parameters) \quad (3.21)$$

In the example of 5-story model, the number of nodes is 5, the convergence with less than 1% error occurs after 4 cycles of iteration, and the selected ARX order is 10. ARX parameters include two groups of autoregressive and exogenous parameters. The autoregressive parameters are each 5 by 5 whereas exogenous parameters can be vectors of size 5. This is based on the fact that the excitations at different nodes are not independent and all are generated by the ground motion. Therefore, the total number of data points is equal to:

$$N_{total}=(4\times5) \times[(10\times25)+(10\times5)]=6000\ (96\ kb)$$

The efficiency of IMID becomes clearer, comparing this approach with centralized computation method. For centralized computation method the data needs to be transferred to the base station. To transfer the collected data, sensors can either send their data directly to the base station (centralized data collection scheme, Figure 3.23-[a]), or send them through the intermediary nodes, which is called multi-hop communication (Figure 3.23-[b]). Use of multi-hop data transmission is essential when the network is long and there are nodes that are not in the radio range of the base station (e.g. implementation of WSN on long-span bridges). When using the centralized data transmission routing, the

total number of data points will be simply $N.n_s$ where n_s is the number of sensors and N is the number of collected data points at each sensor. Also, in multi-hop communication routing, the total transmitted data is $N.n_s(n_s+1)/2$ (Pakzad et al. 2008). In modal identification process, higher the number of collected data samples is, better the estimation of modal properties would be. In this implementation, 25000 samples were collected at each sensor node. Considering use of centralized data transmission, 125000 (2000 kb) will be the total samples need to be communicated. In multi-hop data transmission and routing, which is essential in many wireless sensor network deployments, the significance of the proposed algorithm will be even more evident, as such implementations need $(n_s+1)/2$ time larger transmission when collecting the data at the base station, but the same when using IMID approach.

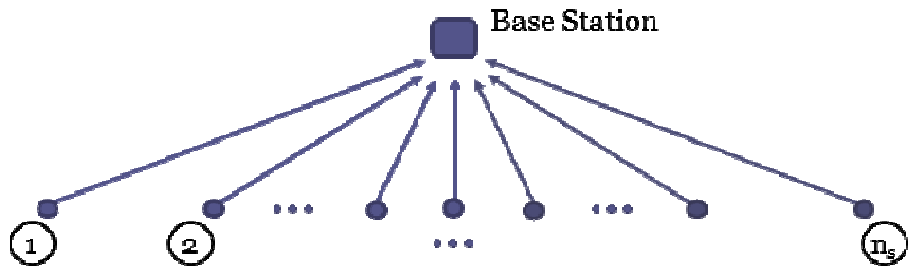

(a)

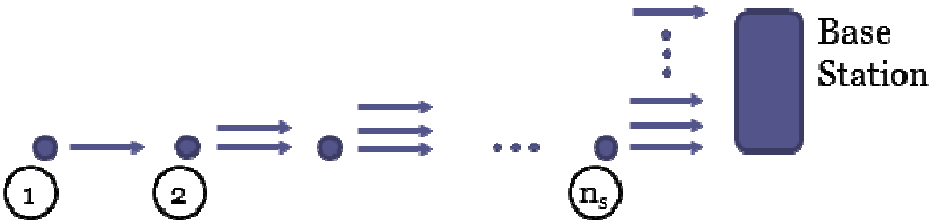

(b)

Figure 3.24. The centralized data transmission routing (a) and multi-hop data transmission routing (b)

Comparison of the total energy:

Considering the results and specifications of the experimental implementation, the energy consumed by the two approaches, namely IMID and centralized system identification, are estimated and compared.

Required energy for data transmission can be calculated simply from Equation 3.2, by having the volume of the data, transmission rate, and the power consumption rate:

$$E_{trsmission}=[1/transmission\ rate(Kbps)]\times[power\ consumption\ rate(mW)]$$

where the nominal transmission rate of the embedded transceiver on Imote2 is 250 kbps (Crossbow, 2007) and the power consumption rate, while transmitting the data, is 245 mW (Figure 3.2).

Estimating the required energy for data processing is more challenging since it needs an estimate of computation time. Chang et al. (2011) conducted a comprehensive study on the required computational time for several different time domain system identification algorithms. In this study the required number of operations is presented as a function of model order, number of outputs and the signal length. Then the computation times in different algorithms are presented and compared. It is concluded through simulated examples that the total consumed time for performing the entire identification process for a system with 5 outputs and order of 10 is just a fraction of second (less than 0.1 second).

The computational time for the numerical simulation of the response, using ARX model is also measured for the 5 DOF system of the presented example and resulted in less than 0.05 second CPU time. Considering these estimations of computational time at each node, 4 cycles of iteration, and 184 mW power consumption rate (Figure 3.2) of the Imote2 in data processing mode (radio off), the consumed power for computation is about 400 mW-sec. Also, the required energy for transmission of 96 kb data, using Equation 3.2, will be about 94 mW-sec which results in 494 mW-sec total energy.

For application of the centralized data processing to this example, considering transferring 2000 kb data, the total required energy will be 1960 mW-sec.

This estimation shows 75% saving in the consumed energy for IMID versus the centralized method. However, there are a few important considerations that should be noted: (i) the computational time may increase depending on the micro controller that is responsible for on-board processing. If high performance processors are utilized in the next generations of wireless sensor units, this processing time can further decrease for the decentralize analysis; (ii) the transmission rate considered in this study is the nominal rate presented in the datasheet of CC2440 transceiver. However in practice, the actual transmission rates are less since there is a communication overhead due to packet loss and collisions in the wireless communication (for example, see Nagayama et al. 2010, which reported maximum of 83 kbps communication rate in single-hop transmission in laboratory experiments). Smaller communication rate causes higher energy demand for data transmission task which adversely affects the centralized processing methods disproportionately; (iii) in these estimations, it is assumed that the transmission scheme is centralized and single-hop. The use of multi-hop data transmission results in longer data collection time. Therefore, the benefits of IMID will be more significant when multi-hop data transmission scheme is utilized.

3.8.Limitations of IMID

There are limitations associated with this algorithm: (i) it needs an initial estimate of the system parameters and (ii) it needs the excitation load. It was discussed that the initial estimate for the system parameters can be available by either a constructed finite element model of the structure or from prior dynamic testing of the structure. Both these scenarios

for addressing this limitation may make the implementation of the algorithm somewhat challenging and restricted in certain cases.

The need for availability of excitation load also limits the application of the algorithm to input-output problems, where the excitation load is measured (in the case of impact testing the excitation is also known).

Following presents some modifications which eliminate the need for initial estimate of the system parameters and the excitation load. The approaches are explained and validated through numerical and experimental examples.

3.9. Cumulative System Formation

Initial estimate of the system

One of the limitations of IMID is its need for starting points for iteration process. In many applications an initial estimate of the system can be provided from previous implementations or finite element model of the structure. However, since in many applications this information may not be available a cumulative system formation approach is developed here which can estimate the modal properties based on a similar principles but is independent of initial values.

In IMID, sensing units, in addition to measurement of the structural response at their location, simulate the response at other locations to complete the data for performing system identification. To start the iteration, therefore, the first node needs system

parameters to simulate for the rest of the nodes. These parameters for this node are estimated using only measured data at its location (single output problem). The second node then receives estimated parameters from the first node and uses them to simulate first node's measurement. Together with its locally measured data, second node updates the estimated systems parameters (two outputs). The third node performs similar process with three outputs and the process continues up to the last node in the array, each time the number of outputs increases by one. As the estimation reaches the last node, one cycle of iteration is completed and the estimated system is formed from multiple outputs. At this stage, the estimated parameters are capable of simulating as many outputs as participated in the first cycle because they are extracted from a multiple-output model. For the next iteration cycles, a multiple-output system will be updated through the network and updating continues until convergence. The challenge in this approach is that models estimated with only a few outputs are not accurate estimates of the true system. However, in implementation examples, it is shown that the accuracy improves quickly as estimation is updated through the network. Figure 3.24 also demonstrates the strategy for application of IMID.

As mentioned earlier, in implementation of IMID, careful consideration should be given to the selection of model order. When applying cumulative system formation approach, model order selection becomes even more important for the few first cycles. The reason is that system parameters which are identified from fewer number of outputs are expected to carry the entire system characteristics and therefore, estimation may need

higher model order to accomplish the task. For example, the first node is supposed to estimate the system from its only measured output. To do this, the model order should be selected high enough to capture all high and low-level dynamic characteristics of the measured signal. For the rest of the iteration cycles, selection of model order should also be based on the accuracy in simulation of response. However, in general, it is important to use optimum model order which results in accurate results since increasing the model order increases the communication burden for the network. In previous examples, it was shown that the optimum order can be obtained such that the residual rations corresponding to the selected order are minimums.

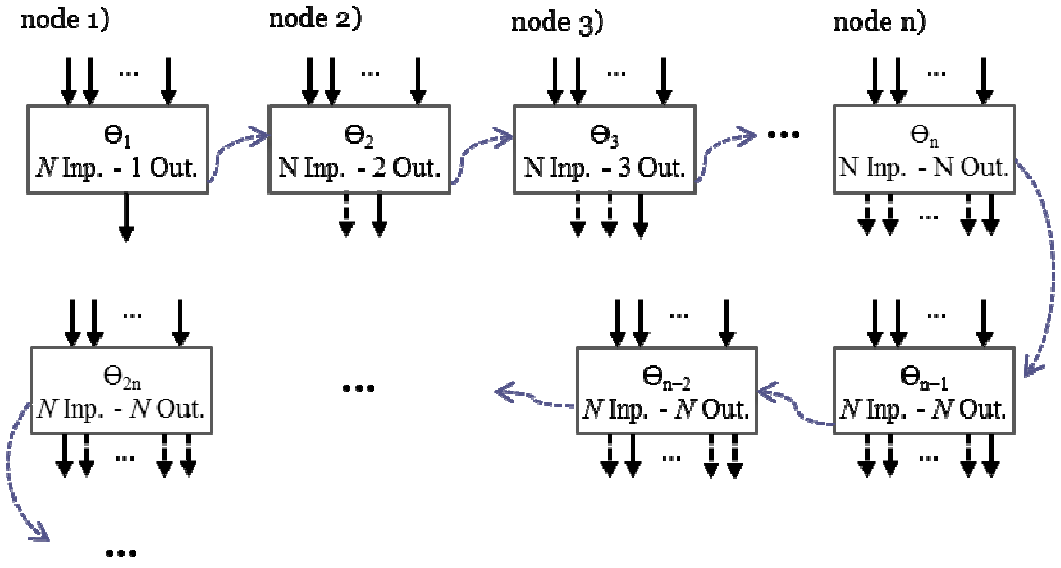

Figure 3.25. Iteration cycles in IMID

AR-ARX Analogy

AR-ARX is a two steps process which is a popular implementation of ARMA (Ljung, 1999) model that can be fit to the data from output-only systems. In this approach, the system with relatively broadband input is characterized by ARX parameters in two steps: (i) applying an AR model with relatively high order which is fit to the output data (y) and provides an estimate of the output ($\bar{y}$), and (ii): fitting an ARX model with relatively low model order in which the estimation error (residuals) in step (i) is considered as the exogenous input of the model. An analogous strategy can be utilized in the implementation of IMID. However, different steps are applied in different iteration cycles. In this strategy, the first iteration cycle uses AR model and the later iterations use ARX model (using residuals of the AR model) for estimating the system parameters and predicting the response. Similar to AR-ARX approach, the ARX models use residuals as the input. The available residual at the sensor location is the difference between the locally measured signal and the predicted one from simulation. The process is outlined in Figure 4.25. Deploying this approach in implementation of IMID enhances the results of the algorithm.

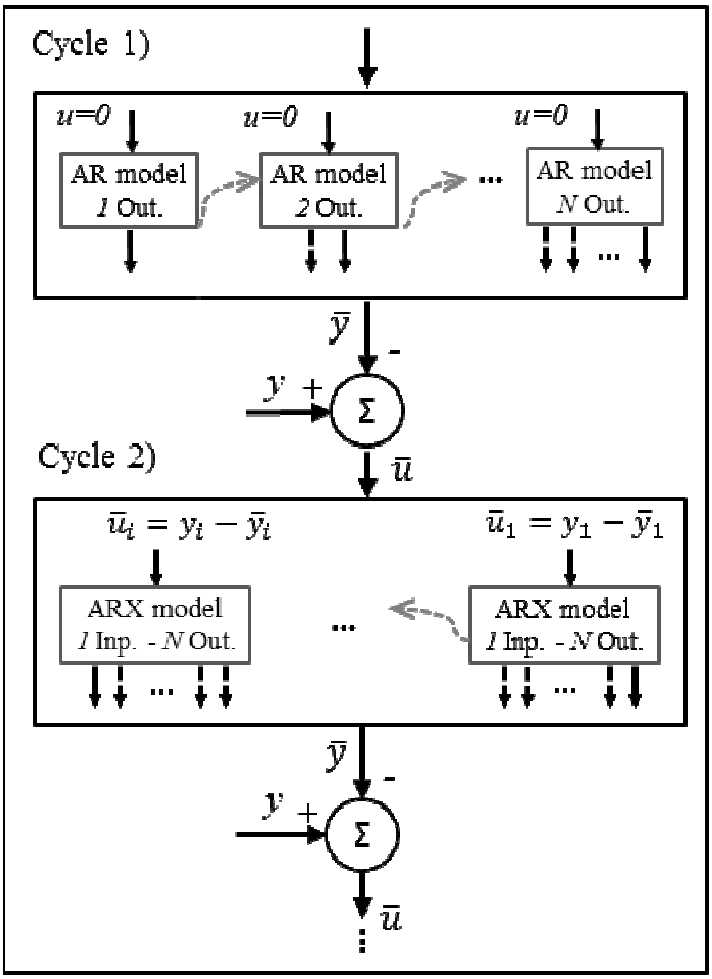

Figure 3.26. Block chart presenting AR-ARX analogy in application of IMID

Validation through implementation on an experimental laboratory truss

To validate the idea of cumulative system formation in IMID, the algorithm is applied in modal identification of the three dimensional steel truss structure presented earlier in this chapter (the 9 m. truss with 6 panels as shown in Figure 3.17).

Auto Regressive with Exogenous model (ARX) is used as a numerical model for characterizing the system. ARX models can be used for both simulation and identification steps.

For IMID based on ARX model, ARX parameters are communicated throughout the network to represent the structural system. These parameters (α_i and β_i) can be estimated by least square approach (minimizing the sum of squared errors) having the response (estimated response). Using ARX to predict the output response, a sensor only needs AR parameters of the system which is estimated in previous sensor and is passed through the network.

Implementation and Results

The objective of this implementation is to identify the modal parameters of the truss structure. For this purpose, the system parameters are estimated through the iteration cycles. Beginning from one node, network runs iteration following the estimation/simulation steps. To make the implementation more efficient, the network is divided into different sub-networks where each runs the iteration and transmits the converged result to the base station separately. The idea of dividing the network into sub-networks has been used in several distributed modal identification algorithms presented in the literature (Sim et al, 2009). Figure 3.26 shows a few examples of different alternative topologies for dividing the network in this experiment.

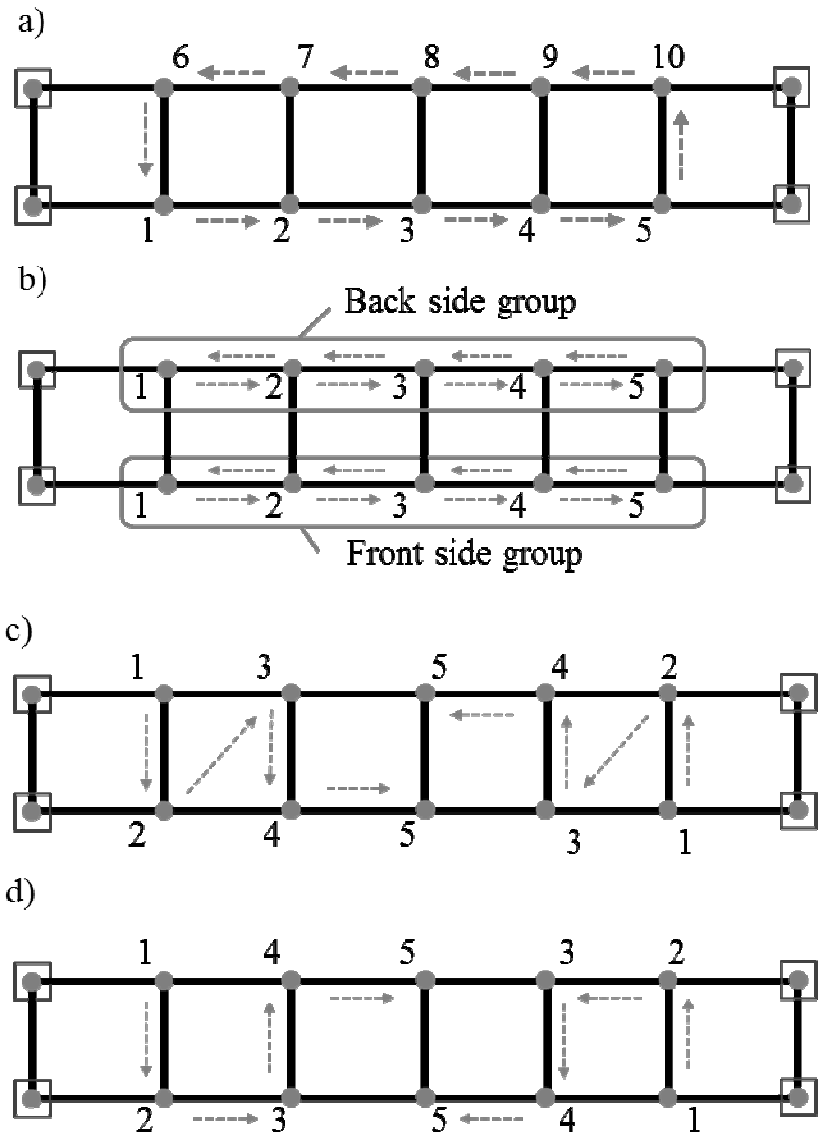

Figure 3.27. Different sub-networking topologies for communication

As the results are converged and the parameters are transmitted to the base station, the complete response is simulated and the global modal parameters are estimated. Among different topologies presented in Figure 4.26, the best results are obtained from topology (b). This is because in this sub-networking topology, the most structurally correlated

nodes are clustered in the same group (each sub-network includes nodes from either the front or the back 2-D trusses).

To check the convergence, at each node, the root mean square (RMS) of residual (simulated signal subtracted from measured signal) is compared to the RMS of the measured signal. Figure 3.27 shows the residual-to-signal ratio of 3 cycles of iteration. Note that the convergence check assigns an extra task to individual nodes. As Figure 3.4 presents, different tasks of sensing nodes in IMID are to receive the estimated parameters, update them by the use of their measurement, and send them to the next nodes for further updating. Part of updating task is to check the convergence, for which the response is simulated using the updated parameters, and is compared to the measured response. Therefore, for an efficient implementation, convergence check can be assigned to only the node which is located at the end of each iteration cycle.

The model order for this implementation is 30 for the first cycle and 10 for the rest of the cycles. These model orders are selected based on minimum simulation error. As metioned earlier, alternative approaches for model order selection are Akaike's Information Criterion (AIC) and partial auto-correlation analysis presented in Box *et al.* 1994.

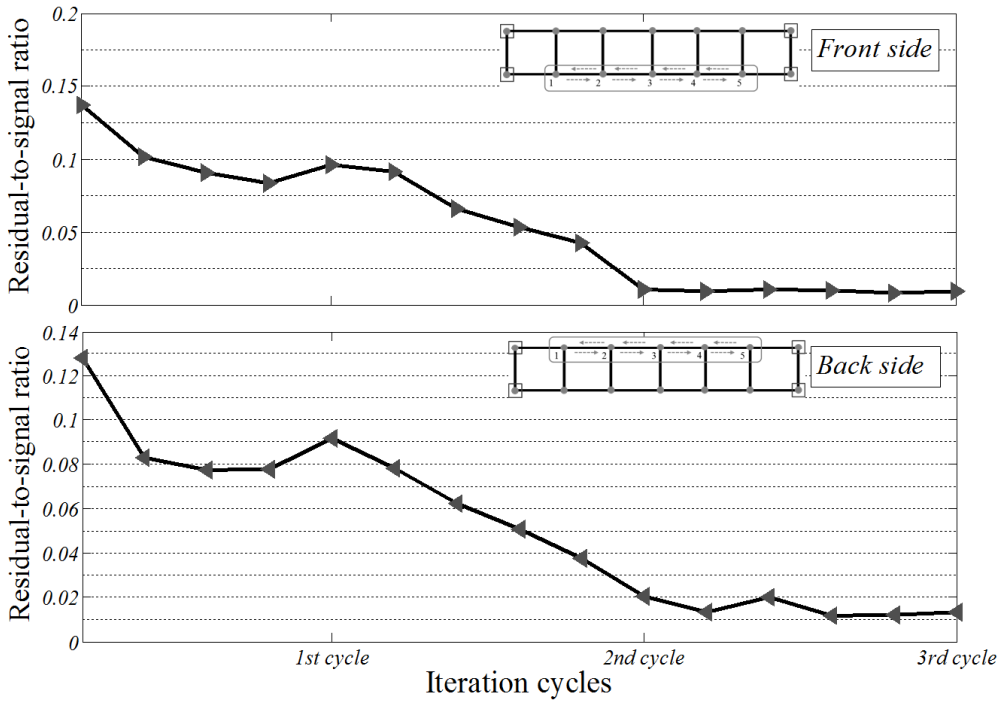

Figure 3.28. Residual to signal ratio throughout iteration cycles

Having the converged parameters at the base station, the response of the complete structure is simulated and the modal parameters are extracted using any system identification algorithm. Table 3.4 presents the identified modal parameters and compares the two centralized and IMID approaches.

To evaluate the performance of IMID in this example, the number of transmitted data points is calculated. Equation 3.22 provides the total number of communicated data points:

$$N_p = n_g \times [p_1(\sum_{k=1}^{n_s} k^2) + (n_c - 1) p_2 {n_s}^2] \tag{3.22}$$

where n_g is the number of groups of nodes, n_s is the number of nodes in each group, n_c is the number of iteration cycles ([n_c-*1*] is used in the equation to exclude the first cycle), and p_1 and p_2 are model orders in the first cycle and the rest of the cycles, respectively. Considering model orders p_1=*30* and p_2=*10*, the grouping scheme which is shown in Figure 3.27-(b), and 3 cycles of iteration, the total number of communicated data points (system parameters) will be 11,600 which is about 10% of communication cost for a centralized modal identification method.

Table 3.4. Modal Parameters of the truss, identified by IMID and Centralized approach

	Freq. (Hz) Centralized	*Freq. (Hz) IMID*	*Error (%)*	*Damping (%) Centralized*	*Damping (%) IMID*	*Error (%)*	*MAC (Cent. vs. IMID)*
Mode 1	11.245	11.140	1.47	0.600	0.54	11.11	0.998
Mode 2	13.982	14.231	1.78	0.700	0.595	17.65	0.982
Mode 3	16.196	16.470	1.72	2.500	2.29	9.17	0.985
Mode 4	16.958	17.270	1.84	0.900	0.77	16.88	0.956
Mode 5	27.453	28.020	2.05	2.800	2.55	9.80	0.975
Mode 6	29.459	30.530	3.81	1.612	2.001	19.44	0.948

3.10. IMID for Output-Only Identification

Output-only modal identification for structural systems is important as performing input-output tests in many cases is either infeasible or very expensive. On the other hand, the proposed algorithm requires individual sensors to simulate the system response, using the estimated parameters, and to perform the simulation, the excitation load is needed.

Therefore, it is important to devise a strategy which eliminates this requirement and makes IMID applicable to output-only modal identification.

One solution to such a limitation is the use of impulsive loading in which the input is known (e.g. hammer testing for the truss example presented earlier in this paper). Considering the fact that the cross-correlation function between two measured responses is an estimate of unscaled impulse response, IMID can be adopted to estimate the parameters of correlation functions instead of the response. The concept of on-board computation of correlation function is previously proposed by Nagayama and Spencer 2007.

In this approach one node, as the reference, sends its measured time history data to the rest of the nodes in the network. The other nodes, then, calculate the cross-correlation functions and send them to the base station for modal identification. IMID can utilize similar step to allow all the nodes to have the cross-correlation functions (between their measured data and the reference node data). The rest of the process is identical to the implementation of IMID when impulsive loading is applied. As an alternative, the unscaled impulse response can be estimated through the use of Random Decrement (RD) technique (Cole, 1968). It is shown that for a linear, time invariant system with stationary white noise excitation, the RD function is proportional to the correlation function (Vandiyer et al., 1982). Using RD technique, the correlation function, $h_{pq}(\tau)$, between two outputs (p and q), is estimated as:

$$\hat{h}_{pq}(\tau) = \frac{1}{N}\sum_{k=1}^{N} x_p(t_k : t_k + \tau) | \{a_1 \le x_q < a_2\} \quad (3.23)$$

where x_p and x_q are the responses at the two locations, a_1 and a_2 are the lower and upper bounds for the trigger at x_q, t is the time index, τ is the lag and N is the length of the RD function. Triggering values are determined in different ways and are well described in the literature (Asmussen et al, 1996; Asmussen et al, 1997; Gul et al, 2008). A common triggering approach is level crossing triggering condition which puts a_1=0 and a_2=∞ (Gul et al, 2008).

Sim *et al.* (2010) proposed use of RD in decentralized wireless network for system identification. The advantage of RD technique in decentralized approaches is that the reference node only sends the trigger information, instead of time history data, to the rest of the nodes for estimating the unscaled impulse response. In this way, the overhead due to transmission of reference node time-history data is reduced significantly, since the trigger information is a lot smaller. Regardless of the technique applied for estimation of unscaled impulse response at different nodes, IMID concentrates on estimating and updating the system parameters throughout the network.

To validate the functionality of the IMID algorithm for output-only (ambient input) systems, the method is applied for modal identification in two examples. The first example consists of a numerically simulated beam subjected to a stationary white noise excitation. The second example uses data from ambient vibration testing of Golden Gate Bridge with wireless sensor network. These examples are explained in the next sections.

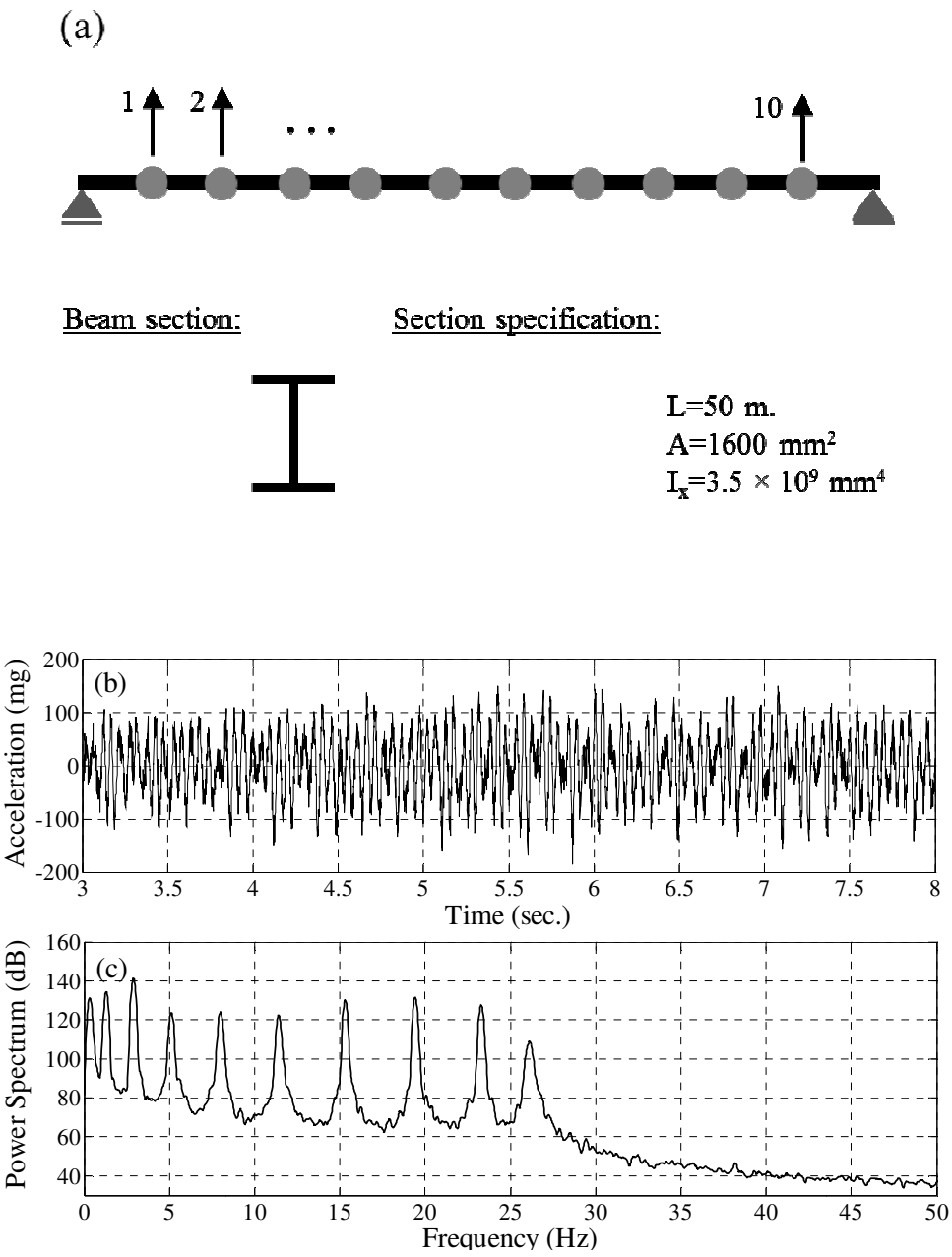

Figure 3.29. (a) Beam example specifications, (b) time-history of acceleration response at mid-span, (c) Power spectral density of response

Numerically simulated beam

The model is a simply supported steel beam with 10 lumped masses along the span. Figure 3.28-(a) shows the specifications of this simulated beam. The masses are determined based on the weight of the beam element and a uniform load. The acceleration response of the beam to a stationary white noise excitation is simulated and used for modal identification with IMID. Measurement noise as Gaussian white noise with RMS ratio of 5% of the response signal is added to the simulated response. Figures 3.28-(b) and (c) show the time-history response of the beam at location 4 and the corresponding power spectral density.

In this example, the objective is to compute the cross-correlation functions between each node and a selected reference node, and then use IMID to estimate the system parameters and update until the converged parameters provide the modal properties of the beam. Two different references, node 2 and node 4, are selected for this example. As the first step, all the nodes calculate the correlation functions to begin the iteration. IMID then starts by estimating the AR parameters and updating them through the network. To track the convergence of the iteration, similar to the truss example, prediction errors (residuals) are investigated. Figure 3.29 presents the comparison of the measured and the predicted correlation functions at node 5 during different iteration cycles. This figure illustrates how the simulated signal converges to the true signal in just a few iteration cycles. Figure 3.30 shows the residual-to-signal RMS ratio at different nodes in all steps of iteration up to the third cycle. It can be seen that the ratio drops down to lower than 5%

in the third cycle which results in less than 2% error in the identification of natural frequencies (presented in Table 3.5). Figure 3.31 also presents the mode shapes of the beam identified by IMID, next to the true mode shapes. The Modal Assurance Criterion (MAC), shown on the mode shape plots, presents the accuracy of each identified mode shape. In this implementation, model orders are selected as 30 for the first iteration cycle and 15 for the rest of the cycles.

Through this example, it is shown that the estimated system parameters can be updated and converge to true system parameters during just a few iterations. The updated parameters can be used to simulate the measured response or directly provide the desire modal parameters.

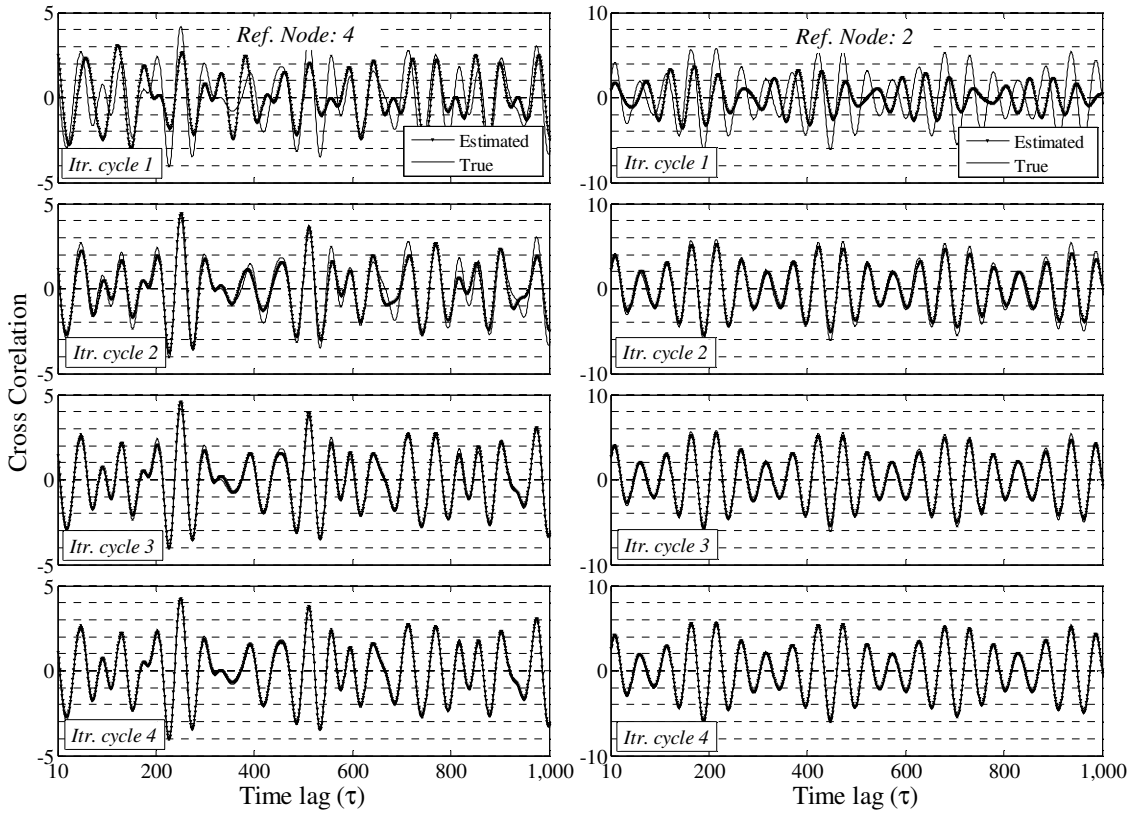

Figure 3.30. Estimated signal versus true signal at different iteration cycles

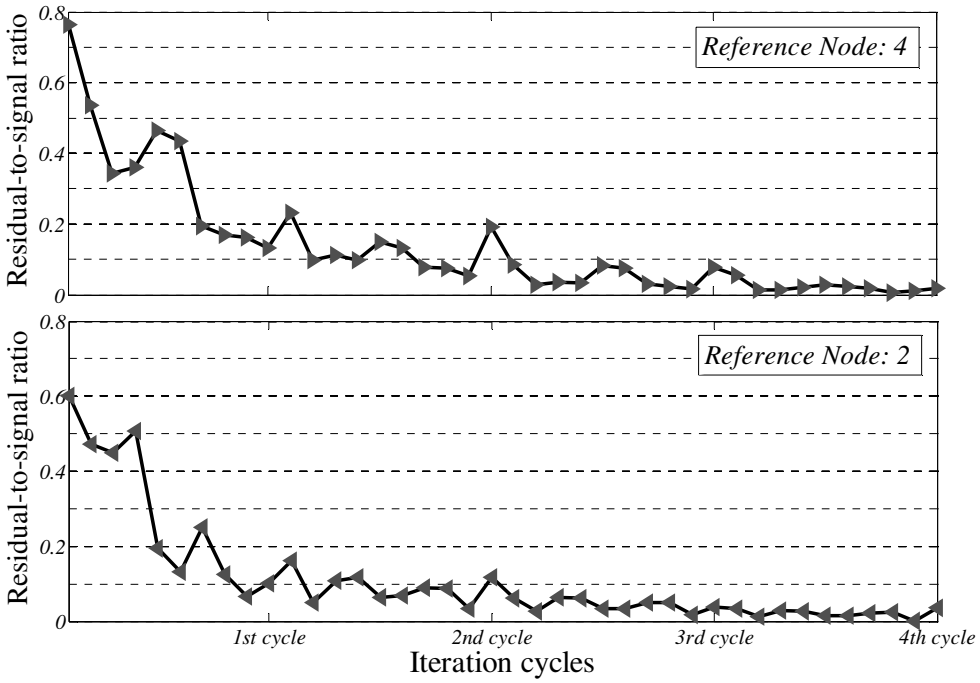

Figure 3.31. Residual to signal ratios in different iteration cycles

Table 3.5. Natural frequencies, identified by IMID and Centralized approach

	Mode 1	*Mode 2*	*Mode 3*	*Mode 4*	*Mode 5*	*Mode 6*	*Mode 7*	*Mode 8*	*Mode 9*	*Mode 10*
True Freq. (Hz)	0.321	1.284	2.888	5.128	7.989	11.427	15.330	19.453	23.321	26.191
Identified Centrally	0.344	1.309	2.912	5.130	8.011	11.420	15.327	19.433	23.302	26.142
Identified by IMID	0.324	1.301	2.929	5.206	8.080	11.491	15.234	19.538	23.597	26.634
Error in IMID (%)	0.93	1.32	1.42	1.52	1.14	0.56	0.63	0.44	1.18	1.69

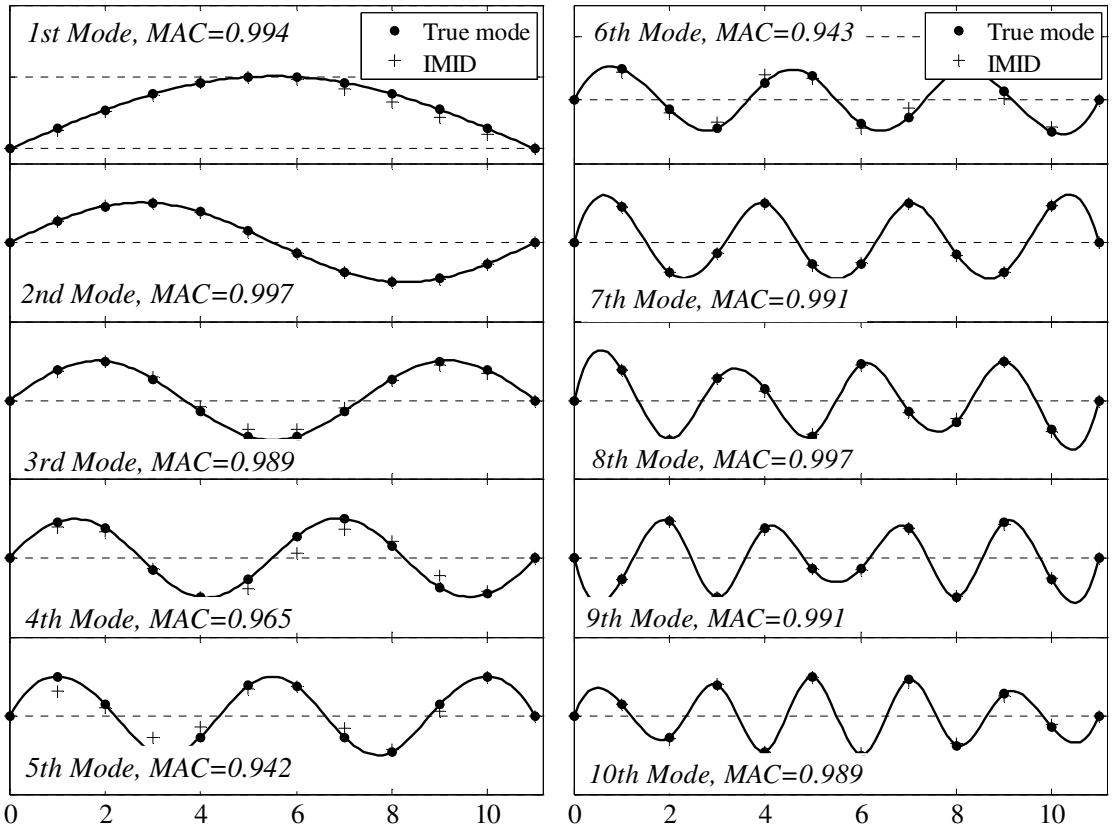

Figure 3.32. Identified mode shapes of the beam example using IMID approach

Implementation on Golden Gate Bridge data:

This section presents the implementation of Output-Only IMID on the ambient vibration data from Golden Gate Bridge. The acceleration data was measured using a WSN, consisting of 65 sensing units, during a three month deployment period (Pakzad et al. 2008). For this example, however, as a validation of the approach, a subset of 10 sensors along the main span of the bridge is selected. The locations of selected sensors on the main span are shown in Figure 3.32.

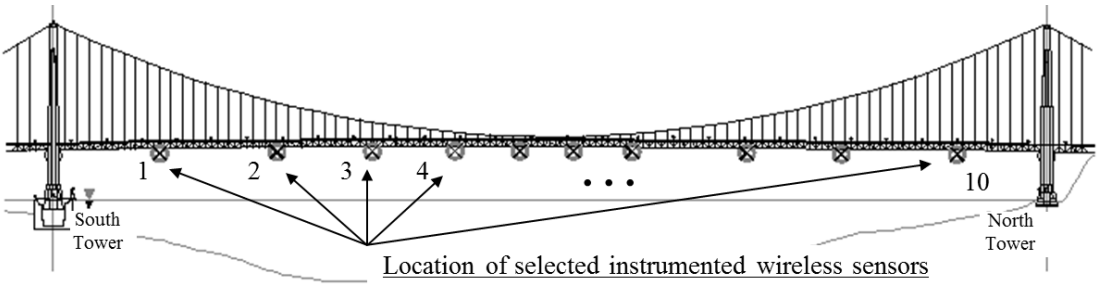

Figure 3.33. Location of selected nodes along the main span of Golden Gate Bridge

Similar to the implementation on the truss example, sensor nodes are divided into two groups of five (south and north) and data transmission and parameter updating are performed separately in each group. In this example, node 4 is selected as the reference and the cross correlation functions are computed between this node and the rest of the nodes in the network. Figure 3.33-(a) presents both the cross correlation function between nodes 4 and 5 as well as the estimated cross correlation function using the updated model parameters.

Iteration results are shown in Figure 3.33-(b) for both groups of nodes. Since the data is obtained from a real ambient test and is affected by environmental noise and structural nonlinearities, the model order is selected to be 40, which is higher than the previous examples. Equation 11, for calculating the number of data point for communication, is slightly modified to account for the transmission of the reference node data (or triggering information, when using the RD technique):

$$N_p = N_{ref} + n_g \times [p_1(\sum_{k=1}^{n_s} k^2) + (n_c - 1)p_2 {n_s}^2] \quad (3.24)$$

where N_{ref} is the length of data transmitted from the reference node to the rest of the nodes in the network. Other parameters in Equation 3.24 are defined similar to those of Equation 3.22. Applying this equation and a calculation similar to the truss example, the number of data points that should be communicated for modal identification of the bridge's span using IMID is 8,800 samples plus the length of the data sent from the reference node. The total length of the data in each test in the monitoring of Golden Gate Bridge, after averaging and down-sampling to 200 *Hz* is 48000 (Pakzad et al., 2008). However, the data is low-pass filtered and further down-sampled to 50 Hz on-board before communication. This low-pass filtering helps the modal identification, as the natural frequencies of the span are in the 0 to 5 Hz frequency range. Additionally, filtering and down-sampling makes the transmission more efficient, particularly for centralized data collection, since in this approach all the sensors transmit their measured data to the base station and the higher volume of the raw data directly affects the communication time. Considering 12,000 samples as the length of the reference node signal (after filtering and down-sampling), the total number of data points is 20800 which is about 17% of 120,000 (10×12,000) for the centralized approach.

Application of RD technique reduces the length of communicated data from reference node to the rest of the network to 4,570 samples when the level crossing-triggering condition is applied (different triggering conditions result in different length for crossing information; the largest length will be resulted when level crossing-triggering is applied.

Information regarding different ways of determining trigger levels in RD technique can be found in Asmussen et al, 1996; Asmussen et al, 1997; Gul et al, 2008. The total number of data points in the case of using RD technique is 13,370 which is about 11% of the centralized approach.

It should be noted that while using distributed identification approaches helps the efficiency by reducing the data communication, they add an extra processing burden which consumes energy at the node. However, it is shown earlier that the extra energy consumed in the on-board processing task does not have significant effect on the efficiency of these algorithms since it is much smaller than the energy cost of communication.

Finally, the modal properties of the bridge span are extracted having the updated system parameters. Table 3.6 presents the first fifteen identified modal parameters of the main span in the vertical direction, using centralized and IMID approaches. The corresponding errors are presented for identified natural frequencies. MAC values are also presented to compare the identified mode shapes from IMID to those of centralized approach.

Moreover, to compare the accuracy of the identified modes, Consistent Mode Indicators (CMI), developed by Pappa et al. 1993 are calculated (for both methods) and presented in this table. To calculate these indicators along with the modal parameters of the system, Eigen Realization Algorithm (Juang and Pappa, 1985) is used. CMI is defined as the product of Modal Amplitude Coherence (MAC) and Modal Phase Collinearity

(MPC) which both can be extracted when ERA is used. MAC measures the coherence between extracted modal amplitude history and the modal amplitude which is formed by extrapolating the initial value to later points in time, using the identified eigenvalues. MPC also quantifies the spatial consistency of the identified mode shapes. More information about these parameters can be found in Pappa *et al* 1993.

Table 3.6 shows that in almost all the identified frequencies, the results of IMID are comparable and close to those of the centralized approach. Figure 3.34 shows examples of identified mode shapes of the main span using both IMID and centralized method. In this figure also the comparable results can be observed. Results of this example show that a sensing network with IMID is capable to provide modal parameters of the system with almost the same accuracy as centralized networks but with significantly less communication burden.

Table 3.6. Natural frequencies, damping ratios, MAC values and Consistant Mode Indicators of vertical modes of the main span of Golden Gate Bridge, identified by IMID and Centralized approach

Mode	Frequency (Hz)			Damping (%)		MAC	Consistency of Mode (CMI)	
	Centralized	IMID	Error (%)	Centralized	IMID		Centralized	IMID
1 A	0.1079	0.1082	0.31	6.223	7.880	0.996	0.991 (well)	0.999 (well)
2 S	0.1408	0.1370	2.74	5.898	5.453	0.998	0.956 (well)	0.979 (well)
3 A	0.2348	0.2245	4.39	2.272	3.855	0.989	0.540 (mod.)	0.468 (poor)
4 A	0.3565	0.3758	5.40	1.172	1.619	0.981	0.317 (poor)	0.502 (mod.)
5 S	0.4585	0.4593	0.20	1.606	2.517	0.992	0.975 (well)	0.827 (well)
6 A	0.5572	0.6005	7.76	0.571	0.898	0.999	0.872 (well)	0.695 (mod.)
7 S	0.6593	0.6566	0.40	0.799	0.904	0.997	0.989 (well)	0.407 (poor)
8 A	0.6843	0.6611	3.39	1.401	1.301	0.957	0.820 (well)	0.958 (well)
9 S	0.8151	0.8324	2.13	1.254	1.915	0.911	0.814 (well)	0.935 (well)
10 A	0.9347	0.9403	0.60	0.592	1.662	0.993	0.951 (well)	0.915 (well)
11 A	1.0671	1.0736	0.61	0.552	1.296	0.834	0.960 (well)	0.747 (mod.)
12 S	1.1486	1.1544	0.50	0.452	1.731	0.994	0.614 (mod.)	0.414 (poor)
13 A	1.2708	1.2665	0.33	0.175	1.423	0.972	0.660 (mod.)	0.418 (poor)
14 A	1.3903	1.3852	0.37	0.322	0.359	0.838	0.932 (well)	0.898 (well)
15 A	1.4563	1.4343	1.51	1.619	2.386	0.803	0.873 (well)	0.665 (mod.)

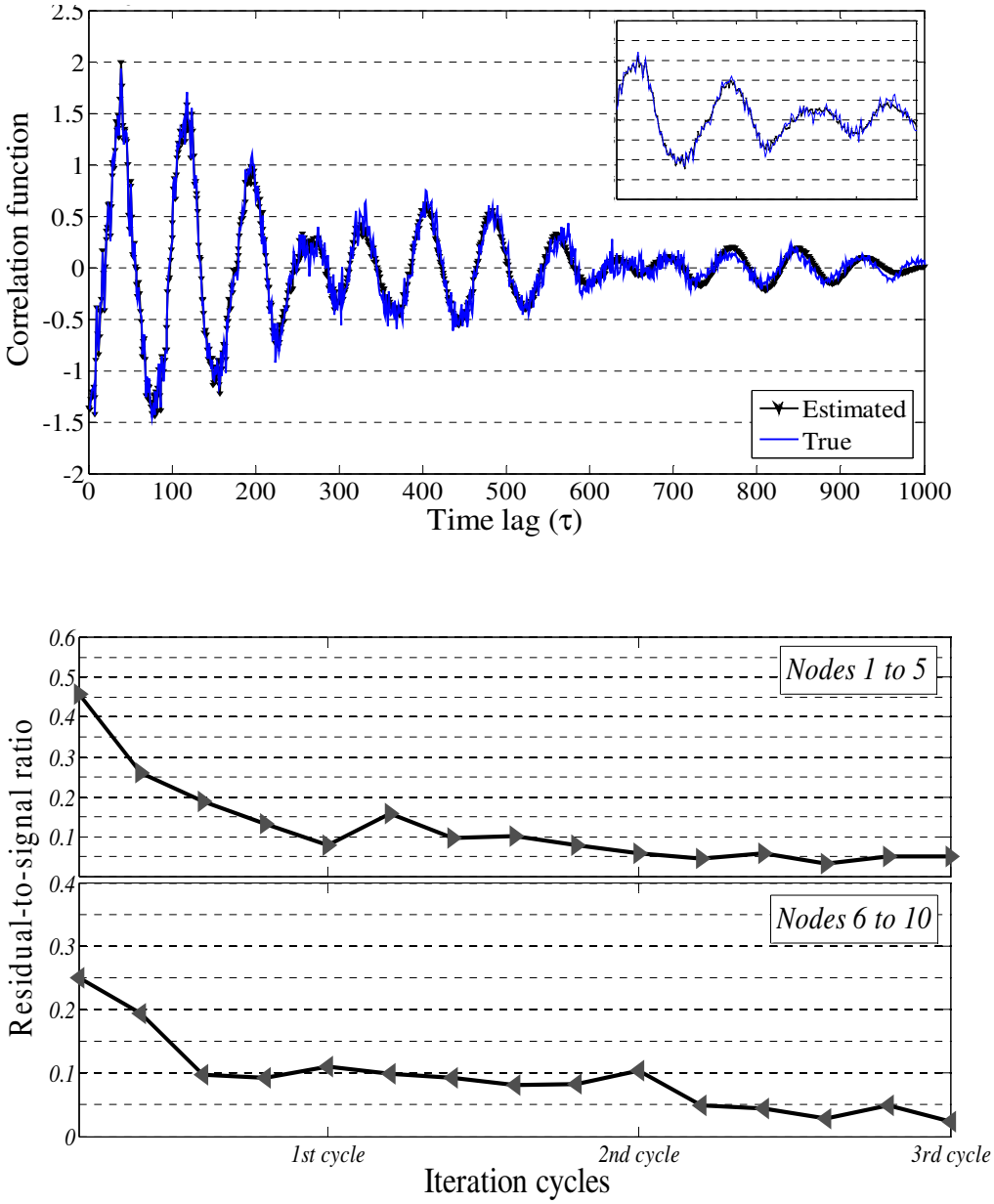

Figure 3.34. (a) Estimated versus true cross correlation function between node 5 and node 4 (b) Residual to signal ratio at different iteration cycles

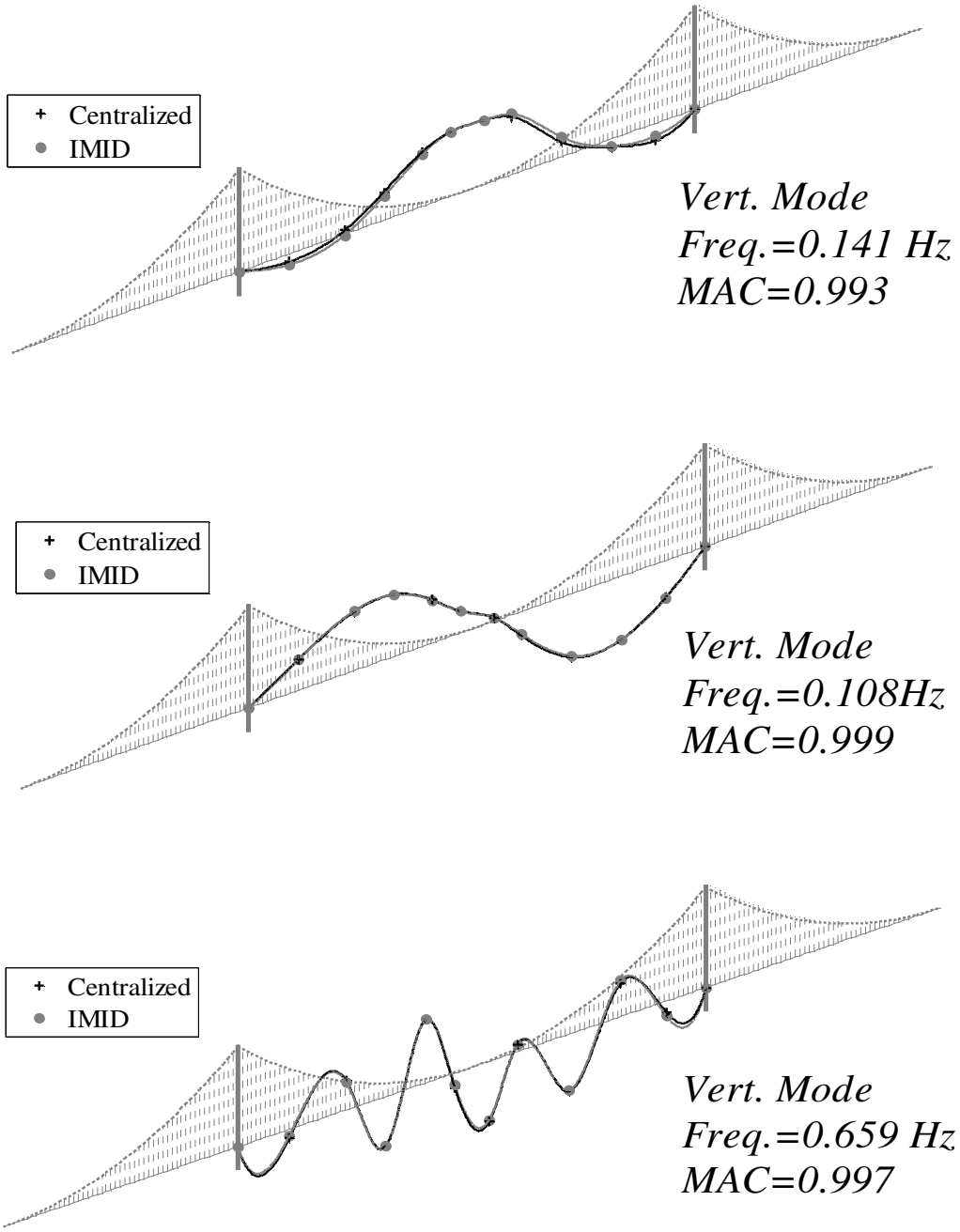

Figure 3.34. Instances of identified vertical modes of the main span of Golden Gate Bridge using IMID and Centralized approach

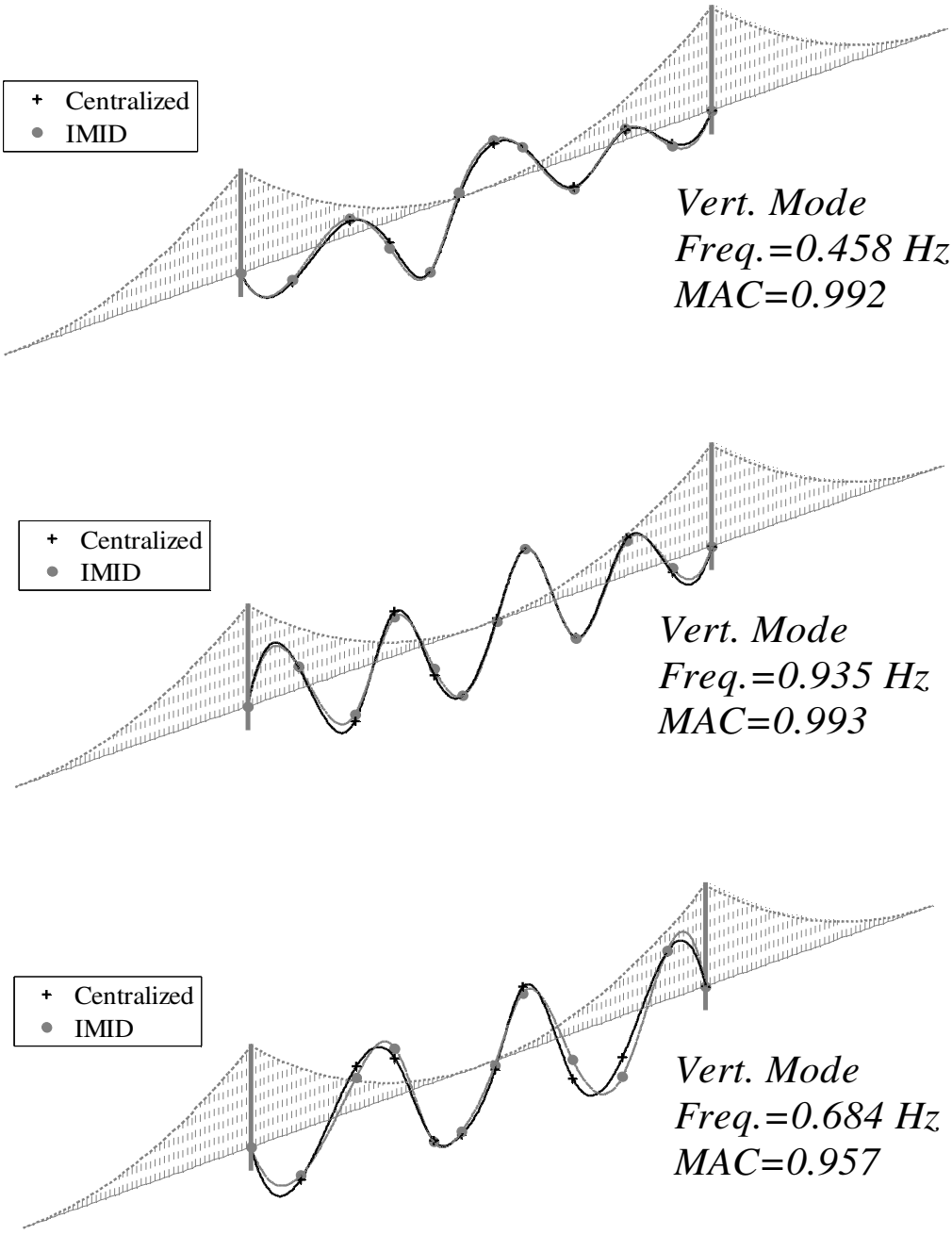

Figure 3.35 (Cont'd). Instances of identified vertical modes of the main span of Golden Gate Bridge using IMID and Centralized approach

3.11. Summary of the Distribute Data Processing

This chapter presented a new distributed modal identification algorithm, called IMID, to address challenges in application of WSN in health monitoring of structural systems. The proposed algorithm is structured similar to iterative EM series of algorithms which estimate unknown parameters in the presence of hidden information. The main objective in developing such an algorithm is to reduce the communication burden in WSN, as a smart way of saving computation time and communication power. Latency and energy consumption are two factors which prevent WSNs from prompt response to earthquake events and also restrict their application in long term monitoring. Significant reduction in the total transmitted data by incorporating the on-board computational capability of wireless sensors is achieved by the proposed algorithm. To verify the performance of IMID, two numerically simulated models and two experimental models are used as the implementation test-beds. The results illustrated the convergence of modal parameters after a few iteration cycles. Also, the algorithm is further improved such that the need for availability of excitation load and initial estimate of the system parameters are eliminated. Thus, IMID can be used for modal identification of structural systems under ambient loading without need for prior information about the system parameters. The improved version of the algorithm is validated through implementation on a simulated model, laboratory specimen data, and ambient vibration data of Golden Gate Bridge.

The advantageous characteristic of IMID is its flexibility in collaboration with a broad range of identification and simulation algorithms. In this implementation, Newmark's

numerical method and ARX algorithms are used for simulation and identification steps. Further studies are required to evaluate the efficiency of IMID if other methods are used for these steps.

Comparison of the required data transmission and energy consumption for IMID with the few other existing centralized processing methods, clarifies that a substantial reduction in the network communication and the total consumed energy is achieved. For the input-output experimental model up to 95% reduction in communication is achieved. For the 3-D steel truss model 90% reduction and for the implementation on the ambient response data from Golden Gate Bridge 83%~89% reduction in communication is achieved. Complete comparison with other distribted system identification methods (such as Sim, et al. 2009 and 2010 and Nagayama and Spencer 2007) may not be possible since IMID is an iterative process and the total computation/communication cost depends on how fast convergence is happened. However, it can be realized that the achieved reduction is significantly higher than what is achieved through other state-of-the-art approaches (e.g. 20~25% reduction in communication through algorithm developed by Sim et.al. 2010). Moreover, the other existing algorithms are just partially distributed and there is still a portion of computation which is assigned to a centralized computer. The simulated and experimental results presented in this paper shows significant improvement in both agility and energy efficiency of the sensor network. The reduction in communication, which is the result of novel approaches developed in this dissertation, clearly results in a reduction in energy consumption (e.g. the total energy is estimated to have up to 75% reduction) and also

agility of the sensing network. An automated long-term monitoring system, which is time-efficient and energy-efficient, can be established based on use of this algorithm.

The application of this algorithm is particularly beneficial in long term structural health monitoring in which the current state of the system can be considered as the initial estimate. These modal parameters are updated using data collected during the monitoring period. Having the identified modal properties of the system along the time, applications such as damage detection and/or finite element model updating can be utilized in the system, as well. The algorithm can be also considered as a basis for damage detection in long-term monitoring as it provides the updated modal parameters through the time.

The future work in this study is implementation of the algorithm on a network of wireless sensors for actual, on-board modal parameter identification and evaluation of its performance (energy- and time-efficiency) when wireless sensor's processors perform the required computations. The advantage of the proposed algorithm is that it can use different identification and simulation methods in its implementation. Considering this flexibility, the future work will be also devoted to evaluating the performance of the algorithm, in terms of accuracy and efficiency, through the use of different identification methods. Finally, it should be also noted that while IMID preserves the energy by reduction in communication, the accuracy of final results is limited to the convergence threshold. Thus, it is important to, based on the subsequent application, decide about the required accuracy and determine the convergence thresholds. Of course when higher

accuracy is required, the number of iteration cycles will be increased and there will be higher energy consumption, as the price for higher accuracy.

Chapter 4

Effects of Measurement Noise on Modal Parameter Identification

4. Effects of Measurement Noise on Modal Identification

4.1. Significance of the Noise Effect Assessment

As discussed in previous chapters, identification of dynamic characteristics of constructed structures is one of the fundamental steps in many structural health monitoring applications. In practice, dynamic characteristics of constructed structures are obtained through vibration monitoring tests and applying system identification algorithms on the measured data. Over the past three decades, vibration monitoring techniques have improved from several points of view, from advanced instrumentation technology to enhanced data processing and system identification algorithms. The objectives of the improvements in vibration monitoring fall into three basic categories: enhancing the accuracy of the estimated results, minimizing the cost, and easement of the implementation.

One of the distinguished improvements, introduced to the vibration monitoring systems, is deployment of wireless technology for data communication in a sensing network. While researchers have shown the effective role of WSN in improving the affordability of vibration monitoring (ease of implementation and reducing the costs), their possible impact on the reliability and accuracy of the results is still a research question. Fundamental factors, affecting the performance of a vibration monitoring system, are (i) software characteristics: the implemented data processing techniques and procedures, and (ii) hardware characteristics: the monitoring system including sensors

and data acquisition system (e.g. the embedded analog filters, Analog-to-Digital-Convertors, etc.).

Perhaps, the most significant distinction between WSNs and their traditional counterparts, wired systems, is the wireless communication which is the objective of their invention. However, some challenges in the design of wireless sensor units, such as the trade-off between the functionality and the power consumption, and also attempts for minimizing the cost, will cause limitations in their architecture which do not necessarily exist in the design of wired systems. Although a large number of wireless sensing unit prototypes with different embedded sensors and filters is presented in literature (Lynch *et al* 2006), the number of commercially available platforms with integrated quality sensors is limited. Therefore, it is important to carefully investigate the impact of sensor quality on modal identification results.

As the source of measurement noise, the selected sensors may introduce an epistemic uncertainty into the results of system identification (Moon *et al* 2006). Depending on the subsequent application of the system identification (e.g. damage detection, Finite Element model updating, etc.) the level of uncertainty in the results can be very important. On the other hand, despite the development of numerous system identification methods and many successful implementations on structural systems (Juang and Papa, 1985, Pandit, 1991, James *et al*, 1992, Overschee, 1994, Roeck *et al.,* 1995, and Farrar and James, 1997), relatively limited effort has been devoted to evaluation of the results in terms of accuracy and credibility. Even the limited research is mainly concerned about

the uncertainties associated with environmental and operational conditions (Peeters and DeRoeck 2001a&b, Sohn 2007), excitation characteristics (Reynolds *et al* 2004, Nagayama *et al* 2008) and data processing methodology (Grimmelsman & Aktan 2005, Reynolders *et al* 2007, Zhang *et al* 2010), and less attention is paid to the impact of measurement system and the possible uncertainties derived from measurement noises. The lack of research about the effects of uncertainties on system identification results is even more critical in the area of large-scale structural monitoring, where many different sources of noise exist.

A major challenge in such studies is that the existing accuracy indicators in modal identification are mostly relative indicators which are useful when comparing different identified parameters. For example, Pappa *et al* (1985) introduced two parameters (Modal Amplitude Coherence and Modal Phase Collinearity) that can be utilized to determine the confidence level of each identified modal parameter when the ERA is used. Although these parameters are very helpful in selecting structural modes and eliminating the spurious modes, they cannot indicate the general performance of the whole sensing system. However, it will be beneficial to use them to compare the performance of two sensing systems in terms of accuracy of results.

This study evaluates the influence of measurement system quality on modal parameter estimation, using ERA-NExT algorithm. Physical Contribution Ratio is introduced, which reflects the level of contribution of physical modes in the estimation of impulse response versus noise and computational modes, when ERA-NExT is used. The

parameter is validated through implementation on a numerically simulated example. Additionally, the developed parameter is implemented on data collected from the vibration monitoring of Golden Gate Bridge which was performed by Pakzad *et al* (2008), using wireless sensor network. The sensor boards in this vibration monitoring test utilized two types of accelerometers with low and high characteristic noise levels for measuring a broad range of ambient vibrations. The performance of the two sensing systems in estimation of Golden Gate Bridge's modal parameters is examined and the results are presented. Modal Phase Collinearity (MPC) and Modal Amplitude Coherence (MAC), developed by Pappa *et al* (1993), are also used for investigating the accuracy and purity of each modal parameters identified by both sensing networks. Furthermore, the consistency of the identified modal parameters through the increase of model order in ERA-NExT is evaluated and the results of different sensing systems are compared and discussed.

4.2. Modal Identification using ERA-NExT

ERA-NExT algorithm for output-only modal parameter identification was presented in Chapter 2. In this section the concept and a brief description are presented which provide background for derivation of physical contribution ratios later in this chapter.

Natural Excitation Technique:

NExT is an approach to modal testing which allows structures to be tested in their ambient environments (James et al 1993). The fundamental idea of this approach is that

the cross-correlation function between two measured displacements (or acceleration) of a structure satisfies the homogeneous differential equation of motion (Caicedo et al 2004). Consider the equation of motion for a multi-degree-of-freedom, linear time invariant system (Equation 2.1) and assuming that the excitations are stationary random processes and the structural parameters (M, C and K) are deterministic, it was shown that Equation 2.1 can be written as Equation 2.15 as follow:

$$M\ddot{R}_{qq_i}(\tau) + C\dot{R}_{qq_i}(\tau) + KR_{qq_i}(\tau) = 0 \tag{4.1}$$

where $R(.)$ denotes the correlation function. This equation shows that the correlation function of displacement satisfies the homogeneous differential equation of motion and it is shown that the correlation function of acceleration response also satisfies this equation (Beck *et al* 1994). Therefore, for structural systems under ambient vibration (e.g. wind, traffic and ground motions), the free decay response can be estimated by computing the correlation function of their acceleration responses. The estimated free decay function is required in many modal parameter identification algorithms such as ERA (Juang and Pappa 1985) or Polyreference (Vold and Rocklin 1982).

Eigensystem Realization Algorithm:

It was mentioned in Chapter 2 that one of the effective and commonly used time-domain system identification techniques is ERA, developed by Juang and Pappa (1985). This method uses the system's impulse response to derive system's parameters, without considering external force in its formulation. When the ERA is accompanied with the

NExT, the impulse response is estimated by the auto and cross-correlation functions of the measured responses.

To estimate the system's parameters in ERA, the Hankel block data matrix is formed as (Equation 2.16) and decomposed using singular value decomposition, providing observability and controllability matrices. Recalling from Chapter 2, the relationship between the state matrices and the estimated impulse response can be obtained by substituting the impulse function, as the input, into the state space representation of equation of motion:

$$\hat{Y}(n) = CA^{n-1}B \tag{4.2}$$

Therefore, the Hankel matrix is composed of the systems parameters as:

$$H(n-1) = \begin{bmatrix} CA^{n-1}B & CA^{n}B & \cdots & CA^{n+q-2}B \\ CA^{n}B & CA^{n+1}B & \cdots & CA^{n+q-1}B \\ \vdots & \vdots & \ddots & \vdots \\ CA^{n+p}B & CA^{n+p+1}B & \cdots & CA^{(n-3)+p+q}B \end{bmatrix} \tag{4.3}$$

To extract the estimate of system's matrices, the Hankel data block matrix, $H(n\text{-}1)$, is decomposed using singular value decomposition (SVD) for $n=1$:

$$H(0) = P\Sigma Q^{T} \tag{4.4}$$

where P and Q^T are matrices of left and right singular vectors of $H(0)$ respectively, and $\sum$ is the diagonal matrix of singular values. Small singular values along the diagonal of $\sum$

correspond to computational or noise modes (nonphysical spurious modes). Therefore, the rows and columns associated with nonphysical modes are eliminated from the singular-vector and singular-value matrices. The truncated matrices, $\sum_n$, P_n and Q_n are used to estimate the sate-space matrices for the discrete-time structural model as presented in Chapter 2 (Equations 2.18 – 2.20):

$$\hat{A} = \Sigma_n^{-1/2} P_n^T H(1) Q_n \Sigma_n^{-1/2} \tag{4.5}$$

$$\hat{B} = \Sigma_n^{1/2} Q_n^T E_{inp} \tag{4.6}$$

$$\hat{C} = E_{out}^T P_n \Sigma_n^{1/2} \tag{4.7}$$

where E_{inp} and E_{out} are matrices of 1 and 0 with appropriate dimensions based on the size of inputs and outputs ($[I \quad 0]$). Eigenvalue decomposition of the estimated state matrix results in the diagonal matrix of eigenvalues (Λ) and the matrix of eigenvectors (ψ) which are functions of system's natural frequencies (ω_n's), damping ratios (ζ_n's) and mode shapes ($\vec{\phi}_n$'s).

4.3. Sensitivity of identified fundamental natural frequency to the level of noise

In this section, it is attempted to find an expression for the sensitivity of fundamental natural frequency to the level of measurement noise. To achieve this goal, a simple beam model with 10 lumped masses (Figure 4.1) is assumed. The measurement noise is also assumed to be presented by the standard deviation of the noise.

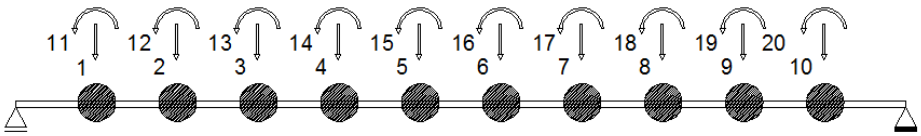

Figure 4.1. A simply supported beam with lumped masses

Assume a structural system and the corresponding equation of motion (Equation 2.1), the natural frequencies of the structure, λi's are theoretically obtained through eigenvalue problem as:

$$[K - \lambda_i M]\phi_i = 0 \tag{4.8}$$

where ϕ_i's are also natural modeshapes of the structure. In practice, the process of finding these modal parameters of the structure is called Modal Parameter Identification. The sensitivity of the eigenvalues of the system to changes in different structural variables can be obtained using classic formulation available in the literature. For example, suppose the structural system can be described by a set of m parameters, $g=\{g_1, g_2, \ldots, g_m\} \in R^m$, so that the mass, stiffness, and damping of the system can become a function of g. The rate of change in natural frequencies with respect to change in g can be obtained as:

$$\frac{\partial \lambda_i}{\partial g_i} = \lambda_i \frac{\phi_i^t [\frac{\partial K}{\partial g_i} - \lambda_i^2 \frac{\partial M}{\partial g_i} + i\lambda_i \frac{\partial C}{\partial g_i}]\phi_i}{\phi_i^t [\lambda_i^2 M + K]\phi_i} \tag{4.9}$$

which represents the rate of change in i^{th} eigenvalue with respect to the change in any of structural properties.

Despite the calculation of the rate of eigenvalues change due to structural properties, the rate of change of identified eigenvalues due to the uncertain identification parameters (e.g., level of excitation, variation of environmental parameters, measurement noise, etc.) is not well studied in the literature.

As the solution to this problem is algorithm dependent, the identification method, in which the formulation is based on, is first selected to be ERA-NExT. Applying NExT, an estimate of impulse response will be available and can be used in ERA algorithm which provides an estimate of the system and its modal properties. Considering application of NExT, the first step is to find the cross correlation function of the measured signal. Assuming that the measured signal consists of real response and the measurement noise, it can be written as:

$$y(t) = q(t) + n_s(t) \tag{4.10}$$

where $q(t)$ is the real response and the $\vec{n}_s(t)$ is the measurement noise. The impulse response is also estimated by the cross correlation function as:

$$\hat{Y}(\tau) = R_{qq}(\tau) + R_{nn}(\tau) + R_{qn}(\tau) + R_{nq}(\tau) \tag{4.11}$$

Considering that the measurement noise is uncorrelated to the true response of the structure, the two last terms in the right hand side of Equation 4.11 will be vanished and the impulse response can be estimated as:

$$\hat{Y}(\tau) = R_{qq}(\tau) + R_{nn}(\tau) \tag{4.12}$$

Note that if the measurement noise is a perfect Gaussian White Noise, the autocorrelation of the noise will be just the Dirac function. In other words, the white Gaussian noise is an *i.i.d.* process and the signal at time *t* is independent of the signal at other times:

$$E[n(t)n(t+\tau)] = \delta(0) \tag{4.13}$$

thus,

$$R_n(\tau) = 0 \quad for \quad \tau \neq 0 \tag{4.14}$$

Therefore, in the case of white Gussian measurement noise, the estimated impulse response will be the same as correlation function of actual response for $\tau \neq 0$, or:

$$Y(\tau) \stackrel{\text{m}}{=} R_{\vec{q}}(\tau) \tag{4.15}$$

which suggests that the measurement noise effect will be vanished by taking the non-zero lags in the correlation function. However, in real situation, this condition does not necessarily hold true.

The plot of Figure 4.2 shows a white Gussian signal generated in MATLAB with zero mean and standard deviation of 1. The autocorrelation function of the signal, as can be seen, closely fulfills the explained theoretic condition. It has correlation one at the beginning and very small correlation for the rest of the signal.

To have an idea about the real measurement noise and their correlation functions, the plot of a measurement noise corresponding to accelerometer of SHM-A sensor board is

shown in Figure 4.3. The difference between this signal and the White Gussian signal generated in MATLAB will be clearer when comparing their correlation functions (presented afterwards). It can be seen that the correlation is not merged to zero after the zero-lag. This means that the correlation function of the measured response is not affected only at $\tau = 0$, but in longer range of time-lags.

Therefore, use of $R_{\vec{n}}(\tau)$ to represent the statistics of the noise, compared to the standard deviation of the noise signal, is more comprehensive. It is worth noting that $R_{\vec{n}}(0)$ is the same as the standard deviation as:

$$R_{\vec{n}}(0) = E[n(t)^2] = \sigma \tag{4.16}$$

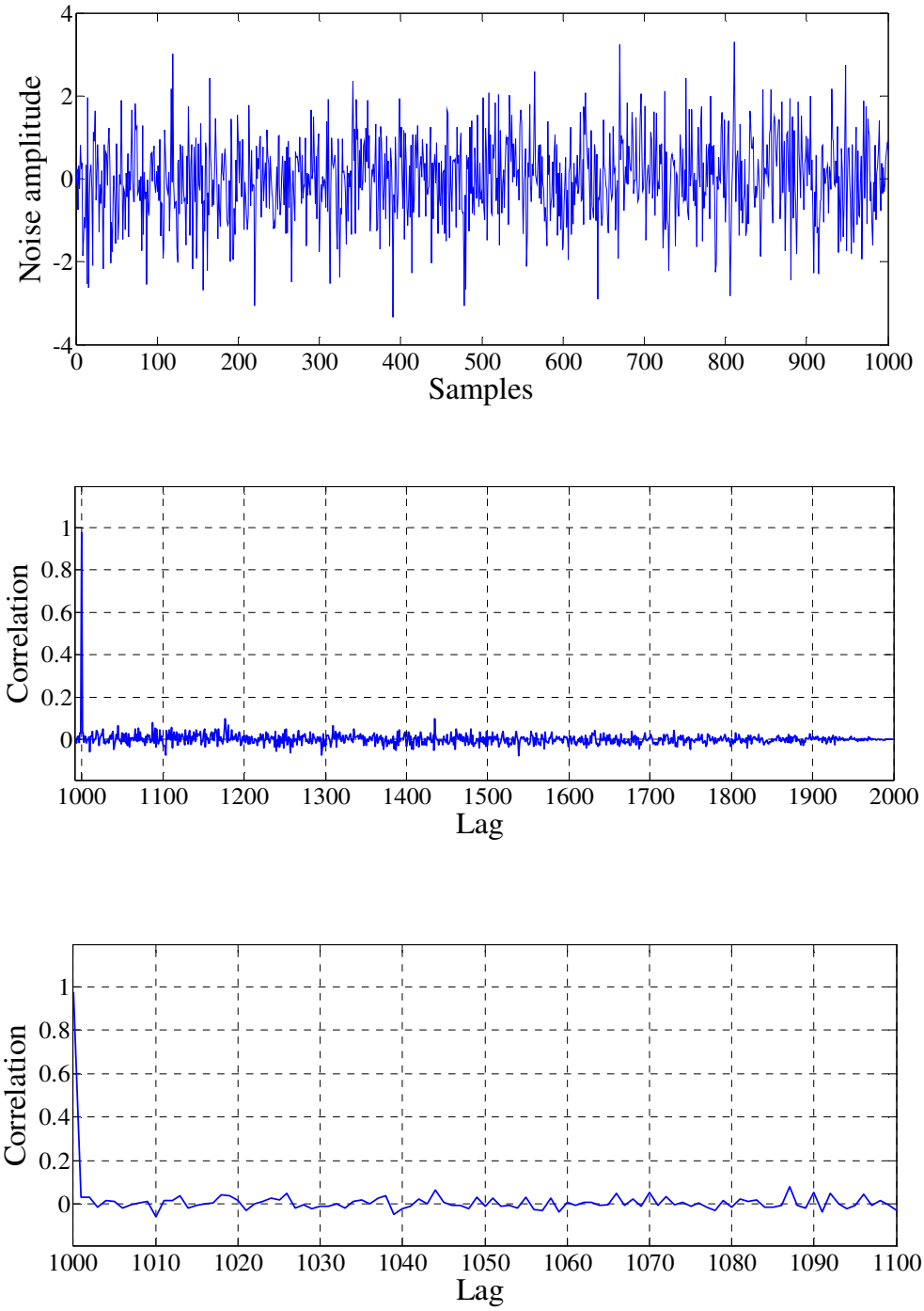

Figure 4.2. Gaussian white noise generated in MATLAB: time history and correlation function

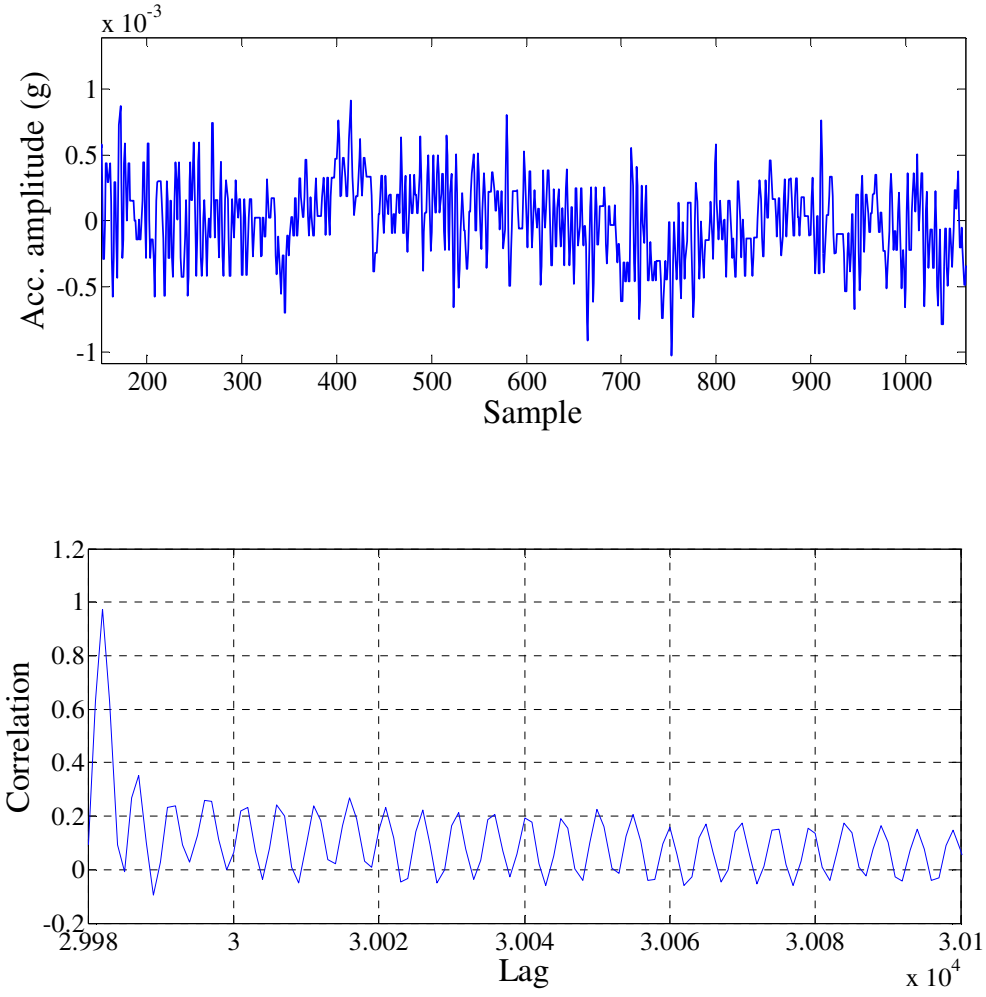

Figure 4.3. Measured SHM-A sensor board's noise: time history and correlation function

Assuming that the noise characteristics are reflected in the $R_{\vec{n}}(\tau)$, Equation 4.12 shows that the measurement noise has a direct impact on the estimated impulse response. Therefore, sensitivity of the estimated parameter to the noise characteristics can be seen in sensitivity of the parameter to the estimated impulse response:

$$\frac{\partial(identified\ parameters)}{\partial\ R_{\vec{n}}(\tau)} = \frac{\partial(identified\ parameters)}{\partial\ R_{\hat{Y}}(\tau)} \cdot \frac{\partial\ R_{\hat{Y}}(\tau)}{\partial\ R_{\vec{n}}(\tau)} \tag{4.17}$$

Also, it can be assumed that there is no correlation between measurement noises in different sensors. Thus, the focus will be just on diagonal components of the correlation function (or the estimated impulse response). The remaining step is just to find the relationship between the estimated impulse response and the identified modal properties.

Disregarding the details in the identification process, the relationship between the identified state matrices and the estimated impulse response can be written as:

$$Y(n) = CA_d^{n-1}B_d \tag{4.18}$$

Transforming the system from physical into the modal coordinate ($A = \psi\,\Lambda\,\psi^{-1}$), this can be written as:

$$Y(n) = C\psi\,\Lambda^{n-1}\,\psi^{-1}B \tag{4.19}$$

where ψ is the matrix of eigenvectors and $\Lambda\,(=[\lambda_i])$ is the diagonal matrix of eigenvalues in discrete form. Also:

$$C\psi = [\vec{\phi}_1 \quad \cdots \quad \vec{\phi}_m] \quad \text{and} \quad \psi^{-1}B = \begin{bmatrix} \vec{b}_1 \\ \vdots \\ \vec{b}_m \end{bmatrix}$$

where ϕ_1 to ϕ_m are simply modeshapes of the system and b_1 to b_m are row vectors of corresponding participation factors (the participation factor of the particular mode when impulse is applied at different nodes). Also, *m* represents the order of the system, or the size of the considered state vector. Expanding the estimated impulse response as the sum of *m* identified poles of the system, it can be written as:

$$\hat{Y}(n) = \begin{bmatrix} \sum_{i=1}^{m} \phi_{1i} b_{i1} \lambda_i^{n-1} & \sum_{i=1}^{m} \phi_{1i} b_{i2} \lambda_i^{n-1} & & \sum_{i=1}^{m} \phi_{1i} b_{iN} \lambda_i^{n-1} \\ \sum_{i=1}^{m} \phi_{2i} b_{i1} \lambda_i^{n-1} & \sum_{i=1}^{m} \phi_{2i} b_{i2} \lambda_i^{n-1} & & \\ \vdots & & \ddots & \vdots \\ \sum_{i=1}^{m} \phi_{Ni} b_{i1} \lambda_i^{n-1} & \cdots & \cdots & \sum_{i=1}^{m} \phi_{Ni} b_{iN} \lambda_i^{n-1} \end{bmatrix} \tag{4.20}$$

where *N* is the number of outputs. The non-diagonal elements of this estimated impulse response are assumed to be unaffected by the noise characteristics (as it is assumed that there is no correlation between measurement noise at different sensors). Therefore, the relation between the eigenvalues of the system and the noise characteristic can be observed from the following equation:

$$\begin{bmatrix} R_{y1y1}+R_{n1n1} & R_{y2y1} & & R_{yNy1} \\ R_{y1y2} & R_{y2y2}+R_{n2n2} & & \\ \vdots & & \ddots & \vdots \\ R_{y1yN} & \cdots & \cdots & R_{yNyN}+R_{nNnN} \end{bmatrix} = \begin{bmatrix} \sum_{i=1}^{m}\phi_{1i}b_{i1}\lambda_i^{n-1} & \sum_{i=1}^{m}\phi_{1i}b_{i2}\lambda_i^{n-1} & & \sum_{i=1}^{m}\phi_{1i}b_{iN}\lambda_i^{n-1} \\ \sum_{i=1}^{m}\phi_{2i}b_{i1}\lambda_i^{n-1} & \sum_{i=1}^{m}\phi_{2i}b_{i2}\lambda_i^{n-1} & & \\ \vdots & & \ddots & \vdots \\ \sum_{i=1}^{m}\phi_{Ni}b_{i1}\lambda_i^{n-1} & \cdots & \cdots & \sum_{i=1}^{m}\phi_{Ni}b_{iN}\lambda_i^{n-1} \end{bmatrix}$$

(4.21)

Having this equation, the sensitivity of the estimated modal parameter to the noise characteristic is directly related to the contribution of each mode in the diagonal components of the matrix of estimated impulse response. If the measurement noise is identical for all the sensors, it can be assumed that the second terms in diagonal components of the correlation matrix are constant and the last equation can be rewritten as:

$$\begin{bmatrix} R_{y1y1}+R_{n} & R_{y2y1} & & R_{yNy1} \\ R_{y1y2} & R_{y2y2}+R_{n} & & \\ \vdots & & \ddots & \vdots \\ R_{y1yN} & \cdots & \cdots & R_{yNyN}+R_{n} \end{bmatrix} = \begin{bmatrix} \sum_{i=1}^{m}\phi_{1i}b_{i1}\lambda_i^{n-1} & \sum_{i=1}^{m}\phi_{1i}b_{i2}\lambda_i^{n-1} & & \sum_{i=1}^{m}\phi_{1i}b_{iN}\lambda_i^{n-1} \\ \sum_{i=1}^{m}\phi_{2i}b_{i1}\lambda_i^{n-1} & \sum_{i=1}^{m}\phi_{2i}b_{i2}\lambda_i^{n-1} & & \\ \vdots & & \ddots & \vdots \\ \sum_{i=1}^{m}\phi_{Ni}b_{i1}\lambda_i^{n-1} & \cdots & \cdots & \sum_{i=1}^{m}\phi_{Ni}b_{iN}\lambda_i^{n-1} \end{bmatrix}$$

(4.22)

This equation provides N simultaneous equations which correlate the eigenvalues to the R_n. Among the N equation, the one in which λ_1 has a less contribution (smaller $\phi_{j1}b_{1j}$) will result in a higher sensitivity. Also, for identification of the first mode, it is not necessary to include all the correlation function matrices into the process. For this beam example, the first mode has the most contribution in the correlation function of

response at the 5th and 6th locations and the least contribution in that of 1st and 10th locations. The shown spatial distribution of the load in Figure 4.4 is due to the ground excitation which is transferred to the degrees of freedom relative to the lumped masses.

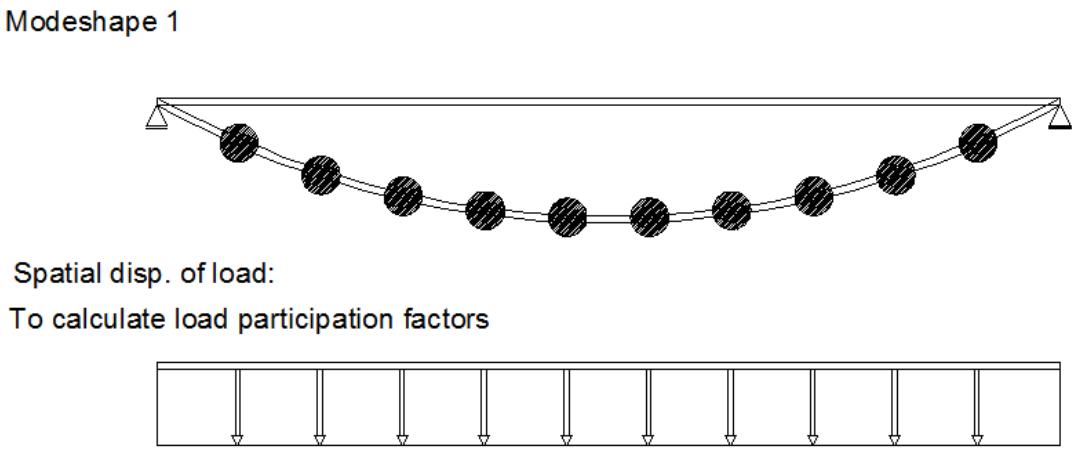

Figure 4.4. Uniform spatial distribution of the load along the beam

Since the estimated impulse response is a function of time step, the contribution can be measured by the integration of the modal response over time or summation in discrete domain. In the other words, the participation of the mode can be measured by its sharing in the power of the estimated impulse response.

Defining the sensitivity of first mode to measurement noise as the partial derivative of the 1st identified pole to the autocorrelation function of the noise ($S = \frac{\partial(\lambda_1)}{\partial R_n(\tau)}$), it can be written as:

$$S = \frac{\partial(\lambda_1)}{\partial \int R_n(\tau)d\tau} = \frac{\partial(\lambda_1)}{\partial \sum \hat{y}_{jj}(n)} = \frac{\partial(\lambda_1)}{\partial \sum_n \sum_{i=1}^{m} \phi_i b_i \lambda_i^{n-1}} = \frac{1}{\sum_n (n-1)\phi_{j1} b_{1j} \lambda_1^{n-2}} \quad (4.23)$$

where j is the location index and can be chosen from different locations. As mentioned before, the index that results in the smaller $\phi_{j1} b_{1j}$ (e.g. locations closer to the ends for this example) will result in higher sensitivity. In the process of identification, however, the poles are extracted from all the correlation functions that are included in the Hankel matrix.

This sensitivity equation shows that the sensitivity of the identified frequency to the measurement noise at the sensor location is a function of:

1. Modal displacement amplitude of the node where the sensor is located due to the identified mode;
2. Participation of the identified mode in the estimated impulse response;
3. The amplitude of the pole.

Note that λ is the identified complex pole in the discrete domain and higher frequencies have smaller magnitudes in this domain. Also recall from $R_{\vec{y}} \overset{m}{=} R_{\vec{x}} + R_{\vec{n}}$, the linear relation between R_y and R_n, means that the sensitivity to R_n is the same as the sensitivity to R_y.

Different measurement noises at different locations:

In this section, a special case, where the following conditions exist, is studied:

1. The spatial distribution of the load is not uniform as before, but is random (Figure 4.5).
2. The measurement noise at different locations is different.

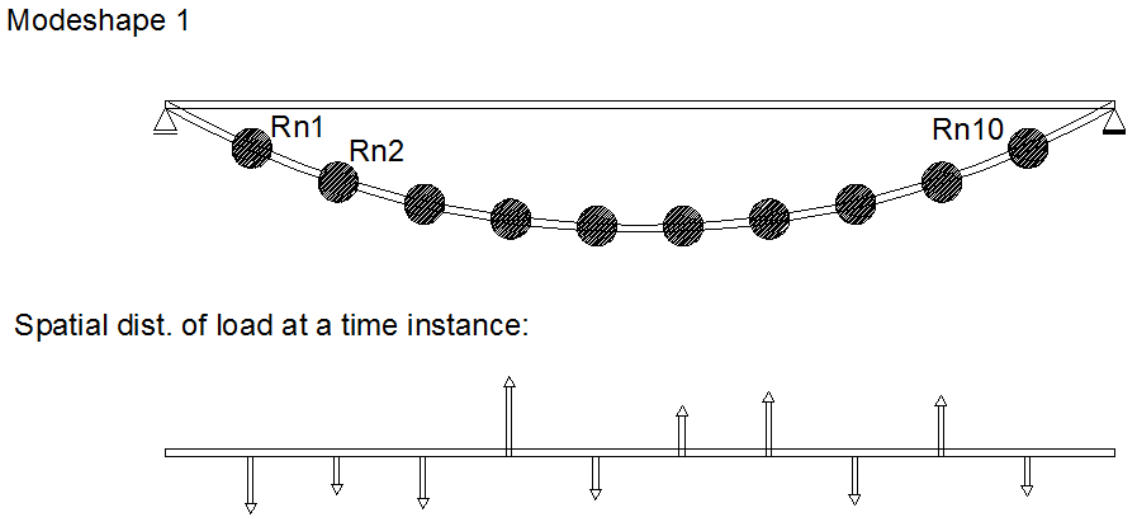

Figure 4.5. Random spatial distribution of the load along the beam

Both conditions will be considered by expressing the sensitivity of different eigenvalues with respect to each of the locations. In this case, the sensitivity of mode *k* to the measurement noise at node *j* is defined as the partial derivative of the k^{th} identified pole to the autocorrelation function of the noise at j^{th} sensor ($S_{kj} = \frac{\partial(\lambda_k)}{\partial R_{nj}(\tau)}$). It can be written as:

$$S_{kj} = \frac{\partial(\lambda_k)}{\partial \int R_{nj}(\tau)d\tau} = \frac{\partial(\lambda_k)}{\partial \sum \hat{y}_{jj}(n)} = \frac{\partial(\lambda_k)}{\partial \sum_n \sum_{i=1}^{m} \phi_{ji} b_{ij} \lambda_i^{n-1}} = \frac{1}{\sum_n (n-1)\phi_{jk} b_{kj} \lambda_k^{n-2}} \quad (4.24)$$

where, *j* is the location index, and *k* is the particular pole which the sensitivity is formulated for (e.g. for the first mode *k=1*).

Verification through simulation:

In this section, the sensitivity of the fundamental natural frequency of the beam to the measurement noise is assessed through a simulated example which is made in MATLAB.

A simply supported beam with length L is considered for this verification example. The specifications of the structure are assumed as:

E=29e+6 lb/in^2

I=500 in^4

L=1000 in

A=50 in^2

Mass density= 500/(386.4*12^3)=7.3386e-4 (slugs/cubic inch)

To create a 10 DOFs system, the beam is divided to 10 pieces and the stiffness elements are calculated and assembled (Figure 4.6). Then, the rotational degrees of freedom are eliminated from the final stiffness matrix using stiffness matrix condensation. Based on these parameters, the stiffness and mass matrices are extracted and modeshapes (Figure 4.7) and modal frequencies are calculated.

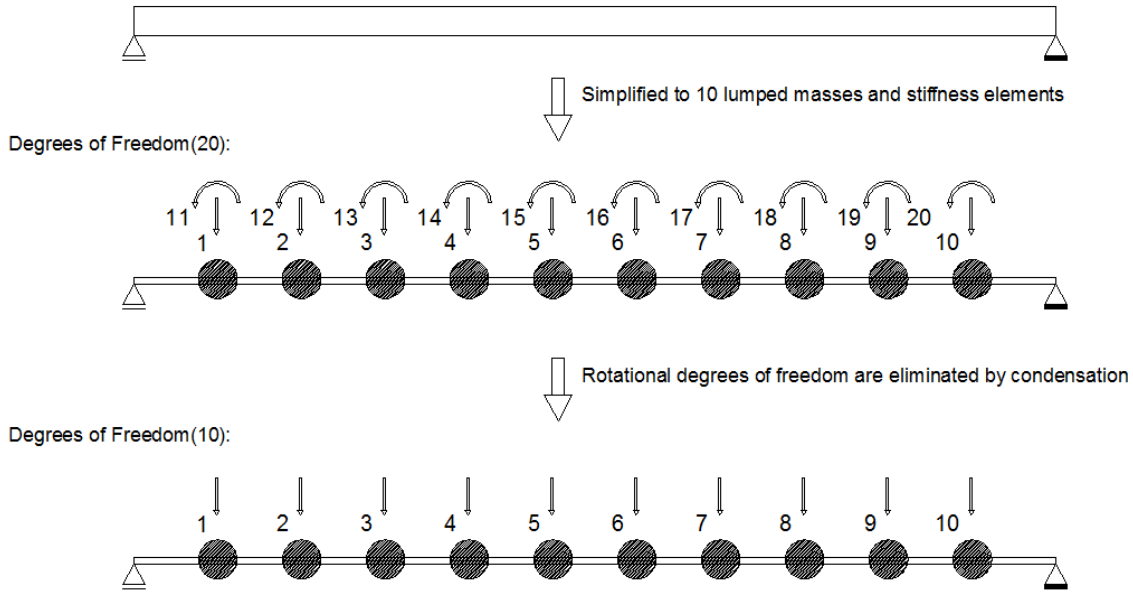

Figure 4.6. Discretizing the uniform beam to 10 DOFs and lumped masses

Condensed Stiffness Matrix (lb/in):

190621.7	-183502	80196.82	-21488.7	5757.872	-1542.81	413.3857	-110.728	29.52755	-7.38189
-183502	270818.5	-204990	85954.7	-23031.5	6171.258	-1653.54	442.9132	-118.11	29.52755
80196.82	-204990	276576.4	-206533	86368.08	-23142.2	6200.785	-1660.92	442.9132	-110.728
-21488.7	85954.7	-206533	276989.7	-206644	86397.61	-23149.6	6200.785	-1653.54	413.3857
5757.872	-23031.5	86368.08	-206644	277019.3	-206651	86397.61	-23142.2	6171.258	-1542.81
-1542.81	6171.258	-23142.2	86397.61	-206651	277019.3	-206644	86368.08	-23031.5	5757.872
413.3857	-1653.54	6200.785	-23149.6	86397.61	-206644	276989.7	-206533	85954.7	-21488.7
-110.728	442.9132	-1660.92	6200.785	-23142.2	86368.08	-206533	276576.4	-204990	80196.82
29.52755	-118.11	442.9132	-1653.54	6171.258	-23031.5	85954.7	-204990	270818.5	-183502
-7.38189	29.52755	-110.728	413.3857	-1542.81	5757.872	-21488.7	80196.82	-183502	190621.7

Mass Matrix (slugs):

5.1057	0	0	0	0	0	0	0	0	0
0	3.4038	0	0	0	0	0	0	0	0
0	0	3.4038	0	0	0	0	0	0	0
0	0	0	3.4038	0	0	0	0	0	0
0	0	0	0	3.4038	0	0	0	0	0
0	0	0	0	0	3.4038	0	0	0	0
0	0	0	0	0	0	3.4038	0	0	0
0	0	0	0	0	0	0	3.4038	0	0
0	0	0	0	0	0	0	0	3.4038	0
0	0	0	0	0	0	0	0	0	5.1057

Natural Frequencies and modeshapes calculated from eigenvalue problem:

Mode	**Frequencies (rad/sec)**
Mode1	0.978
Mode2	3.910
Mode3	8.794
Mode4	15.615
Mode5	24.327
Mode6	34.794
Mode7	46.680
Mode8	59.235
Mode9	71.010
Mode10	79.748

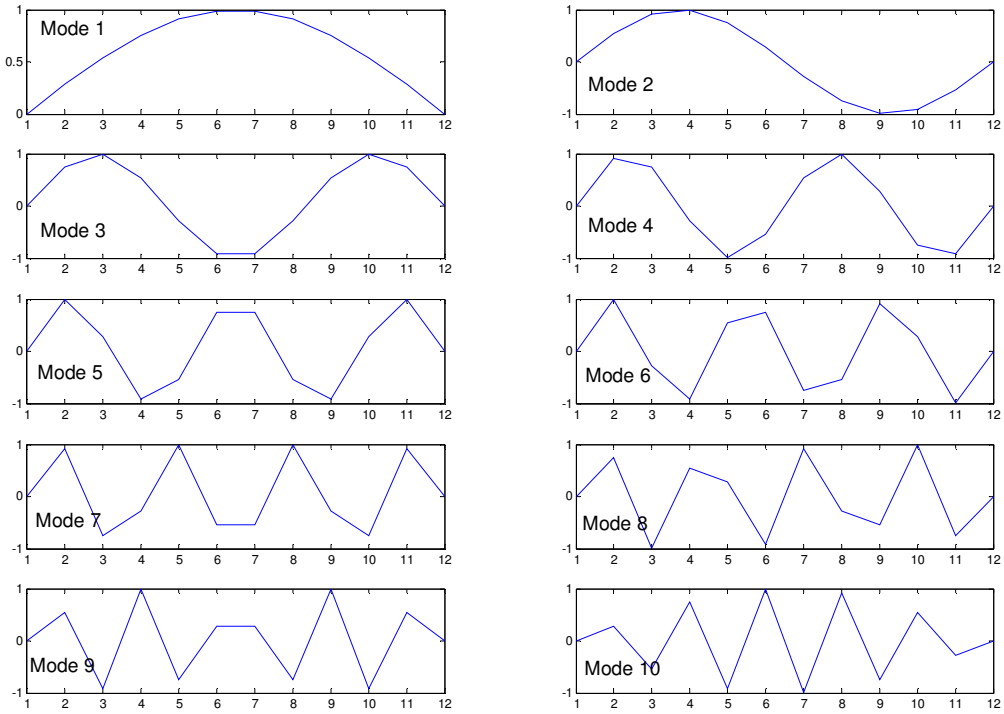

Figure 4.7. Modeshapes of the simply supported beam

Simulation for one measurement noise at all locations:

To calculate the sensitivity of the identified natural frequencies to the measurement noise, the beam is subjected to a Gaussian noise excitation and the response of the structure plus measurement noise is used to identify the natural frequencies. For modal parameter identification, ERA-NExT, output-only algorithm is used. Different steps of the process are:

1. A vector of random Gaussian white noise with zero mean and standard deviation of one is generated using "random" function and is applied to the mass matrix to simulate the external force on the beam.

2. The response to this excitation is then calculated using Newmark numerical algorithm (damping ratios are assumed to be zero).
3. Another vector of random Gaussian white noise is generated by variable standard deviation (to be increased through cycles) and is added into the simulated response.
4. The output signal (summation of response and noise) is fed into the NExT function to calculate the correlation functions and estimate the impulse response function of the structure.
5. The correlation functions are used to estimate the natural frequencies (in particular the first natural frequency) of the beam.
6. The measurement noise, added in step 3, is scaled up from 2% to 200% of the RMS of the excitation by 2% increments. At each increment, the first natural frequency is estimated and finally their values are plotted versus the noise percentage.

Figure 4.8 shows the first identified frequency versus the level of noise.

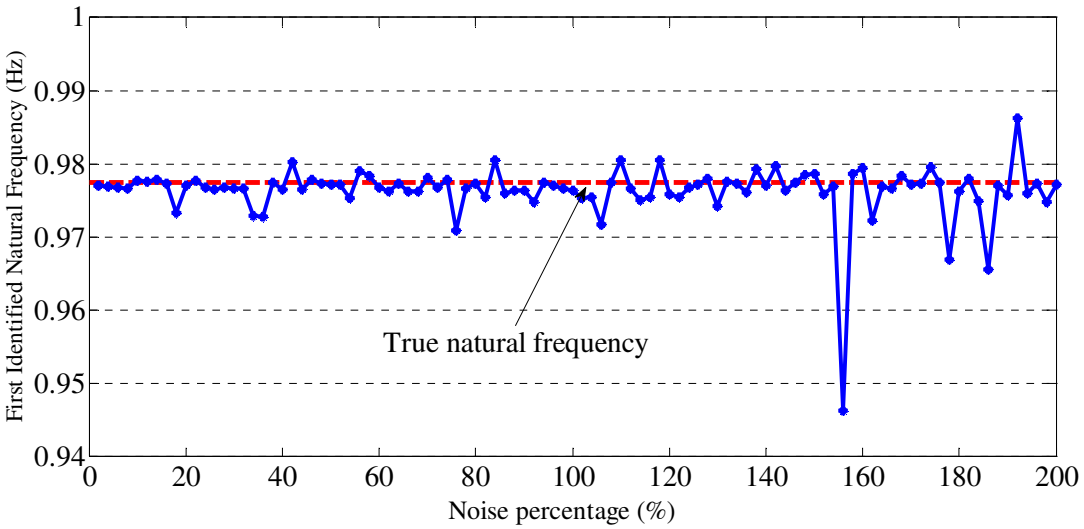

Figure 4.8. Variation of the first identified natural frequency versus increase of noise percentage in the response

As discussed earlier, the real ideal white noise will not have much influence on the estimation result perhaps because it has an auto-correlation function which is very close to Dirac function. To have a more realistic simulation, the random noise is generated by passing the white noise through a band-pass filter. The design parameters are selected in a way that generate a noise close to real noises associated with sensors. The frequency contents are selected to be high in low and high frequencies. The FFT of the generated noise is plotted in Figure 4.9.

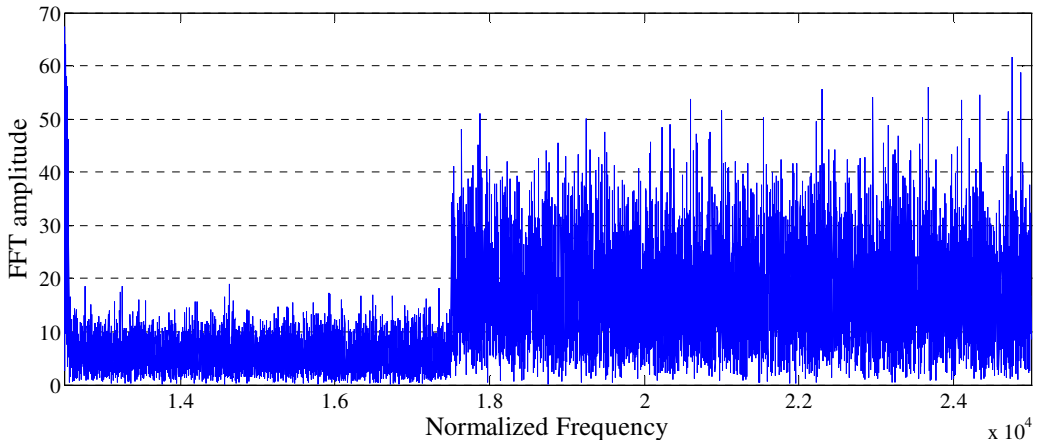

Figure 4.9. Frequency contents of a generated noise with higher low and high frequency contents

The result for increase of standard deviation of this generated noise is plotted in Figure 4.10. The result showed that the variation is not increased significantly by changing the frequency contents of the noise. The more accurate results may be obtained by deploying more details in design of realistic measurement noise or use of real sensor noise in the simulation.

To have a better understanding of the effect of the measurement noise, the variation of the first natural frequency is inspected. For this purpose, a window of length 10 is moved throughout the vector of the first identified natural frequencies (for different noise levels) and the deviation of the frequency is calculated. Figure 4.11 presents the variation of results and demonstrates the effects of noise in the measured response.

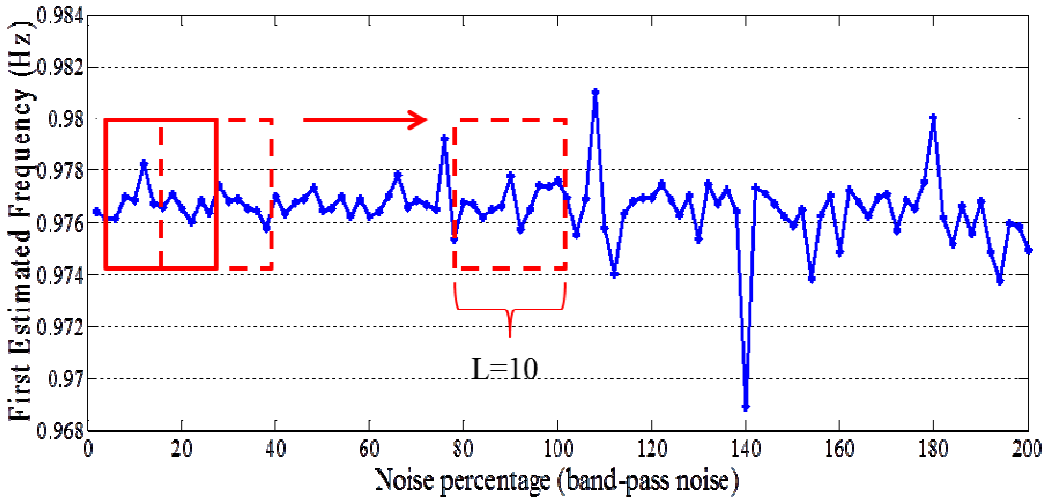

Figure 4.10. Variation of the first identified natural frequency versus increase of generated noise percentage in the response

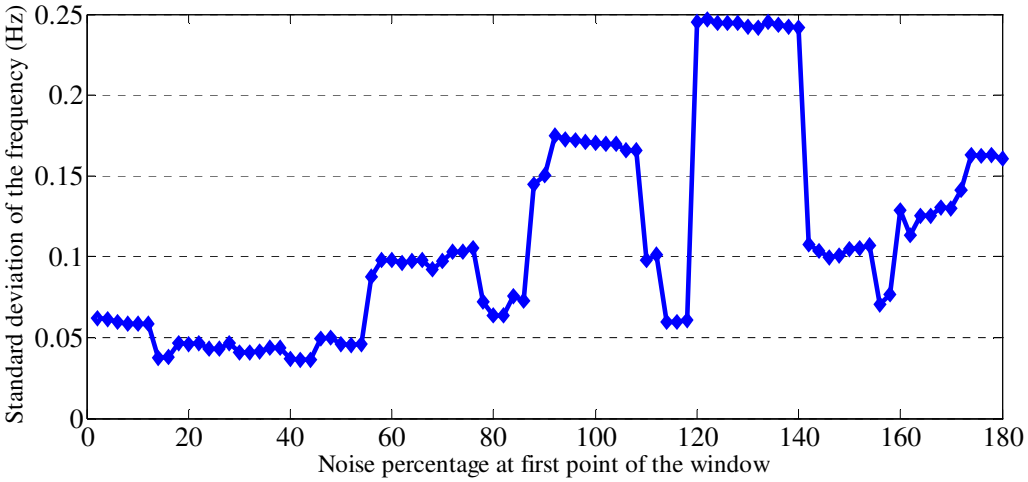

Figure 4.11. Standard deviation of the first identified natural frequency versus increase of generated noise percentage in the response

This simulation problem has only one variable which is the standard deviation of the noise that is added to all DOFs. Therefore, the verification of the theoretical result will be

just confirming the fact that the increase of noise level causes the increase of uncertainty. The plot of identified frequencies versus the noise percentage shows a lot of random behaviors which is due to randomness of the noise and therefore, it is hard to make a concrete conclusion from the plots. However, it can be observed that the variation of the identified results increases through the increase of the noise level.

Simulation for different random noises at different locations:

In this section the loading of the structure is different, as each DOF is subjected to a separate white noise excitation. Also, the addition of measurement noise is one at the time which means at each step, a percent of noise (with increasing scale) is added to the response of one DOF. Therefore, different steps of the process will be:

1. 10 vectors of random Gaussian white with zero mean and standard deviation of one are generated and applied to the DOFs of the beam to simulate the external force.

2. The response to the excitation is then calculated using Newmark numerical algorithm (damping ratios are assumed to be zero).

3. For each of the DOFs the following tasks are carried out:

   (a) A vector of random Gaussian white noise is generated by variable standard deviation (to be increased through cycles) and is added into the simulated response at that particular DOF.

(b) The output signal (summation of response and noise) is fed into the NExT function to calculate the correlation functions and estimate the impulse response function of the structure. Then the correlation functions are used to estimate the natural frequencies (in particular the first natural frequency) of the beam.

(c) The measurement noise is scaled up from 2% to 200% of the RMS of the excitation by 2% increments. At each increment, the first natural frequency is estimated

4. Finally, the first identified natural frequency corresponds to a particular level of measurement noise at a specific DOF (totally 10 × 200 different frequencies). At the end the estimates of the first frequency are plotted versus the noise percentage and noise location.

The 3D plot in Figure 4.12 shows the errors in estimating the first natural frequency correspond to variation (increase) of noise level in the response.

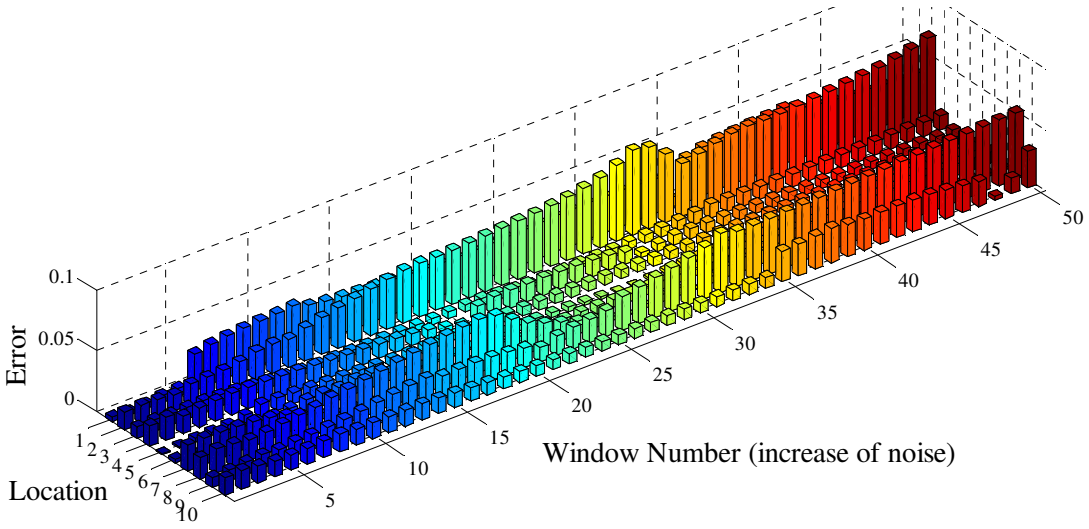

Figure 4.12. Errors in estimating the first natural frequency correspond to increase of noise level percentage in the response

In contrary to the plots from addition of single noise to all location, the variations of results are smoother when 10 different noises are added. The reason for this behavior is that the noise increases once at the time and at a location. Therefore, the difference in estimation between two successive steps is not as significant as what is presented for addition of one noise to all of the nodes.

It is also observed from the results that the estimation error is in overall higher when the noise is added into the outer locations, rather than middle locations. This can be seen better having the results of noise addition for locations 1 and 5, next to each other. This result is plotted in Figure 4.13.

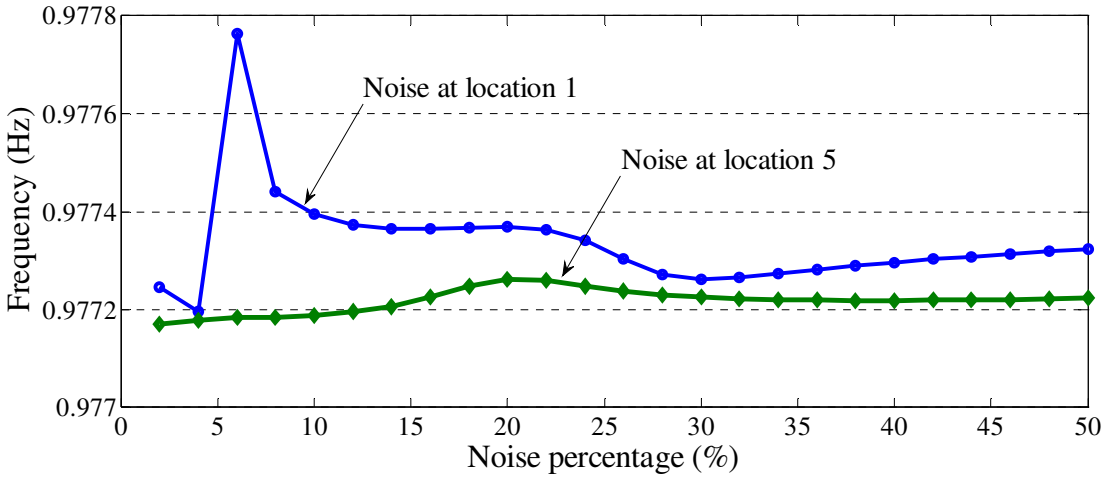

Figure 4.13. Variation of the first frequency due to increase of noise level percentage at locations 1 and 5

This behavior is in agreement with the relation which was derived for sensitivity of eigenvalues to the correlation of the noise. Recall from the previous section:

$$S_{kj} = \frac{\partial(\lambda_k)}{\partial \int R_{nj}(\tau)\, d\tau} = \frac{\partial(\lambda_k)}{\partial \sum \hat{y}_{jj}(n)} = \frac{\partial(\lambda_k)}{\partial \sum_n \sum_{i=1}^{m} \phi_{ji} b_{ij} \lambda_i^{n-1}} = \frac{1}{\sum_n (n-1) \phi_{jk} b_{kj} \lambda_k^{n-2}}$$

which gives the sensitivity of mode k to measurement noise at node j. As the first mode has the highest modal displacement in the middle of the beam and the least at two sides, it is reasonable to observe higher sensitivity for the side locations. This means higher variation of results due to the addition of noise to side locations. It should be noted that the level of the noise is relative to the excitation and not the response. Hence, the Signal-to-Noise-Ratio (SNR) of different locations is related to the response amplitude at different locations.

To have an overall comparison, the average error obtained through addition of noise to different locations is plotted in Figure 4.14. The plot shows higher sensitivity of eigenvalues to the noise at two side locations. However, there are some inconsistencies in the result which might be due to randomness of the noise signal and very small level of error.

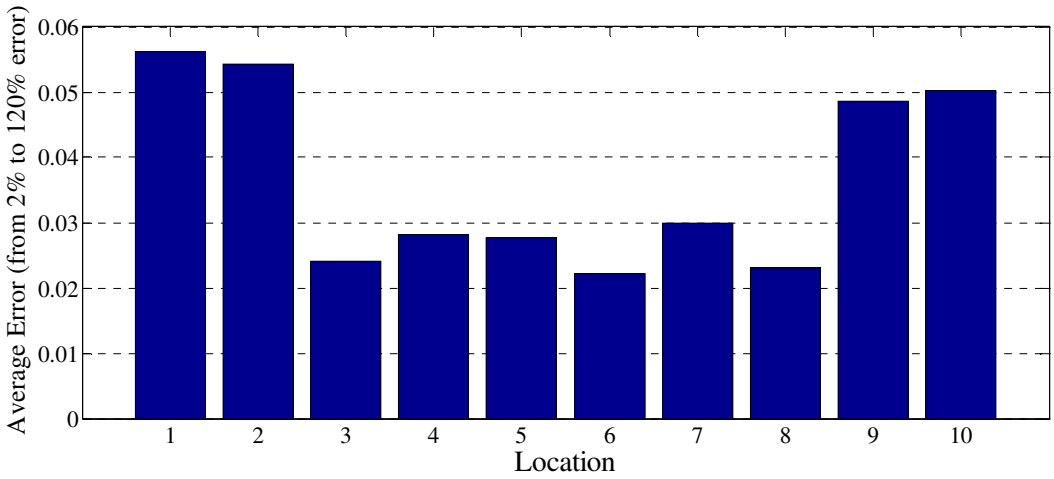

Figure 4.14. Average error due to addition of noise to different locations

4.4.Contribution Ratio of Physical Modes in Measured Signals

This section presents the formulation of a parameter, called Physical Contribution Ratio (PCR), which quantifies the participation of physical modal vibrations in the estimation of impulse response and modal parameters. The performance of this parameter is examined later, through implementation of a numerical example and data collected from ambient vibration test of Golden Gate Bridge.

As mentioned earlier, using NExT, the impulse response of the structure is estimated and can be used in the ERA or a similar algorithm for modal parameter estimation. The objective is to quantify what portion of this estimated impulse function is driven from physical modal vibration compared to noise. The portion of estimated impulse function which is driven from structural modes (PCR) reflects the level of noise contamination in the modal identification process. Considering the measured signal as a combination of real response and the measurement noise, it is shown that (Equation 4.12):

$$\hat{Y}(\tau) = R_{qq}(\tau) + R_{nn}(\tau) \tag{4.12}$$

Assuming that the noise characteristic is reflected in $R_n(\tau)$, Equation (4.12) shows that the measurement noise has a direct impact on the estimated impulse response. Also, as mentioned before, it can be assumed that there is no correlation between measurement noises of different sensors. Thus, mainly the diagonal components of the correlation function are assumed to be contaminated by the measurement noise in the system.

As the relation between noise characteristics and the estimated impulse response is clarified, the next step in correlating the noise effects to the identified modal parameters is to find the relationship between the estimated impulse response and the estimated modal properties. Considering the discrete state space model, the A, B and C matrices of the system can be estimated based on the estimated impulse response, using ERA. The relationship between the state matrices and the estimated impulse response follows

Equation 4.18. As presented earlier, transforming the system from physical coordinate into the modal coordinate ($A^n = \psi \Lambda^n \psi^{-1}$), also provides Equation 4.19:

$$\hat{Y}(n) = C\psi\Lambda^{n-1}\psi^{-1}B \tag{4.19}$$

where ψ is the matrix of eigenvectors and Λ is the diagonal matrix of eigenvalues ($\lambda_i's$) in discrete form. Also, $C\psi = E_{out}^T P \Sigma_n^{1/2} \psi$ and $\psi^{-1}B = \psi^{-1}\Sigma_n^{1/2} Q_n^T E_{inp}$ are mode shapes and modal amplitudes, respectively, which are the outcomes of minimum realization in ERA. It is also shown that mode shapes and modal amplitudes can be rewritten as:

$$C\psi = [\vec{\phi}_1 \quad \cdots \quad \vec{\phi}_m] \quad \text{and} \quad \psi^{-1}B = \begin{bmatrix} \vec{b}_1 \\ \vdots \\ \vec{b}_m \end{bmatrix}$$

where $\vec{\phi}_1$ to $\vec{\phi}_m$ are column vectors of mode shapes, and $\vec{b}_1$ to $\vec{b}_m$ are row vectors of corresponding modal amplitudes (the modal amplitude of a particular mode when impulse is applied at different nodes); *m* is the order of the system or the size of the state vector. It should be noted that the order of the system is usually selected higher than what is minimally required (twice the number of outputs) to reduce the estimation bias, but in the over parameterized model noise and computational spurious modes will also appear.

Expanding the estimated impulse response as sum of *m* identified modes of the system, it can be written as:

$$\hat{Y}(n) = \begin{bmatrix} \vec{\phi}_1 & \cdots & \vec{\phi}_m \end{bmatrix} \Lambda^{n-1} \begin{bmatrix} \vec{b}_1 \\ \vdots \\ \vec{b}_m \end{bmatrix}$$

$$= \begin{bmatrix} \sum_{i=1}^{m} \phi_{1i} b_{i1} \lambda_i^{n-1} & \sum_{i=1}^{m} \phi_{1i} b_{i2} \lambda_i^{n-1} & \cdots & \sum_{i=1}^{m} \phi_{1i} b_{iN} \lambda_i^{n-1} \\ \sum_{i=1}^{m} \phi_{2i} b_{i1} \lambda_i^{n-1} & \sum_{i=1}^{m} \phi_{2i} b_{i2} \lambda_i^{n-1} & & \\ \vdots & & \ddots & \vdots \\ \sum_{i=1}^{m} \phi_{Ni} b_{i1} \lambda_i^{n-1} & \cdots & \cdots & \sum_{i=1}^{m} \phi_{Ni} b_{iN} \lambda_i^{n-1} \end{bmatrix}_{N \times N} \tag{4.25}$$

where N is the number of outputs and b and ϕ are components of mode shape and modal amplitude vectors (e.g. ϕ_{ij} is i^{th} component of the j^{th} mode shape and similarly, b_{jk} is the j^{th} mode's amplitude at k^{th} location). This equation presents each component of the estimated impulse response as the summation of contribution of all the estimated modes (in terms of mode shapes, modal amplitudes and eigenvalues). Having this expansion for $\hat{Y}(n)$, the contribution of each mode can be identified. Since the impulse response is a function of time, the PCR parameter is defined by the integration over time (summation in discrete domain) which is a measure of signal's power. Therefore, the PCR of j^{th} mode in k^{th} diagonal component of estimated impulse response (auto-correlation function of signal with k^{th} node as the reference) is defined as:

$$PCR_{kj} = \frac{\sum_n \phi_{kj} b_{jk} \lambda_j^{n-1}}{\sum_n \sum_{i=1}^{m} \phi_{ki} b_{ik} \lambda_i^{n-1}} \tag{4.26}$$

where n is the time index.

When the noise contamination is constant for all the modes, it is evident that the higher PCR will correspond to less sensitivity of the mode to the noise. In the other words, higher amplitude results in higher signal-to-noise ratio, in modal coordinate. Therefore, those modes with higher contribution in the auto-correlation function of a particular node are less sensitive to the noise level of the corresponding sensor.

4.5. Validation of Physical Contribution Ratio through a Simulated Example

To validate the performance of the PCR in presence of measurement noise and also environmental and operational condition changes, a simulated model is developed. The model is a simply supported steel beam with 5 lumped masses along the span. Figure 4.15 shows the specifications of this beam model. The masses are determined based on the weight of the beam element and an assumed 3 *meter* tributary of 6 kN/m^2 uniform load. The acceleration response of the beam to random noise at 5 locations is simulated and used for modal identification process. ERA-NExT with model order 10 is selected to extract the 5 fundamental modes of the beam model. The identified natural frequencies and modeshapes of the beam are shown in the plots of Figure 4.16.

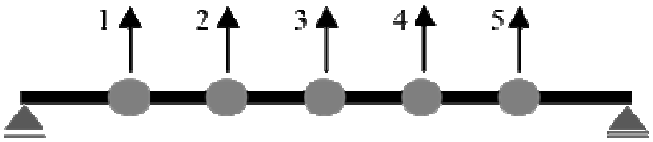

Beam section:

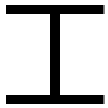

Beam specification:

L = 25 m
A = 1600 mm^2
$I_x = 3.42 \times 10^9$ mm^4

Figure 4.15. Beam example specifications

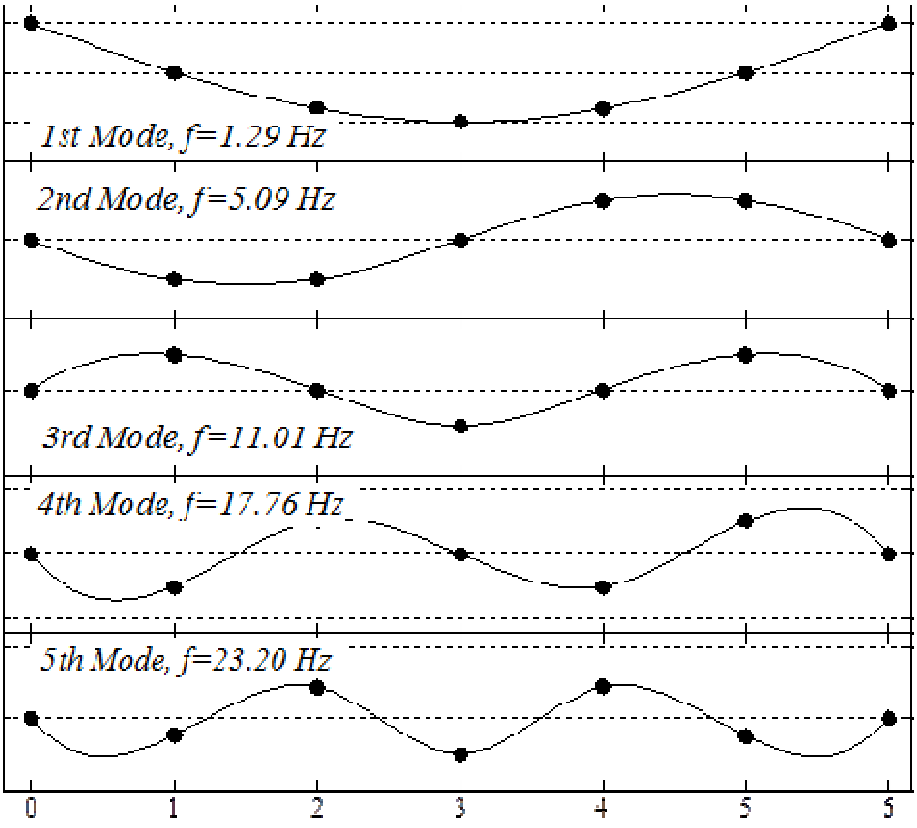

Figure 4.16. Identified modal frequencies and modeshapes

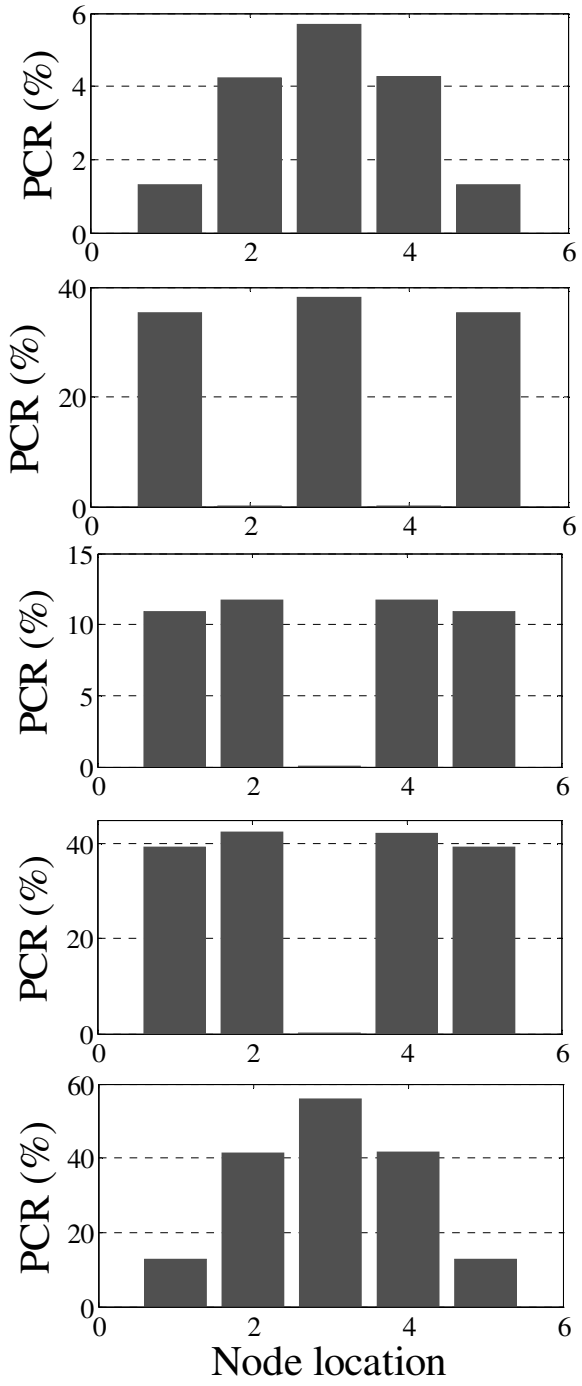

Figure 4.17. PCR values of different nodes at different modes

The PCR values at different nodes for each of the fundamental modes are computed and presented in Figure 4.17. Comparing these plots with the mode shapes of the bridge, it is evident that the PCRs are proportional to the modal ordinates. However, PCR also accounts for the modal amplitude factor (b) and modal frequency, as predicted by Equation 4.26. It can be seen that the PCR value is relatively small in a couple of nodes for some of the vibration modes. These nodes correspond to small (or zero) modal displacement. It is also observed that the PCR is larger for higher modes, which is consistent with the acceleration response's power spectrum of this model. In this example, the participation of the first and second modes in acceleration responses is small as their angular frequencies are less than unity. It is worth noting that the sum of the PCRs at each node over the 5 natural frequencies is almost 100%. This is obvious as the response is noise-free.

To see the effect of measurement noise on the PCR, artificial stochastic white noise is added to the acceleration response and the variation of these ratios is inspected as the root mean square (RMS) of noise increases and the signal to noise ratio (SNR) decreases. As expected, the noise causes attenuation of the PCR, since it adds into the frequency contents of the measured response at non-fundamental frequencies. This behavior can be clearly observed in Figure 4.18 where it shows the PCR for each mode, and also the overall PCR for all modes.

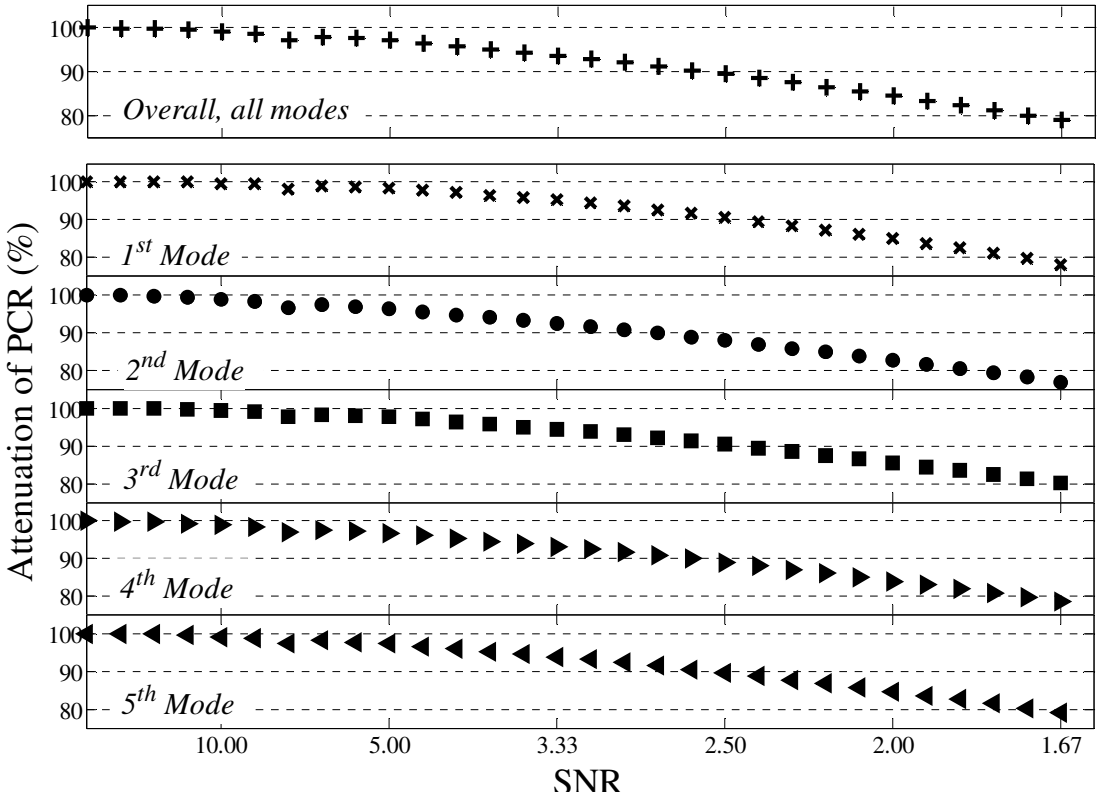

Figure 4.18. Variation of PCR values at different nodes due to increase of artificial noise (decrease of SNR)

The PCR is developed to reflect the noise contamination of the response which is due to non-physical variables (e.g. measurement noise). However, to further investigate the performance of the PCR in presence of environmental and operational changes, its behavior under different structural perturbations is also inspected. For this purpose, the changes in the PCR against random changes in the structural stiffness and also addition of random impulsive loads are evaluated. The stiffness perturbation is to represent the variation of structural properties due to different environmental conditions (e.g. temperature change effects) and addition of random impulsive loads is also to reflect the existence of non-stationary loads on structures (e.g. random heavy traffic loads). Also,

addition of random masses is to reflect the level of uncertainty in the corresponding mass of the system. Of course in the real world structures, many parameters are affected by these types of environmental and operational changes. In this example, however, only the effects of these three factors are considered.

For the stiffness perturbation, the components of stiffness matrix are subjected to a random change with increasing mean values and the corresponding changes in the PCR are inspected. The results are shown in Figure 4.19 where the PCRs are plotted for each mode and also the summation of all modes versus stiffness perturbation percentages. It can be seen that, in contrast to the noise contamination, the changes in the PCR do not follow any decreasing trend and the overall values (summation of all fundamental modes) are almost 100% for all cases. This is reasonable as the physical changes in the structure only alter the contribution of different modes and do not decrease the overall PCR in the modal estimation process. Similar process is applied to observe the effects of random masses on the value of PCR. Figure 4.20, where the PCRs are plotted for each mode and also the summation of all modes versus mean of additional random mass percentage, shows a behavior similar to what is obtained from perturbation of stiffness.

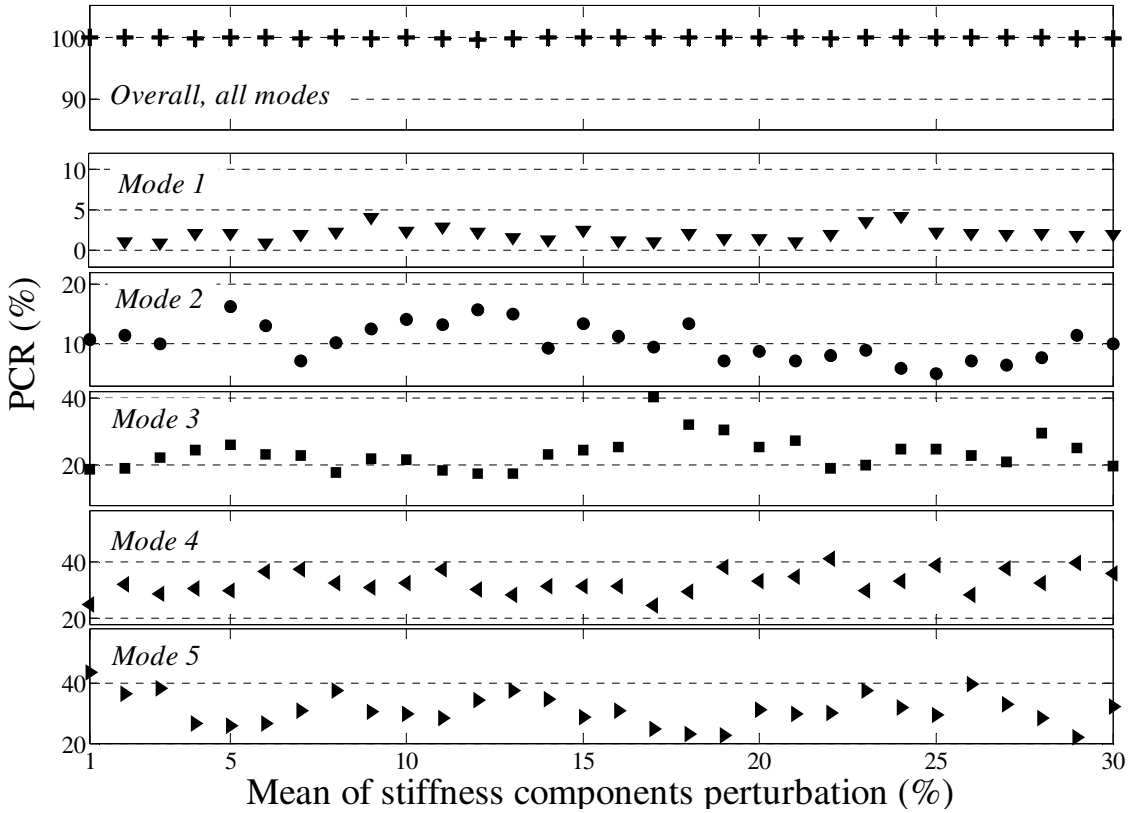

Figure 4.19. Variation of the PCR due to increasing random perturbation of stiffness components

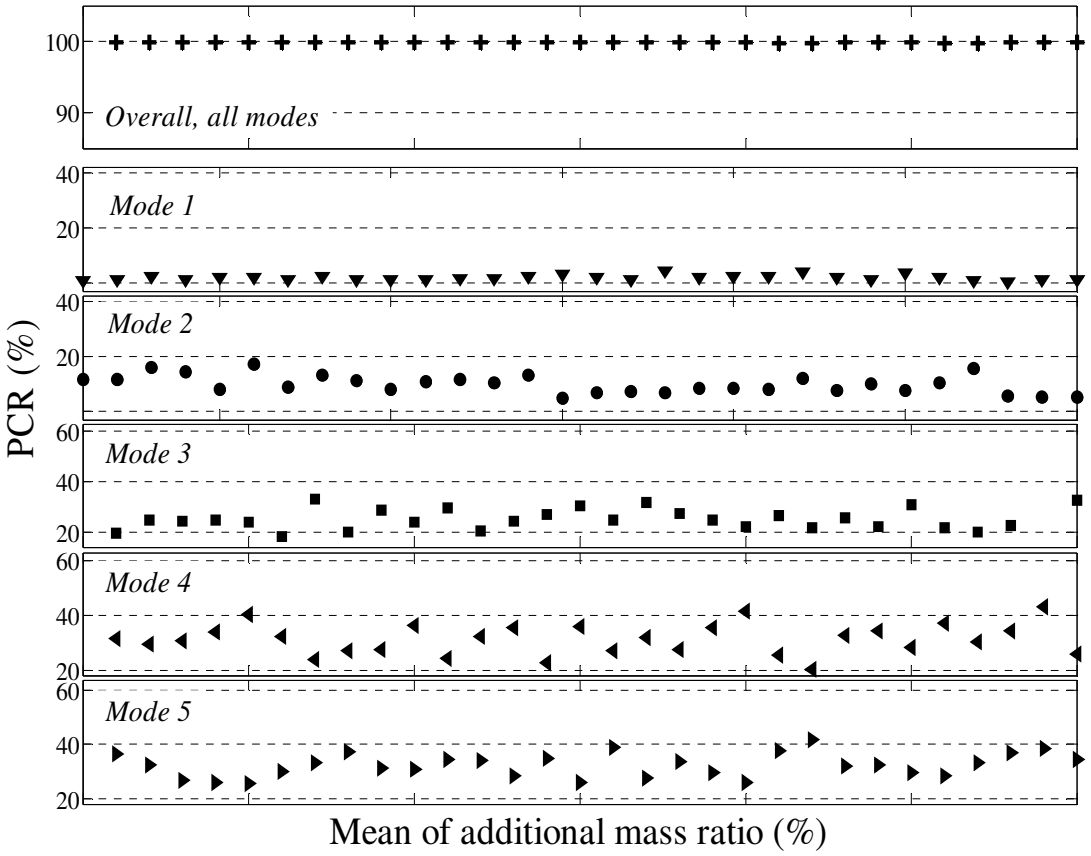

Figure 4.20. Variation of the PCR due to increasing random masses

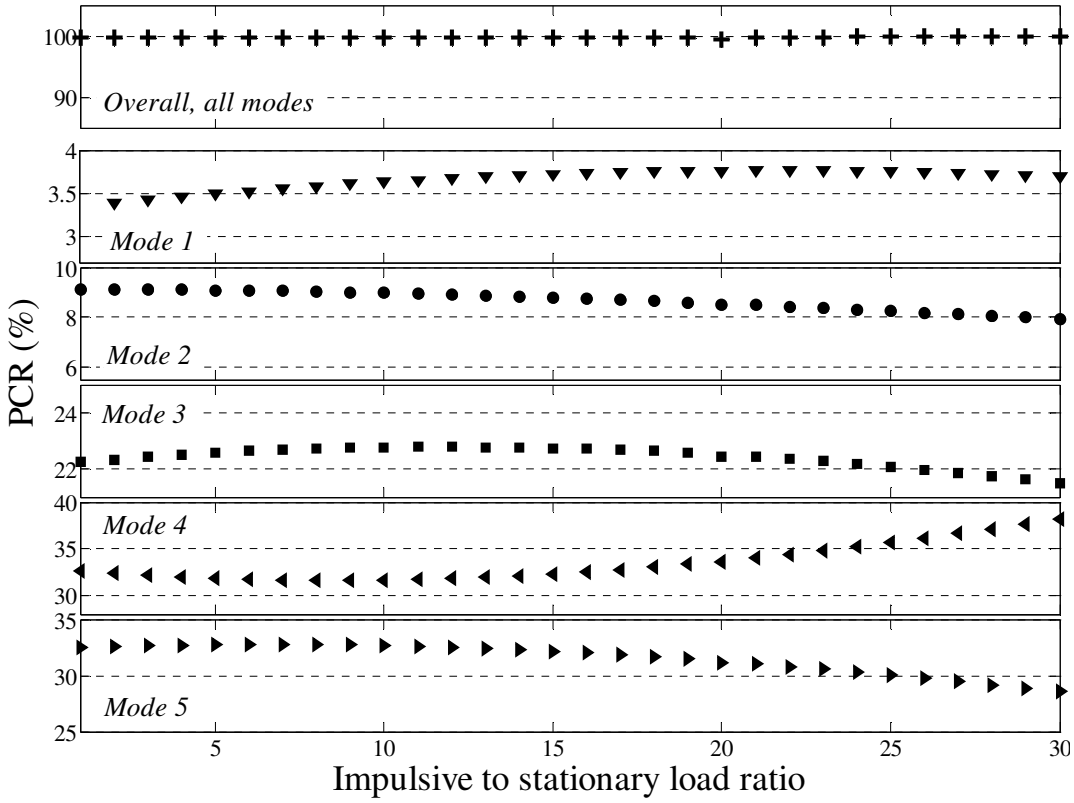

Figure 4.21. Variation of the PCR values due to increasing ratio of random impulsive load to the stationary load RMS

Similar process is applied to observe the effects of adding random impulsive loads on the PCR values. The loads are selected based on possible scenario of truck passing over a bridge structure. Thus, the loads are applied to different nodes at different times (i.e. moving load) and their amplitudes are selected as random values with increasing mean up to 30 times the applied stationary loads RMS (the maximum impulsive load generates *L/1000* deflection at the mid-span). The result of PCR variation is plotted in Figure 4.21. It can be seen that the overall PCR for all modes are almost unchanged as the random impulsive loads increase. The contributions of different modes however change due to

the increasing impulsive load which is again expected as random impulsive loads may alter the load shape function and, as a result, change the participation of different modes.

Through this numerical example, it is observed that the PCR is sensitive to the level of noise in the measured response. However, the overall value of the PCR (for all modes) is not sensitive to the structural changes (e.g. environmental and operational changes), though their values in different modes change due to changes in modal participation of different modes.

4.6. Accuracy Assessment of the Identified Modal Parameters using MAC and MPC

In order to validate the identified modal parameters, it is necessary to assess the accuracy of the results, particularly when there are different sources of uncertainty in the vibration data (e.g. environmental affects, measurement noise, etc.). This section focuses on approaches which quantify the uncertainties of each identified mode and provide parameters to measure the accuracy of modal identification results.

A study of the effects of noise on modal identification, using ERA, was performed by Juang and Pappa (1986), and a mathematical foundation was established for determining the accuracy of identified genuine modes versus those associated with noise. In this study, Modal Amplitude Coherence (as a special case of Degree of Modal Purity parameter) is introduced which quantifies the consistency of identified modes versus time. Another indicator developed also by Juang and Pappa (1985) is Modal Phase

Collinearity (MPC) which measures the strength of the linear functional relationship between the real and imaginary parts of the mode shapes for each identified mode.

Modal Amplitude Coherence (MAC):

The modal amplitude coherence is defined as the coherence between modal amplitude history and the one formed by extrapolating the initial value to later points in time, using the identified eigenvalue. As the result of minimum order realization, the triple [z, $E_p^T P \Sigma_n^{1/2} \psi$ and $\psi^{-1} \Sigma_n^{1/2} Q_n^T E_m$] is available where z and ψ are eigenvalues and eigenvectors of the A matrix (state matrix). The second element, $E_p^T P \Sigma_n^{1/2} \psi$, is the matrix of mode shapes and the third element, $\psi^{-1} \Sigma_n^{1/2} Q_n^T E_m$, is called initial modal amplitudes. The initial modal amplitude can be expressed as:

$$\psi^{-1} \Sigma_n^{1/2} Q_n^T E_m = [b_1, b_2, \cdots, b_n]^* \tag{4.27}$$

where the asterisk means complex conjugate transpose of the matrix.

The modal amplitudes can be extrapolated in time as:

$$\bar{q}_j^* = [b_j^*, z^{t1} b_j^*, \ldots, z^{tn} b_j^*] \tag{4.28}$$

where t_i's represent the sequence of time in which the initial modal amplitude is extrapolated. The counterpart sequence would be the identified modal amplitude time history, obtained from decomposition of the Hankel matrix:

$$\psi^{-1}\Sigma_n^{1/2}Q_n^T = [q_1, q_2, \cdots, q_n]^* \tag{4.29}$$

As a function of these two modal amplitudes (extrapolated and identified), the MAC_j is defined as:

$$MAC_j = |\bar{q}_j^* q_j| / (|\bar{q}_j^* \bar{q}_j| \, |q_j^* q_j|)^{1/2} \tag{4.30}$$

This parameter obtains values between 0 and 1 where the values close to 1 indicate that the estimated system eigenvalue and the initial modal amplitude are close to the true system. Also values that are far away from 1 indicate that the identified mode is a noise driven mode. This parameter determines the level of the purity of identified mode in presence of measurement noise (Juang and Pappa 1885).

Modal Phase Collinearity:

Modal Phase Collinearity (MPC) quantifies the spatial consistency of the identified mode shapes. When the modes are normal (which is expected in an ideal lightly damped system) the vibration of all locations on the structure are either in-phase or out-of-phase with one another (Juang and Pappa 1993). However, in practice, usually the phase angles of the identified modal displacement vectors are not consistent. This behavior is not necessarily due to structural properties (e.g. non-proportional damping), but can be a result of noise in the process. Particularly in lightly damped structures, modes are normal and the non-consistent phase angles are often the result of poor data quality. MPC is an indicator which quantifies the collinearity of the phase angle in the identified mode shapes and determines their accuracy.

For each identified complex mode shape vector, consider the variance and covariance matrices of imaginary and real parts:

$$S_{xx} = \mathrm{Re}(\phi_i)^T . \mathrm{Re}(\phi_i) \tag{4.31a}$$

$$S_{yy} = \mathrm{Im}(\phi_i)^T . \mathrm{Im}(\phi_i) \tag{4.32b}$$

$$S_{xy} = \mathrm{Im}(\phi_i)^T . \mathrm{Re}(\phi_i) \tag{4.33c}$$

The eigenvalues of the covariance matrix will be:

$$\lambda_{1,2} = \frac{S_{xx} + S_{yy}}{2} \pm S_{xy}\sqrt{\eta^2 + 1} \tag{4.34}$$

where η is defined as ($\frac{S_{xx} + S_{yy}}{2S_{xy}}$). The MPC for mode *i*, is defined by Juang and Pappa (1993) as:

$$MPC_i = \left(\frac{\lambda_1 - \lambda_2}{\lambda_1 + \lambda_2} \right)^2 \ (\times 100\ \%) \tag{4.35}$$

Similar to MAC, MPC values are also ranged from 0 to 1, where 0 indicates uncorrelated phase angles in the identified mode, and 1 represents a perfect normal mode.

4.7. Evaluation of Measurement Noise Effects using Golden Gate Bridge Data

In this section the data collected in a deployment of wireless sensor network on Golden Gate Bridge is used as an example to apply the PCR, MAC, and MPC parameters

for quantification of modal identification accuracy. The data includes measurements by two synchronized sensor networks with different sensor sensitivities. Having two synchronized data sets allows the examination of accuracy parameters in presence of only uncertainties derived from measurement noise (as the same response with same environmental and operational conditions is measured by the two sensor types). Therefore, the performances of sensor types can be compared by comparing the accuracy of the results.

Utilized Wireless Sensor Network

Pakzad *et al* 2008, presents the results of a long term ambient vibration monitoring on Golden Gate Bridge where the acceleration data was measured using a WSN, consisting of 65 sensing units, during a three month deployment period. The sensing units in this network utilized three hardware components: sensors, filters and microcontroller, and radio for wireless communication. For the measurement of low-level and high-level accelerations, two Micro-Electro-Mechanical System (MEMS) accelerometer sensors are used each in two directions. The use of two accelerometer types in the sensor board design is a cost-effective solution and allows examination of performance-price tradeoffs. Analog Device's ADXL202 is the high-level sensor (Figure 4.22-a) which provides a ±2 *g* range with a sensitivity of 1 *mg* at 25 *Hz* (Analog Devices 1999). For low- level vibrations, Silicon Design 1221L (Figure 4.22-b) is used which has higher sensitivity and is suitable for ambient structural vibrations (Silicon Designs 2007). The acceleration range of the Silicon Design 1221L accelerometer is reduced from ±2 *g* to ±0.15 *g* to

achieve a higher resolution from the 16-bit Analog to Digital Convertor (ADC). Table 4.1 shows the detailed specifications of the two accelerometer sensors, integrated in the sensor board.

The measured signal from MEMS accelerometers is fed to a single-pole anti-aliasing low-pass filter with a cutoff frequency of 25 *Hz*. The cutoff frequency is high enough to capture many high vibration modes of this long span bridge (Pakzad *et al* 2008). The filtered analog signal is then fed to a 16-bit ADC for each of the channels. The acceleration data is collected with a high frequency sampling of 1 kHz and is downsampled on-board to 200 Hz to reduce the noise level of the measured signal. For a detailed description of the implemented WSN architecture, the system software, and the full scale deployment on the bridge, the reader is referred to Pakzad 2010.

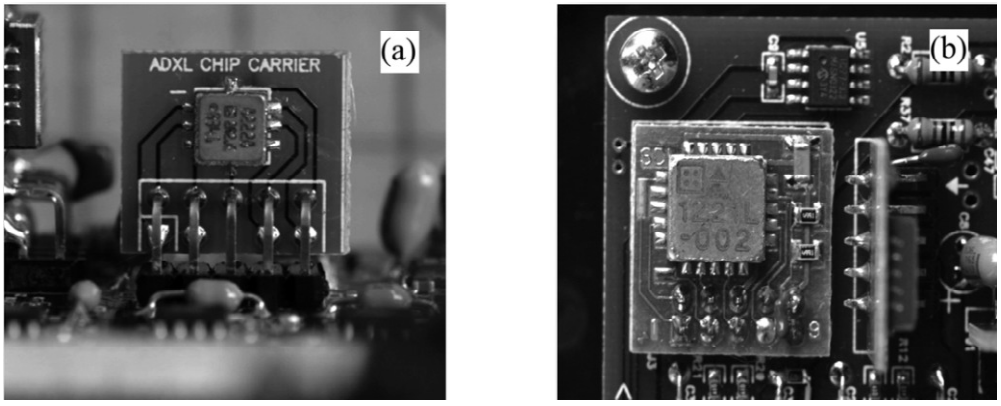

Figure 4.22. ADXL202 (a) and Silicon Design 1221 (b) accelerometers

Table 4.1. Specifications of Silicon Design 1221 and ADXL202 accelerometers

Specification	Silicon Design 1221L Accelerometer	ADXL202 Accelerometer
Acceleration Range	± 0.15 g (reduced from ± 2 g)	± 2 g
Frequency Response	0 to 400 Hz	0 to 500 Hz
Nominal Output Noise	2 μg/√Hz	500 μg/√Hz
Temperature Range	-55 ºC to +125 ºC	-40 ºC to +85 ºC
Dimension	3.5 × 3.5 × 1.05 (mm)	5 × 5 × 2 (mm)
Cost	~ $150 (in 2005)	~ $10 (in 2005)

Before application of the sensor board in vibration monitoring of Golden Gate Bridge, sensors were validated through static and dynamic tests, using a reference Wilcoxon 731-4A low-noise piezoelectric accelerometer (Pakzad 2010). The result of the validation showed that the Silicon Design 1221 accelerometer behaves very similar to the low-noise reference sensor in both time and frequency domains, whereas the ADXL 202 sensor presents higher noise in the data, especially in the low-frequency range. Considering the distinguished difference in the cost ($10 versus $150 in 2005), it is important to evaluate the significance of lower noise level of the more expensive accelerometer in modal identification process.

Table 4.2. Identified natural frequencies and damping ratios of vertical modes identified by ERA-NExT, using data collected by ADXL202 and Silicon Design 1221 accelerometers

Mode	Frequency (Hz)		Damping Ratio (%)	
	ADXL202 sensors	SD1221 sensors	ADXL202 sensors	SD1221 sensors
1 A	0.1067	0.1067	2.1031	1.7599
2 S	0.1326	0.1330	2.2178	1.9824
3 S	0.1708	0.1711	1.4182	0.9943
4 A	0.2164	0.2170	2.1239	2.0639
5 S	0.3015	0.3012	1.1098	1.1078
6 A	0.3705	0.3701	1.2066	1.4229
7 S	0.4610	0.4607	0.5531	0.6631
8 A	0.5491	0.5458	2.4465	2.3976
9 S	0.6620	0.6620	0.5082	0.5407
10 A	0.7691	0.7664	0.8779	1.0146
11 S	0.8884	0.8905	0.8451	0.8692
12 A	1.0042	1.0040	1.2559	0.8739
13 S	1.1330	1.1312	0.7320	0.6391
14 A	1.2565	1.2641	0.7099	0.8225
15 A	1.5234	1.5195	0.6339	0.7918
16 S	1.6573	1.6596	0.5997	0.6314
17 A	1.7659	1.7764	0.5260	0.3653
18 S	1.9281	1.9295	0.6840	0.6692
19 A	2.0623	2.0713	0.5221	0.4724
20 S	2.1797	2.1954	0.4829	0.6695
21 A	2.3187	2.3248	0.5614	0.5998
22 A	2.5739	2.5929	0.2970	0.3761
23 S	2.7082	2.7127	0.4910	0.3537
24 A	2.8397	2.8399	0.2722	0.3363
25 A	3.7677	3.7605	0.3257	0.4901

Identified Modal Parameters of the Golden Gate Bridge

The data collected by two accelerometer sensor types from the ambient vibration of Golden Gate Bridge are used for modal parameter identification of the bridge, using

ERA-NExT. A summary of identified natural frequencies and damping ratios of vertical modes, resulted from ADXL202 and SD1221 accelerometer data, are presented in Table 4.2. Figure 4.23 also shows the first 9 identified vertical mode shapes, resulted from the two sensor types. More detailed information about the identified modal properties of Golden Gate Bridge using the ambient vibrations can be found in Pakzad and Fenvas 2009.

By comparing the modal properties, it is clear that both sensor types are capable of estimating the fundamental modal parameters of the bridge. However, some inconsistencies in results of two sensor types, especially in damping ratios and mode shapes, can be observed. Applying PCR, MAC, and MPC parameters on the estimated modal parameters, the performance of the two sensing systems, in terms of accuracy and consistency of results, is investigated.

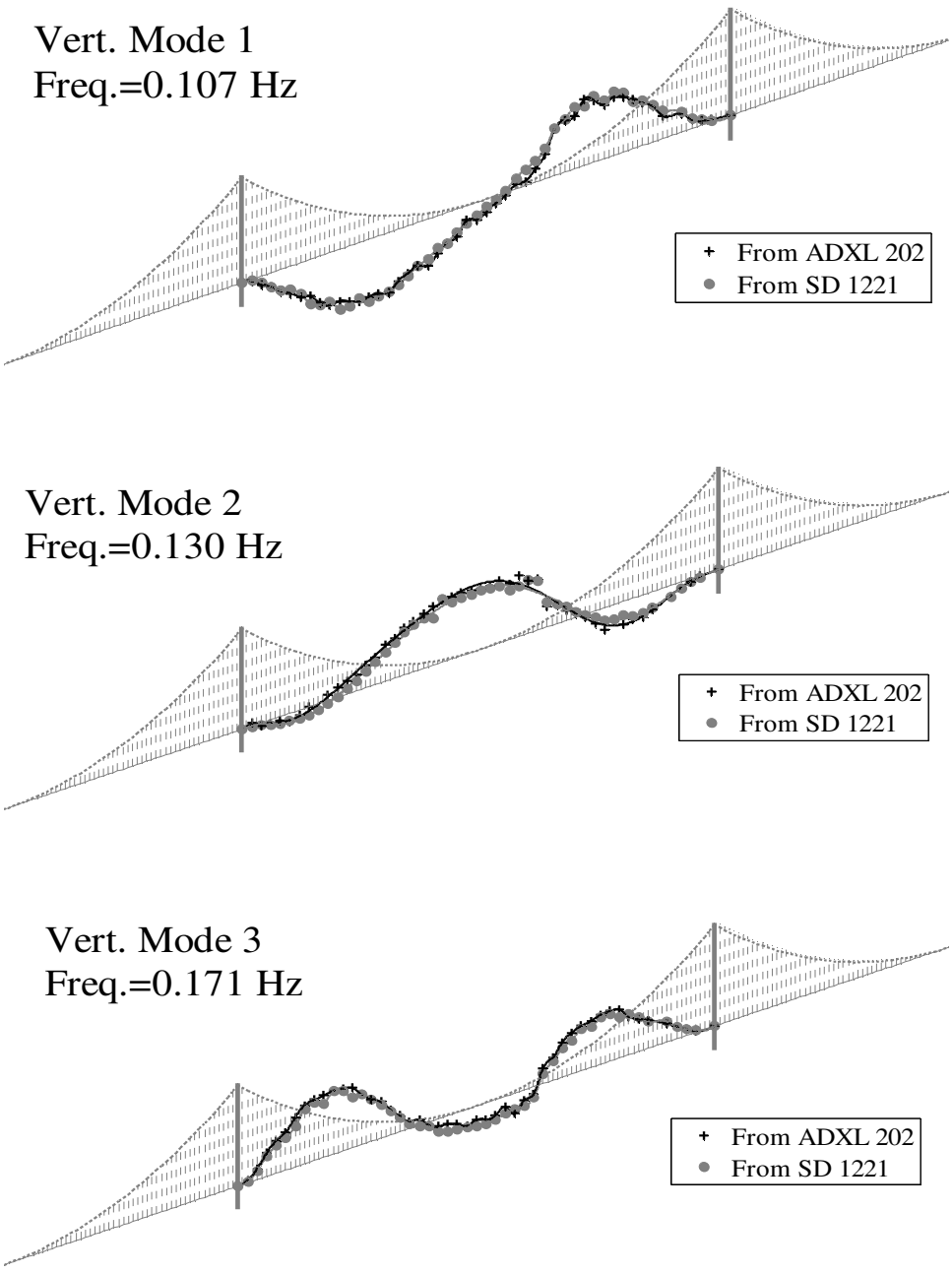

Figure 4.23. First 9 identified vertical modes of the main span of Golden Gate Bridge

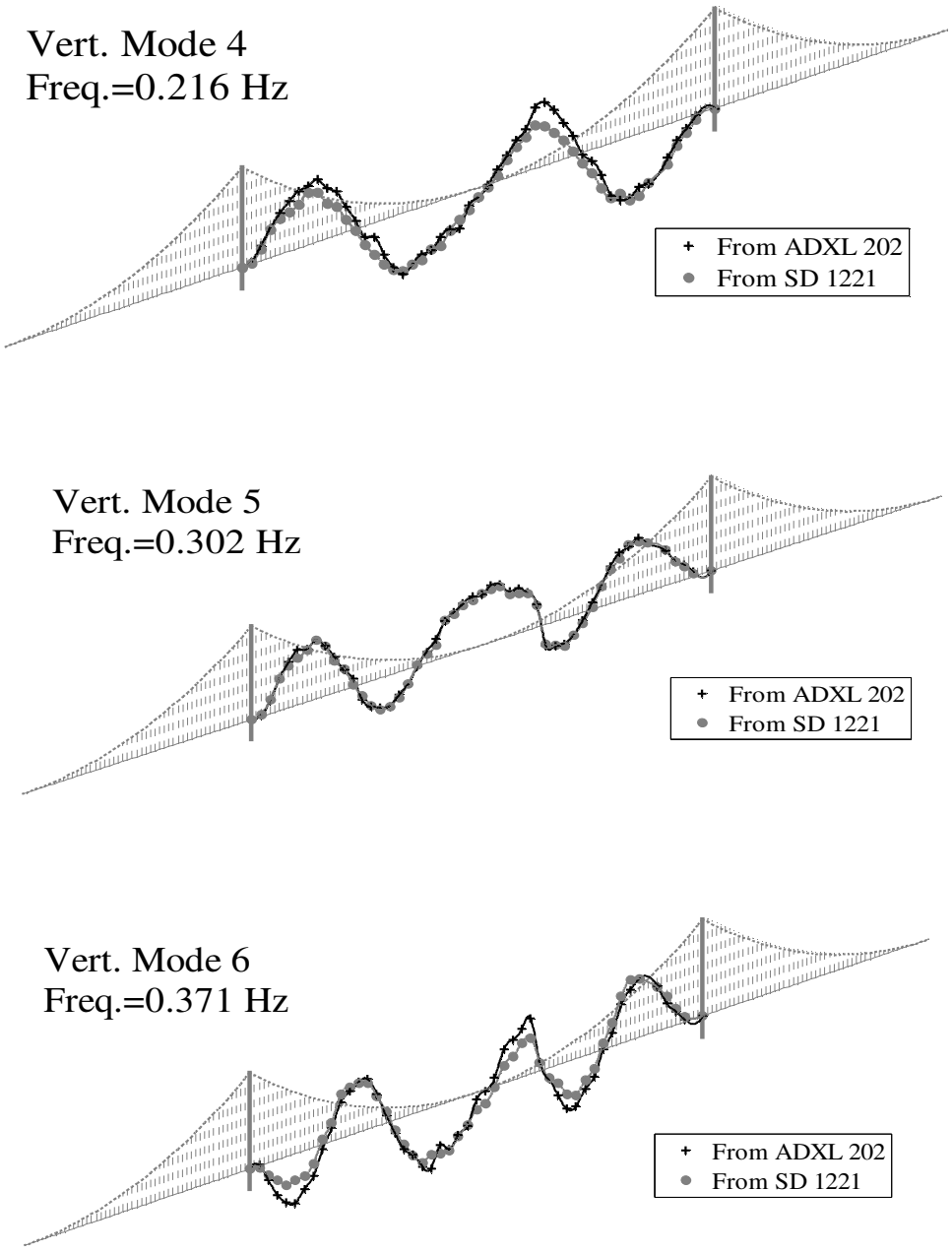

Figure 4.23 (Cont'd). First 9 identified vertical modes of the main span of Golden Gate Bridge

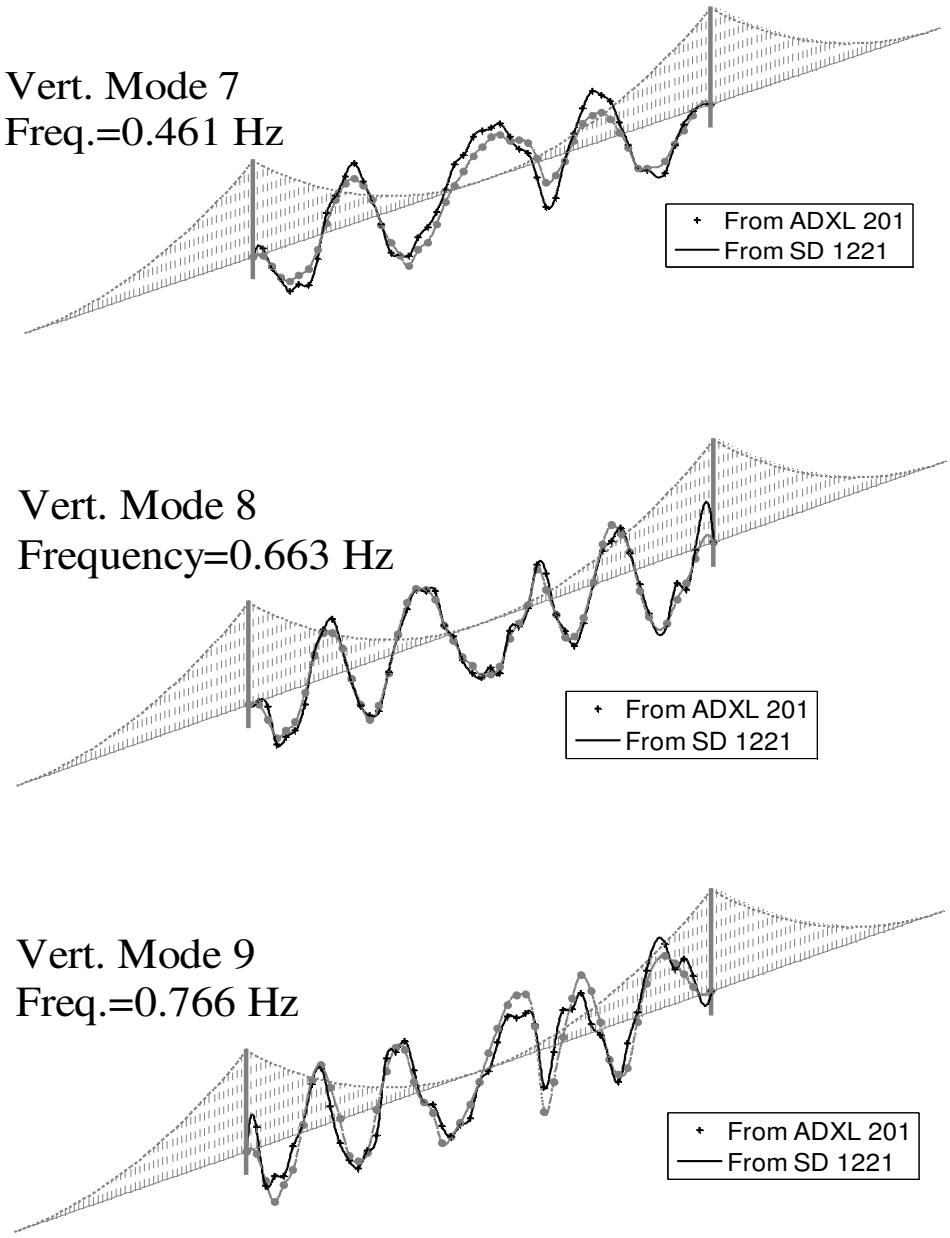

Figure 4.23 (Cont'd). First 9 identified vertical modes of the main span of Golden Gate Bridge

Evaluation of Results, using Physical Contribution Ratio

The *PCR* of each mode is computed for all sensing nodes of the implemented sensor network on Golden Gate Bridge. Figure 4.24 shows these ratios for first 9 vertical modes. Similar to the results of the numerical example, PCRs are proportional to the modal ordinates. In addition, these ratios also depend on the modal amplitude factor (*b*) and modal frequency.

Due to the long span of the bridge, many modes (with natural frequencies up to the Nyquist frequency) contribute in the measured response. Therefore, the contribution of each mode of vibration in the measured response is expected to be small. This is evident as comparing the amplitudes of PCR values of this implementation with those of the 5 DOF simulated example.

Figure 4.24 shows that the Silicon Design 1221, which has a lower noise level, presents significantly higher PCR, compared to that of ADXL 202 sensors. This simply means that the noise contamination of the estimated impulse response is higher in the ADXL 202 sensors and therefore, the estimated modal parameters are more influenced by the measurement noise.

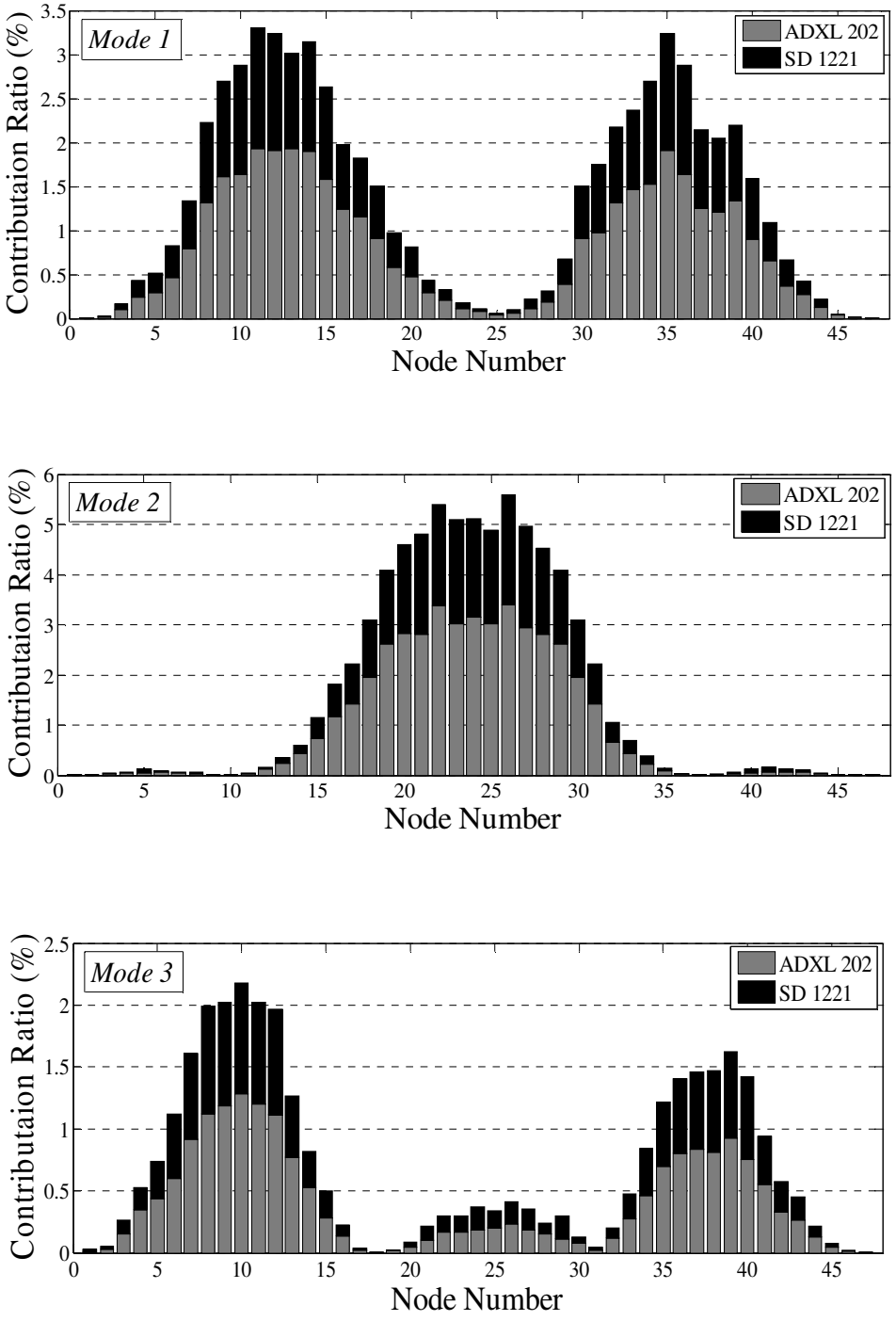

Figure 4.24. Physical Contribution Ratio of four identified modes at different nodes

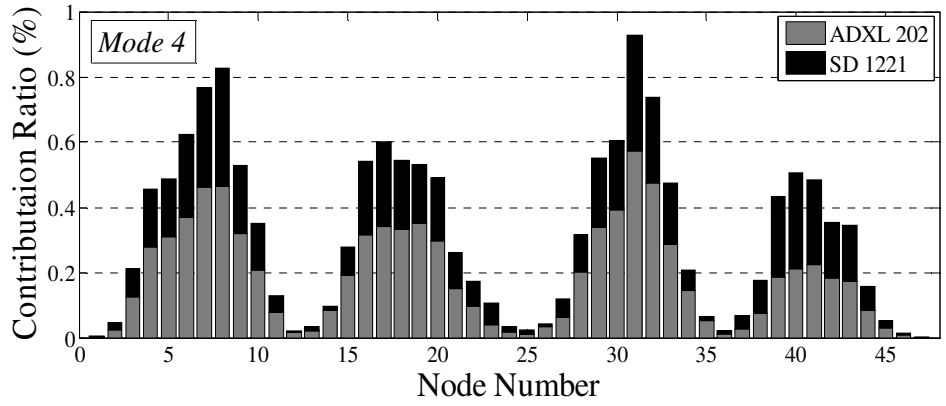

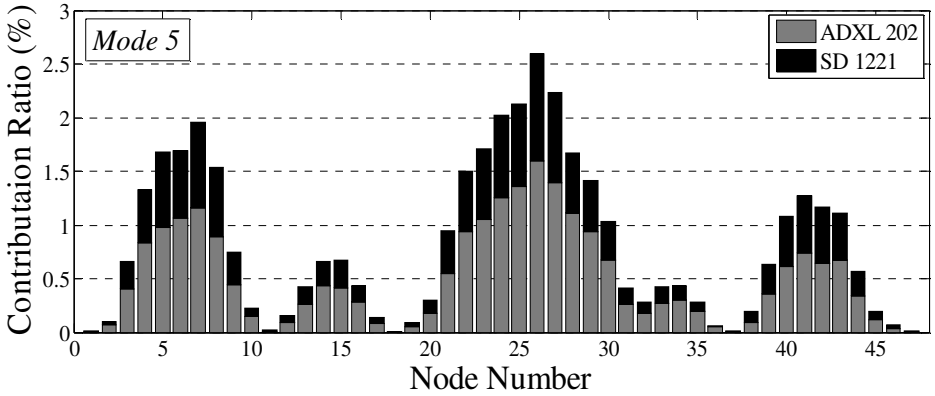

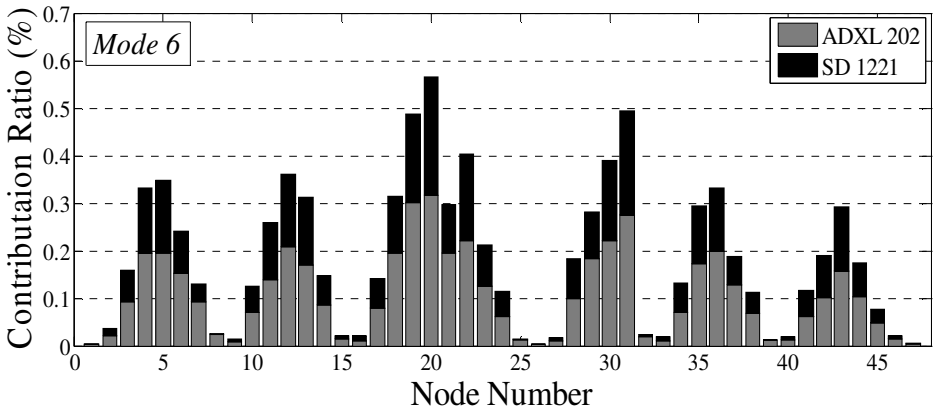

Figure 4.24 (Cont'd). Physical Contribution Ratio of four identified modes at different nodes

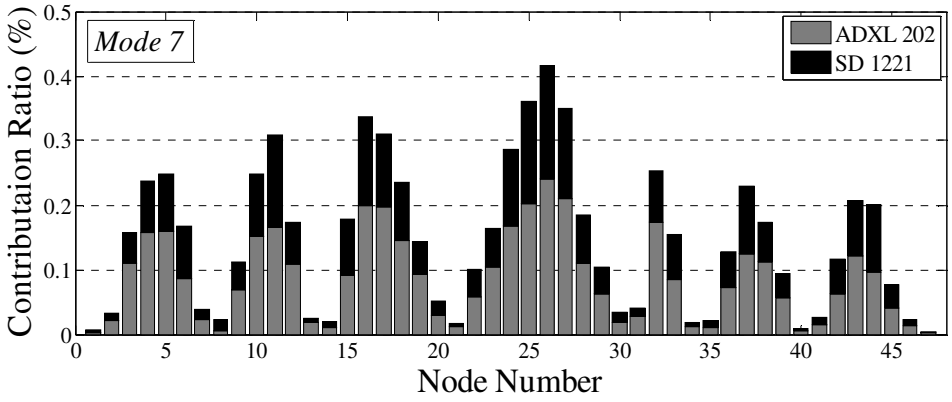

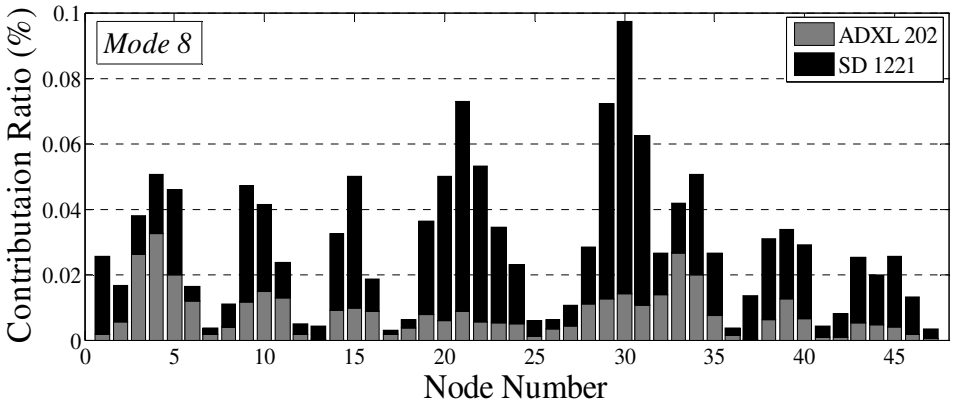

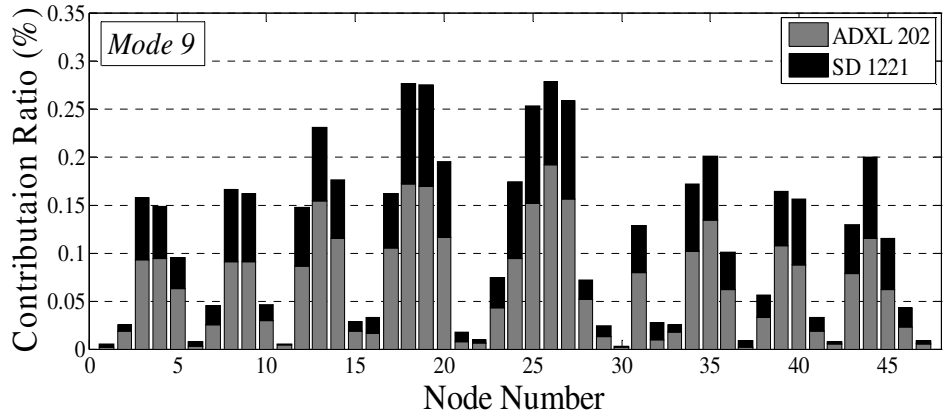

Figure 4.24 (Cont'd). Physical Contribution Ratio of four identified modes at different nodes

Although in theory the higher modes usually have less participation in response and therefore are more sensitive to the noise level, investigation of real data shows that some of the higher modes also have significant PCRs. This is reasonable since the ambient excitation does not necessarily have a perfectly constant spectrum and therefore, some higher modes may be excited more than others. To observe the contribution of different modes in general, the PCR of all the nodes are added together for each mode and plotted in Figure 4.25. This Figure shows that the signal by Silicon Design 1221 accelerometers have higher overall PCRs in almost all of the modes. At the same time, it can be realized that the difference is more significant in lower frequencies (e.g. first 5 modes) rather than the higher ones. This reflects the fact that the Silicon Design accelerometers are significantly more accurate than ADXL accelerometers in low frequencies. This result highlights the importance of sensors with low noise level at low frequencies for monitoring of long span bridges that have low fundamental natural frequencies.

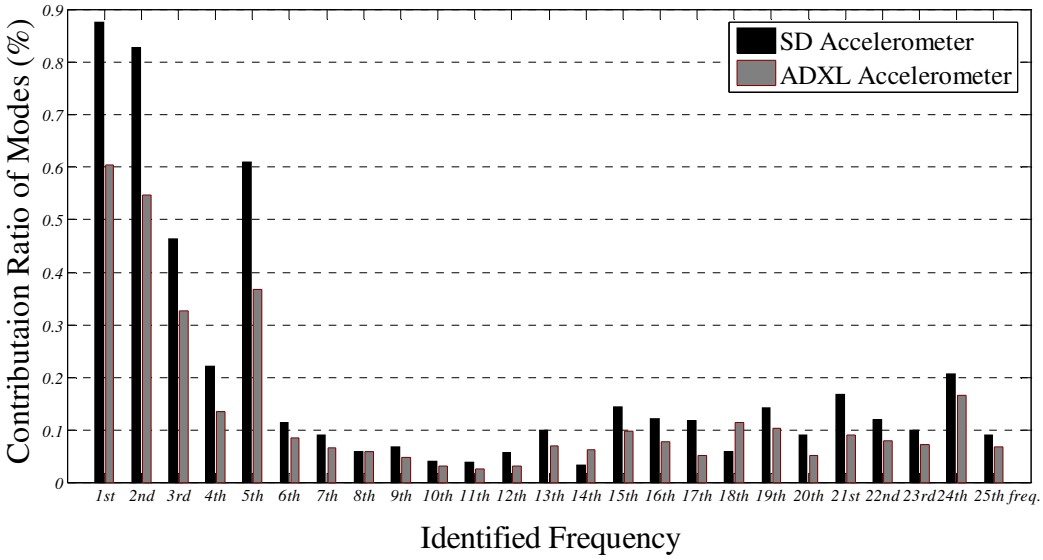

Figure 4.25. Overall Physical Contribution Ratio of identified modes for 25 identified vertical modes

Evaluation of Results, using MAC and MPC

MAC and MPC are both evaluated for the identified modal parameters of Golden Gate Bridge from two networks of Silicon Design 1221 and ADXL202 sensors. Both of these parameters (MAC and MPC) were originally developed as tools to distinguish the structural modes from spurious ones. However, in this work, as accuracy indicators these parameters are used to evaluate and compare the accuracy of identified modes from two different sensor types.

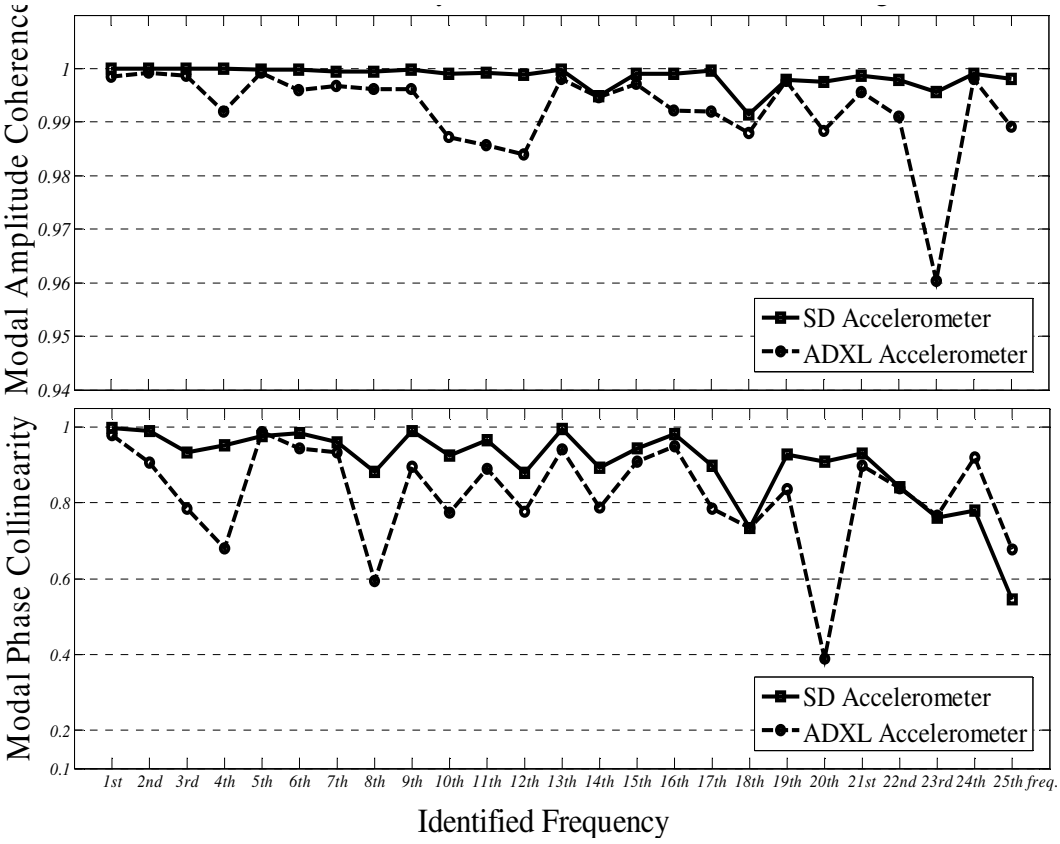

Figure 4.26. Modal Phase Collinearity and Modal Amplitude Coherence of identified modes

Figure 4.26 shows the MAC and the MPC for 25 identified vertical modes. Comparing the results, it is clear that the network of Silicon Design sensors has resulted in more accurate modal parameters.

The low MAC and MPC of the estimated results become more important when the selection of identified modes relays on these indicators. For example, Consistent Mode Indicator (CMI) is defined as the product of MAC and MPC (Pappa *et al* 1998) and is utilized in autonomous algorithms for selection of structural modes from spurious noise and/or computational modes (Pappa *et al* 1998, Nayeri *et al* 2009). A threshold for

acceptance of identified modes, suggested in these two articles, is CMI greater than 80%. Figure 4.27 shows the values of this parameter for different identified modes for the two accelerometer types. It can be seen that many of the modes, identified by ADXL202 sensors, are not acceptable as accurate modes based on this criterion.

Generally, the results of identification for modes with lower frequency are less sensitive to the noise level, since the modal vibration in those frequencies have higher amplitude and therefore, higher SNR in modal coordinates (as can be seen in the results of previous section, [Figure 4.25]). However, Figure 4.27 shows that even in the low-frequency modes (third and fourth mode with frequencies of 0.17 and 0.21 Hz, respectively), identified by ADXL 202 data, the lack of confidence is evident. This is particularly reasonable as the ADXL 202 sensors presented high level of noise in low frequency range and probably the third and fourth identified modes from this sensor have not enough amplitude to overcome the high noise of this frequency range.

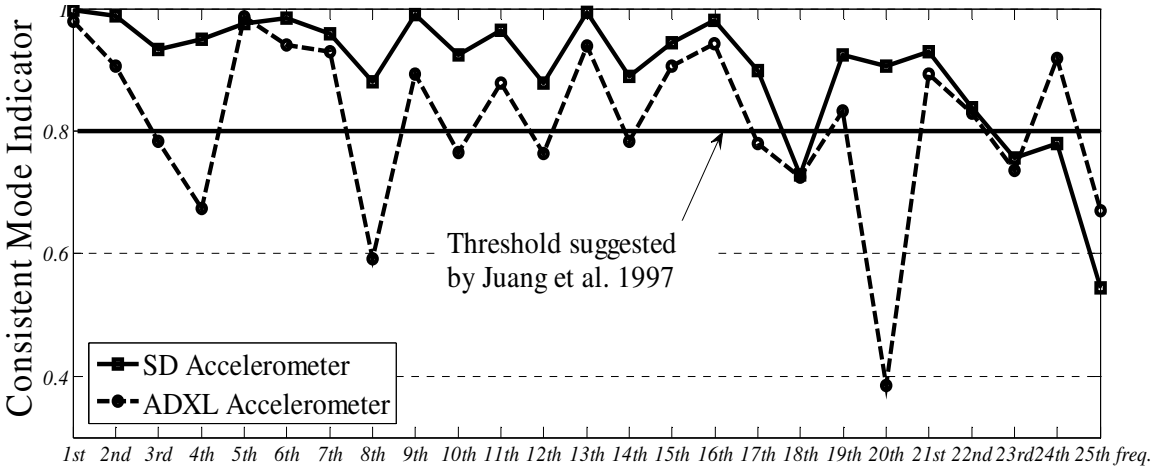

Figure 4.27. Consistency Mode Indicator of identified modes, using ERA-NExT

4.8.Consistency of Results through Increase of System's Order

The last parameter which is evaluated in this study is the consistency of modal parameters through changes in the system order. In the ERA process, the initial model order is usually selected higher than the desired number of modes to be identified. It is also conventional to use stabilization diagrams (Peeters and Roeck 2001a) for selection of the model order which gives the most stable modal parameters. A difficulty associated with the selection of the model order is that the identified modal properties are not constant as the model order increases. This inconsistency is particularly significant for the case of damping ratios since the process of adding pole into the system changes the damping ratios more than other parameters.

To detect the effect of measurement noise on consistency of modal parameters, identified frequencies and damping ratios are inspected as the system's order increases. Figure 4.28 shows the frequencies in 0.1 Hz to 1.0 Hz range versus the selected system's

order for both sensor networks with ADXL 202 and Silicon Design 1221. Figure 4.29-a and 4.29-b also presents the same information for the first 5 damping ratios, identified by the two different sensor types. The mean value and standard deviation of the identified damping ratios are also presented in the plots which help in comparing the consistency of results obtained from two sensor types. For calculating the mean and deviation of results, the damping ratios outside of the 0.5% to 7.5% range are considered as outliers and excluded from this computation. Figure 4.29 shows that the sensors with lower noise level (Silicon Design 1221) result in smaller deviation and are generally more consistent. However, the results for higher orders are fairly similar and stable for both systems. This means that increasing the model order and using the stabilization diagram are quite effective in overcoming the inconsistency issue, associated with identification of modal parameters.

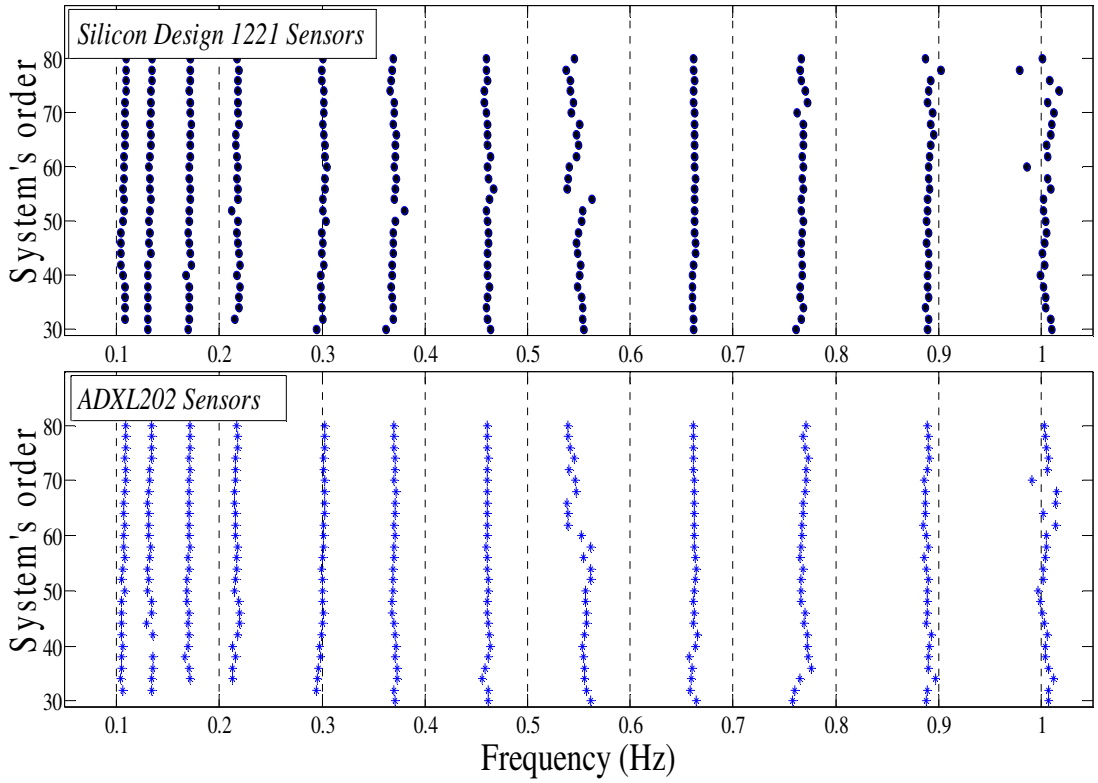

Figure 4.28. Consistency of natural frequencies through increase of model order

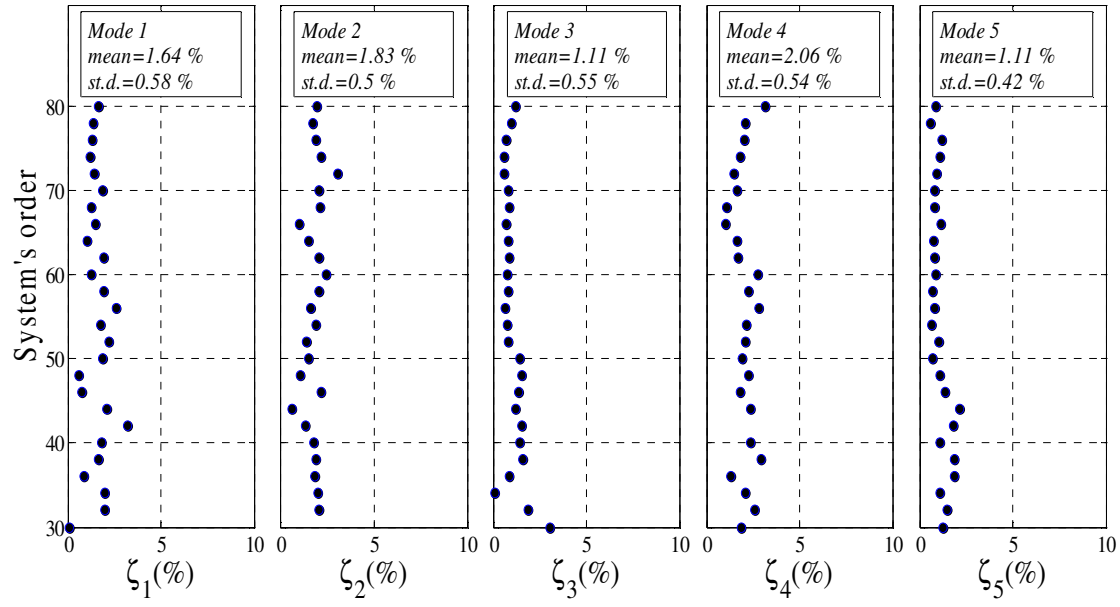

(a)

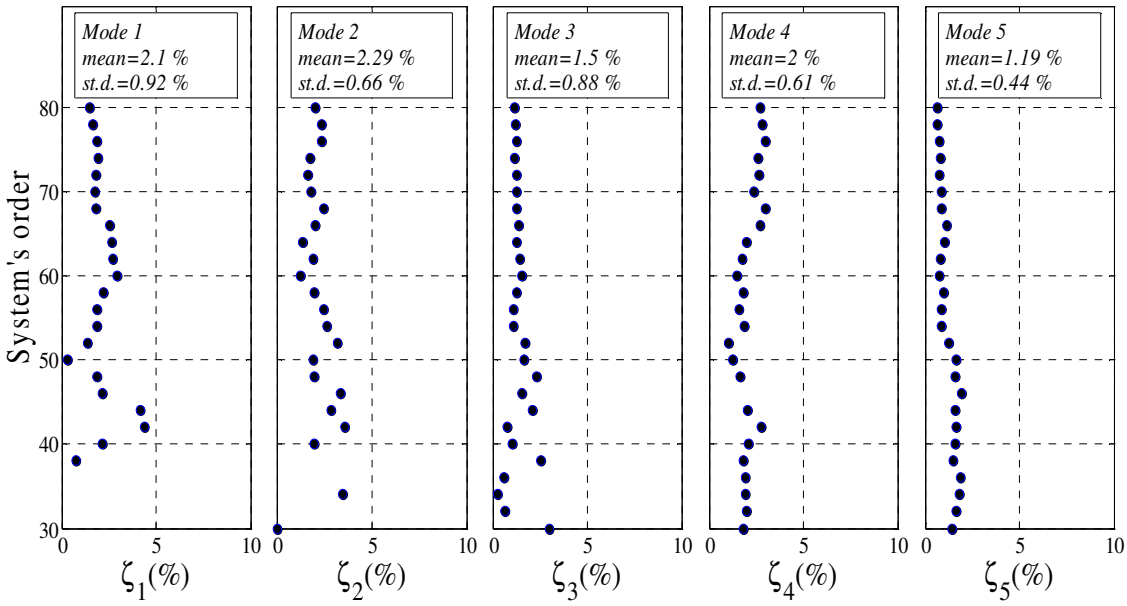

(b)

Figure 4.29. Consistency of damping ratios through increase of model order for (a) Silicon Design Accelerometer and (b) ADXL201 Accelerometer

4.9. Summary and Conclusion on Measurement Noise Effects

In this chapter, the influence of measurement noise on the accuracy and consistency of modal parameter identification is investigated. Physical Contribution Ratio (PCR) is developed to examine the level of contribution of physical modes in the estimation of impulse response. This parameter, PCR, is validated through implementation on a numerically simulated example and its behavior under the effects of artificial noise and random structural changes is investigated. PCR is also implemented on the ambient vibration data of Golden Gate Bridge, measured by two accelerometer sensors (ADXL 202 and Silicon Design 1221) with different noise levels. To evaluate the effects of higher measurement noise, modal parameters identified by the two sensor types are compared and inspected in terms of accuracy and consistency, using the presented parameter. The comparison of results, obtained from two sensor types, showed significantly higher PCR of estimation using the low noise sensor data. Furthermore, to quantify and compare the purity and accuracy of modal parameters, identified by the two measurement systems, Modal Amplitude Coherence and Modal Phase Collinearity are applied. The investigation showed higher purity in the results of low noise accelerometer and failure of some modes, identified by ADXL 202 accelerometer, based on an accuracy criterion. To detect the effect of measurement noise on consistency of modal parameters, as the model order increases, the identified parameters (natural frequencies and damping ratios) are inspected throughout the increase of order, for results of both sensor types. The results showed that the deviation of modal parameters, obtained by the low noise sensors,

is generally less than those identified by sensors with higher noise level. However, the difference is not significant, particularly in higher model orders, and it can be concluded that the inconsistency of results can be resolved by increasing the model order and through the use of stabilization diagram.

The developed parameters can be used as general tools for quantification of the modal identification results. However, as the objective of this study it can be considered as a basis for selection of sensor quality since it targets measurement noise rather than other types of uncertainties. Moreover, as a side application, it can be a basis for selection of sensor location as it provides the physical contribution of response in terms of the location of sensor as well. This application however, needs further study for adaption of parameters and development of a systematic approach which includes optimization into the process (i.e optimizing the location of sensors as to maximize the physical contribution of the structure's response).

It is worth mentioning that measurement noise is not the only root of the uncertainty in modal identification. Environmental and operational conditions (e.g. temperature and randomness of traffic) also have significant impacts on the results. Literature shows some efforts towards this investigation and Chapter 7 also presents some studies regarding the variation of modal parameters due to temperature and traffic loads. Further investigation, however, would improve the current state of this area and can assist with minimizing the uncertainty in the process of modal parameters identification.

Chapter 5

Damage Detection

5. Damage Detection

5.1. Introduction to Damage Detection

Advancements in sensing technology have allowed for the development of new SHM methods that can be applied on a temporary or semi-permanent basis for continual monitoring of structures. The vibration-based SHM approaches are commonly used to extract the dynamic characteristics of the structure from its response. One important application of vibration-based SHM and extraction of structural characteristics is in damage detection. This chapter introduces a statistics-based damage detection algorithm (initially proposed by Pakzad 2008) and presents supplementary statistical frameworks for implementation, and validation through different numerical and experimental models.

Literature presents numerous damage detection methods which rely on changes in identified dynamic characteristics (e.g. natural frequencies, mode shapes, and modal damping) to reveal changes in the physical properties of the structure (e.g. mass and stiffness), i.e. structural damage (Doebling et al. 1998; Alvandi and Cremona 2006). While the concept is intuitive, application of methods which rely on dynamic characteristics of the structure are not without difficulties. Modal properties are indicators of the global state of the structure and are not sensitive enough to local damages (Farrar et al. 1994; Chang et al. 2003). Therefore, these methods are mostly referred to as global-based damage detections. Also, some SHM practices involving global-based damage detection require knowledge of specific structural properties, including mass, stiffness, or damping ratio, for which it is often difficult to determine very accurate estimates (Koh et

al. 1995; Morassi and Rovere 1997; Sohn and Law 1997; and Ratcliffe 1997). On the other hand, local damage detection is desired for structural health monitoring since local damages happen first and then propagate to the entire structure. Literature also presents some effective local damage detection methods, such as damage locating vector (DLV) method (Bernal 2002; Sim et al., 2008; Sim et al, 2011) and two-dimensional gapped smoothing method (Yoon et al. 2005). While effective, these methods have some requirements. For example DLV method requires the knowledge of structural properties, or requires homogeneity of the structural properties as in the two-dimensional gapped smoothing method. In addition, considering the current state of damage detection techniques in practice, more research is still needed to improve existing algorithms, develop more effective techniques, and make damage detection more practical and applicable in real-life monitoring scenarios.

The algorithm which is presented in this chapter is an effective damage detection method, called Influence-based Damage Detection Algorithm (IDDA) that uses vibration responses to achieve localized damage detection without the need for exact knowledge of structural properties. The method is based on regression of the vibration response and estimation of influence coefficients as damage indicators. While the algorithm is effective, it is also very practical as it converts the shear amount of time-history data into condensed information which enables detection of structural changes in the system.

In IDDA, influence coefficients are obtained from linear regression between every two node responses and used as the index for determining and detecting the occurrence of

changes in the structural properties. The change point of time-variant influence coefficients is also determined using a Bayesian statistical framework. The effectiveness of the proposed local damage detection method is demonstrated and verified through implementation on a simulated and two experimental models. In the experimental implementation of the algorithm on one of the models (scaled beam-column connection), two different networks of wired and wireless accelerometer sensors are utilized. In the implementation of the algorithm on the other model (large-scale beam-column connection), however, only wired strain gauge sensors are used. While validating the performance of IDDA, the results of the different sensor networks (particularly wired and wireless) with different characteristics are also evaluated and compared to observe the effect of sensor noise on the effectiveness of the algorithm.

5.2. Localized Damage Detection Method

This algorithm based on the premise that a structure's response changes when physical properties change, i.e., due to damage. The response of the structure is monitored at various locations via a spatially dense sensor network, and linear regression influence coefficients are extracted. When damage occurs, this linear relationship changes, which is reflected in the influence coefficients indicating the existence of damage. In addition to identifying that damage has occurred, considering the locations of sensors associated with changing coefficients allows for localization of the damage as well. Furthermore, a statistical framework that utilizes hypothesis testing can be implemented to determine whether damage exists at a significant confidence level.

5.2.1 Structural Model

Damage detection methods can be classified in a number of ways. One common classification is as identification of linear or nonlinear damage. The definition of linear damage is "the case when the initially linear-elastic structure remains linear-elastic after damage" (Doebling et al. 1998). One advantage of studying a linear damage state is that the linear equations of motion still apply after damage. Additionally, a linear damage method can utilize finite element models to predict the structure's response to certain damage states. The method proposed in this work relies on this assumption of linearity before and after damage.

In order to demonstrate the linear-elastic assumptions of this method, a rigid beam-column joint is considered, as shown in Figure 5.1. This simplified example is used for demonstration as it can lead to a laboratory experiment, explained later in this chapter. The general free body diagram has 9 unknowns (x_i, y_i, r_i, x_j, y_j, r_j, x_k, y_k, and r_k) assuming the joint to be restrained out-of-plane. The displacement at any point along the structure, u_n, can then be defined as a function of each of these unknowns as follows:

$$u_n = f(x_i, y_i, r_i, x_j, y_j, r_j, x_k, y_k, r_k) \tag{5.1}$$

Because the joint represents a small portion of the structure, the member lengths create small angles. Small angles correspond to negligible rotations reducing the number of degrees of freedom (DOFs) to 6 independent translational DOFs (x_i, y_i, x_j, y_j, x_k, and y_k).

This number of DOFs can be further reduced with the practical assumptions of inextensibility of the column and beam members.

A structure that is being monitored will experience excitations of the ambient type for a majority of its useful life. Other more extreme excitations should be considered as occurring during the damaging event, in which case the linearity assumption does not hold true. Because this method involves the comparison of the structural state pre- and post-event, as opposed to during the nonlinear damaging event, it is reasonable to consider the structure within a linear-elastic range. Thus it is valid to consider Equation (5.1) as a linear function.

Another important assumption for the application of this method is that the contributing mass at the considered portion of the structure is negligible. This assumption allows local dynamic effects to be neglected such that the structure can be considered in its linear static state. Pakzad 2008 and Chang 2010 have presented several simulated examples that support neglecting mass for this implementation. Both found that because the stiffness of elements forming the connection is much larger in comparison to their contributory mass when considering a local portion of the structure, the effect of the mass term becomes negligible and the dynamic equation of motion can be reduced to a static relationship. However, it is important to note that this assumption only applies to a local joint. Therefore, the linear relationship between nodes that are within the same local joint and share a relatively stiff portion of the structure should be assessed for this algorithm.

This may translate to small clusters of dense sensor networks within a larger-scale instrumentation network.

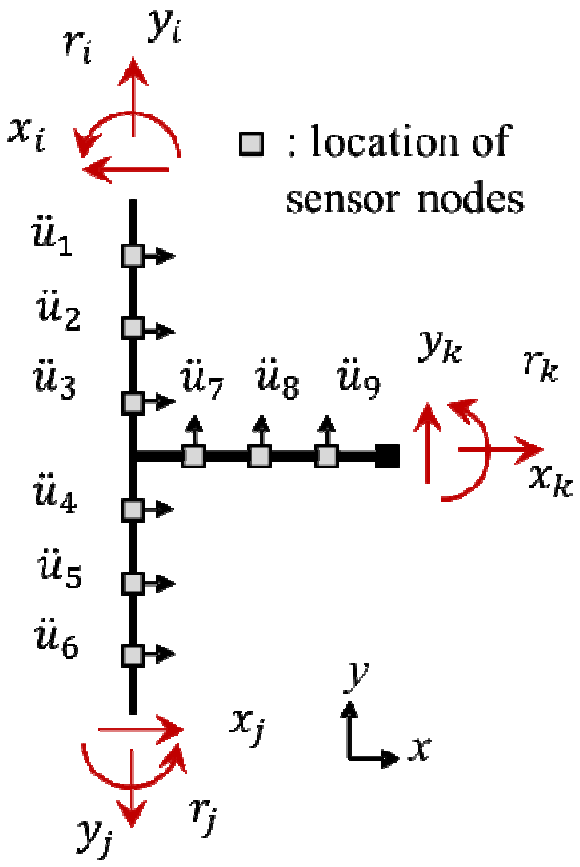

Figure 5.1. Free body diagram of a rigid beam-column joint

Considering a small portion of the structure (the beam-column connection shown in Figure 5.1) as a linear static system, any displacement response along the connection is a linear function of the response at other locations. In the other words, the relationship between the response at any two locations, nodes *i* and *j*, can be defined as:

$$u_j(n) = \beta_{ij} + \alpha_{ij} \cdot u_i(n) + \varepsilon_{ij}(n) \tag{5.2}$$

where, $u_i(n)$ and $u_j(n)$ are structure's response at nodes i and j, respectively, and at time n, β_{ij} is intercept value of regression between nodes i and j, α_{ij} is influence coefficient of regression between nodes i and j, and ε_{ij} is the residual of the regression model.

5.2.2 Mathematical Model

Auto Regressive with Exogenous (ARX) model is discussed in Chapter 2 in the context of system identification. As a more general application, ARX can be used to model systems and establish the relationship between different outputs (responses at different locations of a structure) as follow:

$$\sum_{p=0}^{P} a_p y(n-p) = \sum_{q=1}^{Q} b_q x(n-q) + \varepsilon(n) \tag{5.3}$$

where y and x are output and input respectively, α_i's and β_i's are ARX coefficients, $\varepsilon(n)$ represents the residuals, n is the time index, and P and Q are orders of the autoregressive and exogenous parts of the ARX model, respectively. Based on this mathematical representation, the response at any time step can be estimated having the past inputs and outputs and the current input.

In a linear structural system, each output is a linear function of input excitations and therefore, the linear relationship holds between different outputs, as well. Therefore, the ARX model can be written to correlate outputs of a system as follow:

$$\sum_{p=0}^{P} a_{jp} y_j(n-p) = \sum_{i=1}^{k} \sum_{q=0}^{Q} b_{iq} y_i(n-q) + \varepsilon(n) \tag{5.4}$$

where output at node j is related to current and previous outputs at nodes i=1 to k. This equation establishes a relationship between one output and other outputs of the system. The accuracy of this model depends on the selected model orders. While higher model orders, in general, deliver more details of the system and reduce the estimation bias, it is always desired to keep the order at the minimum level to avoid over-parameterization. Considering the special case of the linear system with negligible mass (absence of inertia force), described in the previous section, the corresponding ARX model can be developed by assuming P and Q equal to zero:

$$y_j(n) = \sum_{i=1}^{k} \frac{b_i}{a_j} y_i(n) + \beta_{ij} + \varepsilon(n) \tag{5.5}$$

which correlates the response at node j to current responses at nodes i (=1 to k). Addition of intercept (β) into Equation (5.5) is in order to account for the initial condition, since the effects of previous time steps are removed from the equation. Note that Equation (5.5) represents a multi-variable version of Equation (5.2) (i.e. considering k=1 and $b_i / a_j = \alpha_{ij}$, the same equation will be obtained).

5.3. Influence Coefficients as Damage Indicators

IDDA takes responses of the structure and uses the assumed linear relationship between different nodes, or sensor locations, with one another. This pair-wise relationship between node responses is defined by utilizing regression analysis. By calculating influence coefficients, α_{ij}, between two nodes i and j, based on vibration-

induced acceleration response data, the correlation between these responses is determined according to Equation (5.2).

The comparison of the resulting influence coefficients from the initial undamaged state with that of the damaged state of the structure serves as a "damage indicator" when it yields a significant change in the value of the coefficients from state to state. More specifically, the influence coefficients exhibit a much more significant change when nodes *i* and *j* are located on opposing sides of the damaged segment versus when they are on the same side. When damage occurs between two node locations, *i* and *j*, the element becomes structurally more flexible, affecting the correlation between responses at two locations u_i and u_j. From linear regression, this translates to a change in the value of α_{ij} from that of the original undamaged case. This characteristic allows for the identification of the damage location by inspection of the pattern in which influence coefficients exhibit significant changes.

5.4. Influence Coefficient Accuracy and Estimation Error

Once the coefficients are estimated, the accuracy of the data must be assessed and verified before damage detection can be performed. This is done through consideration of both the accuracy of the pair-wise coefficients and the estimation error. The product of influence coefficients α_{ij} and α_{ji}, yields the evaluation accuracy, EA_{ij}, of these coefficients, indicating which node responses are linearly related to one another with the least amount of error, ε_{ij}, and thus are more accurate predictors. An evaluation accuracy of 1.0 signifies a strong accuracy of estimation, while a product of less than 1.0

corresponds to progressively higher values of noise and nonlinear behavior of the physical structure.

The second parameter that is used for data verification is normalized estimation error, which is calculated as:

$$\gamma_{ij} = \frac{\sigma_{\alpha_{ij}}}{\alpha_{ij}} \tag{5.6}$$

where α_{ij} is influence coefficient between nodes i and j and $\sigma(\alpha_{ij})$ is standard error of the influence coefficient estimates α_{ij} and can be estimated by the following equation:

$$\sigma_{\alpha_{ij}} = \frac{\sigma_{\mathrm{e}}}{(\sum y_i^2)^{1/2}} \tag{5.7}$$

In Equation 5.7, σ_e is the standard error of the residuals, e (the difference between the estimated and true response).

Normalized estimation error allows for a direct comparison of the amount of error associated with the estimation of each influence coefficient as a damage indicator. This parameter is used to determine which influence coefficients should be used for damage detection. A low estimation error, resulting from a low standard error of the estimated influence coefficient, will correspond to a more accurate predictor. Once the accuracy and error have been assessed for each coefficient, post-processing of the best influence coefficients can be performed for damage identification and localization.

When the influence coefficients have been assessed for accuracy and error, the most reliable of these are chosen for use in damage detection. As was previously discussed, changes in the physical properties of the structure, such as loss of material stiffness or change in boundary conditions due to damage, are reflected in changes in the behavior of the structure which can also be seen directly in the influence coefficients; the linear relationship between certain locations of the structure will change to differing degrees depending on the location of the damage. A high change in the coefficient indicates that the structural response is different in one or both of the locations, *i* and *j*, from that of the original healthy state. The degree to which certain coefficients change can indicate the location of the damage.

5.5. Statistical Framework

In order to determine what defines a "significant change" in the influence coefficients, a statistical framework has been developed and applied. This framework is useful for processing large volume of data as a structure is monitored over time. A Bayesian Statistic is used to determine the change point, the point at which the data indicates damage, at a 95% confidence level (Chen and Gupta 2000). This statistical inference method tests the hypothesis that the mean of the influence coefficients for each successive test is equal to the mean of the influence coefficients from the initial undamaged state,

$$H_0: \alpha_1 = \alpha_2 = \cdots = \alpha_N = \bar{\alpha}, \tag{5.8}$$

against the one-sided alternative hypothesis that the values of the influence coefficients beyond the change point, denoted as *r*, are greater (or smaller) than that of those prior to this point by a significant amount,

$$H_A: \alpha = \alpha_1 = \alpha_2 = \cdots = \alpha_r < \alpha_{r+1} = \cdots = \alpha_N \tag{5.9}$$

N represents the number of tests. The change point *r*, mean μ, and standard error σ of the influence coefficient are all unknown. The statistic that is developed to test the aforementioned hypothesis is a Bayesian statistic as follow:

$$S_N = \sum_{i=\mathrm{r}}^{N-1} i(\alpha_{i+1} - \bar{\alpha}) \tag{5.10}$$

where *r*, the change point, can be any point from 1 to *N*-1. This Bayesian statistic, in fact, assigns a weight (*i*) to changes that happen successively. In the other words, as the offset in the mean value of the influence coefficients persists, the difference between the mean and the baseline will be accumulated by increasing factors. To test the significance of change and conclude the alternative hypothesis, H_A, with a certain confidence level, the following normalized *t*-statistic is utilized:

$$t = \frac{S_N}{\hat{\sigma}\sqrt{\frac{N(N-1)(2N-1)}{6}}} \tag{5.11}$$

where $\hat{\sigma}$ is the estimated error of the influence coefficient and the denominator of the equation is the deviation of S_N. The test statistic *t*, has a *t*-distribution with *N*-2 degrees of freedom (Sen and Srivastava 1975). In this work, the hypotheses are tested at a 95% confidence level.

The physical significance of this hypothesis testing is such that the alternative hypothesis, H_A, indicates that the structure has incurred damage, while the null hypothesis, H_0, means that there is not adequate evidence to establish that damage exists. These hypotheses are tested for those node pairs that have been identified as significant damage indicators in the assessment and verification stage of the method.

Influence-based damage detection algorithm with its different steps is outlined in Figure 5.2. There are three phases in the implementation of this algorithm: (i) data retrieving and parameter extraction, (ii) validation and accuracy assessment, and (iii) post-processing and decision making. The next sections of this chapter will present the implementation of the algorithm on different simulated and experimental models.

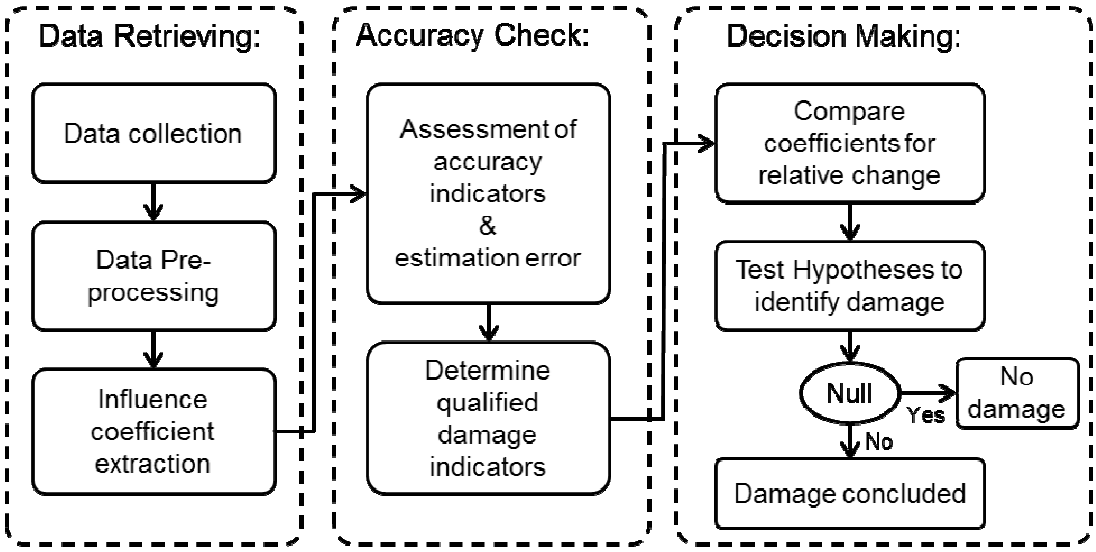

Figure 5.2. Methodology for damage detection

5.6. Simulated Beam-Column Connection

Since IDDA is developed for detection of local damages, the evaluations are presented based on a beam-column connection (which is a local and also a critical structural element) as a testbed structural component. In this section, IDDA is validated using a simulated model of the beam-column connection. The finite element simulation is created using SAP2000. The beam-column shown in Figure 5.1 represents a localized portion of a larger structure, for example a single joint in a larger building frame. A joint is a location in a structure that is prone to damage due to high stress concentrations at the connections. The ability to determine not only the joint, but the location within the joint where damage has occurred can lead to more efficient and cost-effective repair solutions in a structure.

The column portion of the joint is fixed at both ends while the beam cantilevers out from the centerline of the column. Two simulation conditions are performed which include (1) an undamaged baseline condition and (2) a damaged condition, characterized by a reduction in the beam stiffness (15% reduction in stiffness). For each of these models, displacement response is simulated at each of the 9 nodes for a white noise excitation applied at the free end of the beam in the *y*-direction. Measurement noise is accounted for by adding a Gaussian noise with a standard deviation equal to 5% of the root mean square (RMS) of each response signal. Figure 5.3 shows the schematic of the simulated beam-column connection and the displacement response at two nodes before and after the damage is applied.

The influence-based damage detection algorithm is then applied to the simulated data and the parameters are extracted. The relative changes in the influence coefficients between the undamaged and damaged states are shown for each pair-wise node relationship in Table 5.1. The influence coefficients α_{ij}, $1 \leq i, j \leq 6$ all experience very small (less than 5%) changes between the undamaged and damaged states. This implies that the physical properties between these nodes have not changed significantly. However, the coefficients of nodes 1 through 6, paired with nodes 7, 8, and 9 show relative changes of between 20-30%. When nodes are on opposite sides of the damage, i.e. nodes 1 through 6 are located on the undamaged column, while nodes 7, 8 and 9 are located on the damaged part of the beam, the physical properties between the paired nodes changes. This physical change is reflected in a more significant relative change in the value of influence coefficients. Furthermore, the influence coefficients α_{ij}, $7 \leq i, j \leq 9$ also experience a noticeable change in coefficients (about 5-10%). This signifies that the physical properties of the structure between the nodes associated with α_{78}, α_{79}, and α_{89} have changed. Therefore, damage is more likely to exist between these nodes. This is consistent with the simulated damage which was applied by stiffness reduction of the beam. While functionality of the algorithm is showed throughout this example, its performance still needs to be evaluated throughout experimental data. The next section shows the implementation of IDDA, including accuracy assessment, post-processing and decision making steps, on a beam-column connection model constructed in the laboratory.

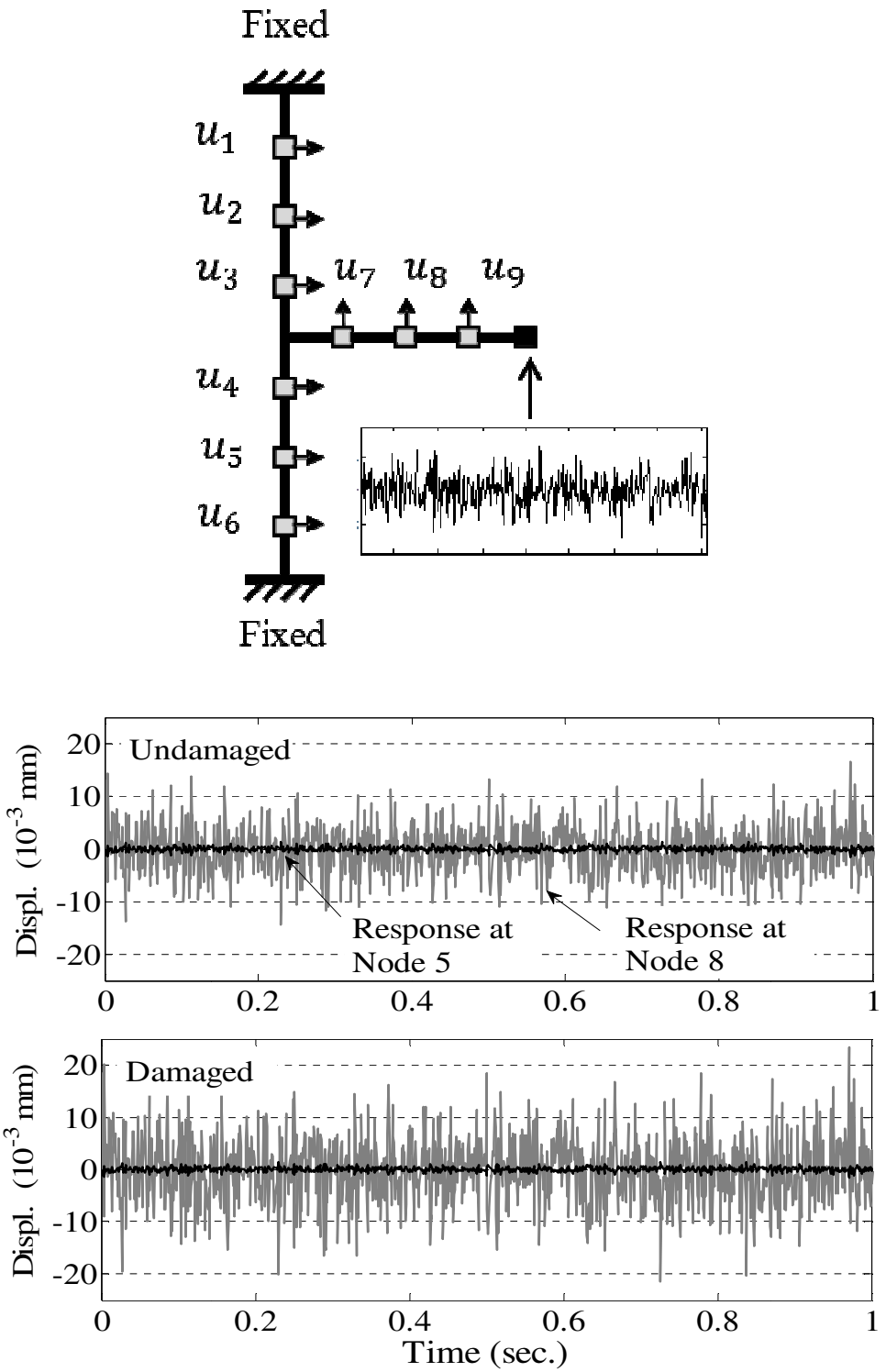

Figure 5.3. Simulated model and the displacement response in undamaged and damaged states

Table 5.1. Relative change in influence coefficients, α_{ij}, from undamaged to damaged states for simulated structure

	1	2	3	4	5	6	7	8	9
1		-3.98	-4.25	-4.93	-4.36	-3.64	17.31	24.09	27.16
2	0.05		-0.83	-1.53	-0.89	-0.79	21.39	28.39	31.58
3	0.32	-0.27		-1.14	-0.57	-0.41	21.75	28.76	31.97
4	0.88	0.28	0.12		0.11	0.08	22.53	29.59	32.81
5	0.03	-0.51	-0.74	-1.32		-0.59	21.49	28.50	31.68
6	-2.44	-3.60	-3.77	-4.51	-3.77		17.82	24.61	27.71
7	-17.54	-18.11	-18.32	-18.83	-18.35	-18.20		5.76	8.39
8	-22.02	-22.56	-22.77	-23.25	-22.79	-22.65	-5.45		5.49
9	-23.92	-24.45	-24.64	-25.12	-24.67	-24.53	-7.74	-5.43	

5.7. Experimental Beam-Column Connection

IDDA is further verified through implementation on a laboratory beam-column connection model. The prototype represents a portion of the beam and column members as they come to a local joint. The specimen is tested for both an undamaged and a damaged state. To simulate damage in the location of the connection joint, the beam member was switched out for a member of lesser wall thickness (corresponding to a 40% stiffness reduction). Note that this just represents a reduction in stiffness near the connection and not the entire beam element.

The structure is instrumented with two sensor networks; one of 9 wired accelerometers and another of 9 wireless accelerometers, as shown in Figure 5.4. The wireless accelerometers used in this implementation consist of Imote2 processing board combined with SHM-A sensor board, integrating tri-axial LIS3L02AS4 (STMicroelectronics, 2005) accelerometer with 50 μg/√Hz noise density, developed by Rice and Spencer (2008 & 2009). The wired sensors, on the other hand, are capacitive accelerometers (PCB Piezotronics, Inc. 2004) with 3 μg/√Hz noise density. Due to the lower noise level of the wired sensors and their more reliable network, the wired results are used as a direct comparison point for the WSN. The reason for having two sensor networks is to compare the performance of each and assess the effects of sensing network quality on the damage detection process and the level of confidence for decision making.

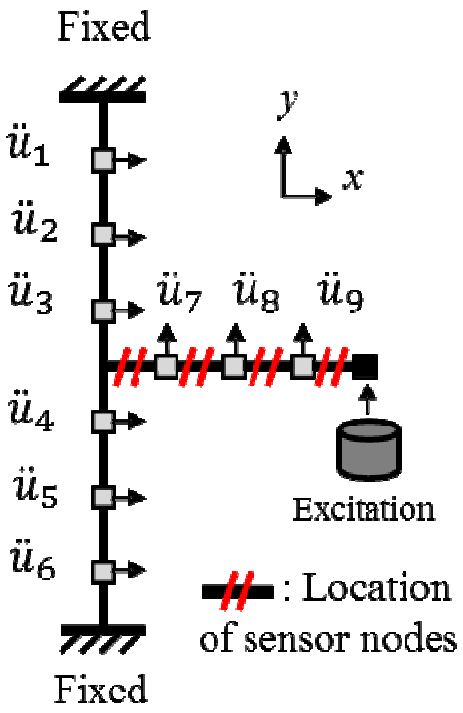

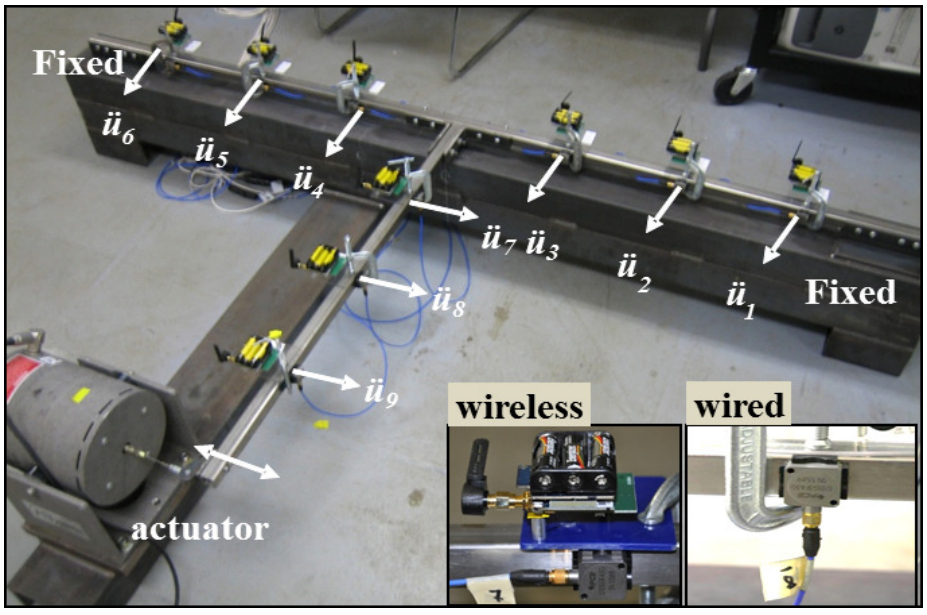

Figure 5.4. Experimental test bed for beam-column prototype instrumented with wired and wireless accelerometers

To generate acceleration responses, the free end of the cantilever is attached to an actuator and excited by harmonic force at a 15 Hz frequency. The wired data is collected at a 250 Hz sampling rate with each test lasting 40 seconds. The wireless data is collected with the same length as wired data. Using both wired and wireless sensors, the data collection is performed simultaneously for direct comparison. The undamaged and damaged structures are each tested 15 times. The collected data samples are then processed through IDDA to detect the occurrence of damage. This experiment serves as both a validation of the method with a real structural connection as well as a comparison of efficiency of the two sensor networks with different noise levels, which reveals the sensitivity of method to the sensing quality. The results of the implementation of the algorithm using wired sensors are presented in this section and the comparison of sensor network results are discussed in the next section.

Accuracy Assessment and Verification of Influence Coefficients

Having 9 sensors, 72 influence coefficients can be obtained by performing linear regression and presented in Table 5.2. Once the coefficients have been calculated from the acceleration data, the estimates must be assessed to identify the most significant indicators, which can then be used for damage detection. The evaluation accuracy, EA and estimation error, γ are integral for this accuracy assessment. By inspection of these parameters, different trends can be identified in the undamaged and damaged parameters, with different estimation errors and evaluation accuracies. These trends have been designated as six different regions, whose mean values are presented in Table 5.3. In this

table, the average accuracy of pairs at different regions is rated from high to low and their corresponding locations are presented to describe the reason for different accuracies. Region 1 in the table corresponds to the least estimation error and highest accuracy, and region 6 corresponds to the greatest estimation error and lowest accuracy. Therefore, parameters in region 1, consisting of α_{ij}, $7 \leq i\ , j \leq 9$, are the most accurate and have the least error. This is a reasonable outcome as the actuator applies force at the end of the beam, closest to nodes 7, 8, and 9. This proximity and boundary condition result in larger amplitude of excitation at these nodes compared with that of the column nodes, thus, corresponding to a higher signal-to-noise ratio (SNR) of the data at these nodes. A higher SNR correlates to better quality data and more accurate results.

On the contrary, region 6, which consists of parameter α_{16}, exhibits the poorest accuracy and the greatest estimation error. This can be accounted for by the fact that each of these nodes is located at either end of the column near the fixed ends. These boundary conditions restrict the column from movement closest to the support, greatly reducing the magnitude of the acceleration signal and thus, the SNR of these nodes. Figure 5.5-(a) to (f) show examples of α from different regions and their corresponding EA and γ. Figure 5.5-(a) shows that EA is almost equal to unity and γ is almost equal to 0 for region 1. The EA and γ values for a region 3 pair, shown in Figure 5.5-(c) also exhibit accurate values, although not quite as accurate as region 1. Figure 5.5-(f), however, shows a much lower EA and a noticeably higher γ associated with region 6. Based on similar data for all 6 regions, it can be concluded that regions 1 through 3 contain the most accurate data and

thus the most useful damage indicators. On average, these influence coefficients exhibit accuracy greater than 98% and estimation error less than 0.2%.

Post Processing and Damage Detection

Based on the accuracy assessment, region 1, 2, and 3 coefficients are considered for damage detection. Figure 5.6-(a) shows the average percent changes of a few pair-wise coefficients in different regions on their corresponding locations. This further supports the theory that nodes on opposite sides of damage show the greatest change, while nodes with no damage between them show a significantly smaller change. Pairs with nodes within the damage location show some change, but not as large as that of nodes on opposite sides. The reason for this is that when both nodes are within the damaged area, both nodes experience similar increases in flexibility, resulting in a less severe differential. Therefore, inspection of the pattern of changes in pair-wise coefficients points to the location of damage within the structure (i.e. damage between nodes 2 and 7, 3 and 8, and so forth).

Table 5.2. Relative change in influence coefficients, α_{ij}, for experimental structure

Node	1	2	3	4	5	6	7	8	9
1		2.91	5.22	8.57	2.26	1.37	16.65	27.39	31.76
2	2.16		1.21	12.75	6.36	6.40	21.44	32.65	37.22
3	4.15	1.10		13.22	6.96	7.19	22.56	33.91	38.54
4	12.17	15.04	16.64		6.44	6.87	4.63	14.24	18.12
5	5.67	8.62	10.21	6.68		0.22	12.21	22.50	26.65
6	7.09	9.17	10.59	5.51	0.86		11.36	21.55	25.64
7	15.54	18.10	19.24	6.35	11.93	12.03		9.28	13.06
8	22.78	25.11	26.13	14.40	19.51	19.62	8.52		3.49
9	25.44	27.67	28.65	17.37	22.30	22.42	11.63	3.38	

Table 5.3. Trend regions according to average estimation error (γ) and evaluation accuracy (EA)

Region	Influence Coefficients	Location of pairs on the beam-column connection model	γ_{ij} Average	EA_{ij} Average
1	α_{78}, α_{79}, and α_{89}	Between nodes on the beam	0.0001	1.000
2	α_{23} and α_{45}	Between nodes on each side of column (except 1 & 6)	0.0005	0.998
3	α_{27}, α_{82}, α_{29}, α_{37}, α_{38}, α_{39}, α_{47}, α_{48}, α_{49}, α_{57}, α_{58}, and α_{59}	Between nodes on the beam with those on the column (except 1 &6)	0.0012	0.985
4	$\alpha_{12,}$ $\alpha_{13,}$ α_{46}, α_{52} and α_{56}	Between nodes on the column	0.0015	0.975
5	$\alpha_{17,}$ $\alpha_{18,}$ $\alpha_{19,}$ $\alpha_{67,}$ $\alpha_{68,}$ and α_{69}	Between nodes on the beam with those on the column's ends	0.0018	0.967
6	α_{16}	Between two ends of the column	0.0161	0.889

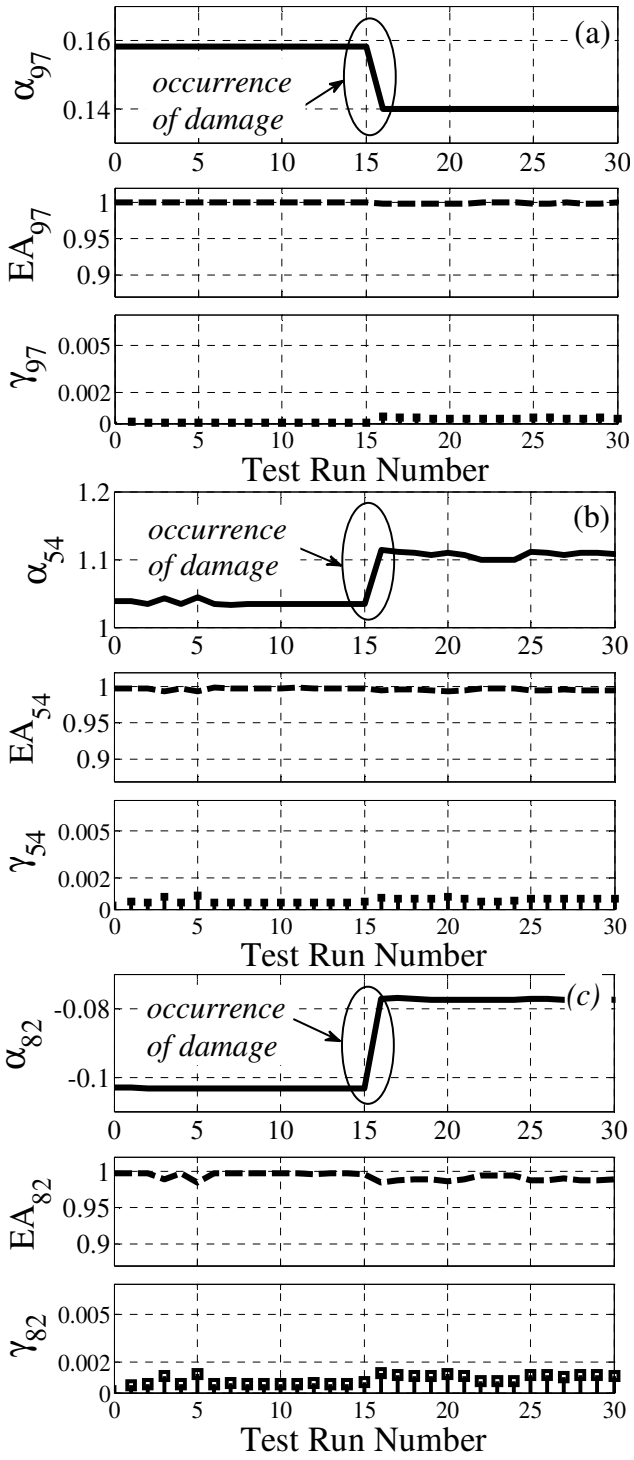

Figure 5.5. Pair-wise coefficients (α), estimation accuracy (EA), and evaluation accuracy (γ), for region 1 (a) to region 6 (f)

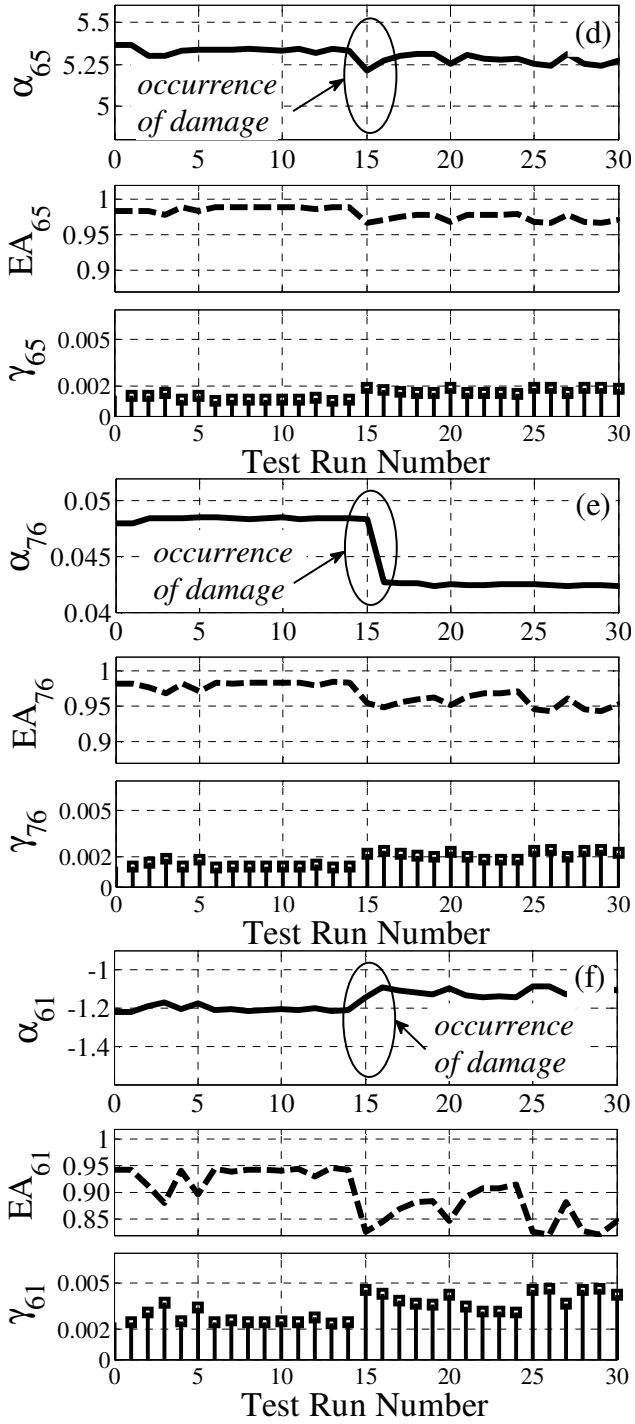

Figure 5.5 (Cont'd). Pair-wise coefficients (α), estimation accuracy (EA), and evaluation accuracy (γ), for region 1 (a) to region 6 (f)

Hypothesis Testing for Significant Damage

The difference between undamaged and damaged coefficients can be indicative of the existence and location of damage in a structure. However, in practical scenarios, it is not easy to determine when damage has occurred, and make inferences at different confidence levels. Therefore, another element must be added for complete damage detection: a statistical framework.

The hypothesis testing plot graphically shows the change point of damage, the point at which damage is identified at a certain confidence level, by plotting the test statistic against the test run number. A graph in which the data crosses the confidence bounds, either positive or negative, corresponds to a positive hypothesis, previously defined as H_A in Equation (5.9), indicating the detection of damage. If the accuracy and estimation error associated with the nodes being considered are high and low, respectively, the prediction of the hypothesis test will be more exact and will cross the confidence bounds closer to the occurrence of damage. In order to demonstrate this behavior, the test statistic from the 15 damaged state tests were plotted against their run number. Because damage exists for all of the plotted data, the more accurate damage indicators will yield a plot in which the confidence bounds are crossed closer to the occurrence of damage.

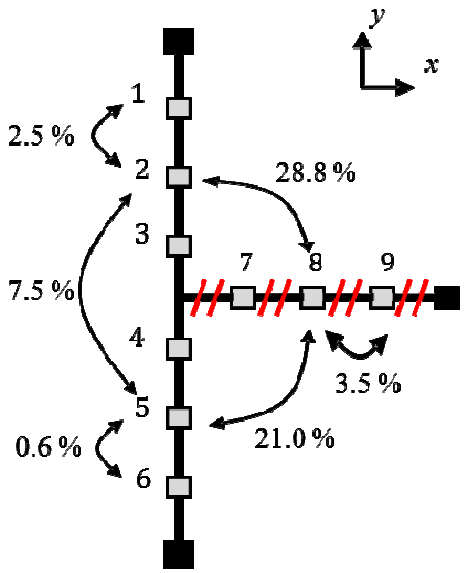

(a)

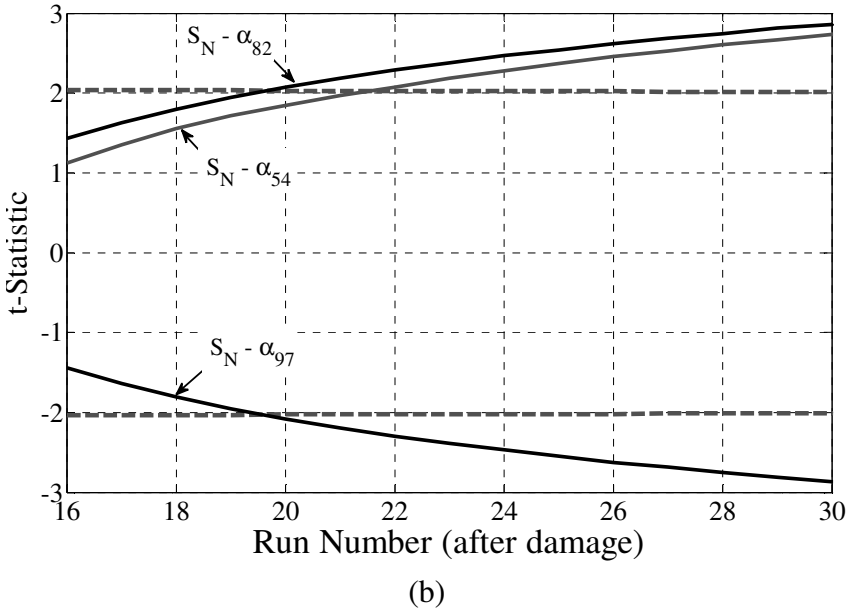

(b)

Figure 5.6. Relative change of some of coefficients, (b) hypothesis testing results for regions 1 to 3

Considering Figure 5.6(b), it can be determined that a coefficient with a larger change between the damaged and undamaged states tends to show damage earlier than a coefficient of comparable accuracy with a smaller change. It was shown previously that

the region 1 and region 3 coefficients in Table 5.2 (regions shown in Table 5.3) experienced 4-14% and 10-30% average changes, respectively. These parameters cross the bound after only 4 and 5 runs, respectively, whereas, the region 2 coefficients, with 1 to 7% change, take 7 runs to confidently show damage. This suggests that when a statistic crosses the bound first, compared to coefficients of similar accuracy, it is more important to the damage location. Therefore, these plots demonstrate that damage is detected by hypothesis testing, making this method a reliable means of damage detection.

Comparison of Wired and Wireless Sensor Networks

In order to consider realistic application of the proposed damage detection method, there must be a reliable and affordable sensor network with which to instrument the structure. Continued advancements in wireless sensor technology strive to fulfill that role. Although researchers have shown the effective role of WSN in improving the affordability of monitoring (ease of implementation and reducing the costs), their possible impact on the reliability and accuracy of the results is still a question. As discussed in Chapter 4, it is important to assess the effects of application of WSNs on reliability of results in SHM applications. By having the two wired and wireless sensor networks installed on the specimen for simultaneous data collection, direct comparison of result is possible. This way the sensitivity of the proposed algorithm to the characteristics of the sensor can be also investigated.

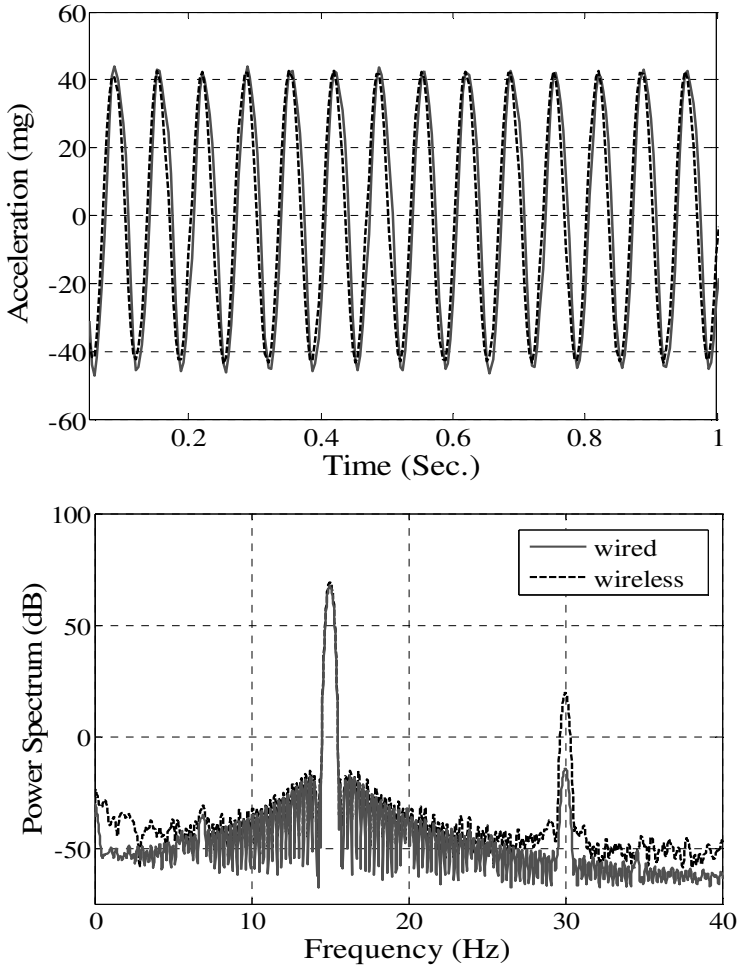

Figure 5.7. Comparison of wired versus wireless data in both the time and frequency domains

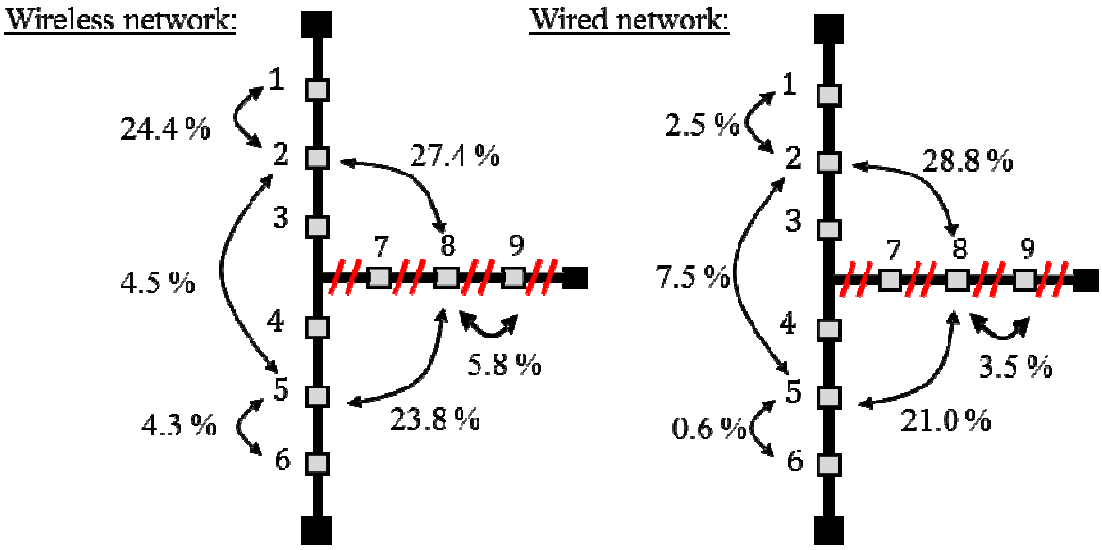

Figure 5.8. Comparison of relative change of coefficients between wireless and wired sensor data

During the tests data was collected using two previously mentioned sensor networks (wireless and wired) simultaneously. By collecting data at the same time, differences in results due to varied environmental noise between the two datasets are avoided. Therefore, any differences that appear between the two sets can be attributed to sensing network quality. Figure 5.7 shows a comparison of the data collected at node 9, the node with the largest recorded amplitude, in both the time and frequency domains. Both signals show the harmonic response due to the harmonic excitation clearly with low visible noise. Similarly, the frequency content of each sensor type is comparable; both show a dominant peak at the forcing frequency of 15 Hz. However the wireless data contains more noise at high frequencies as well as at very low frequencies.

Figure 5.8 also shows the relative change for selected nodal pairs of the WSN and wired datasets. The changes at α_{85}, α_{82}, and α_{52} of the WSN are comparable to the

changes expected from the wired results. The change at α_{89} from the WSN is a bit larger than that of the wired, but still on par with other nodal pairs of its type (beam-beam within damage). On the other hand, a notable inconsistency is seen in two of the column-column nodal pairs, α_{12} and α_{56}. The WSN shows significantly larger changes, almost 10 times larger than those seen in the wired results. This drastic variation can be explained by the EA and γ values of these two coefficients having significantly lower accuracies (less than 0.9) compared to the other four WSN values and the wired values. Lower accuracy correlates to lower reliability. Consequently, these coefficients would not be considered as trusted damage indicators.

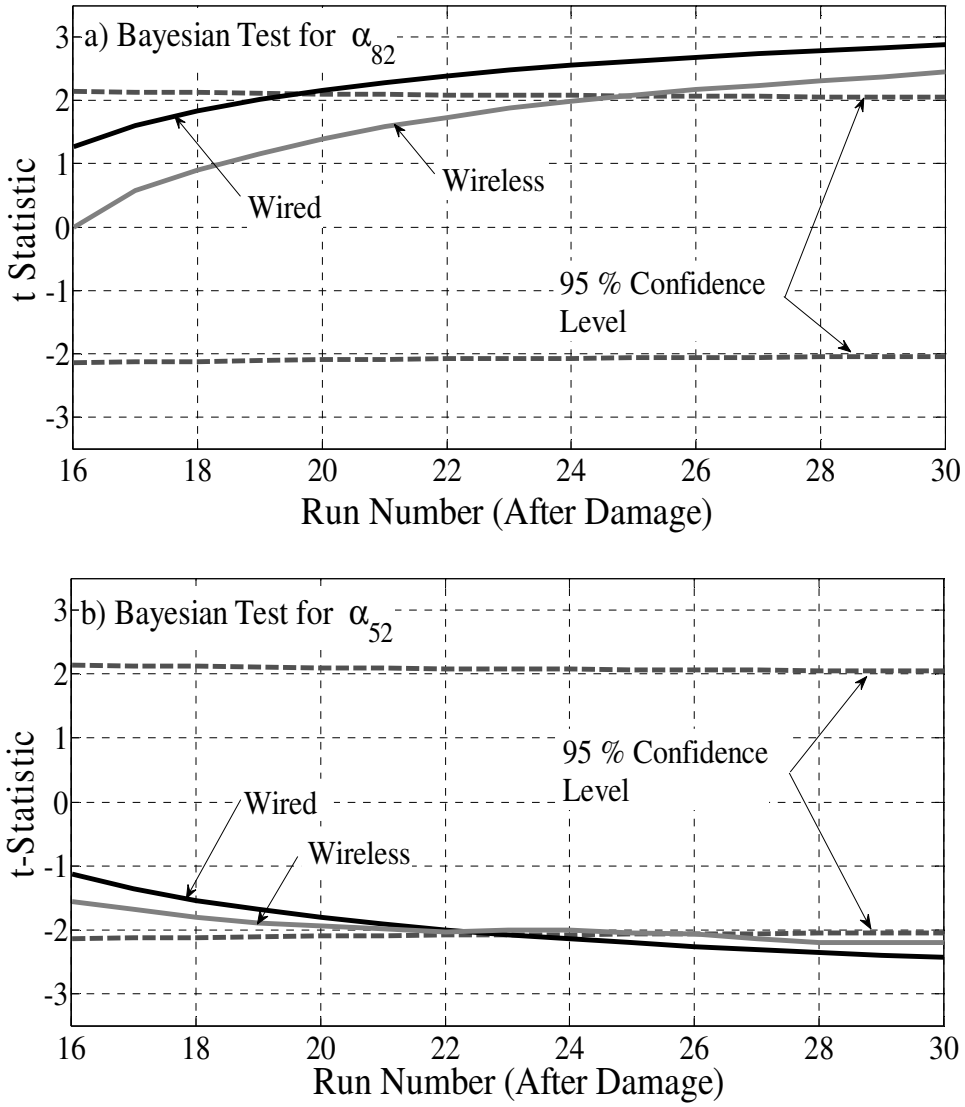

Figure 5.9. Comparison of Bayesian Testing Results, wired vs. wireless networks

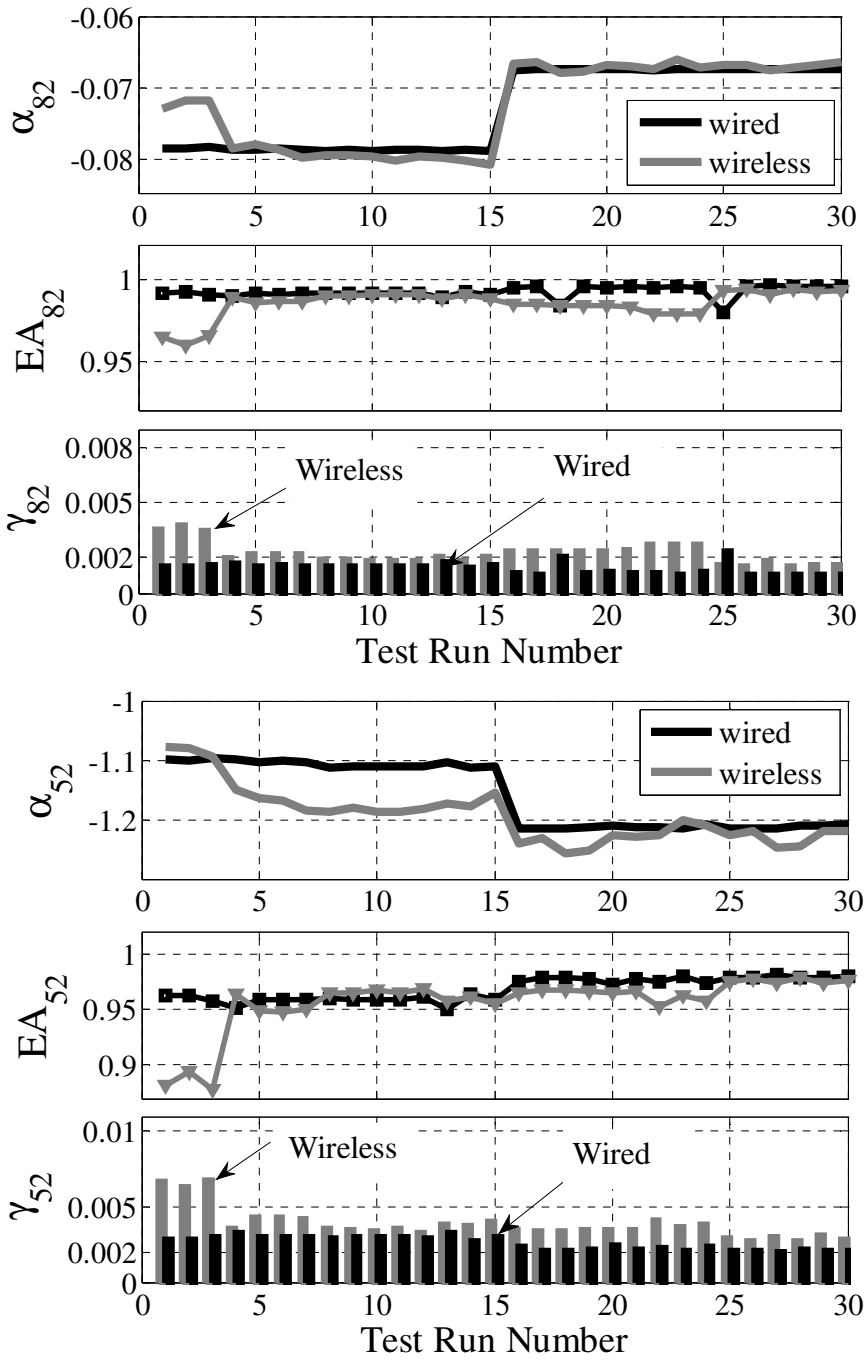

Figure 5.10. Comparison of influence coefficient changes, evaluation accuracies and estimation error for two pair-wise nodes (8-2 and 5-2), wired vs. wireless networks

A further verification of the wireless sensor network is obtained via inspection of the hypothesis testing results. The corresponding result for pair-wise coefficient 8-2 and 5-2 is presented in Figure 5.9. The first observation from these plots is that the wired sensor system is the first system that identifies the occurrence of damage. This is reasonable based on the higher accuracy associated with wired system compared with this particular WSN in all the results. Figure 5.10 shows a direct comparison of influence coefficients α_{82} and α_{52} and their corresponding evaluation accuracy and estimation errors. While both sensor networks reflect the change in the influence coefficients (i.e. indicate the damage), the accuracy of wired sensor results is higher. The performance of wireless sensors, however, is still acceptable since it does detect the damage with 95% confidence level, according to the hypothesis tests, even though this is detected after its detection by the wired system. Based on the presented comparison points it can be seen that the WSN, while exhibiting higher noise than the wired network, is still effective in localizing the onset of damage. This higher noise is a worthwhile tradeoff when considering the significant difference in the cost and implementation difficulties between the two networks.

5.8. Large-scale Experimental Prototype for Validation of the Algorithm

The model of the previous applications has idealized the damage as the beam is replaced with a member of known characteristics to simulate damage. Also, the entire beam section, designed to mimic the portion of the beam closest to the connection, has uniform damage, which is unlikely to occur in a real structure. Therefore, there is a need

to verify this method for full-scale structures exhibiting more realistic damage scenarios. Moreover, the performance of this algorithm is validated through the use of acceleration response and it is important to verify the use of other commonly used and affordable sensor types, in this case strain gauges, as well. In this section, the performance of the damage detection algorithm is evaluated for a large-scale steel moment connection, constructed and tested at the Advanced Technology for Large Structural Systems (ATLSS) Center at Lehigh University. The testbed structure was designed for use in an earthquake-prone structure and was tested for validation and performance evaluation.

Large-Scale Implementation - Test Setup

A new design of moment-resistant beam-column connection was developed by engineers at a design corporation for implementation in large-scale building structures to resist seismic loads. Because the designed connection was to be implemented in an important building structure in an earthquake prone area (a hospital in California), it is subject to the seismic qualification requirements as set forth by the California Building Code (CBC). Therefore, the sample specimens were tested under increasing cyclic loads at the ATLSS Center at Lehigh University for design verification and performance evaluation.

According to these requirements, the specimen must sustain at least two full cycles of an inelastic drift angle of 0.03 radians and at least two full cycles of an inter-story drift angle of 0.04 or more radians without failure. Progressive drift sequences were applied using parallel hydraulic actuators at the end of the beam, with the columns fixed to the

strong wall and the strong floor. A view of the tested specimen is shown in Figure 5.11 and the drift sequence is summarized in Table 5.4. The required displacement at the end of the beam is calculated from the inter-story drift angle, θ, the length of the beam, L_b, measured between the column centerline and the line of applied load's action.

The beam and column members of the subassembly were fabricated from ASTM A992 steel. The beam cross section was W40x294 and the column was W36x395. Plates of the connection also were fabricated from ASTM A572 Grade 50 steel. The specified minimum CVN toughness was 40 ft-lb at 70 °F.

Table 5.4. Drift sequence applied to test structure

Number of cycles	6	6	6	4	2	2	2	2
Angle of drift (radian)	0.00375	0.005	0.0075	0.01	0.015	0.02	0.03	0.045
Beam end displacement (mm)	16.57	22.10	33.15	44.20	66.29	88.39	132.59	198.88

Based on the testing specification, the specimen is subject to increasing cyclic loads until failure. The specimen is instrumented by a variety of sensors (strain gauges, displacement sensors, and rotation sensors) to capture the behavior of the connection throughout the loading. The global behavior of the subassembly is assessed by evaluating the applied load versus beam tip displacement relationship. Figure 5.12 shows the applied load against the beam end displacement. The total displacement at the end of the beam is formed resulting from various action-deformations such as: flexural deformation of the column, shear deformation of the panel zone, shear deformation of the side plates, flexural deformation of the side plate, deformation of the beam at the end of the

connection, and flexural deformation of the beam. Details about the contribution of each action-deformation and the resulted behavior of the connection can be found in Hodgson *et al*, 2010.

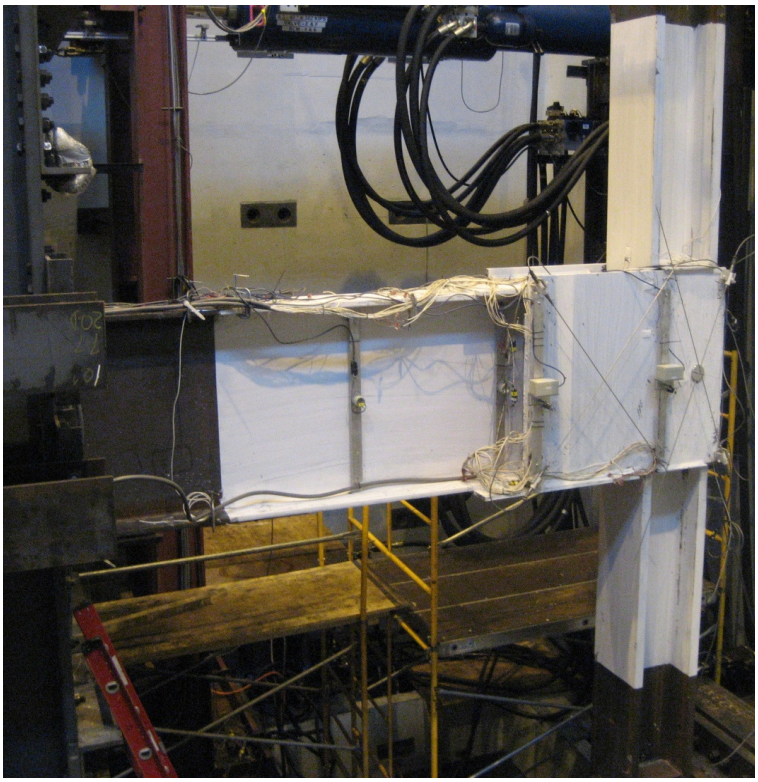

Figure 5.11. Test setup with strain gauge instrumentation plan

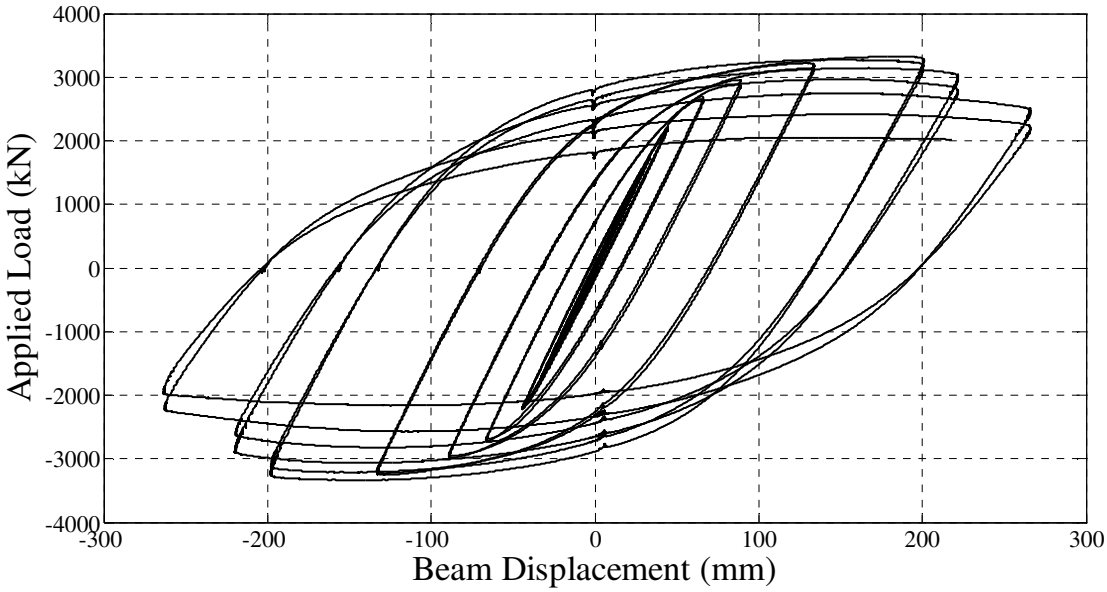

Figure 5.12. Applied load versus the beam end displacement

As the cyclic load is applied increasingly, the connection experiences a progressive damaging scenario, providing a suitable test-bed for examination of the damage detection algorithm. In addition to the densely instrumented sensors for structural performance evaluation, 5 strain gauge sensors are installed for the application of the damage detection algorithm and their location are shown in Figure 5.13. As can be seen in this figure, gauges 1 and 2 are installed at third points on the top flange of the beam, gauge 3 directly below gauge 1 on the bottom flange of the beam, and gauges 4 and 5 on the outside flange at the midpoint of each column. This configuration was designed considering an affordable and practical instrumentation for real-life structural systems. Having 5 sensors distributed around the connection provide effective information while does not cause data overwhelming.

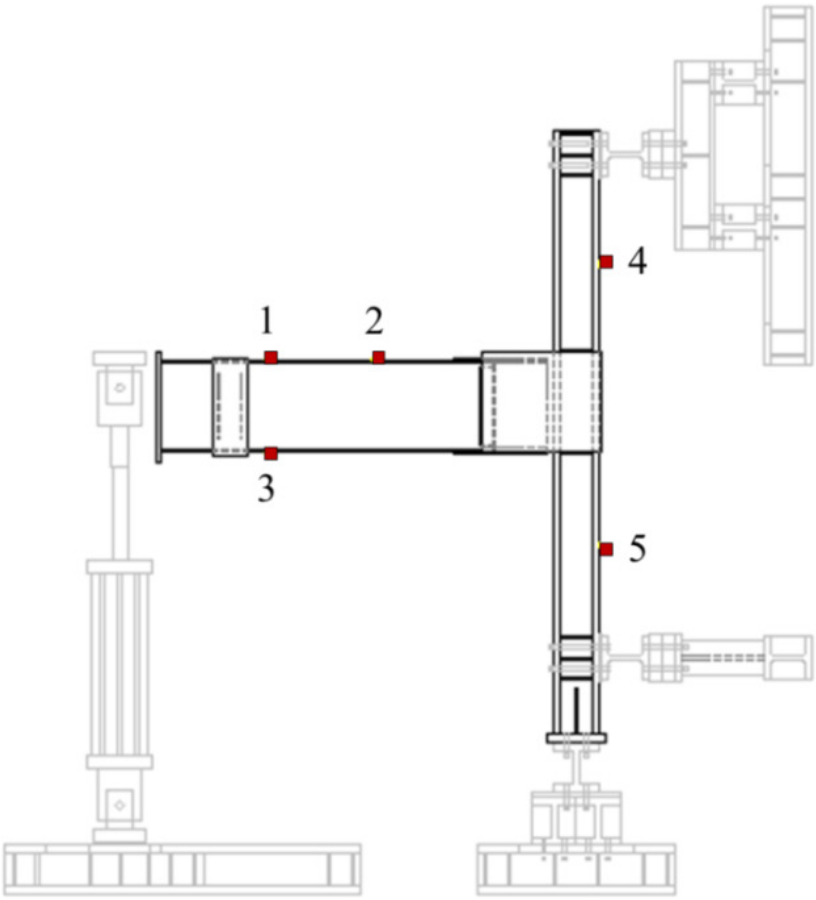

Figure 5.13. The layout of sensor for use in damage detection algorithm

Damage Progression

During the pseudo-static cyclic loading test, as the targeted drift angle increased, connection experienced different damages, ranged from slight yielding in some sections to deep fractures and failure. Inspection of the connection during the loading cycles by means of full monitoring equipment allowed documenting the progression and location of damage (the specimen was whitewashed in order to make yielding visible and help in illustration of damages). Accordingly, damages are classified to 10 damage states (from 0 to 9), where state 0 indicates intact structure and state 9 indicates complete failure of the

connection. The condition of the connection in different damage states are summarized in Table 5.5. Each set of drift cycles is designated with a respective damage classification. The progression of visible damage is also shown in Figure 5.14 beginning with damage class 4. It should be noted that the connections performance was satisfactory as it met the requirements of CBC and AISC 7 for seismic design. Performance of the beam-column connection is explained in depth in Hodgson et al, 2010.

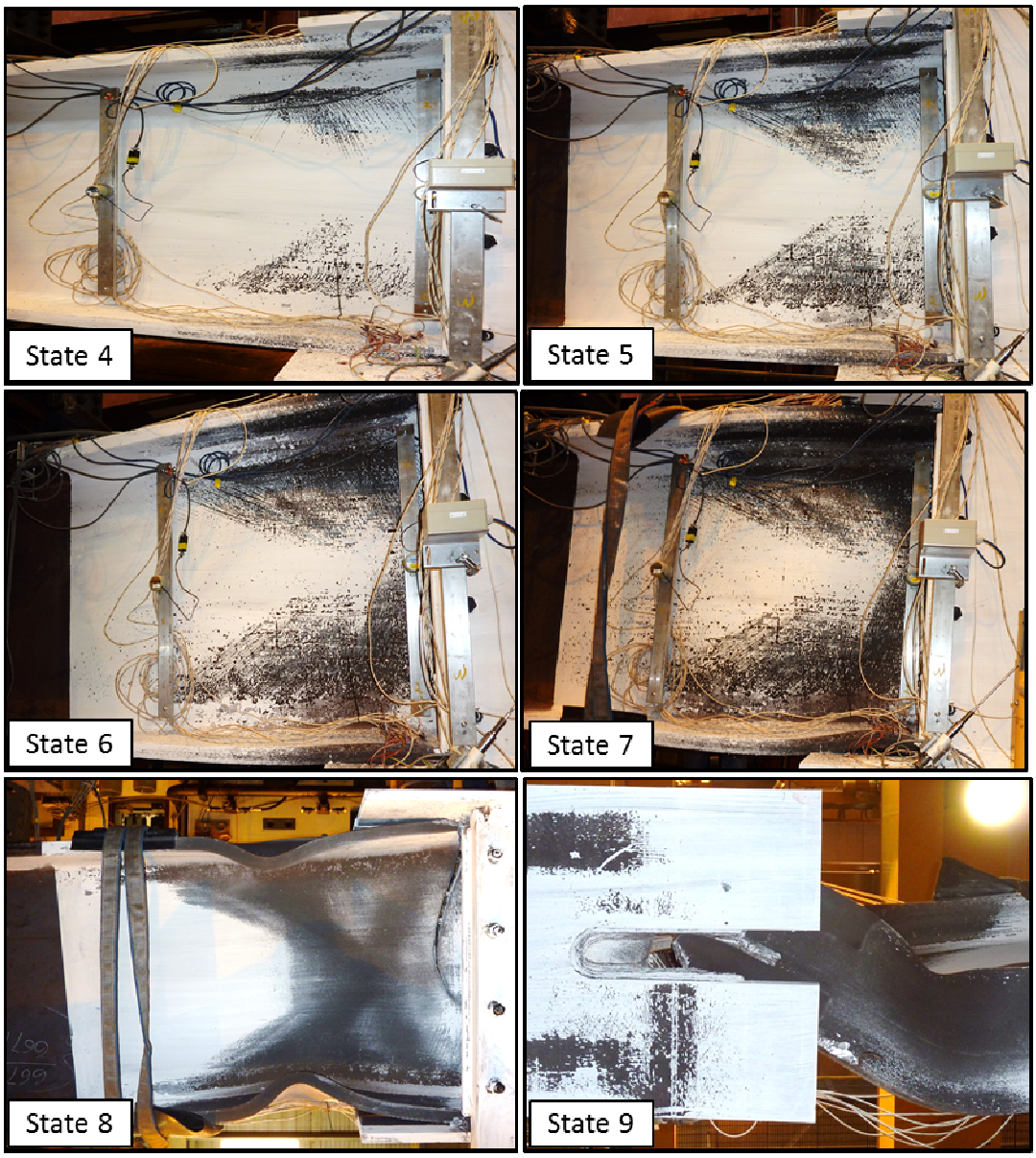

Figure 5.14. Different states of damage

Table 5.5. Observed damages during different angle drifts

Damage State	Angle of Drift (radians)	Damage Observations
0	0.00375 & 0.005	None
1	0.0075	Onset of yielding under bottom of cover plate
2	0.01	Some slight yielding on the beam flange (extreme fiber) / More yielding on the bottom cover plate
3	0.015	Yielding in the web about 1/5 of beam depth / More yielding on the bottom cover plate / Yielding in the through-thickness of beam flange / Yielding in the top and bottom of beam flange
4	0.02	Web yielding of beam increased to 1/3 beam depth / More yielding on the bottom cover plate / More yielding on the beam flanges (top and bottom of both) / Small crack (1/2in) in top cover plate to beam weld (bottom side) / 2 small crack (1in) in top cover plate-to-beam weld
5	0.03	Extremely yielding in the bottom cover plate / Considerable yielding in beam bottom flange / Web yielding more than 1/3 beam depth / Top cover plate separated from beam / Crack of top cover plate-to-beam weld (bottom side) opened up to 2in / Cracks of top and bottom cover plate-to-beam weld (top side at cut-out) opened more than 2.5in
6	0.045	Web start to buckle / Top flange start to buckle / Bottom cover plate separated from the beam / Plastic hinge completely formed / Bottom cover plate-to-beam weld crack propagated / Bottom flange started to buckle (at the end of cycle) / Web buckled at lower depth of beam / Small crack in side plate-to-column weld (left side)
7	0.05	Top flange buckling increased / Web buckling increased / Bottom flange buckling increased / Bottom web buckling increased / Crack in cover plate-to-beam weld stopped where the beam-to-side plate weld starts
8	0.06	Top cover plate-to-beam weld crack propagated to the base metal (beam flange) about 1/4in
9	0.07	Fracture from the bottom flange propagated into the web more than half the depth of beam

Implementation and Validation - Pre-processing of Strain Data

Prior to processing the data through the algorithm, the strain responses were considered in comparison to one another as well as versus time. Figure 5.15 shows the time histories of the strain responses and the applied load. It should be noted that, at the beginning of this plot, the cycles within the data are relatively uniform, but become less uniform as the testing continues, along with the increase of damage. Also, it can be seen that there are intermittent flat portions of the strain data, corresponding to a constantly held load at both the peaks and valleys of each load cycle.

To examine the linearity of the strain response, they are plotted versus one another. Figure 5.16-a presents an example of a strain versus strain plot for the two gauges on the column, while Figure 5.16-b shows a strain versus strain plot for two of the gauges on the beam. Figure 5.16-a shows a case in which the relationship between the two responses remains mostly linear throughout all cycles with small changes in slope over time whereas Figure 5.16-b shows the result of excessive yielding. A structure exhibits linear-elastic behavior prior to a damaging event, experiences nonlinear behavior during an extreme event, and then returns to an altered linear-elastic state following the damaging event. It is clear that using the entirety of the data set produces results with high nonlinearity and error. Therefore, portions of the data which best exhibited a linear relationship are used in implementation of the algorithm (note that the algorithm is based on linearity of the system). For this purpose, the responses corresponding to loads within 200 kips are separated from the rest of the data (strain-strain and load-strain relationships

in these portions are linear). This cutoff is chosen because 200 kips is the maximum load for the first drift in which the structure remained undamaged and purely linear-elastic. This ensures that only strains from before and after the damaging events are used.

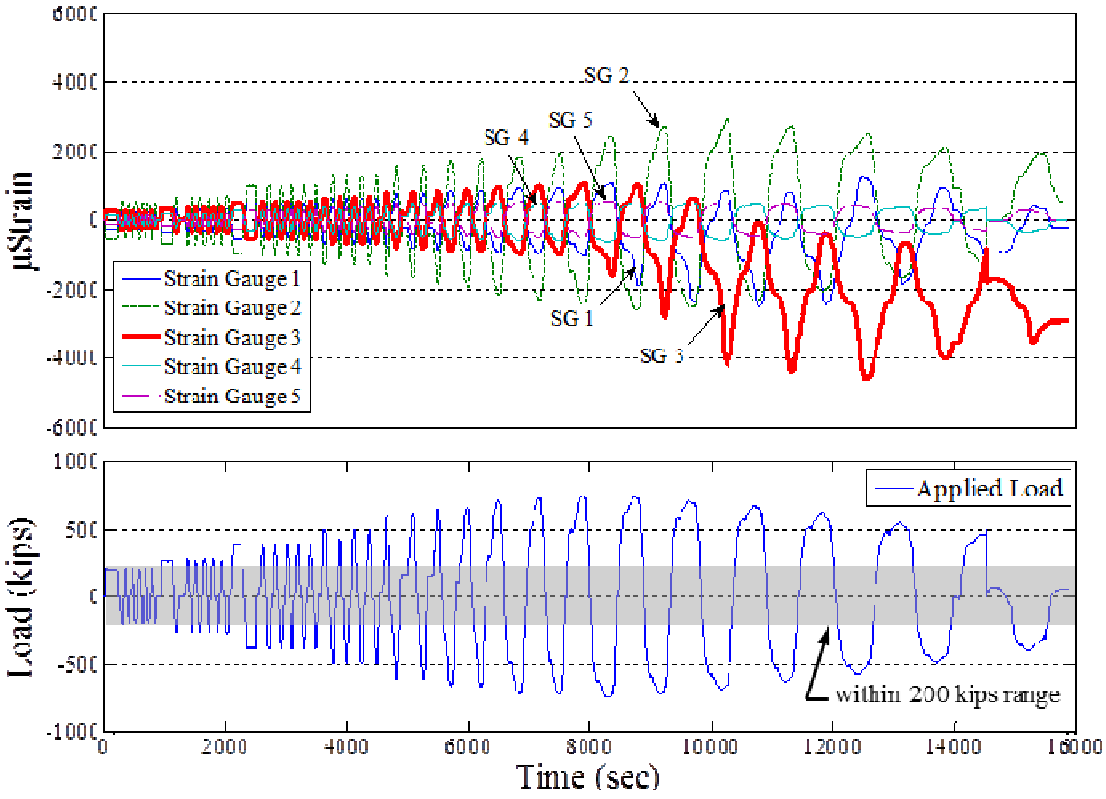

Figure 5.15. Strain response and applied load time histories

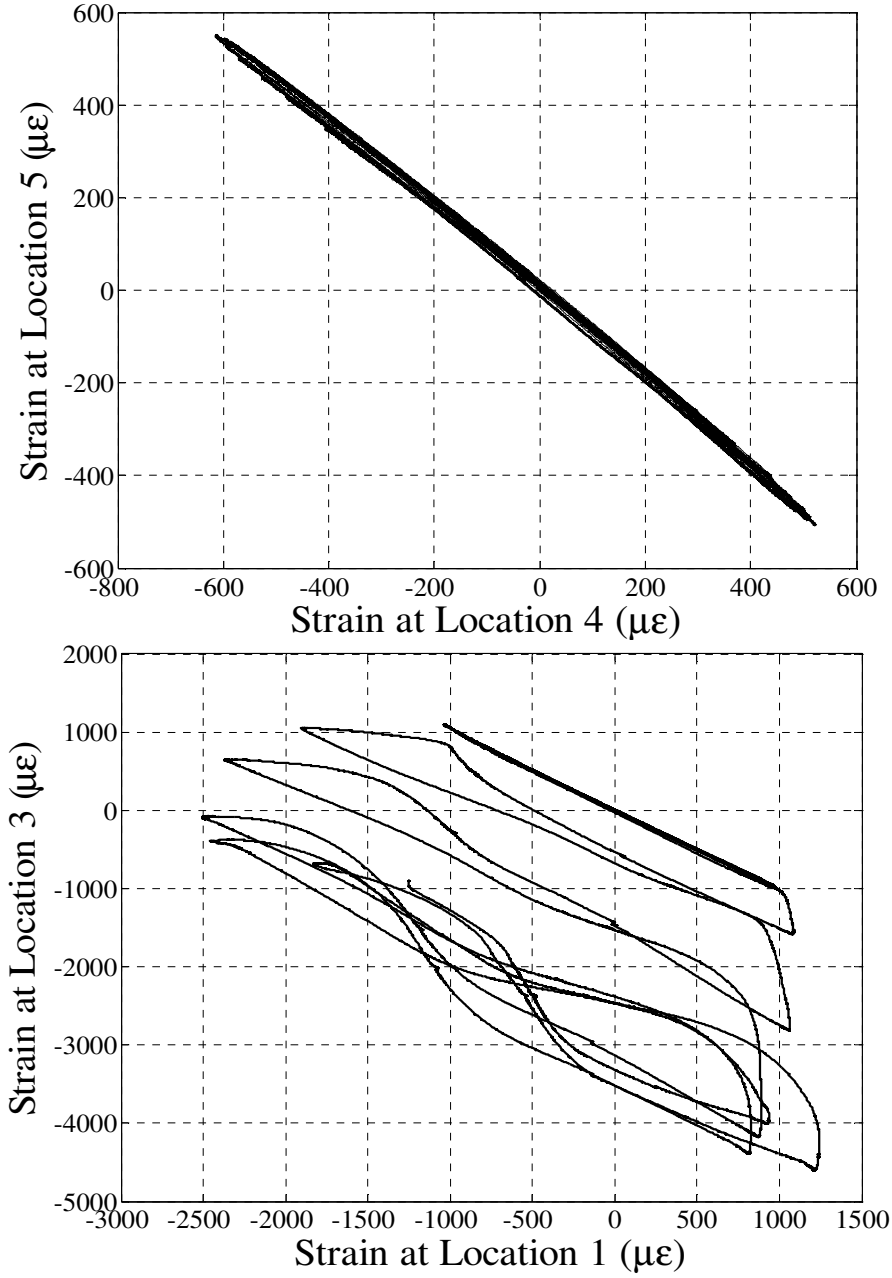

Figure 5.16. Strain response against one another: (a) location 4 vs. 5 and (b) location 1 versus. Location 3

Considering each loading and unloading portions of the recorded responses (when loads are within 200 kips) as a separated monitoring events, total of 135 time-windows are available. During the sequence of time-windows, while the loading range is constant, the structure experiences different damages as stated in Table 5.5. The influence coefficients corresponding to each of time-windows are computed for pair-wise nodes. Figure 5.17 shows the influence coefficient corresponding to nodes 2 (on the beam) and 4 (on the column). In this figure, different damage states are shown along the influence coefficients to illustrate the sensitivity of this damage indicator to the health/damage state of the beam-column connection. As Figure 5.17 shows, due to progression of damage, the influence coefficients start increasing variation above and below the baseline value. This non-monotonic change in their values is due to non-symmetric damaging events (e.g. yielding of either top or bottom and fracture in one side of the connection) and different behaviors under downward and upward, loading and unloading. For example, if there is a crack in the top of the beam, when the beam is loaded downward, this crack will open further showing more damage. However, when the beam is loaded upward, this same crack will likely close and the structure will see less asymmetry. To further investigate the variation of influence coefficients due to the progression of damage, the loading and unloading sections are considered separately and the changes percentages in the coefficients are inspected for each. Figure 5.18 shows the influence coefficient between nodes 2 and 4 in different loading scenarios: upward loading, upward unloading, downward loading, and downward unloading.

Figure 5.17 and 5.18 show that the migration of influence coefficients from the baseline becomes noticeable as soon as the damage state 2, where some slight yielding on the beam flange (extreme fiber) and on the bottom cover plate is observed. These damages have happened due to loadings and achieving 0.01 radian drift angle in the prior step. As the yielding propagates in the other locations like web and flanges of the beam (damage state 3), the variation of influence coefficients becomes even more noticeable. Figure 5.18 also represents the two parameters of evaluation accuracy and normalized estimation error. As explained earlier, these parameters reflect the reliability of the influence-coefficient in detecting changes in the structural behavior. It can be seen that in the least accurate portion of the data, the value of evaluation accuracy is still less than 0.01 and the normalized estimation error is beyond 0.95.

To correlate the different states of the damage to the changes in the influence coefficients in different locations, one loading scenario is selected and the changes are tracked throughout the damage progression. The first loading condition to be considered is the downward loading (DL) in which the free end of the beam is being pushed downward. The percent change values for each DL damage class compared to the baseline DL values are shown for select node pairs in Table 5.6. It can be seen that in damage state 1 all of the percent change values are less than 1%. These negligible changes are consistent with the mild yielding observed on the bottom cover plate and the beam flange.

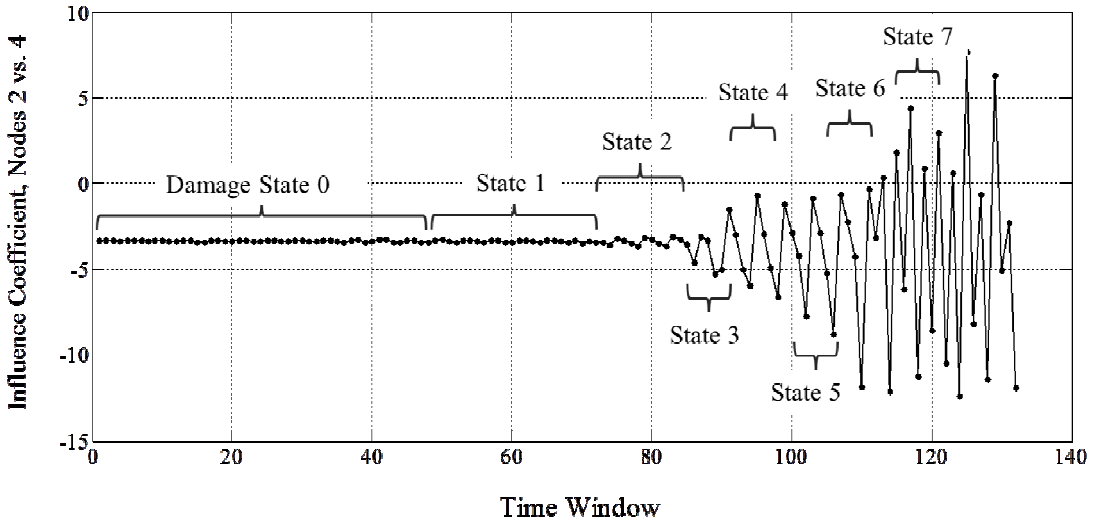

Figure 5.17. Variation of influence coefficient between nodes 2 and 4 in different time windows

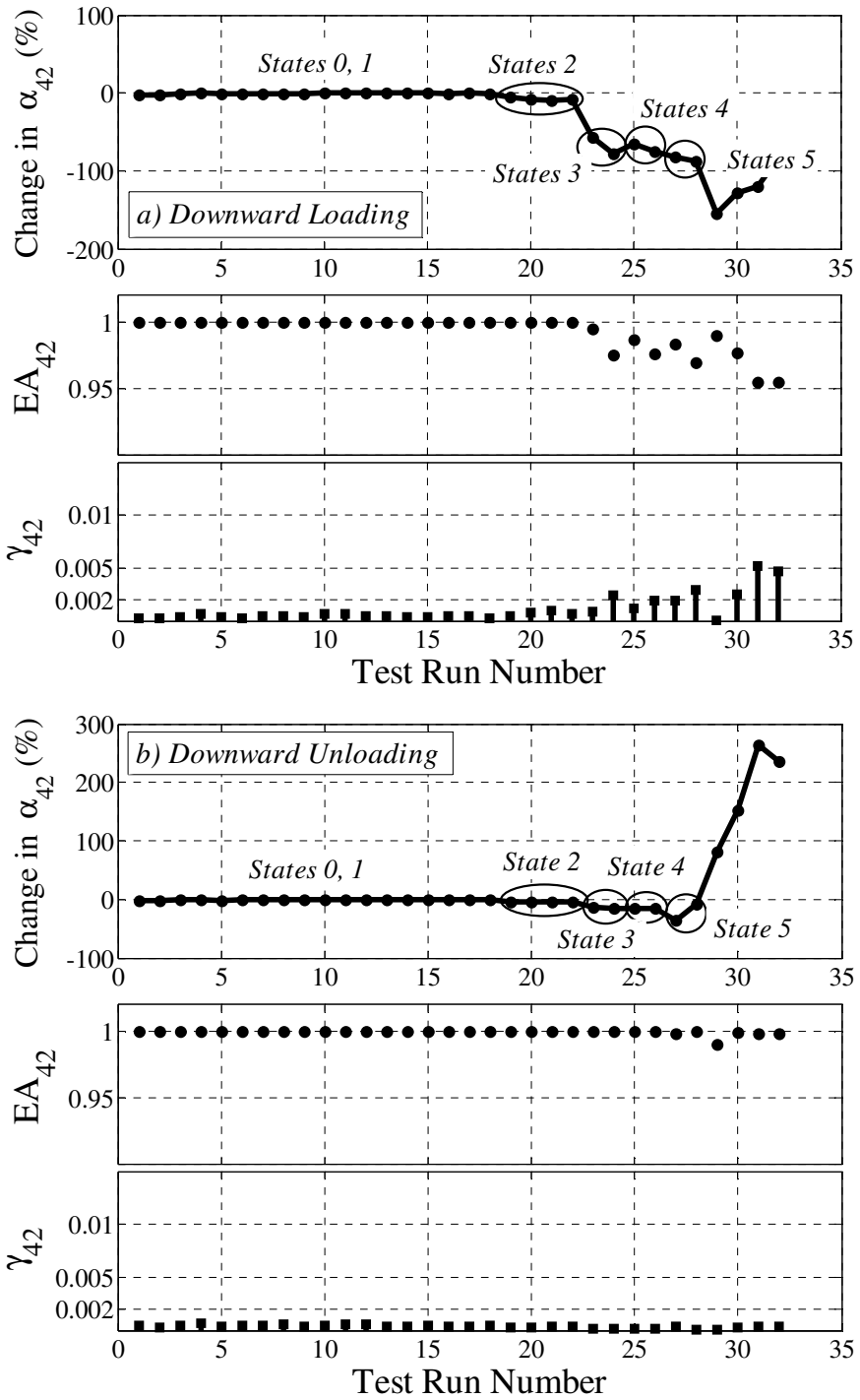

Figure 5.18. Variation of influence coefficient between nodes 2 and 4 for different loading scenarios

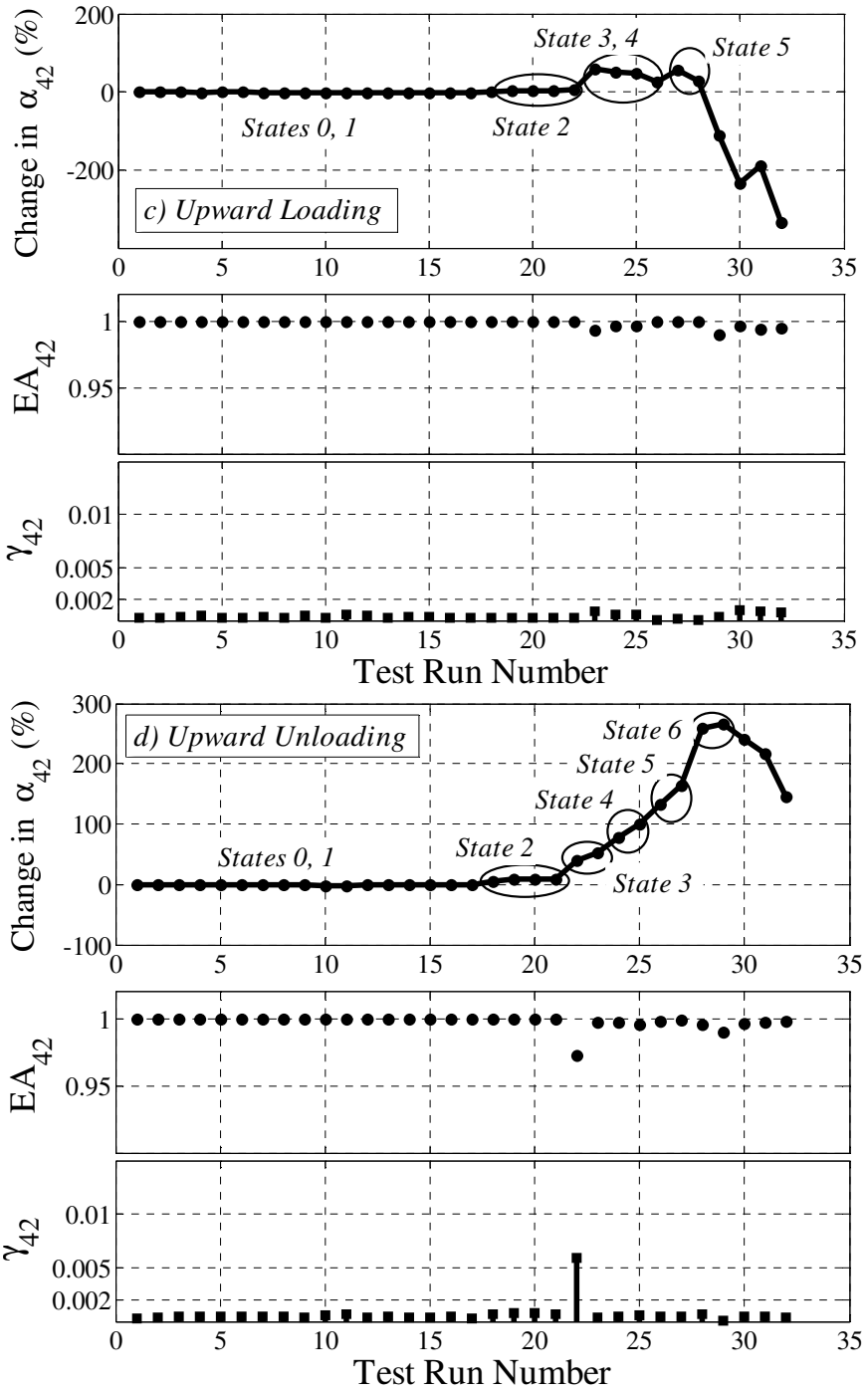

Figure 5.18 (Cont'd). Variation of influence coefficient between nodes 2 and 4 for different loading scenarios

Table 5.6. Change percentages during different damage states

	Influence coefficient	Change Percentage (%)						
		Damage state 1	Damage state 2	Damage state 3	Damage state 4	Damage state 5	Damage state 6	Damage state 7
Two sides of damage	4 and 2	0.43	7.15	88.01	88.46	155.21	199.47	135.15
	5 and 2	0.33	5.37	66.01	66.34	116.41	149.60	101.37
One side of damage	1 and 3	0.70	1.67	5.87	1.04	2.35	106.70	132.41
	1 and 2	0.44	1.04	28.35	21.38	23.26	89.19	113.00
	4 and 5	0.18	0.42	5.84	41.72	44.17	71.68	88.54

In the damage state 2 slight increases in change is observed. When yielding is seen in the bottom cover plate, in the top and bottom beam flanges, and at $1/5^{th}$ locations of the web in the vicinity of the connection, more notable changes (5% - 7%) are seen in $\alpha_{2\text{-}4}$ and $\alpha_{2\text{-}5}$, of which have nodes located on either sides of the damage, compared to $\alpha_{1\text{-}3}$ and $\alpha_{1\text{-}2}$ of which have nodes located on one side of the damage. However, the change rates in coefficients of the pairs with nodes on opposing sides of damage ($\alpha_{2\text{-}4}$ and $\alpha_{2\text{-}5}$) are somewhat different. This asymmetry in coefficients is likely due to the asymmetry seen in the damage, with more yielding on one side of the beam.

The damage state 3 presents significant offset in percent changes. During the corresponding drift (0.015 rad), yielding occurred in different locations: beam web, cover plate, and through the thickness and bottom and top of the beam flange. In this damage state, the largest changes are that of $\alpha_{2\text{-}4}$, $\alpha_{2\text{-}5}$ and then $\alpha_{1\text{-}2}$. As nodes on the column are isolated from these damages, the associated influence coefficients experience very slight

percentage changes. The same scenario is applicable for the coefficient between node 1 and 3, as they are distant from the location of the damage.

Another significant offset happens at the damage state 5 when damage is incurred with a considerable beam flange and web yielding, extreme yielding of the bottom cover plate, and separation of the top cover plate from the beam. The largest changes are again seen in $\alpha_{2\text{-}4}$, $\alpha_{2\text{-}5}$ as these coefficients correspond to beam-column pairs with nodes on either side of damage due to the heavily concentrated beam damage.

During damage state 6 severe damages are incurred, including beam web buckling, top and bottom beam flange buckling, bottom cover plate separation from the beam, and the complete formation of a plastic hinge in the beam.

From the damage state 6 to the damage state 7, there is a decrease in the percent changes of coefficients $\alpha_{2\text{-}4}$, $\alpha_{2\text{-}5}$. The likely cause of this is the formation of the plastic hinge, which resulted in out-of-plane bending of the beam which changes the relationship between nodes. Despite the decrease in the change percentage, the noticeable percent changes are still concentrated at nodal pairs surrounding the observed beam damage. The damage observed in this state also consists of severe buckling of the beam flanges.

Based on the data corresponding to downward loading, the coefficients show decisive changes during the damage states 3 and 5. Similar trends are also observed through inspecting other loading scenarios. While the variation of influence coefficients from the baseline through different states represents the existing damage with good accuracy, to

make comparison and have a confident conclusion about existence and location of the damage, a statistical tool is still needed. This is addressed through the use of Exponential Weighted Moving Average (EWMA) process and Cumulative Sum (CUSUM) process for change point detection.

Statistical Change Detection

A statistics which can be used for detection of changes is Exponential Weighted Moving Average (EWMA). This approach is suitable in change detection when here is an online observation of data (i.e. change is to be detected through the as the data is collected). EMWA is an easy to implement control scheme for detecting small shifts in the mean of a process. This is based on the statistic

$$Z_i = \lambda\alpha_i + (1-\lambda)Z_{i-1} \tag{5.12}$$

where Z_i is the EWMA at time index i and λ is the controlling parameter and is selected to be between 0 to 1. This control scheme is always accompanied with upper and lower control limits (UCL and LCL) which are defined as multiples of the standard deviation of the control statistic:

$$UCL = L.\sigma_z \tag{5.13}$$

where L is another parameter of the EWMA and is usually chosen to be around 3 (Amiri and Alahyari, 2011). The standard deviation of the control statistic can be computed from:

$$\sigma_z^2 = [\{1-(1-\lambda)^{2i}\}.\lambda/(2-\lambda)]\sigma_y^2 \tag{5.14}$$

UCL and LCL are used as boundaries for control statistic, Z_i; as the value of Z_i crossed the limits, the change in the observed data can be concluded.

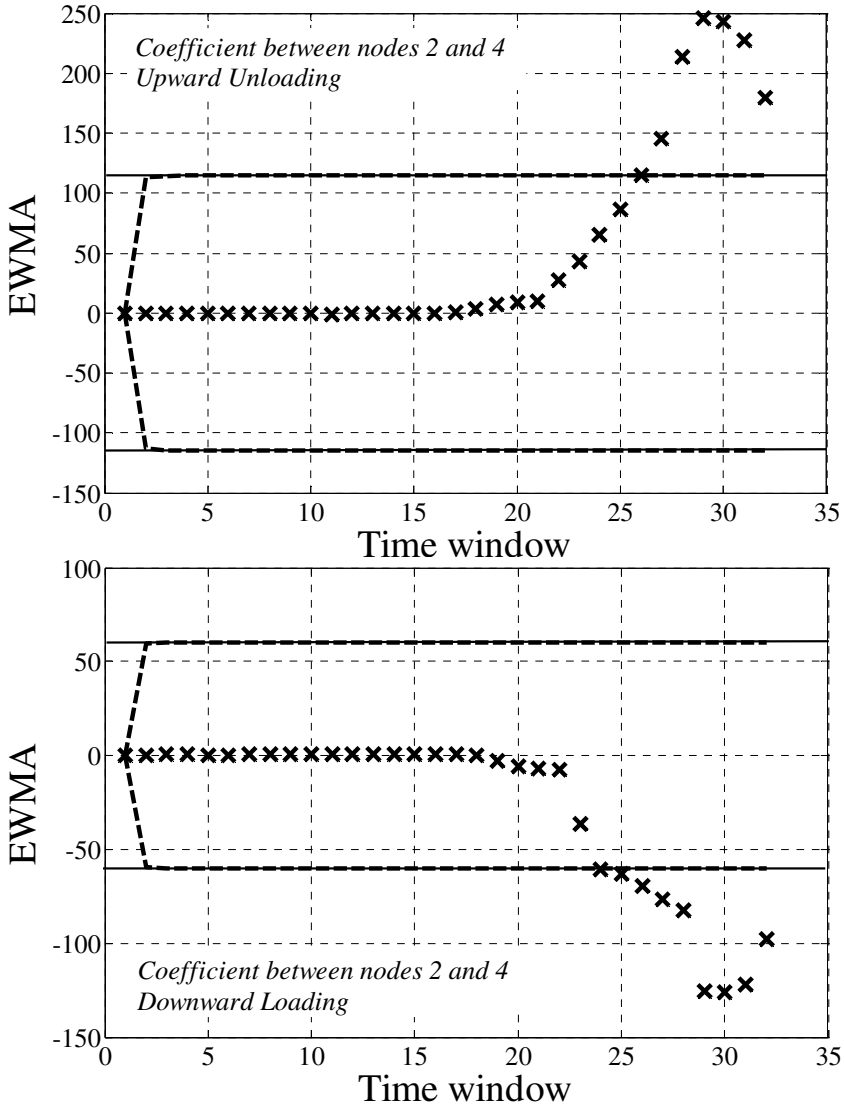

Figure 5.19. Exponentially Weighted Moving Average for detecting the change point during the observations (correlation function between nodes 4 and 2)

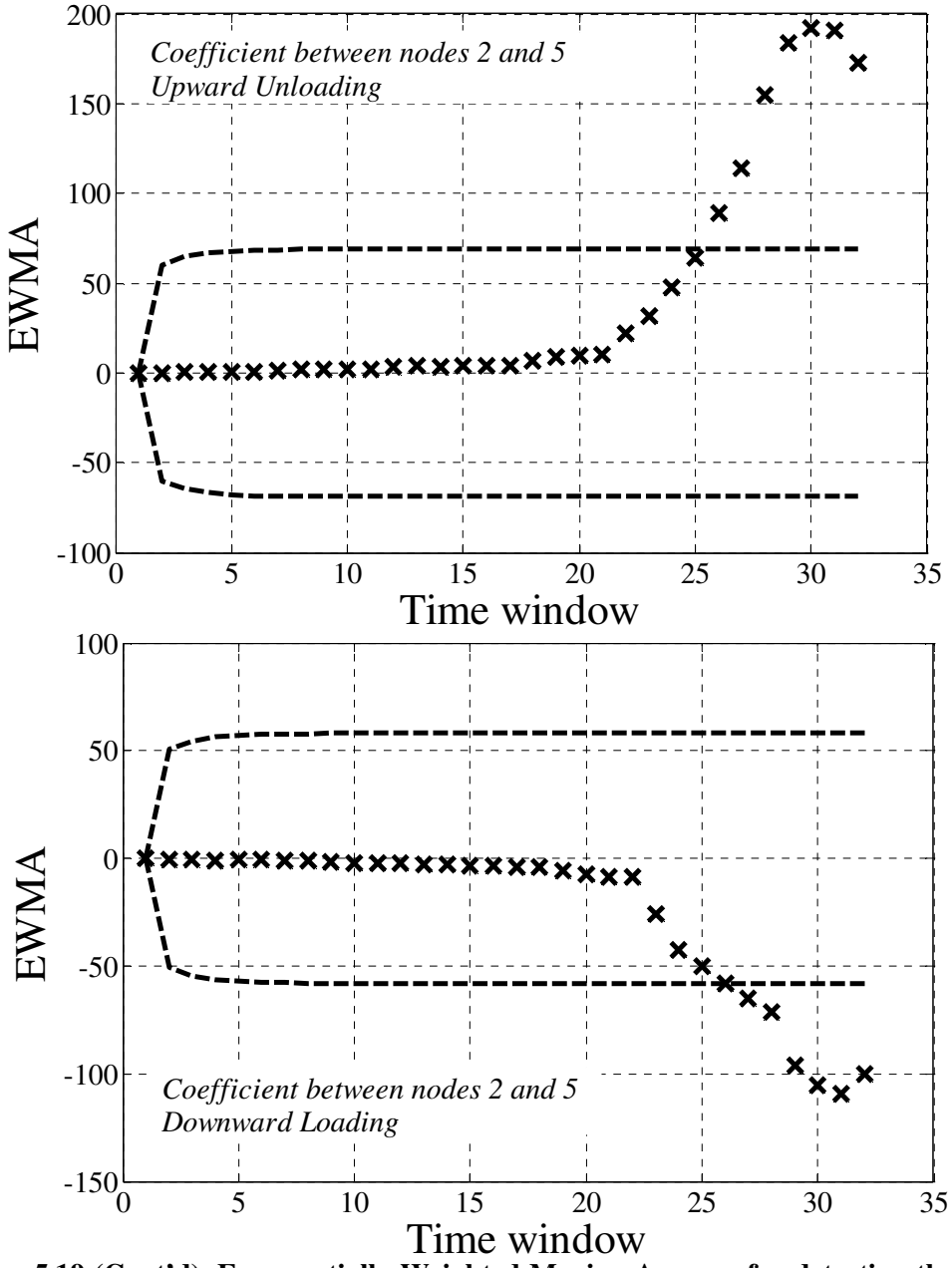

Figure 5.19 (Cont'd). Exponentially Weighted Moving Average for detecting the change point during the observations (correlation function between nodes 5 and 2)

Figure 5.19 shows the EWMA for two sample pairs of nodes (2-4 and 2-5) in two different loading scenarios of downward loading and upward unloading. For extracting the EWMAs for the observed data in this experiment L is assumed to be 3 and λ is

assumed to be 0.6, to follow the literature (Amiri and Alahyari, 2011). It is observed that the results of EWMA from the data of this experiment are not very sensitive to the value of λ, if it is selected to be between 0.3 and 0.6. This statistic highlights the change at around 26th time-window which corresponds to damage state 4. This state represents a relatively intense damage in the connection as it corresponds to web yielding of beam increased to 1/3 beam depth, yielding on the bottom cover plate and the beam flanges (top and bottom of both), and some small crack (1/2in) in top cover plate. One may argue that this state of damage is intense enough not to need statistical framework to realize it. However, when generalizing the approach and using it as an automated algorithm, having a criterion for decision making is essential.

To have a more responsive statistics, a more sensitive process can be selected. Another approach for detecting the change point over a vector of observed data is Cumulative Sum (CUSUM) chart. CUSUM is constructed by calculating and plotting a cumulative sum based on the data and is an easy approach for implementation. Let $[X_1, X_2, \dots, X_n]$ be the influence coefficients, the CUSUM, $[S_0, S_1, \dots, S_n]$, can be calculated as:

$$S_0=0 \tag{5.15}$$

$$S_i=S_{i-1} + (X_i-\bar{X}) \tag{5.16}$$

The CUSUM is the sums of the differences between the values and the average. It should start at zero and eventually end up to zero. A segment of the CUSUM chart with an upward slope indicates a period where the values tend to be above the overall average.

Similarly, a segment with a downward slope indicates a period of time when the values tend to be lower than the average. A change in the slope of the chart indicates a change point in the data. The cumulative sum indicator can be used to tell at which point there is a change. This change point would occur where the magnitude of the CUSUM chart is furthest away from zero considering the chart begins and ends at zero. When using the CUSUM chart for the damage detection in the beam-column connection, there should be one change point: the change from the current state to a point corresponding to a significant damage.

Figure 5.21 presents the CUSUM against the time-windows for two selected pairs of nodes (2-4 and 2-5) for two different loading scenarios of downward loading and upward unloading. As explained earlier, the detected change point in this algorithm is the point in which CUSUM is maximum or minimum (furthest away from zero). Figure 5.21 shows that the detected change point is around the 23^{rd} time-window which corresponds to transition of damage state 2 to damage state 3. It represents the transition from some slight yielding on the beam flange (extreme fiber) and the bottom cover plate to higher level of yielding in the web (about 1/5 of beam depth), the bottom of cover plate and yielding in the through-thickness of beam flange. As can be seen, CUSUM is more sensitive to the change and it identifies the damage state earlier than the EWMA.

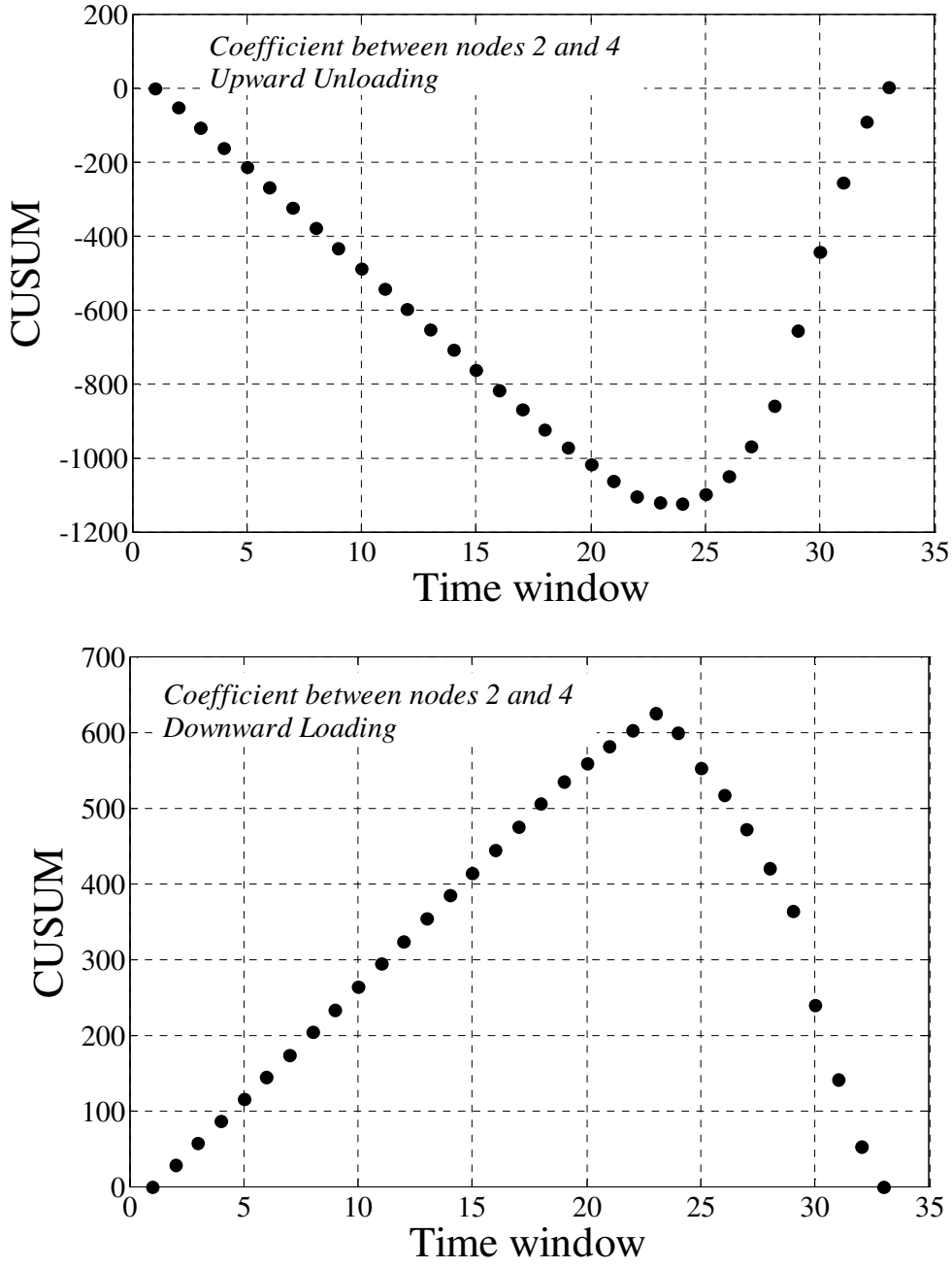

Figure 5.20. Cumulative Sum versus the time-window for detecting the change point in the observed correlation coefficients between points 4 and 2

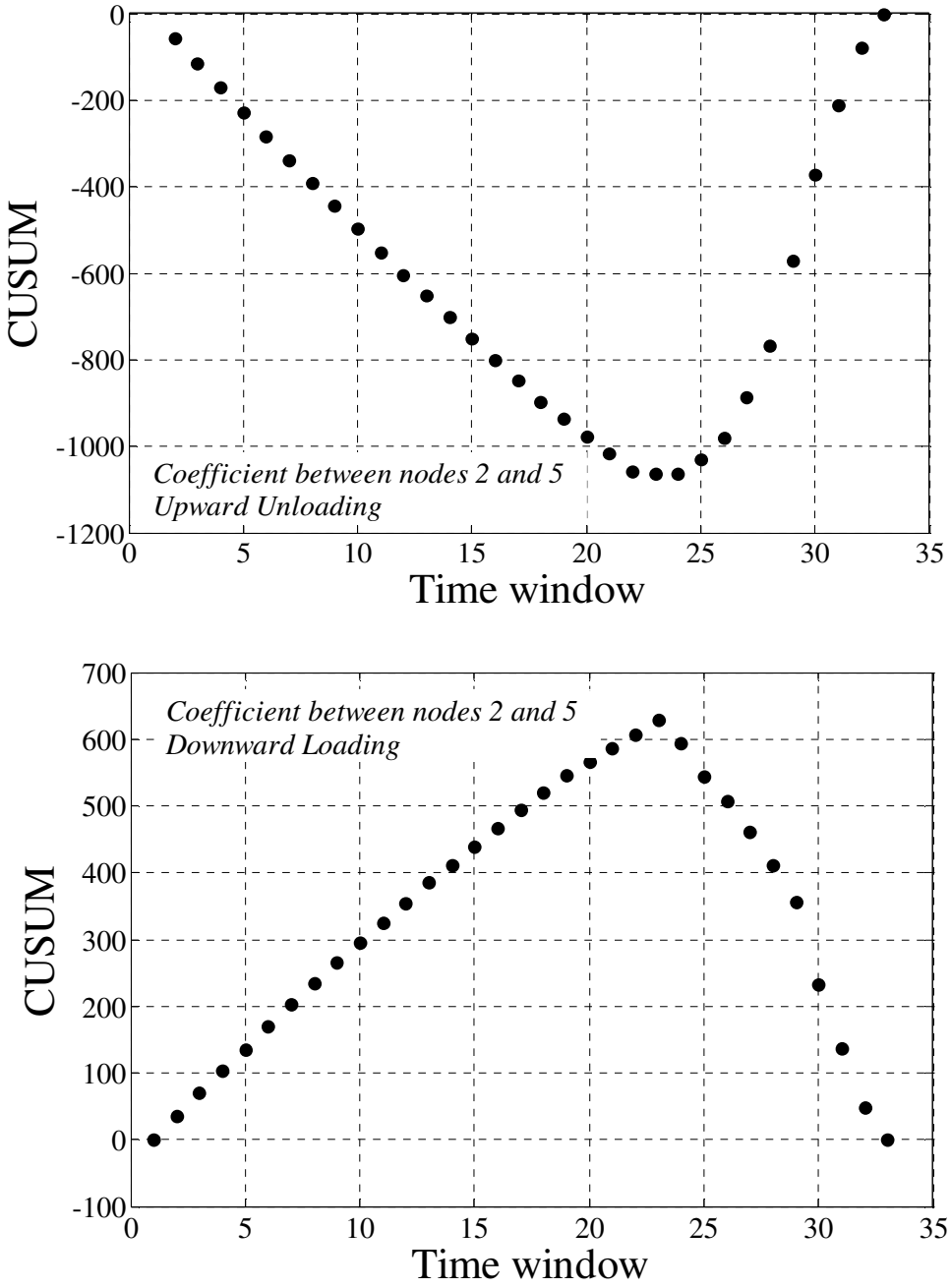

Figure 5.21 (Cont'd). Cumulative Sum versus the time-window for detecting the change point in the observed correlation coefficients between points 4 and 2

5.9. Summary of Damage Detection Algorithm and Validation

An influence-based damage detection algorithm (IDDA) is introduced in this chapter which is based on the regression of the structural response at different locations. The algorithm is integrated with accuracy indicators and statistical frameworks to enable evaluation of the significance of the damage as well as estimation of its location, when the damage is detected. To validate IDDA, it is implemented on an analytical and two experimental models and its performance is evaluated. It is illustrated that the selected damage indicators effectively reflect the structural damage which were simulated in the analytical and imposed to the experimental models. During the implementation of the algorithm on the first experimental model, two different networks of wired and wireless sensors were utilized. While validating the performance of IDDA, the damage detection resulted from data from each of the two sensor networks were compared and the sensitivity of the algorithm to the sensor characteristics was investigated. The result showed that both sensor networks are able to reflect the change in the influence coefficients and detect damage. However, the accuracy of the wired sensor results was higher, as the noise level of the utilized sensors was lower. The performance of the wireless sensor network, however, was acceptable as it detected the damage with 95% confidence level, even though it did later than the wired system.

The second experimental model was a large-scale beam column connection which was tested under cyclic loading up to its failure. In this implementation, strain data collected from a set of 5 strain gauge sensors were used. The damage states were defined based on

the observed yielding of different elements of the beam-column connection, including beam's web and top and bottom flanges, the cover plates, and the column's flanges. The changes in the correlation coefficients were tracked and the point with significant change was identified through the use of two different statistics: EWMA and CUSUM. It is shown that the later approach is more sensitive and the detected point is in an earlier state of damage.

This chapter also presented evaluation of the performance of the introduced damage detection algorithm in presence of different measurement noise. The effect of sensor quality is evaluated by comparing the resulted quality metrics. Additionally the established statistical framework for detection of occurrence of damage is used to evaluate the performance of each measurement systems (wireless versus wired sensor networks). It is shown that the high quality data results in more accurate outcomes and the low quality data results in a delay in indicating damage.

Chapter 6

Field Deployment - Application of state of the art in measurement for vibration evaluation of a tall building

6. Application of state-of-the-art in measurement and data analysis techniques for vibration evaluation of a tall building

6.1. Introduction to the Field Deployment

Advancements in sensing and data acquisition technology have made monitoring of structures and infrastructure more affordable and, at the same time, more comprehensive. Examples of such advancements are application of wireless technology for communication, the utilization of fully automated systems for long-term monitoring, and the remote control of the sensing system over internet. While each of these technologies has been used in different structural health monitoring (SHM) projects in the recent years, inclusion of an all-in-one sensing system represents the state of the art in measurement techniques. This chapter presents the integration of all of above-mentioned advanced monitoring approaches in one sensing system for forensic quantification of an in-service tall building. The inclusive measurement and monitoring system along with advanced data analysis techniques enabled extraction of detailed information about dynamic characteristics of the building structure and development of reliable conclusions regarding its performance. It is shown that the performance of the investigated structural components is satisfactory in terms of strength demand. However, the level of vibration in some portions of the structure does not meet limits of human comfort. In addition, wind speed spectrum, acceleration response spectrum and the modes of lateral vibration are extracted to assist with evaluation of the structure's performance in terms of lateral vibration under the effects of wind speed fluctuation.

6.2. Vibration monitoring of structures

In the past few decades the philosophy of structural design has been complemented by including a focus on the in-service performance of structures. This change is rooted in the concept of performance-based design which is explained, in brief, as "practice of thinking and working in terms of ends rather than means" (Gibson, 1982). A fundamental step in this practice is the validation and verification of the resulted design against the objective performance. This step, in design of new structures, is usually achieved by the means of modelling and simulation. In existing structures, however, reliability is achieved through instrumentation, measurements, and assessment of the constructed structure. The goal of instrumentation and measurement goes beyond validation of design when there are concerns over the performance of a structure or when an evaluation is needed to develop maintenance strategies. Although the literature shows significant research efforts in the advancement of instrumentation techniques for evaluation of in-service structural systems (Lynch & Loh 2006; Wong, 2007), the existing applications still face practical difficulties in many cases. The mentioned difficulties usually result from either limited budget designated to instrumentation, or restrictions imposed by the operation of in-service structures (e.g., limited monitoring duration or limited access to structural elements). For example, instrumentation of Tsing Ma Bridge in Hong Kong (with more than 350 sensing channels) is one of the largest monitoring projects which has provided significant amount of information concerning the performance of the bridge (Ko & Ni, 2003). However, the instrumentation cost is reported to be approximately $8 million (Farrar, 2001) which is

prohibitively high. Celebi (2002) also presents a survey on the instrumentation and monitoring of building structures for seismic studies and estimates $4K per sensing channel (where $2K is allocated to labor and cabling) for monitoring of tall buildings which is not affordable for many building's owners and administrators.

Recent advancements in sensing technology have helped alleviate a lot of challenges in both the economical and practical aspects. For example, current structural monitoring techniques can utilize either the traditional wired sensor network or the relatively new wireless sensor network. In the study presented in this chapter, a combined wired and wireless sensor networks in applied in order to provide a cost- and performance-effective sensing and acquisition solution for SHM. Each sensor network has its advantages and disadvantages. For example, wireless sensors are less expensive, less labor-intensive, and more portable. However, wireless sensors are powered by finite-life batteries and also need line-of-sight for communication which limits the application in long-term monitoring of a building structure. The combination of both wired and wireless networks provided an opportunity to confirm the adequacy of each while producing the necessary short- and long-term data for the performance evaluation of an in-service 16-story building structure suffering from perceptible vibration in different directions. The monitoring system employed in this study includes a broad range of sensors, measuring acceleration, displacement, strain (from which stress can be directly calculated), wind speed and wind direction. Using the portability advantage of wireless sensors, vibrations response from various locations is obtained with minimal effort. Wired sensors, on the

other hand, are installed on fixed locations to perform automated long-term monitoring. The applicability of the sensing system is validated and its performance is demonstrated through evaluation of the measured data. Collecting effective and reliable data from the structure's response at various locations during different modes of excitation enables the extraction of fundamental dynamic characteristics of the building. The information is used in evaluating potential mitigation strategies for maintenance and serviceability of the building in its future operation.

The vibration issues under investigation in the study are those caused by wind and human-structure interaction. In this work, the structure is investigated on two fronts. The first is the vibration-induced demand (i.e., the stresses in critical elements of the structure) in comparison to the structural capacity of the building. This effort entails an assessment as to whether the demand could lead to potential structural failure in the building system. The second is the effect of the demands on the comfort of the occupants of the building. The effort results in an assessment of the vibration in the structure as compared to the acceptability limits (Murray, Allen & Ungar (1997) for vertical vibration and Irwin (1978) for lateral vibration).

6.3. Utilized Sensing System

The monitoring system is arranged to measure acceleration, displacement, strain, wind speed and wind direction. Utilizing a sensing system with different types of sensors and with high spatial and temporal sensing resolution assures that the response of the

instrumented structure is captured and therefore, a reliable evaluation of the structural performance can be achieved.

Wireless sensors are used because of the portability and ease of installation in various locations. Portability makes WSNs very effective tools when there are limitations in access to structural elements and in cases where data from a large number of different locations on the structure is required. These sensors are particularly beneficial for monitoring in-service structures since they eliminate the need for installing wires in an occupied facility and thus, the sensor network can be set up quickly and inexpensively.

The wireless sensor platform of the sensing system is Imote2 with an external antenna (Linderman et al, 2012). When necessary, the external antenna was connected through an extension cable and directed to a clear line-of-sight with the base station to enhance the wireless communication. Imote2 and its specifications are described in detail, in Chapter 2. The sensor board of the platform is SHM-A developed by Rice & Spencer (2009). The tri-axial LIS3L02AS4 (2005) Analog accelerometer manufactured by ST Microelectronics is used on SHM-A which is a low-cost, high-sensitivity Analog accelerometer with 50 μg/√Hz noise density. Figure 6.1 shows the hardware platform of Imote2 and SHM-A sensor board. Table 6.1 also summarized the specifications of Imote2 and SHM-A sensor board.

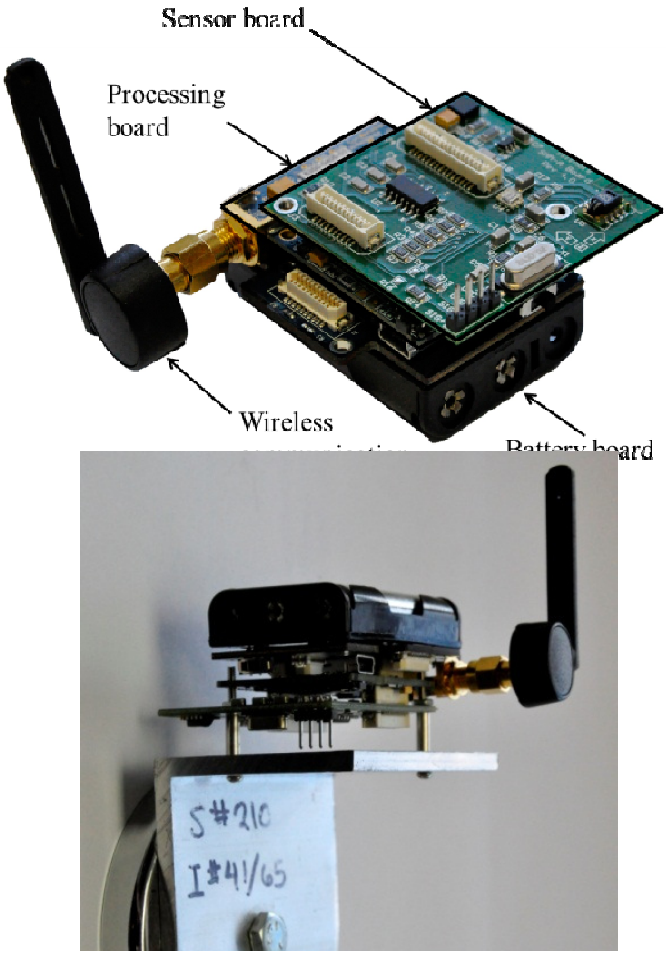

Figure 6.1. Imote2 wireless sensor platform with SHM-A sensor board

Table 6.1. Specifications of Imote2 and LIS3L02AS4

Imote2 Processing Board		LIS3L02AS4 Accelerometer	
Processor	Intel PXA271	Acceleration	±2 g
SRAM Memory	256 kB	Avg. Noise Floor (X&Y)	0.3 mg
Memory	32 MB (SDRAM/FLASH)	Avg. Noise Floor (Z)	0.7 mg
Power Consumption	44 mW at 13 MHz	Resolution	0.66 v/g
	570 mW at 416 MHz	Temperature Range	-40 to 85ºC
Radio Frequency Band	2400.0 – 2483.5 MHz	Dimension	45×45 mm
Dimensions	36 mm×48 mm×9 mm		

While wireless sensor networks are effective tools for response monitoring of structures, maintaining their power by batteries with finite-life makes their application somewhat more challenging for long term monitoring. Thus, a traditional wired sensor network is used in conjunction with the wireless sensors for performing an automated long-term monitoring. The network includes strain gages, accelerometers, displacement transducers, and anemometers:

- Strain gages are uniaxial weldable resistance-type gages with 6.35 mm. length produced by Measurements Group Inc. Weldable strain gages are selected due to the ease of installation in a variety of weather conditions. The "welds" are point or spot resistance welds about the size of a pin prick. The probe only touches the foil that the strain gage is mounted on by the manufacturer. The gage resistance is 350 ohms and an excitation voltage of 10 volts is used. The strain data is converted to stress by multiplying by the elastic modulus of steel which is considered as 2×105 MPa.

- Wired accelerometers are uniaxial and capacitive manufactured by PCB Piezoelectronics, Inc., (model 3701G3FA3G) measuring range of ±3 g acceleration with 3 μg/√Hz noise density. They are specifically designed for measuring low-level, low-frequency accelerations.

- Linear Variable Differential Transformers (LVDTs) are used to measure the displacement response. The sensors are manufactured by Macro Sensors and have a

displacement range of ±25.4 mm. LVDTs are mounted to a heavy steel base to hold the sensor on its zero location.

- An anemometer is included in the sensing system to measure wind speed and wind direction. The anemometer of the system is manufactured by R.M. Young Inc., Model 05103.

Figure 6.2 shows different utilized sensors in the wired network. The data acquisition of wired network is a Campbell Scientific CR9000 (1995). The acquisition system is a high speed, multi-channel 16-bit data logger. CR9000 data logger is configured with digital and analog filters to remove noises from collected data. Remote communications with the data logger is established using a dedicated wireless broadband modem. Utilizing remote communications, wired sensors can be controlled over the network remotely and data can be downloaded automatically via a server located at any desired place.

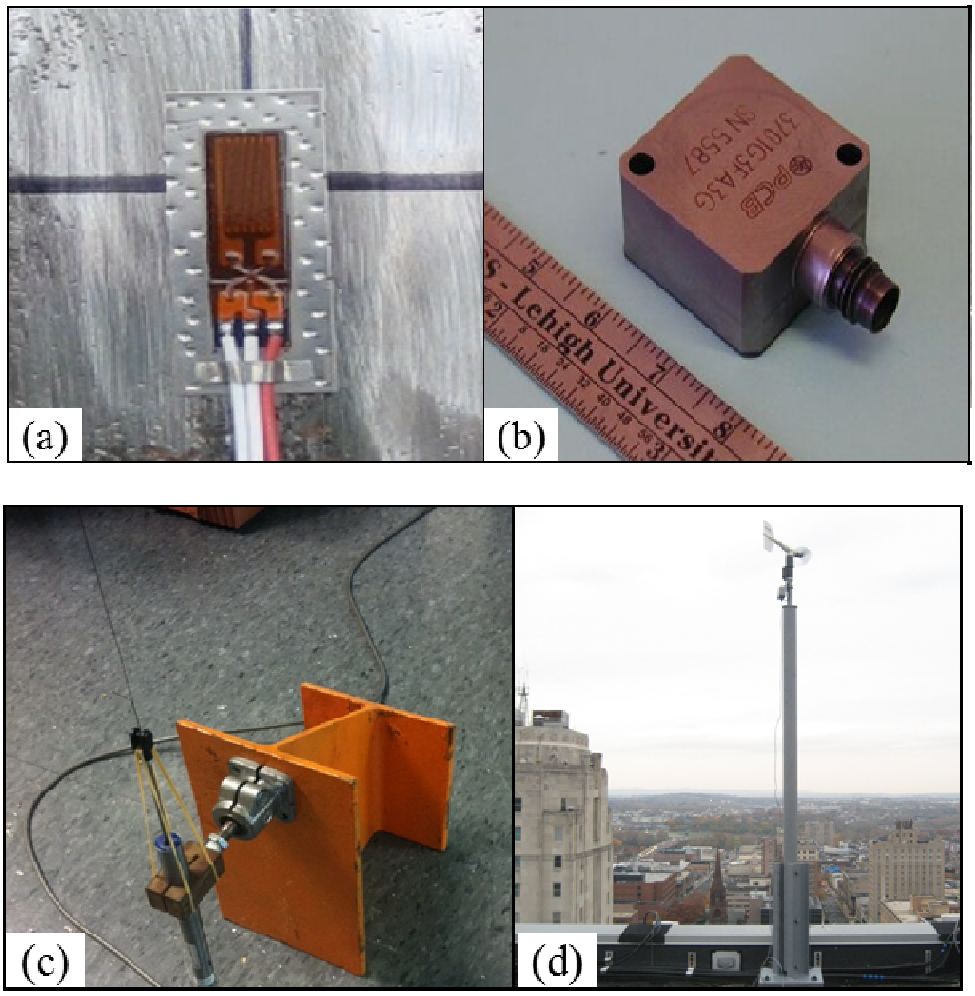

Figure 6.2. Wired instrumentation, (a) strain gage, (b) accelerometer, (c) LVDT, and (d) anemometer

The combination of wired and wireless networks with all different types of sensors is utilized in monitoring of a testbed structure for measuring its vibration performance under in-service loads. The next section describes the building structure and discusses the reason that the structure is selected for instrumentation with the sensing system presented in this section.

6.4. Building Description

The building selected for the study is a 16 story steel structure with 4 floors of parking below grade located in Pennsylvania. The structure is supported on a combination of spread footings and caissons dowelled into suitable rock capable of supporting 1.00 MPa. The main lateral force resistant system for the building is steel braced frames. Two braced frames are used for each transverse axis of the building. Each steel frame consists of two braced frames connected with steel coupling beams. The frames in the North–South axis of the building continue to the roof. The frames in the East-West direction, however, terminate on the 15th floor. While the braced frames in the East-West direction are located on the two outermost lines (north and south sides) in the plan, the braced frames in the North-South direction are located almost on the centrelines in the plan.

The building is clad with masonry and has concrete floors supported by steel beams and girders. The structure has a consistent plan up to the 13th floor where the building face steps back. At this level slender columns support the East face of the upper floors. The East face of the structure and a view of the gym area on the 16th floor are shown in Figure 6.3. A typical plan view of the building is also shown in Figure A6.1.

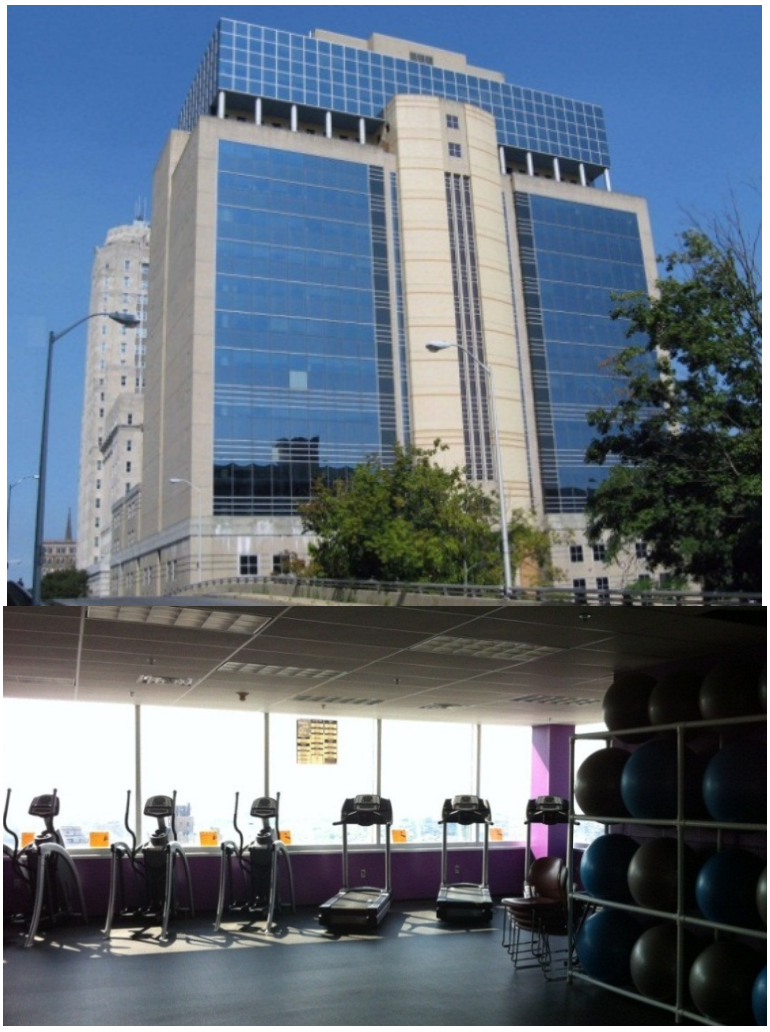

Figure 6.3. Test bed structure and 16th floor exercise room

There have been concerns over building's vibrations which are induced by activities in an exercise room, located on the 16th floor, and also high speed wind gusts. Objections arise from occupants housed next to, and down to several floors below the exercise room when an aerobics class takes place. Locating offices around the exercise room lead to user conflict as the vertical accelerations transmit from the activity room to the adjacent portions of the structure where active motions are not taking place. For example, while

individuals in the aerobics class would not notice the movement, individuals sitting in other portions of the building are very sensitive to the motion. Similar objections exist in regards to lateral vibration when the wind speed is high. The perceptible movements together with some diagonal cracks on the claddings of the structure have intensified occupants' and owner's concerns regarding the general performance of the building. As a result, the vibration evaluation and assessment of the building is the first step for alleviating the issues.

6.5. Background on Vibration and Human Perception

Accurate vibration evaluation is critical in assessing a building's performance under the effects of dynamic excitations. As a serviceability consideration, a proper design of a building should assure that the structure's vibrations do not exceed the level of comfort of its occupants. A few different factors which affect the perception and tolerance level of the human are (i) the magnitude of vibration, (ii) the frequency of vibration, (iii) the occupant's activity, (iv) the occupant's body orientation, and (v) the duration of motion. While the effect of magnitude on human perception is evident, the effects of other parameters may need more elaboration.

Frequency of vibration is a critical factor as, depending on the natural frequency of a human body, the effects of the vibration can be intensified. Fundamental organs of a body have natural frequencies in the range of 5 – 8 Hz (Murray, 1991). Therefore, vibrations with major frequency contents within the range would have significantly more uncomfortable effects on the body, as compared to vibration with frequencies outside of

the range. Perception also varies significantly depending on the type of activity of the individual (Murray, Allen & Ungar, 1997; Irwin, 1978). For example, an individual sitting at a desk would be much more sensitive to floor vibrations than an individual walking around an office or one who is performing exercise. Tolerance is also dependent on the direction of the acceleration and the orientation of the body. High wind gusts induce horizontal and torsional motions in a building, whereas fast walking and aerobics activities induce vertical accelerations. Depending on the frequency, the direction of each of the vibrations may result in different perception levels (e.g., in lower frequencies, the lateral vibration is more perceptible than vertical vibration [Irwin 1978]). Finally, the duration of the motion has considerable influence on the tolerance of people. It is stated in AISC LRFD Commentary (1986) that "Generally, occupants of a building find sustained vibrations more objectionable than transient vibrations". While this reference does not provide an exact duration as a threshold, Irwin 1978 and Boggs 1995 suggest evaluation of vibration over approximately 10 and 20-60 minute duration, respectively, for the purpose of human comfort assessment.

Determination of level of comfort and perception for a human body subjected to vibration is a well-researched area of study. Although a large portion of these investigations are devoted to human response to vibrations in moving automobiles, ships or airplanes, there are many established studies for evaluation of motions in building structures: Irwin (1978) investigated human response to dynamic motion of a structure and presented suggestions for maximum acceptable magnitudes of storm induced

horizontal motion for buildings; International Standard Organization (1989) discussed many building vibration environments and presented acceleration limits for mechanical vibrations as a function of exposure time and frequency, for both longitudinal and transverse directions of persons in standing, sitting, and lying positions; Allen & Murray (1993) proposed criteria for design of gymnasiums subject to rhythmic loads; Murray et al 1997 summarized recommendations and design criteria for floor vibration due to human activity in AISC Design Guide Series 11 (Murray, Allen & Ungar, 1997).

In the building investigated in the study, vibrations are induced due to both wind and human-structure interaction which is caused by rhythmic actions. Recommended tolerances are reproduced from Murray, Allen & Ungar (1997) and Irwin (1978) and shown in Figure 6.4. In this figure, the recommended limits are presented in terms of the frequency of vibration. The limits also depend on occupancy of the building (e.g., office areas or exercise area). The recommended values in the plot are used later for evaluation of the building's performance. Note that while the limits of vertical vibration are in terms of peak acceleration, limits of lateral vibrations are in terms of root-mean-square (RMS) acceleration.

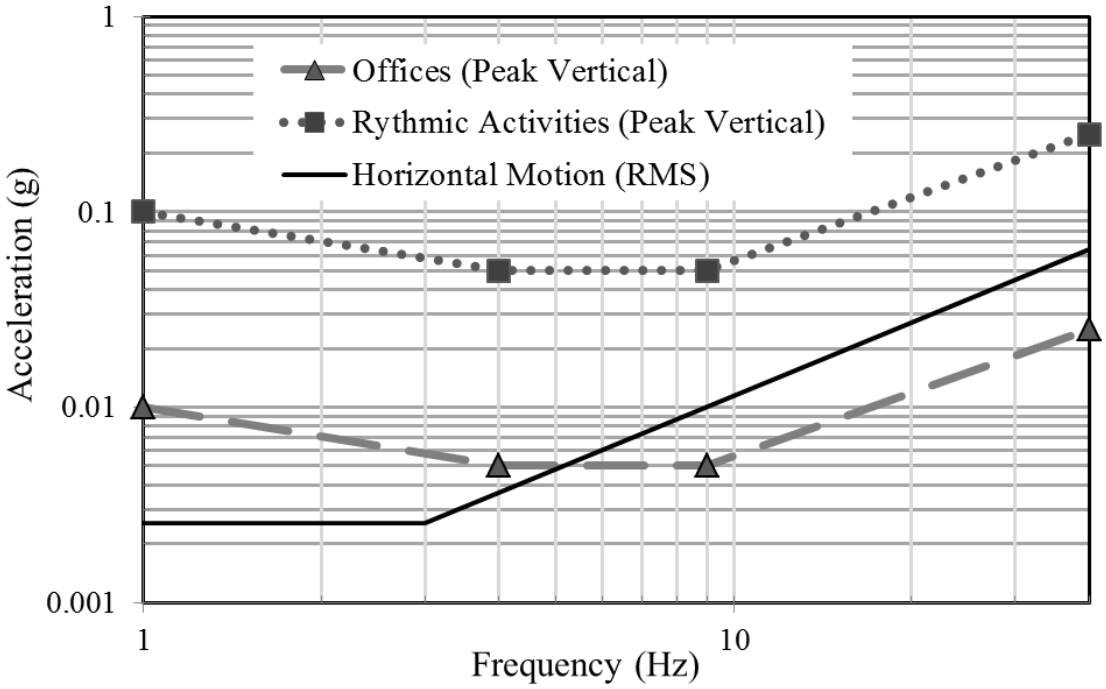

Figure 6.4. Recommended limits on acceleration tolerance

6.6. Instrumentation details

Monitoring of the building took place during a 3 month period and had two phases: onsite short-term monitoring and remote long-term monitoring. The onsite monitoring includes measurement from wireless sensors from multiple locations in the building:

- Measurement of floor vibration from multiple locations on 16th, 15th, 13th, 12th and 7th floors. Wireless sensors provided a significant easement as they were moved around to capture the vibration from multiple locations with minimal effort.

- Measurement of lateral vibration of the building using wireless accelerometers installed on roof, 13th, and 3rd floor, two in each elevation. These sensors

communicated with their base station, which was located outside of the building, through radio signals. The application of wireless sensors provided an economic solution to the lateral vibration monitoring, as a result of absence of wiring. The collected data from the 6 wireless sensors is used for extraction of response spectra and modal parameters of the building.

The remote long-term monitoring includes measurement from wired sensors from multiple locations in the building:

- Measurement of strain/stress data from multiple beam elements on the 16th floor and bracings in different elevations for performance evaluation in terms of strength demand.

- Measurement of floor acceleration and displacement response from multiple locations on the 16th floors for assessment of aerobics induced vibrations and to find maximum occurred vibrations in long term.

- Measurement of wind speed and wind direction using an anemometer installed on the roof level. The measured data is used for extraction of wind spectra.

The automated remote long-term monitoring system is configured to record data under a number of different conditions:

(1) Wind History: for the duration of the monitoring wind data are recorded on 5 minute intervals. For each 5 minute interval, the average wind speed, and direction as well as the maximum wind speed are recorded.

(2) High Wind Events: when the wind speed exceeded a predefined threshold value (14 m/sec), continuous high-speed data are collected from all sensors for a period of approximately five minutes. The data collection continued throughout the 3 months monitoring period.

(3) Aerobics Class Monitoring: continuous high-speed data are collected from each sensor during all aerobics classes in the 3 month monitoring period.

Figure A6.2 shows the location of wired sensors on the 16^{th} floor and different occupancies of the floor. Figure A6.3 also presents the bracing frames of the building and the location of instrumented wired strain gauges. Table 6.2 also presents the the quantity and location of all the sensors that are used for monitoring of the building

Table 6.2. Instrumented sensors for monitoring of the testbed structure

Floor	Sensor type	Quantity	Location(s)
1st floor	strain gauges	4	Lateral Bracings along axes 8 and A
3rd floor	accelerometers	2	on NE and SE corners
7th floor	accelerometers	4	on the floor- under exercise room
12th floor	accelerometers	4	on the floor- under exercise room
13th floor	accelerometers	4	on NE and SE corners
15th floor	accelerometers	4	on the floor- under exercise room
	strain gauges	2	Lateral Bracings along axis 8
16th floor	accelerometers	7	on the floor - gym and office areas
	strain gauges	7	on beam flanges, along axes 9 and C
	LVDTs (Disp. sensors)	2	mid-span of beams along axes 9 and C in gym area
Roof	accelerometers	4 (wired and wireless)	on NE and SE corners
	anemometer	1	on a steel pole on the penthouse roof framing

6.7. Measurements and data processing:

As the vibration issues of the building are classified into floor aerobic-induced vibration and lateral wind-induced vibrations, the data processing related to each of them is presented separately.

6.7.1 Floor Vibration:

The first step in evaluation of vibration is to inspect the collected data in terms of magnitude. Instrumented wired sensors on the 16th floor are shown in Figure A6.2. A typical time-history plot of acceleration, displacement, and stress (from strain gages) at a beam element supporting the aerobics class floor is presented for an hour-long class in

Figure 6.5 to 6.7. The beam element and location of sensors are selected such that the worst case scenario can be represented. The important findings from such a plot are to check whether or not the data is in agreement with the physical actions taking place in the duration and to check the magnitudes of each of these physical quantities. It can be seen in Figure 6.7 that the time-history data is consistent with events that occurred in the class: very low vibrations and low stresses start to increase as people arrive at the exercise class and start to warm-up and at the end of the class, the magnitudes decrease as people leave.

To provide a more reliable evaluation and conclusion the magnitudes are investigated over a longer duration. This became possible by use of automated wired sensor network. The maximum stresses and accelerations of different aerobic classes during the monitoring period are collected and plotted in Figure 6.8.

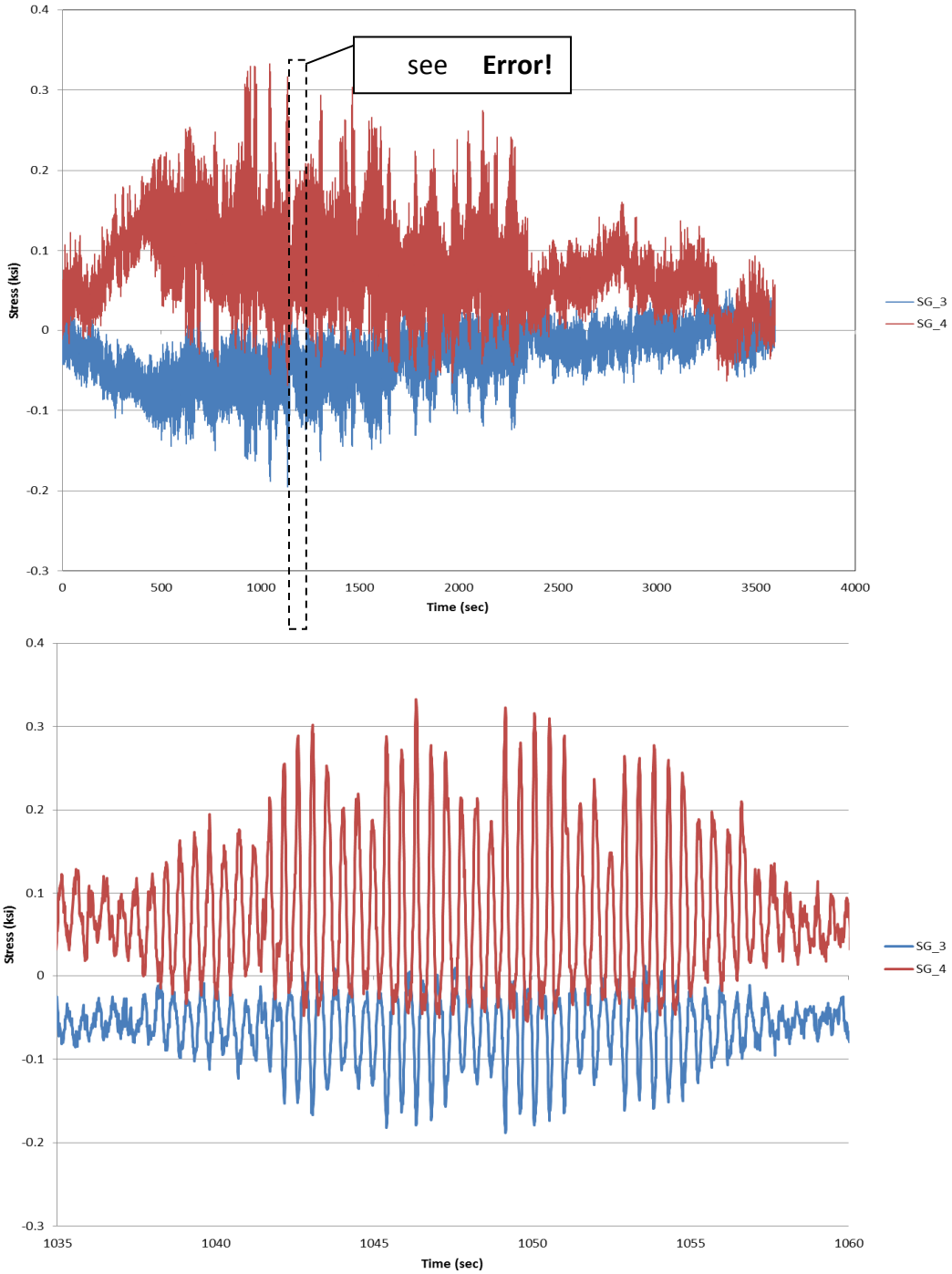

Figure 6.5. Stress time-history plot for top (SG_3) and bottom (SG_4) flange at midspan of beam on Line C between Lines 8 and 9 during aerobics class

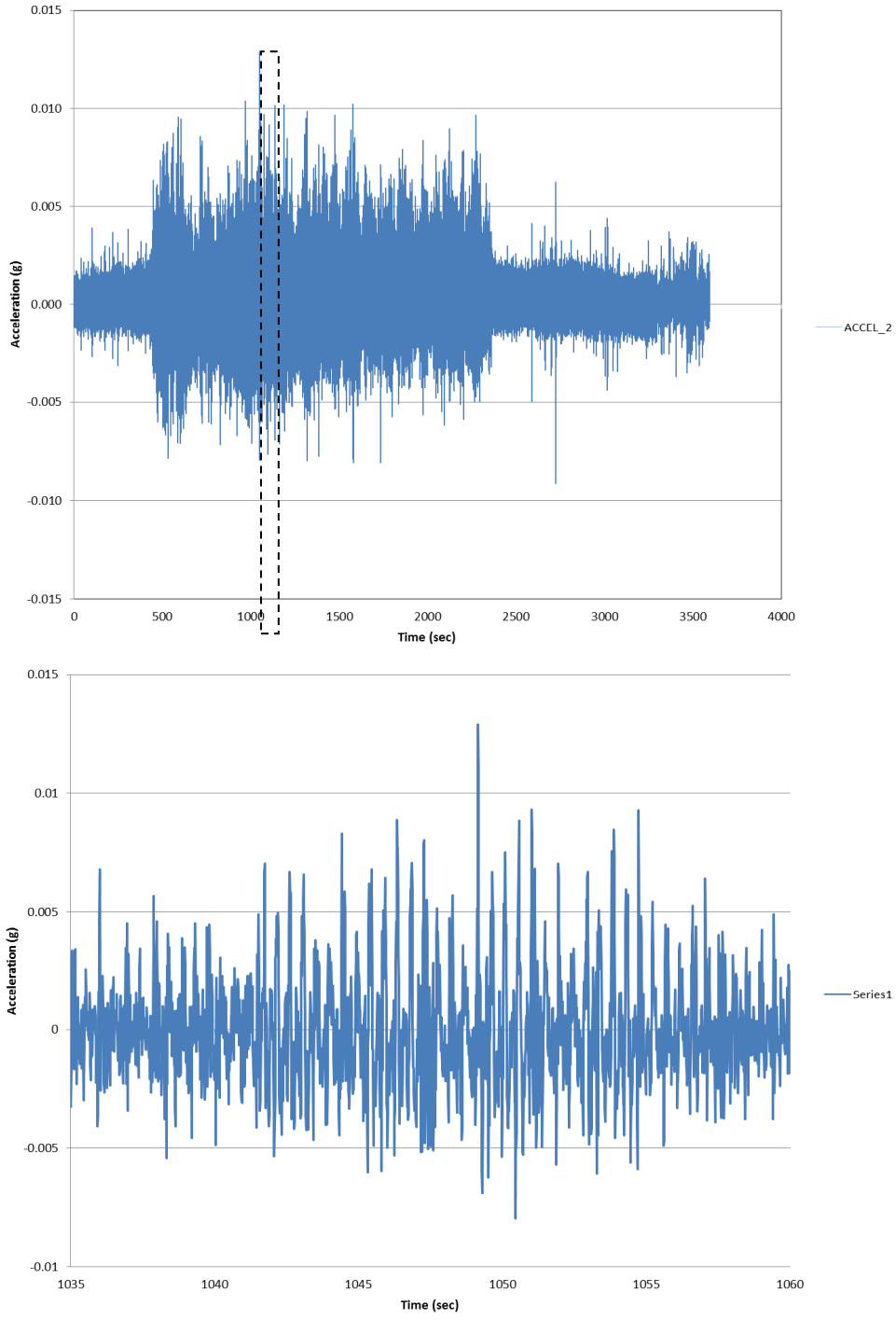

Figure 6.6. Acceleration time-history plot for midspan of beam on Line C between Lines 8 and 9 during aerobics class on November 14, 2011 between 12:17 and 12:18 PM

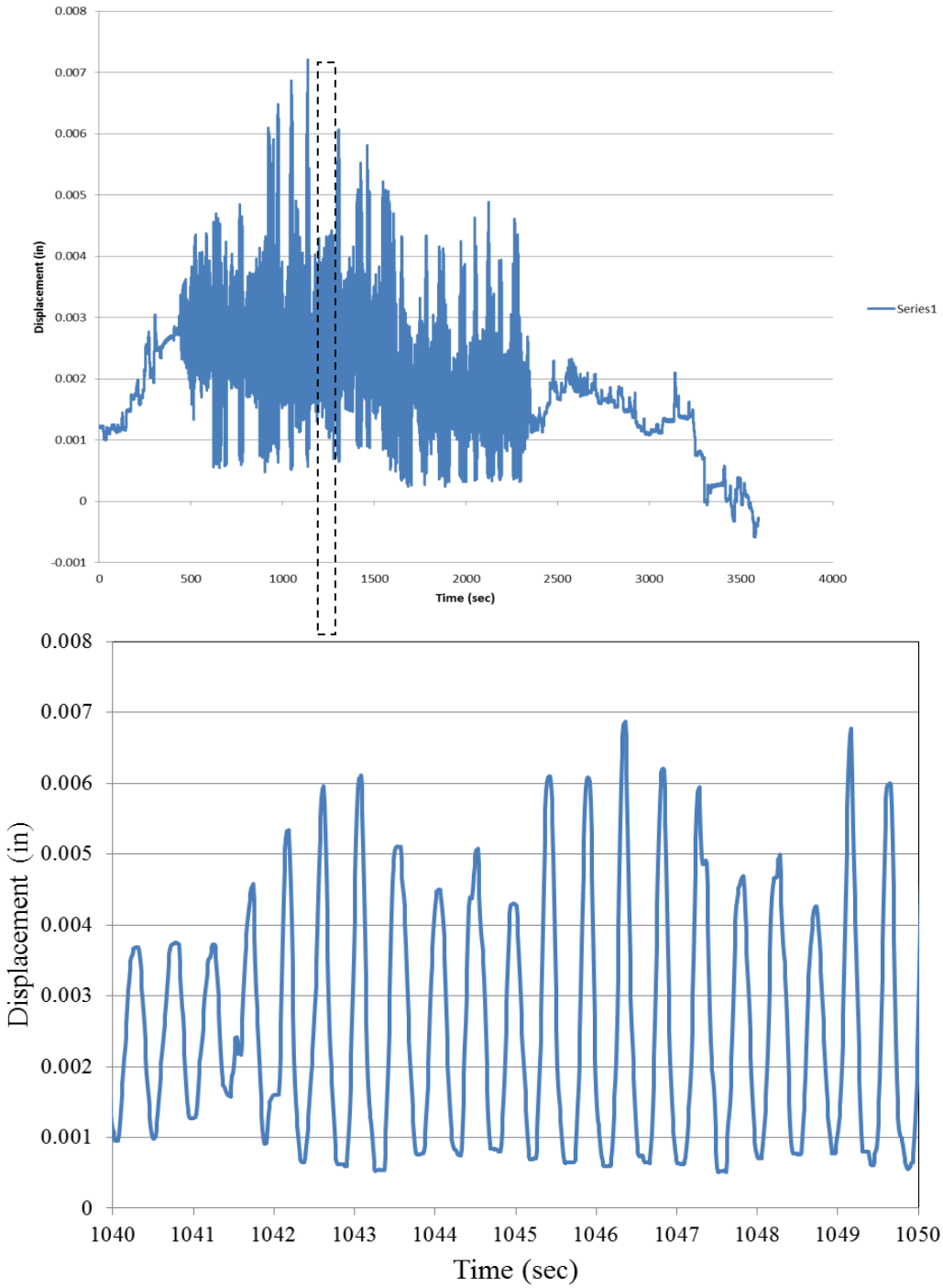

Figure 6.7. Displacement time-history plot for midspan of beam on Line C between Lines 8 and 9 during aerobics class.

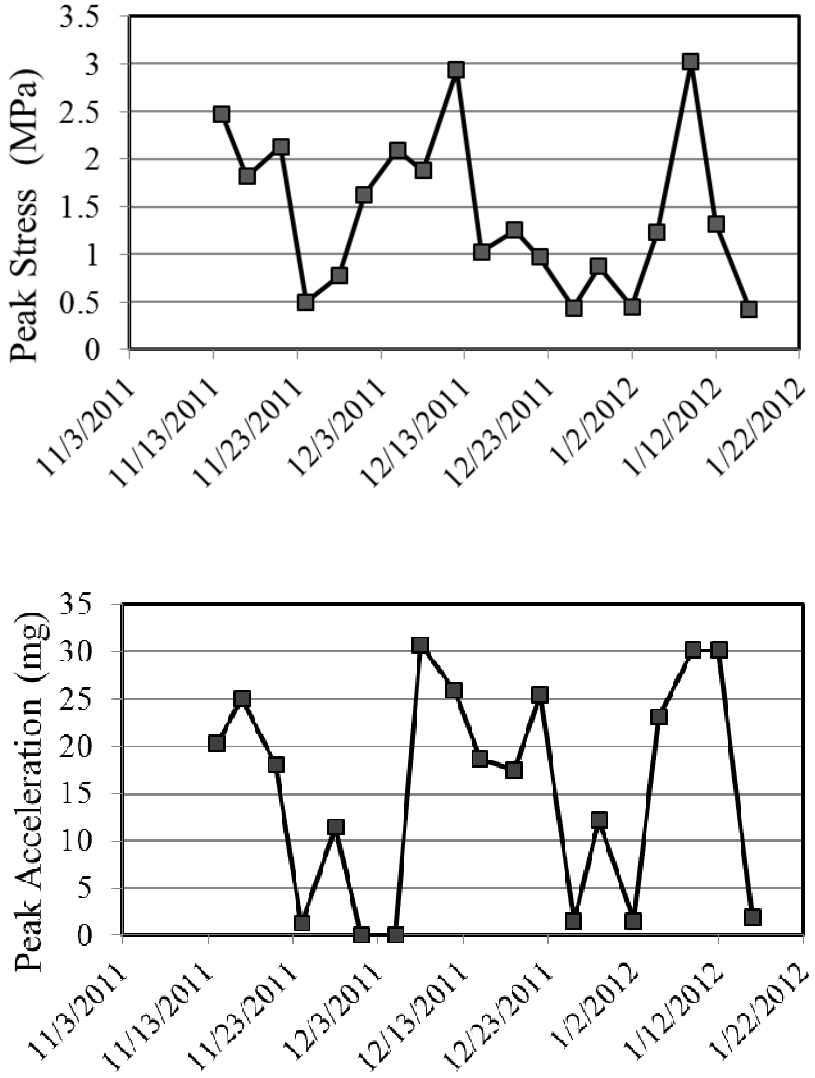

Figure 6.8. Peak stress and accelerations measured under aerobics floor

In addition to estimation of strength demand, the acceleration response is investigated for serviceability concerns. For that reason, the acceleration response is inspected in terms of both magnitude and frequency and is compared to recommended criteria for human comfort (as presented earlier in this chapter).

Additionally, since the occupancy of different portions of the building are different (offices and gym area), the acceleration response of different locations needed to be investigated separately. The need is addressed by use of portable wireless sensor network. The data are collected from various locations on different floors via wireless sensors during the onsite monitoring. Figure 6.9 and also Figures A6.4 through Figure A6.7 present the time-history data collected from different locations of the building along with the Power Spectrum plots which reflect the dominant frequencies of the measured responses.

A summary of vibration amplitudes at different locations (minimum, maximum, and the root mean square of the acceleration signals) are presented in Table 6.3. The color gradient is applied on the minimums and maximums to scale the amplitudes and reflect the attenuation of vibration level (absolute min. and max. values decrease as moving from red to green color). To better demonstrate the amplitude of acceleration in different locations, the Maximum and the RMS of the measured acceleration are also shown in Figure A6.8 through Figure A6.12. It should be noted that the measurement durations are limited and the amplitudes that are presented in Table 6.3 are not the maximum vibrations on the floor in the entire aerobics class duration, but are maximum values of the associated time slots. The results of wired sensor measurements, however, represent the maximum vibrations of the entire aerobics classes. Thus, some inconsistencies in the maximum amplitudes of wired and wireless measurements are reasonable.

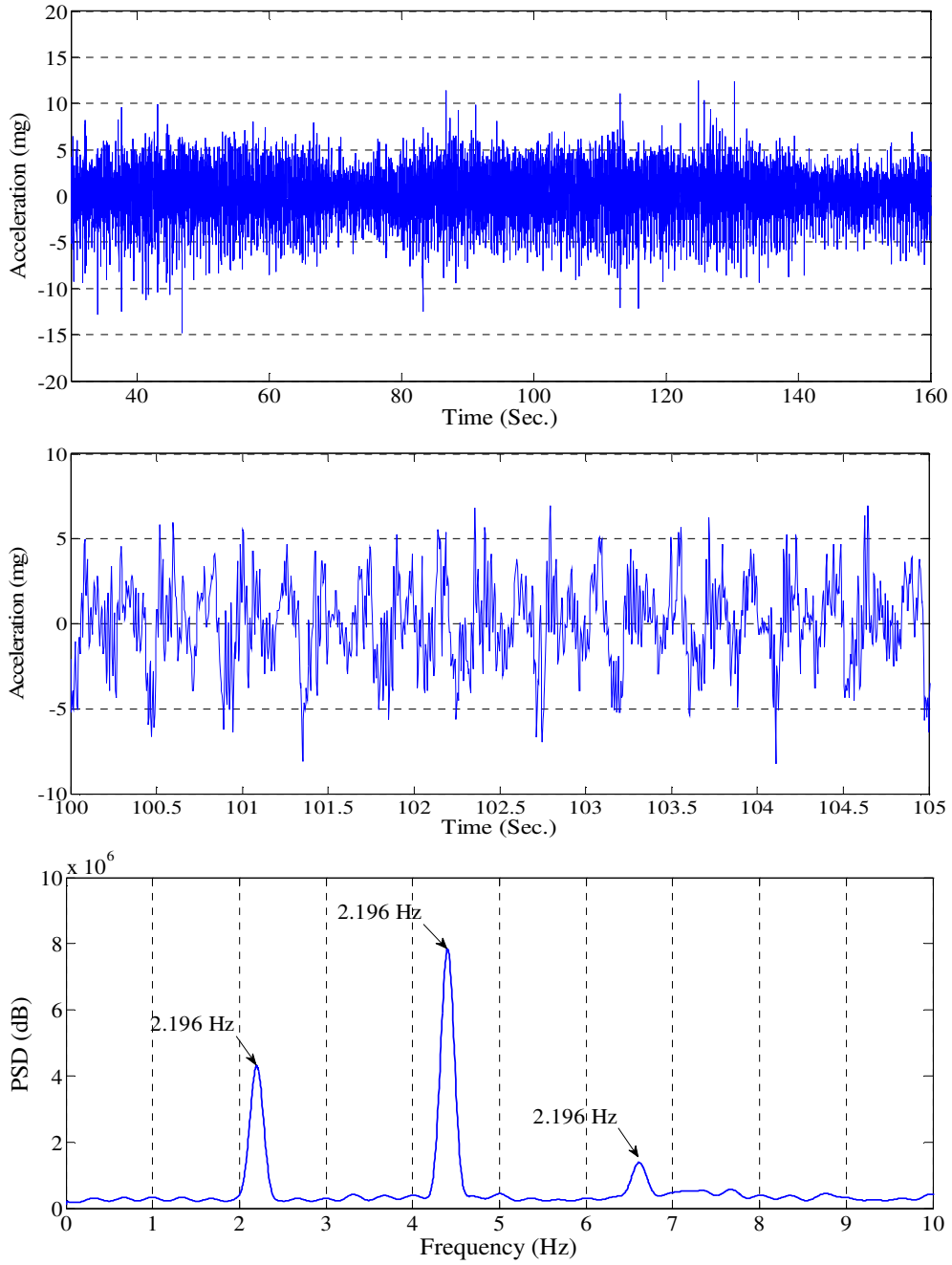

Figure 6.9. Time-history plot and Power Spectrum Density of acceleration from 16th floor between C-9.6 & B-9.6 during aerobics class

Table 6.3. Summary of acceleration response (max., |min.|, and root-mean-square) measured by wireless sensors

Floor	Location	Date	Time	Acceleration (mg)			ACCEL_2 (mg)	
				|Min.|	Max.	RMS	Abs Max	RMS
16	C-9.6 / B-9.6	10/25/2011	12:10	14.82	12.48	2.34		
16	C-7/D-7	10/25/2011	12:50	8.76	8.69	2.49		
16	G-9.9 / F-9.6	10/25/2011	12:38	5.10	7.23	0.88		
16	H-9.6 / I-9.6	10/25/2011	12:28	2.94	2.88	0.59		
15	C-9 / C-9.6	11/17/2011	12:30	8.77	7.35	1.25	22.0	2.28
15	C-9 / D-9	11/17/2011	12:30	9.89	5.39	1.11	22.0	2.28
15	C-9 / D-9	11/17/2011	12:42	4.35	4.70	0.40	9.08	0.41
15	D-9 / E-9	11/17/2011	12:42	1.21	1.40	0.27	9.08	0.41
13	C-10	11/17/2011	12:10	2.91	3.35	0.54	14.6	1.79
13	C-9.6 (mid-col)	11/17/2011	12:10	4.79	6.35	0.82	14.6	1.79
12	C-9 / B-9	11/14/2011	12:25	4.97	5.46	0.87	10.2	1.48
12	C-9 / C-10	11/14/2011	12:25	3.93	4.05	0.64	10.2	1.48
7	C-9 / C-10	11/14/2011	12:40	2.11	2.60	0.36	4.99	0.62
7	C-9 / C-10	11/14/2011	12:44	1.18	1.59	0.27	9.12	0.74
7	C-9 / C-10 (East)	11/14/2011	12:40	2.76	2.87	0.43	4.99	0.62

Figures 6.10-a and 6.10-b show the maximum acceleration amplitude in different locations in the building. The two plots illustrate that the amplitude of vibration attenuates faster on the floor, as getting farther from center of aerobics class, than in the elevation, as going down to lower floors. This is reasonable as the vertical transmission of vibrations through steel columns encounters less damping compared to horizontal transmission through beams and floor slabs. To evaluate the vibration's effects on human perception, it is necessary to find the frequencies of vibration, as shown in PSD plots of the measured responses. Figure 6.11 also shows the acceleration response collected from a beam supporting the aerobics class floor (as an instance) in frequency domain. This plot presents some peaks (2.1, 3.2, 4.3, 6.4, and 8.5 Hz) which are dominant frequencies of the collected acceleration response. The frequencies are consistent in all data collected from different locations during the aerobics class. It is clear that the acceleration response of the floor to the rhythmic exercise forces is not a single harmonic function rather it has a range of dominant frequencies (2 to 8.5 Hz). This is particularly important when assessing the amplitudes based on limits of human comforts.

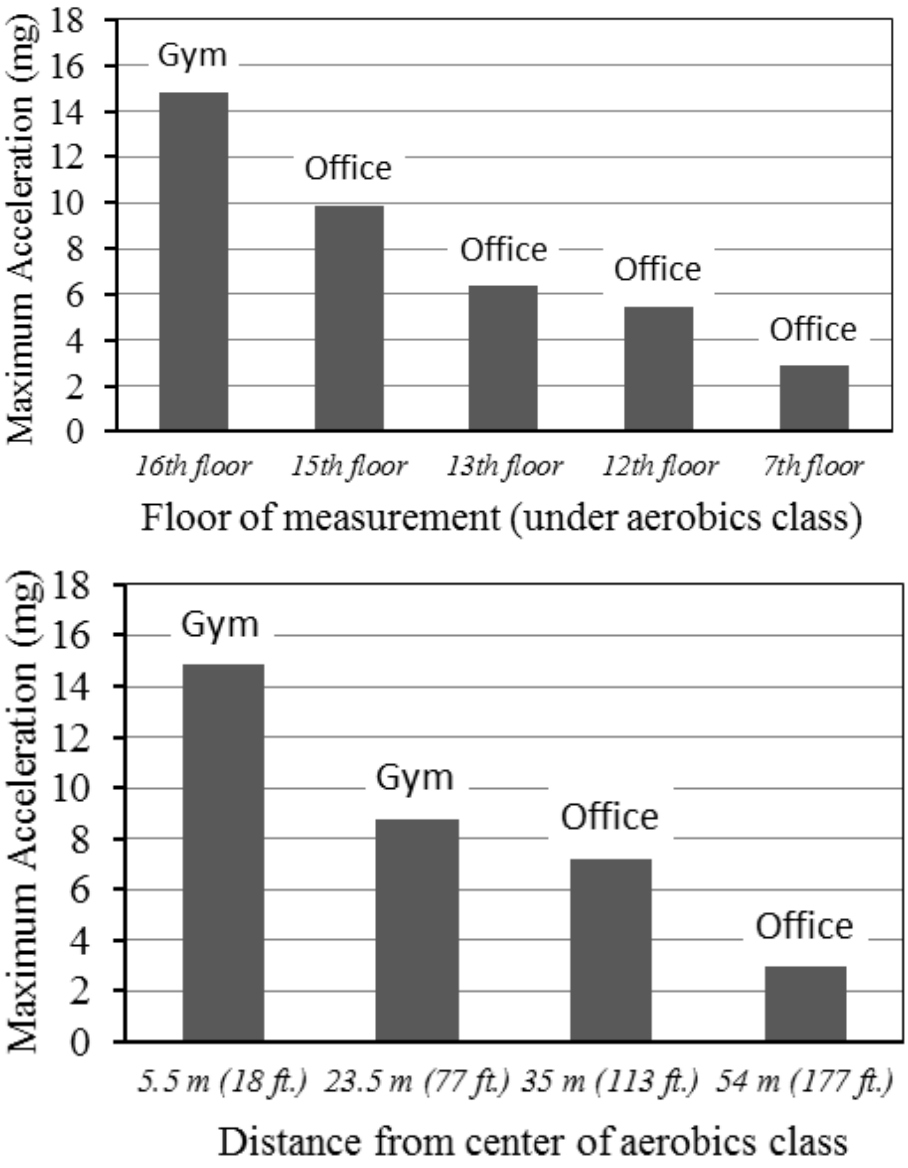

Figure 6.10. Maximum vertical aerobics induced acceleration dispersion through structure

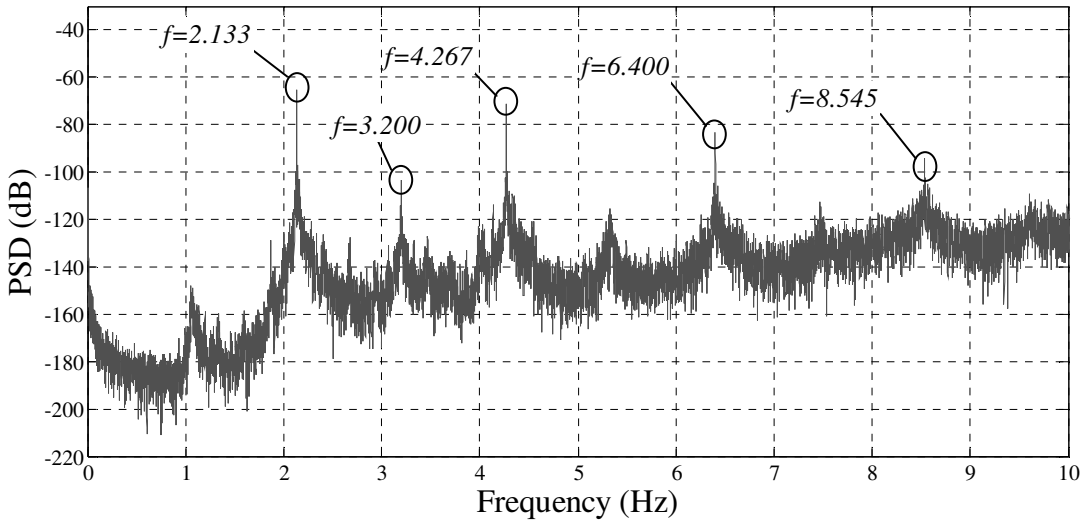

Figure 6.11. Typical frequency content of measured vertical acceleration

Performance evaluation of the floor system in the building has two aspects: (i) strength demands versus capacities and (ii) vibration levels versus comfort limits.

In regards to strength demand, the induced stresses during the applied rhythmic forces are inspected. As Figure 6.5 shows, the magnitudes of stress in the beam are at most bellow 5 MPa (0.5 Ksi) which is significantly lower than strength limits of a steel beam element (400 MPa). Therefore, there is no concern over the performance of the designed floor beams in terms of strength.

For the evaluation of performance of floor in terms of serviceability, criteria suggested in AISC Steel Design Guide Series 11 are used. As the first step, the magnitudes of peak acceleration in different occupancies are compared to the recommended limits. The limits (as shown in Figure 6.4) are 50 milli-g (0.05 *g*) for vertical vibration in areas with

rhythmic activities and 5 milli-g for offices and residential areas, when the vibration frequency is in the range of 4 – 8 Hz.

Additionally, according to AISC Steel Design Guide Series 11, there are two other controls for the evaluation of floor vibration which are related to the fundamental natural frequency of the floor: (i) For floors with fundamental natural frequency above 8 Hz, to account approximately for footstep impulse vibration, the acceleration limit is not increased after 8 Hz, as it would be if Figure 6.4 is used. In other words, the horizontal portion of the curves between 4 Hz and 8 Hz in Figure 6.4 is extended to the right beyond 8 Hz. (ii) If the natural frequency is greater than 9-10 Hz, to account for motion due to varying static deflection, a minimum static stiffness of 1 kN/mm under concentrated load is introduced as an additional check.

To evaluate the floor performance and check if additional considerations are needed, the natural frequency of the floor is estimated using the ambient vibration data collected from the floor and also using the Equivalent Beam Method (EBM) which is recommended in the AISC Steel Design Guide Series 11.

Inspecting the ambient vibration response in frequency domain (e.g. power spectral density of response), the first fundamental natural frequency is observed as 8.53 Hz.

Also, using Equation 1 (from EBM), the first natural frequency of the composite beams can be estimated as:

$$f_n = \frac{\pi}{2}\sqrt{\frac{gEI_t}{wl^4}} \tag{6.1}$$

where f_n is the fundamental natural frequency in Hz, g is acceleration of gravity (9.86 m/sec^2), E is the modulus of elasticity of steel, I_t is the transformed moment of inertia, w is uniformly distributed weight per unit length, and l is the member span. Applying this equation on a *W16x31* section with 150 mm composite concrete slab depth and 5880 mm^2 reinforcement area, the first fundamental natural frequency is estimated to be 8.19 Hz. The estimated frequency is quite consistent with the one obtained from measurement.

Considering the estimated natural frequency, the acceleration limit should not be increased after 8 Hz when using the recommendations of AISC Steel Design Guide Series 1. Additionally the static stiffness of composite beams is checked, though the design guide does not impose it for natural frequencies less than 9 Hz. Having *W16x31* with 150 mm. composite concrete slab depth and 5880 mm^2 reinforcement area, the static stiffness under concentrated load ($48EI/l^3$ for simply supported beam) is 9.5 kN/mm, which is well beyond the limit. Thus, to evaluate the vibration performance of the floor, only the amplitudes of vibration and frequencies are assessed.

Based on the range of frequencies observed in the collected data (2 – 8.5 Hz as shown in Figure 6.11), it is reasonable to consider the horizontal portion of the recommended limitations plot (50 milli-g for rhythmic activities and 5 milli-g for offices and residential areas). In the aerobics class area on the 16th floor, the maximum measured acceleration (Figure 6.10) is below 0.035 g. Consequently, the peak acceleration of floor vibration in

the aerobics class area is below the recommended limits for aerobics activity. However, in the office areas in some portions of the building, the peak values, as presented in Figure 6.10, exceed the threshold of 0.005 g for perceptibility at elevations as low as the 12th floor. Therefore, it is concluded that the performance of the structure in some portions of the building is poor in terms of serviceability, though the structural components meet the measured strength demands.

13th Floor Column Examination

In addition to general floor vibration issues, concern was raised regarding the vibration characteristics of the columns spanning from the 13th floor to the 15th floor along Column Line 9.6 due to the fact that the columns carry gravity load from the 16th floor including the portion of the floor supporting the aerobics class and the fact that the columns are not continuous to the foundation. Rather the columns are supported on W36x155 transfer girders running east-west. Six such columns exist on Column Line 9.6 at Lines B, C, D, G, H, and J.

The mentioned columns are unsupported from the 13th floor to the 15th floor and they support gravity loads from the 15th floor, 16th floor, and roof level. The column on Line B was selected for instrumentation and testing. A single tri-axle wireless sensor module was installed at mid-height (on the 14th floor level) to measure the lateral vibration of the column during aerobics activity.

.

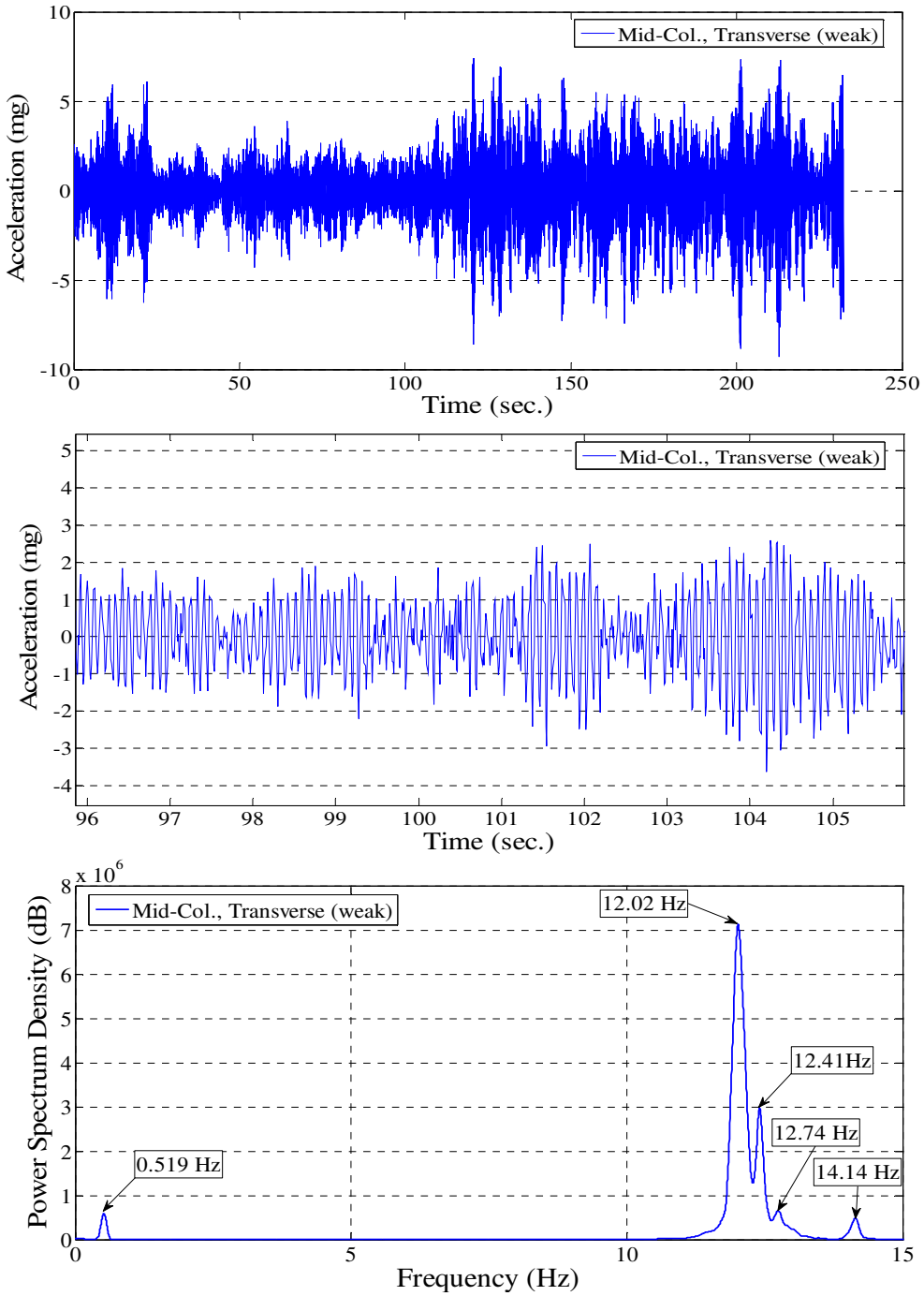

Figure 6.12. Time-history plot and Power Spectrum Density of acceleration from the column from middle of column C-9.6 on 13th floor in transverse direction during aerobics class

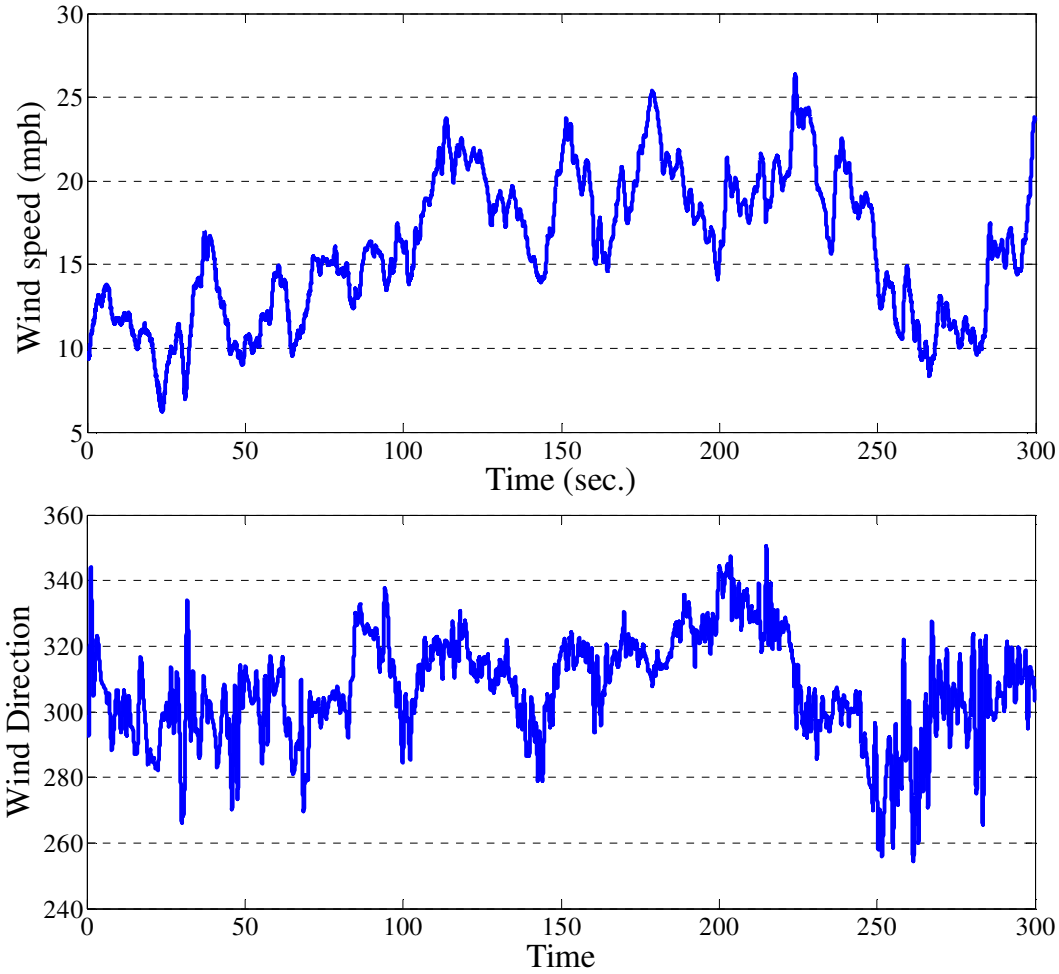

Figure 6.13. Time-history plot of wind speed and wind direction, during aerobics class at the time when the vibration of the column C-9.6 is measured

Figure 6.12 and Figures A6.13 through A6.14 present: time-history and corresponding PSD plots of vibration in the weak axis (north-south), strong axis (east-west), and vertical directions of the column, respectively. The wind conditions at the time of the monitoring are provided in the time-history plots of Figure 6.13. The vibration is measured during aerobics class on Nov. 17, 2011 between 12:10 and 12:15 PM.

The natural frequency of vibration of the column can be estimated using closed-form solutions for pinned-pinned and fixed-fixed beams, including the effects of axial load. The first-mode natural frequency, f_1, is given by:

$$f_1 = \frac{\lambda_1^2}{2\pi L^2}\sqrt{\frac{EI}{m}} \tag{6.2}$$

where

$\lambda_1 = 4.730$ (fixed-fixed boundary)

$\lambda_1 = 3.142$ (simple-simple boundary)

and,

E = modulus of elasticity

I = moment of inertia

L = member length

m = mass per unit length

To account for dead load that is acting on the members, the frequencies calculated above may be modified using the following equation:

$$f_{i,P\neq 0} \cong \left[\sqrt{1 + \frac{P}{|P_{cr}|}\left(\frac{\lambda_1}{\lambda_i}\right)^2}\right] f_{i,P=0} \tag{6.3}$$

where,

$f_{i,P\neq 0}$ = mode "i" frequency considering the effects of axial load

$f_{i,P=0}$ = mode "i" frequency calculated without consideration of axial load (using Eq. 6.1)

P = axial load, equal to tributary floor/roof areas times dead load plus 25% of design live load, = 42.7 kips

P_{cr} = critical axial buckling load (= $4\pi^2EI/L^2$ for fixed-fixed beam, or π^2EI/L^2 for a pinned-pinned beam)

For the column W10x49 column spanning from the 13th to the 15th floor, the calculated natural frequencies are summarized in Table 6.4. It can be seen that the axial load on the column does not have a large effect on the natural frequency.

Table 6.4. Summary of calculated 1st mode natural frequencies

	Calculated 1st Mode Natural Frequency (Hz)			
	Pinned-Pinned		Fixed-Fixed	
Vibration Direction	P =0	P=-42.7k	P =0	P=-42.7k
Strong Axis	14.7	14.4	33.3	33.1
Weak Axis	9.1	8.4	20.4	20.1

From Figures 6.14 and 6.15, it can be seen that the measured weak- and strong-axis natural frequencies were 12.0 and 17.4 Hz, respectively. The estimated values fall in the calculated range between the fixed-fixed and pinned-pinned cases, though are closer to the pinned-pinned case. The plots also indicate that during the aerobics class, peak acceleration amplitudes at mid-height of the column are 5 and 8 mg for the strong and weak axis directions, respectively. For steady-state vibration at the measured natural frequency and peak acceleration, corresponding displacement amplitude and bending stress are calculated. The calculated flexural stress in the column for both weak- and strong-axis directions is very low, less than 10 psi. Under this level of demand the aerobic induced vibrational stresses are not significant.

Lateral Vibration during Exercise

This section presents a discussion on the effects of the vertical exercise-induced vibration on the lateral vibration of the building. Shown in Figures 6.14 is a time history plots and corresponding PSDs of lateral accelerations of the 15th floor between columns C-9 and C-9.6 during the aerobics class, measured using the wireless sensor network. The results indicate that the response at this location is dominated by overall vibration modes of the building with peak frequencies of 0.61 and 0.91 Hz. However, frequencies caused by the exercise-induced excitation is also present in the data, with frequencies of 2.06, 2.92, and 4.27 Hz, though the contribution to the total vibration is small, evidence by the relatively small peaks in the power spectral density plot. A similar set of plots for the lateral acceleration of the 15th floor between columns C-9 and D-9 is presented in Figure 6.15. At this location there is no effect caused by the aerobics activity on the lateral vibration of the 15th floor.

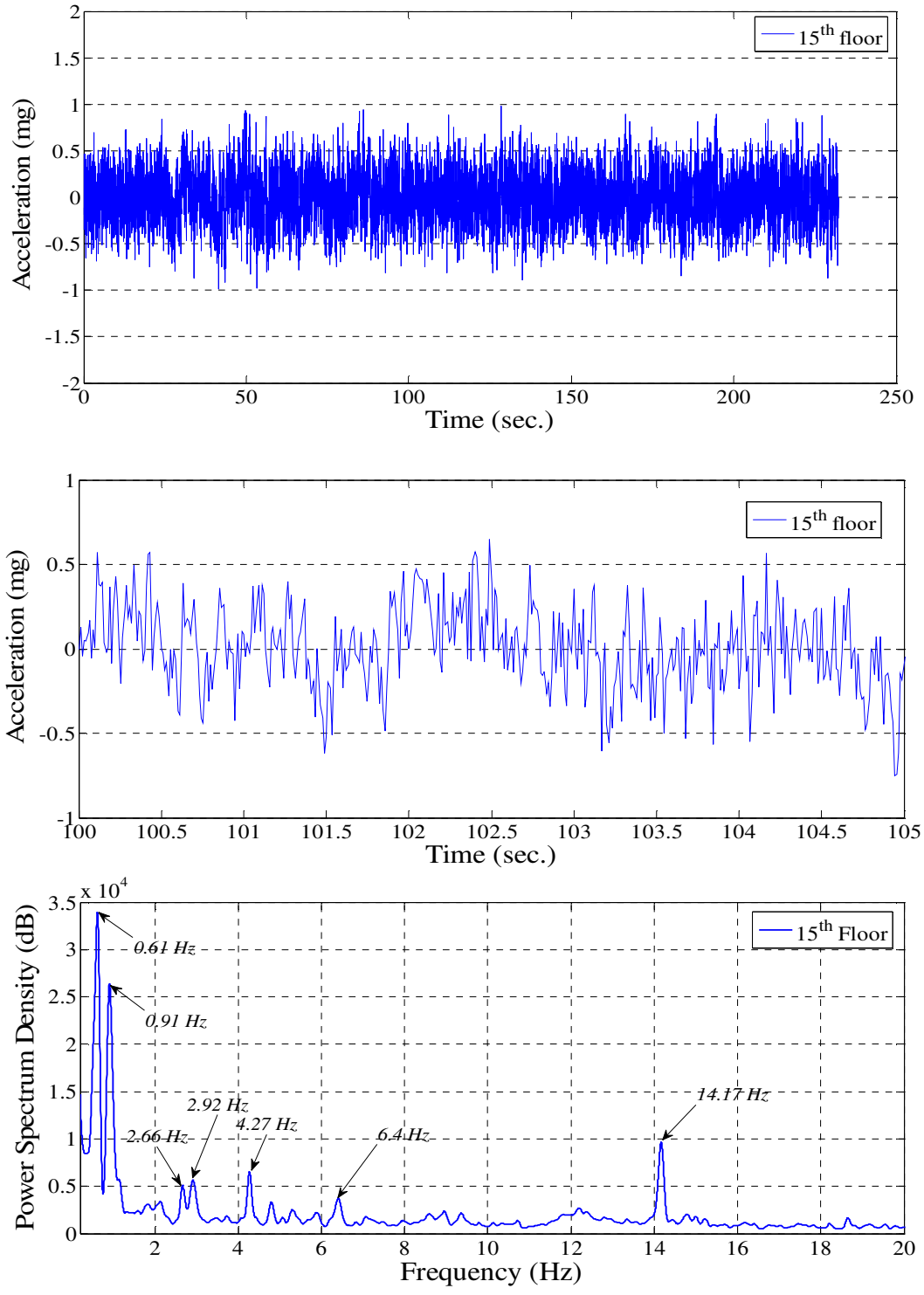

Figure 6.14. Time-history plot and Power Spectrum Density of lateral acceleration from 15th floor between C-9 & C-9.6 during aerobics class

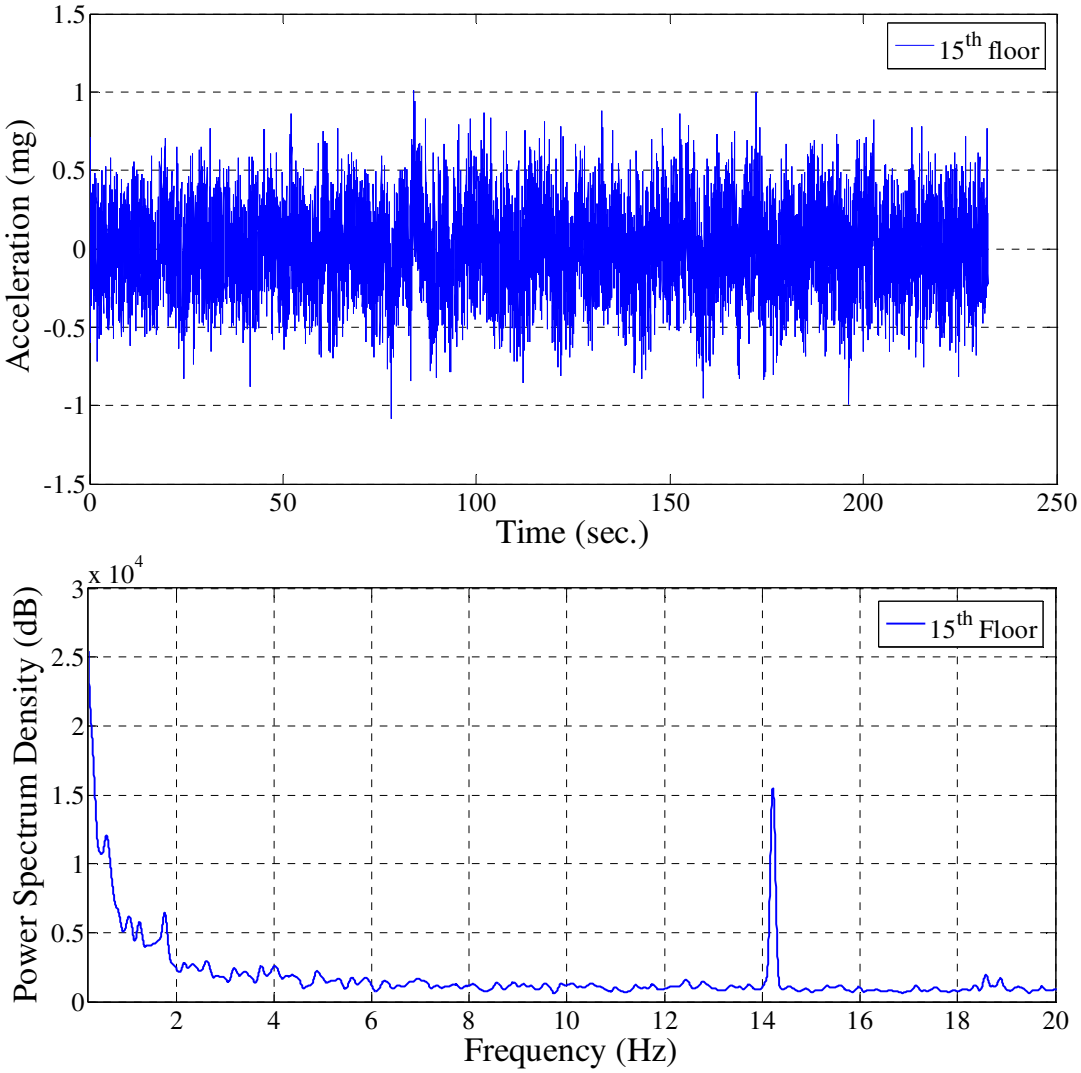

Figure 6.15. Time-history plot and Power Spectrum Density of lateral acceleration from 15th floor between C-9 & D-9during aerobics class

6.7.2 Lateral wind-induced vibration

Wind Load Characteristics:

Wind force is one of the important loading factors in the design of building structures. Effects of wind are classified into static and dynamic effects. In order to ensure the structural safety of the building, both static and dynamic effects of the wind force should be carefully investigated. Some important characteristics of wind are wind speed, wind direction, and wind fluctuation.

During the entire monitoring period the average wind speed and direction and maximum wind speed in 5 minute intervals are recorded using wired sensor network. Additionally, during high wind speed events (defined as wind speed beyond 14 m/sec [~50 mph]), the continuous data are collected from all wired sensors for a period of approximately five minutes. Having collected data, the wind load and the building's response is analysed.

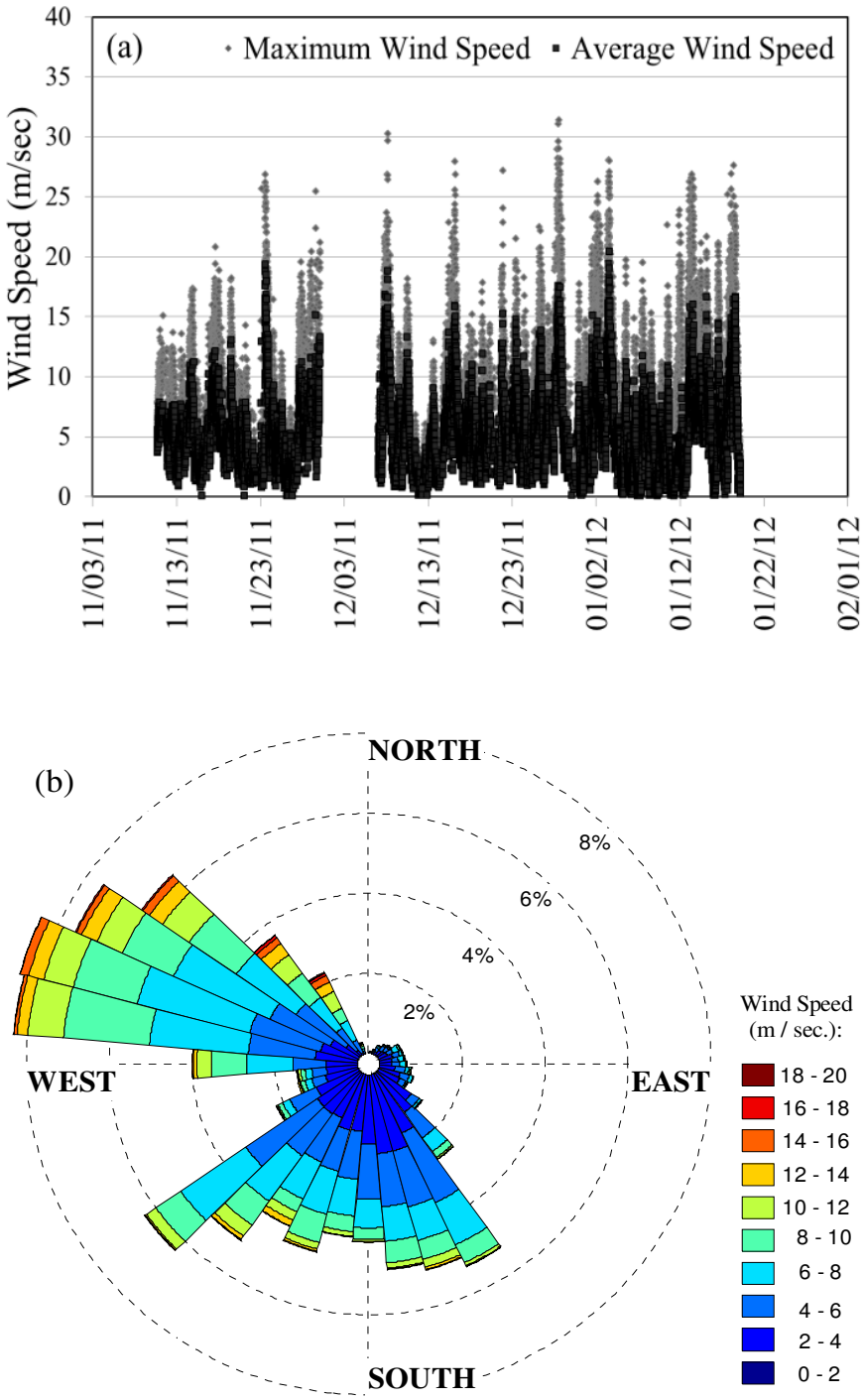

Figure 6.16. (a) Maximum and average wind speed, (b) wind rose presenting wind direction, wind speed average and the frequency of occurrence

In order to evaluate the structure's response to wind, as the first step, the wind characteristics are inspected. Presented in Figure 6.16-(a) is a time-history of maximum and average wind speed for the duration of the monitoring. It can be seen that the wind speed reached a maximum of 32 m/sec, and exceeded 30 m/sec just a few times. Figure 6.16-(b) shows a wind rose plot for the same data, where the wind direction of zero degrees represents a wind out of the north. The total bar height at each direction indicates the frequency of occurrence of wind from a given direction. A discretization of 10 degrees was used. Within each bar, the colour variation provides the makeup of the wind speeds that occurred in each direction bin. It can be seen that the wind was predominantly out of the west-northwest and south.

While the wind speed and direction are main factors in the static loading, the wind speed fluctuation is the more important factor in vibration evaluation. The basic statistical characteristics of the wind speed fluctuation can be represented by intensity of turbulence, wind speed probability distribution, and turbulence spectrum.

The intensity of turbulence is defined as $\sigma_v/\bar{v}$, where σ_v is the root-mean-square (rms) fluctuation and $\bar{v}$ is the mean speed of wind. The intensity of turbulence for wind is usually between 5 to 25%. From the collected data during the high wind speed events, the average intensity of turbulence during different event is calculated and is 25.67% which shows a relatively intense turbulence. The wind speed probability distribution can be assumed as Gaussian distribution which can be defined by mean value and root-mean-square of the wind speed data.

The energy of turbulence fluctuation is distributed over a frequency range which is described by turbulence frequency spectrum density function $S(f)$. Evaluation of the spectrum and frequencies, in which the energy is mainly distributed in, is important when assessing the effect of wind on a structure's vibration. The turbulence spectrum, $S(f)$, is defined as Furrier transform of the correlation function of wind speed $R(\tau)$. The relationship between turbulance spectrum and wind speed variance is:

$$\sigma_v^2 = \int_0^\infty S(f)df \tag{6.4}$$

It is customary to use another form of spectrum, known as *logarithmic spectrum*, which is dimensionless and preserves the relative contribution to variance at different frequencies. The logarithmic spectrum is defined as $f.S(f)/\sigma_v^2$ and its integral is:

$$\int_0^\infty f.S(f)/\sigma_v^2 d[\ln(f)] = 1 \tag{6.5}$$

The logarithmic spectrum of the wind data is extracted using the measurements of wind speed and wind direction. The wind spectrum can be obtained either for along wind direction or for a specific direction. In this work, as the objective is to assess the wind effects on the building structure, the wind speed is projected on each direction and the spectrum is extracted accordingly (from 0 to 360 degree with 10 degree intervals). The logarithmic spectrum of wind fluctuation is presented in Figure 6.17. In this figure the spectrum is plotted for 360 degrees in a 3-dimensional plot as well as the projected spectrum plot for south-north and east-west directions. The extracted spectrum plots, in general, are similar to some of wind turbulence spectrum models presented in literature

(e.g. von Karman type spectrum [Karman, 1948] or Davenport spectrum [Davenport, 1961]). Further investigation of wind spectrum can be obtained by utilizing regression and fitting a model to the obtained spectrum. However, this effort is outside of the scope of the research and the wind spectrum is used only for determination of main fluctuation frequency contents and comparison with fundamental frequencies of the building's response. From Figure 6.17, it is clear that the major frequency contents of the wind fluctuation spectrum are laid in a very low frequency range (0.01 to 0.1 Hz). This range is far behind the fundamental natural frequency of the building, as estimated and discussed later in the modal identification section of the chapter.

As the characteristics of the wind load are investigated, the structure's response and its vibration are also evaluated. Similar to evaluation of human-induced vertical vibrations, the wind-induced lateral vibrations are investigated in terms of both strength demand and the effects on human comfort. Both wired and wireless sensors are used in the evaluation. Wired sensors are shown to be effective for long-term strain/stress monitoring and wireless sensors for lateral acceleration response measurement at different locations.

Structural Response - Strength Demands:

Data from the strain gages installed on the selected wind bracing members on the 1st and 15th stories are collected for high wind speed events. The stresses are presented in the time-history plots for 1st and 15th floor bracings together with the wind-speed time-history for an example of high wind-speed duration in Figure 6.18. The wind speed time-history is presented in this figure to enable the comparison of the load and response. Each

plot contains the raw data and a 50 point moving average to aid in the identification of lower frequency trends.

It can be seen that on the 15th floor [Figure 6.18-(b)], there does not appear to be a strong correlation with the wind history of Figure 6.18-(a) in that there is not a well-defined peak in stress history corresponding to the time of the large wind gust. It is also seen that on the 15th floor, the stress magnitudes are very low, all less than 0.5 MPa.

The design wind load for the building is 40 m/sec. To roughly estimate the level of stress in the bracing members caused by a 40 m/sec design wind, the building response could be scaled by the square of the ratio of the wind speeds, or $(40/30 \text{ m/sec})^2$ which is equal to 2.25. However, 2.25 times the stresses measured in the braces during the high-wind event shown in Figure 6.18-(b) would still be less than 1.2 MPa, well below the design stress for these members. Table 6.6 also presents the level of the maximum stress in different locations during the high wind events.

On the 1st floor bracing, the stress history shown in Figure 6.18-(c) exhibited a more identifiable trend expected for the response of a tall building to dynamic wind loading. In Figure 6.18-(c) in particular, there is a spike in the response inducing tension in the brace element caused by the large wind gust. However, the measured stresses are again low, less than 1.00 MPa for this event. The low level stress demand is less than 0.3% of the lower bound yield strength of the steel members. Therefore, there is no concern over the performance of lateral load resisting system in terms of strength demand.

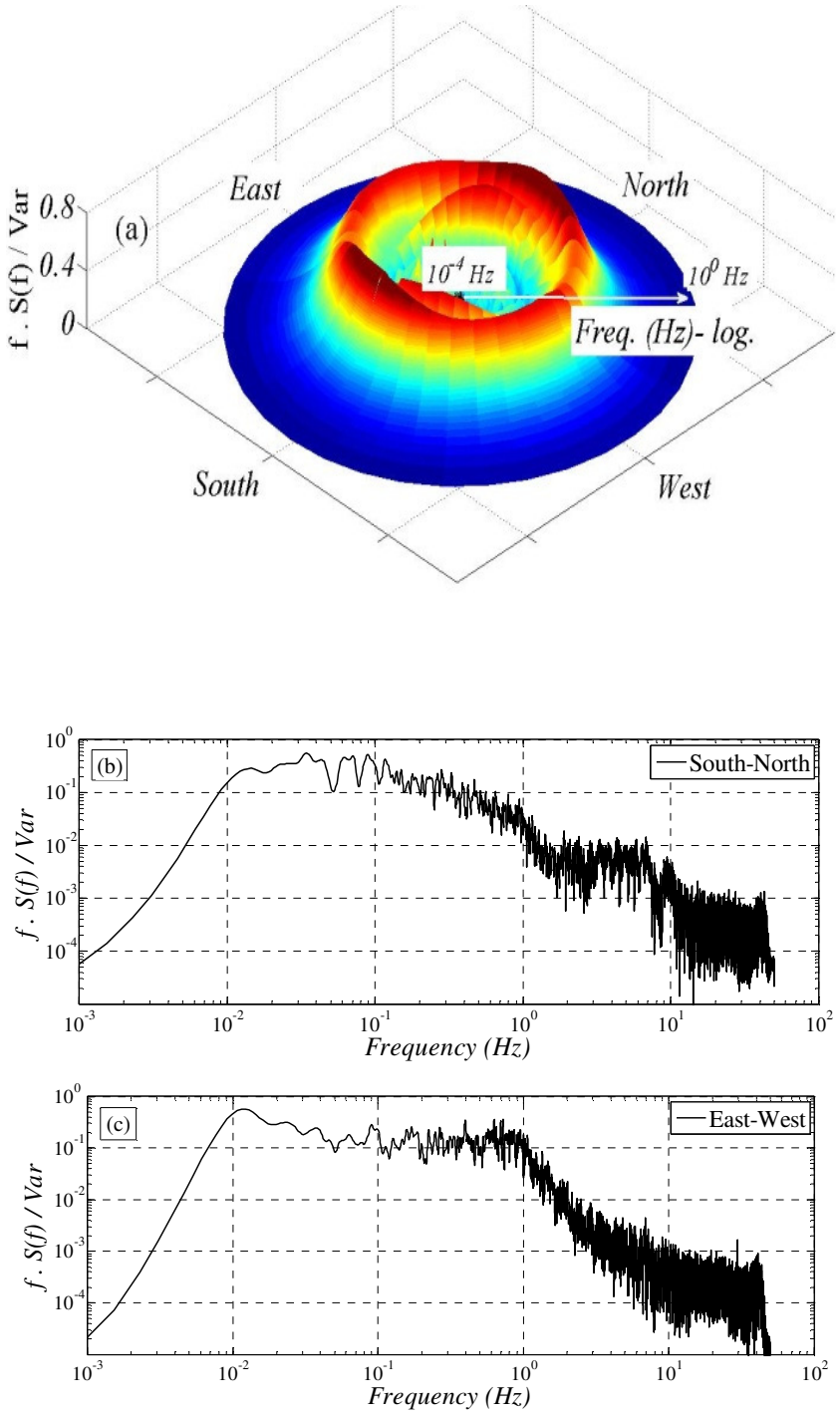

Figure 6.17. (a) Logarithmic spectrum of wind speed projected different directions, (b) and (c) logarithmic spectrum of wind speed in South-North and East-West directions respectively

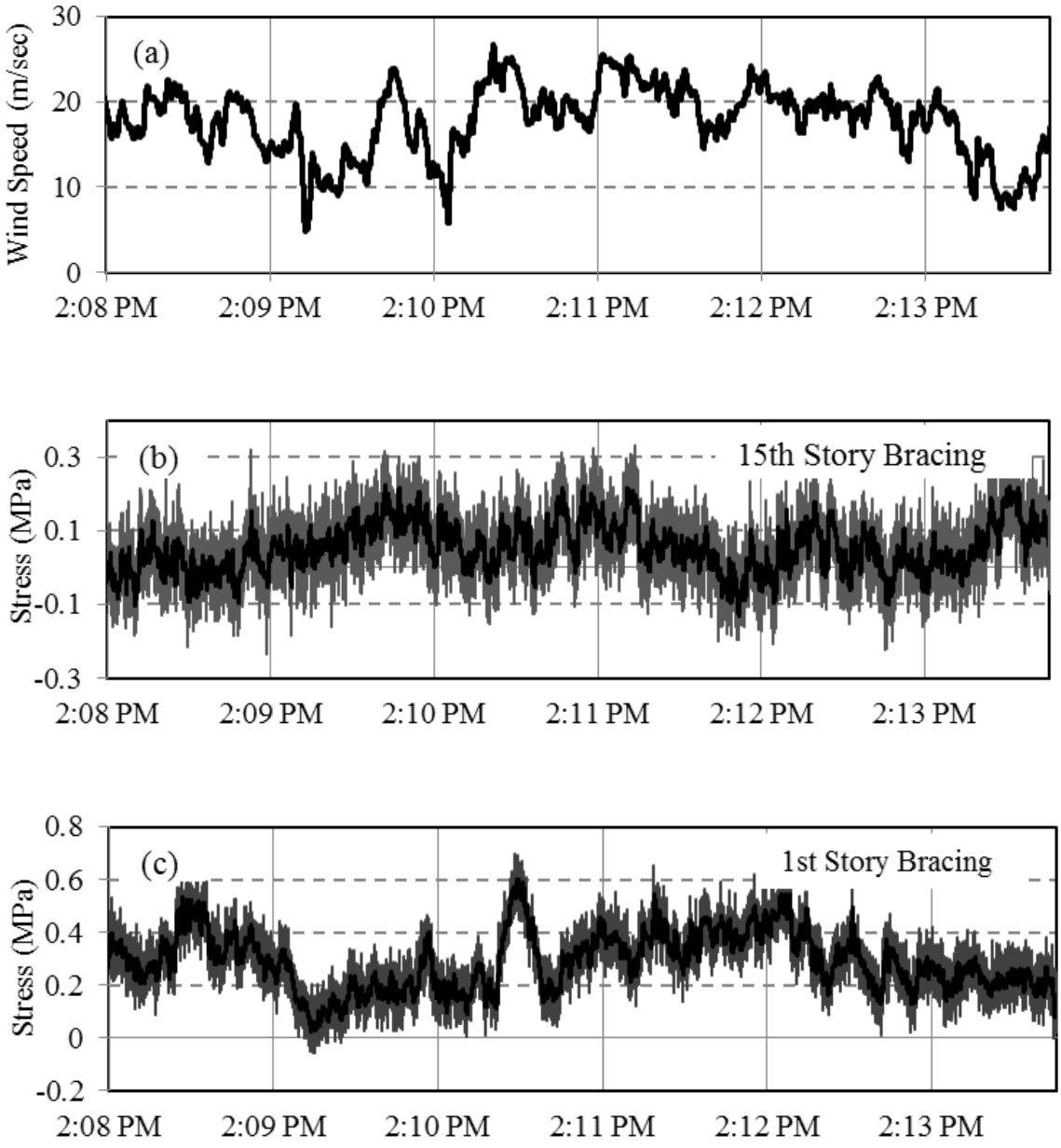

Figure 6.18. Stresses response at bracings (a) wind speed, (b) and (c) stresses in bracings of 15th and 1st floor, respectively

Table 6. 6. Peak measured stress in instrumented bracing members during high wind event November 23, 2011 2:10 PM (WS_{max} = 60 mph)

Bracing Location	Maximum Stress (ksi)
Line 8 – 15th story	0.07
Line 8 – 1st story	0.1
Line A – 1st story	0.09

Table 6.7. Peak measured acceleration at various elevations during high wind event November 17, 2011 between 11AM-12PM (WS_{max} = 31 mph)

Bracing Location	Maximum Acceleration (g)
Roof	<0.010
13th Floor	0.002
3rd Floor	<0.001

6.7.3 Structural Response – vibration Performance:

To evaluate the performance of the building in terms of lateral vibrations, the acceleration response is inspected. Figure 6.19-(a to c) shows an example of wind speed, wind direction and acceleration response time history data collected from the roof level. As can be seen in the figure, the peak accelerations are between 3 to 4 milli-g. The maximum acceleration during the period of measurement on the 3rd and 13th floor, and the roof level are also presented in Table 6.7.

For cross-verification of the measurement results, one wired accelerometer was located on the roof level (the same location as one of the wireless sensors) to measure lateral vibration and verify the measurements of wireless sensors. Having time stamps in

the collected data from wired and wireless sensors makes comparison of measurements possible. Figure 6.21 shows the power spectrum acceleration response from the two sensing systems (since the two sensors have different noise characteristics and different sampling rates it is more reasonable to compare measurements in frequency domain rather than time domain). It can be seen that both sensors show similar power spectrums and have agreement about the dominant frequencies of lateral vibration. The consistency confirms the reliability of measurements by these sensors.

The peak frequencies in the power spectrum plot are important in understanding of lateral vibration as well as in comparison of peak accelerations with the recommended limits (Figure 6.4). As can be seen in Figure 6.21, there are several dominant frequencies distributed in the range of 0-15 Hz, starting from 0.62 Hz which is the first identified natural frequency of the building. The vibration modes at each of the frequencies are presented later in the next section. For evaluation of vibration amplitude also, the limits are considered to be as low as the horizontal portion of the plot in Figure 6.4 as the lower frequencies are less than 2 Hz.

Since the limit for lateral vibration is in terms of RMS acceleration, the RMS of vibration is inspected. To identify RMS acceleration amplitude, a 100 seconds window is moved over the acceleration data, collected during high speed wind events, and the RMS of each window is calculated. The length of window is selected as 100 seconds since this length is believed to be a reasonable duration of steady vibration which may disturb human comfort (100 seconds is a conservative assumption as literature [Boggs, 1997]

suggests even longer durations [20 to 60 minutes]). The maximum RMS obtained from 100 seconds windows moved over the entire acceleration data is 1.2 milli-g, which is well below the limits of Figure 6.4 for all vibration frequencies. It shows that the lateral vibration issues are not as severe as the vertical vibrations.

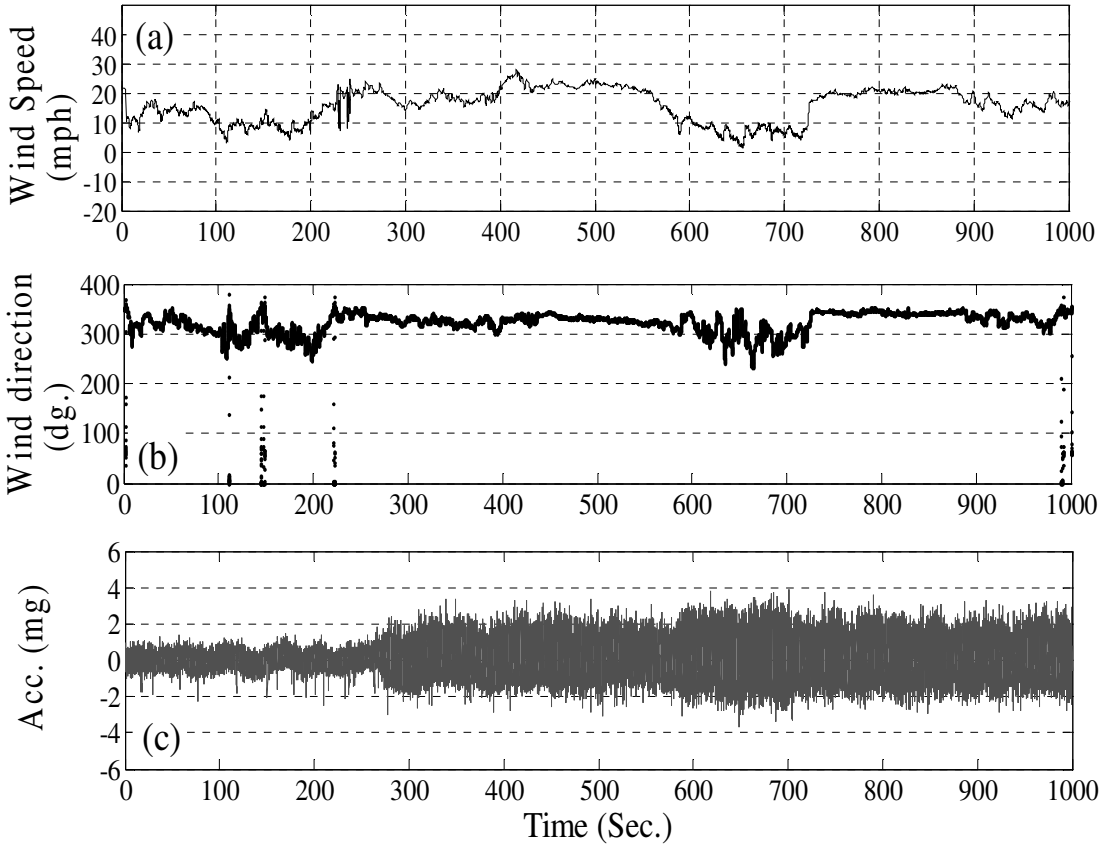

Figure 6.19. Sample building response to wind (a) wind speed, (b) wind direction, (c) acceleration at roof

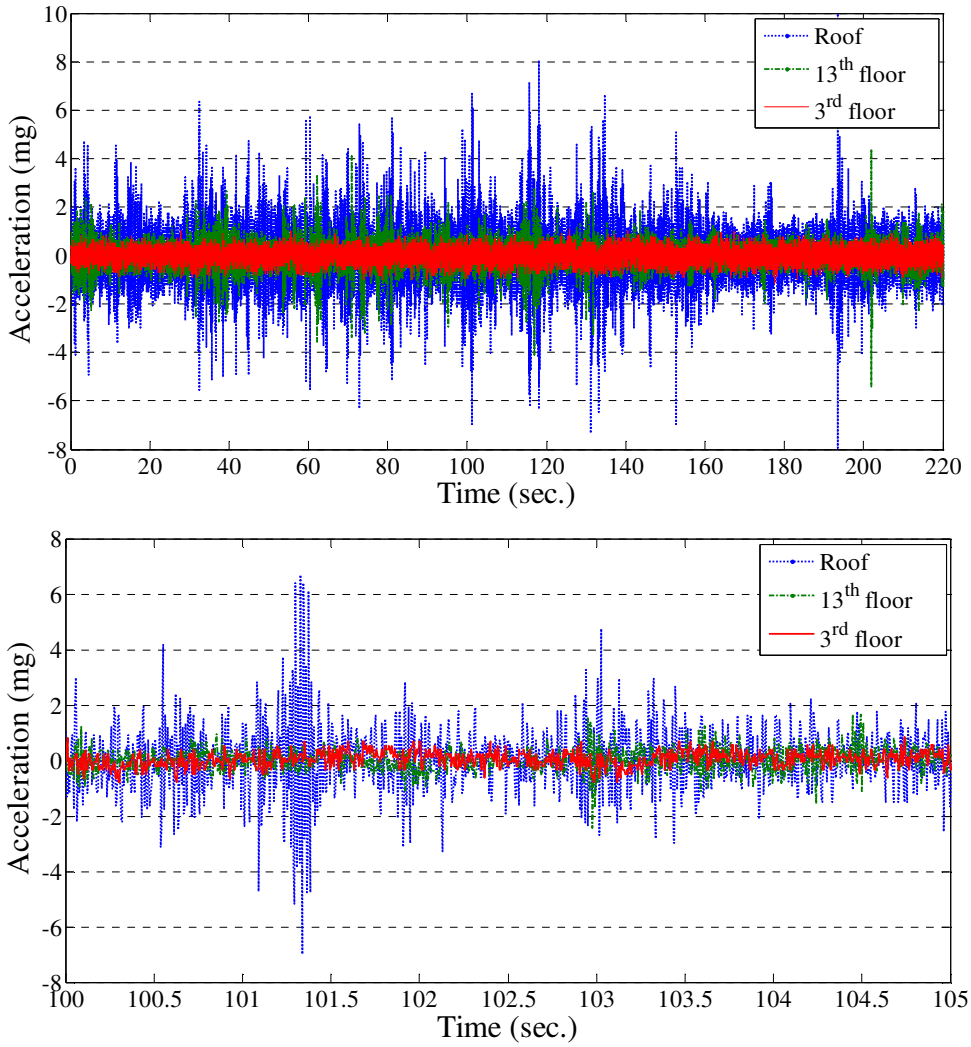

Figure 6.20. Acceleration time history measured by wireless sensors from lateral vibration of different floors on November 17, 2011

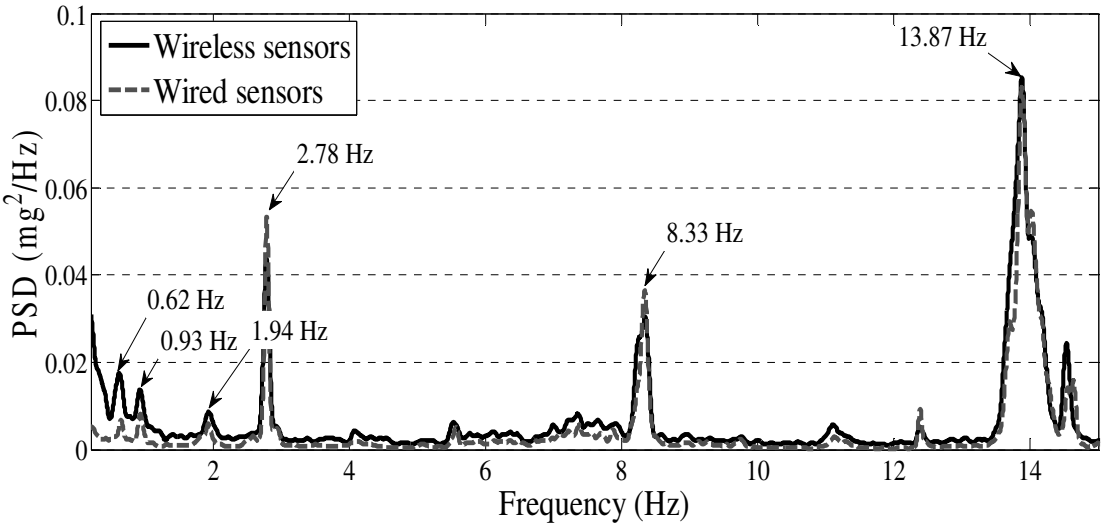

Figure 6.21. Power spectrum of the acceleration response at roof from wired and wireless sensors

To further investigate the lateral vibration of the structure and different modes of vibration, the acceleration data collected from wireless sensors at different stories is used in modal parameter identification in the next section.

6.7.4 Modal Parameter Identification:

This section presents the modal identification of the building using the measured data from different floors by the means of wireless sensors. For large structural systems, such as buildings structures, the excitation loads are usually not measurable and thus, output-only system identification algorithms are applicable. The assumption in output-only algorithms is that the excitation load is stationary stochastic process (as discussed in Chapter 2) and not a function of frequency. Although the wind load exhibits some frequency contents (as shown in the wind frequency spectrum), compared to the response

spectrum, the wind load is only a weak function of frequency. Therefore, wind excitation can be assumed as a stationary and stochastic input for output-only system identification (Brownjohn, 2003).

For modal identification of the structure, Auto Regressive (AR) time-domain algorithm (Ljuang, 1999) is selected. The methodology is explained in Chapter 2 and some of the estimated modeshapes are presented graphically in Figure 6.23. Since the sensors were located only on three elevations of the building (3^{rd}, 13^{th} floor and roof), the modal displacements of intermediate floors is not available. The limitation on sensor placement was imposed by building's accessibility. Therefore, modal displacement of only the 6 points (two N-E and S-E corners of each elevation) of the structure is shown in the mode shape plots. The lateral vibration modes of the structure can be categorized into flexural transverse and torsional modes based on the in-phase or out-of-phase modal displacements of sensors in two corners of the building. Using the results of modal identification, the type of vibration at each dominant frequency can be identified. It should be noted that the modeshapes identified through modal identification process are those that were properly excited by the ambient wind loads. From the Figure 6.23, it can be seen that most of the excited modeshapes are torsional modes. The torsional modes correspond to the peaks in the response power spectrum (0.93, 2.78, 5.567, and 14.53 Hz), presented in Figure 6.23. Considering the dominant torsional modes, it can be concluded that perceived lateral vibrations on the higher floors of the building are rooted mostly in torsional modes. This hypothesis is consistent with some diagonal cracks on the

claddings of the structure. A possible reason for such behaviour can be the configuration of lateral load resisting systems (bracings) in the structure's plan. As explained in the building's description, the braced frames in the East-West direction are located on the two outermost lines (north and south sides) in the plan and the braced frames in the North-South direction are located almost on the centrelines in the plan. The arrangement of the braced frames and the wind direction are shown in Figure 6.22, as well. The designed stiffness distribution does not provide much torsional resistance for the structure.

The evaluation examined different aspects of structural performance. Many of these results are obtained by only a limited measurement effort through the use of mobile wireless accelerometers. However, the combination of wired and wireless sensors was the key point which made a comprehensive sensing system for short-term and long-term vibration evaluation of the building structure.

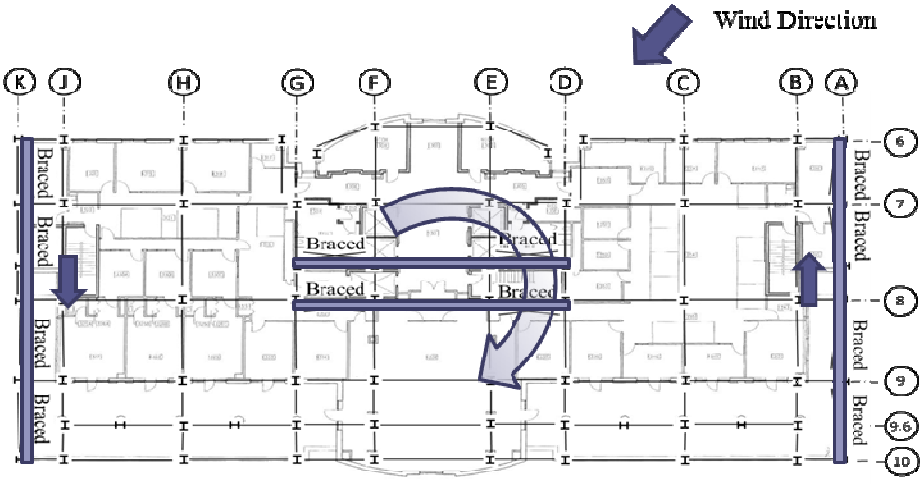

Figure 6.22. Wind direction with respect to the arrangement of Braced Frames

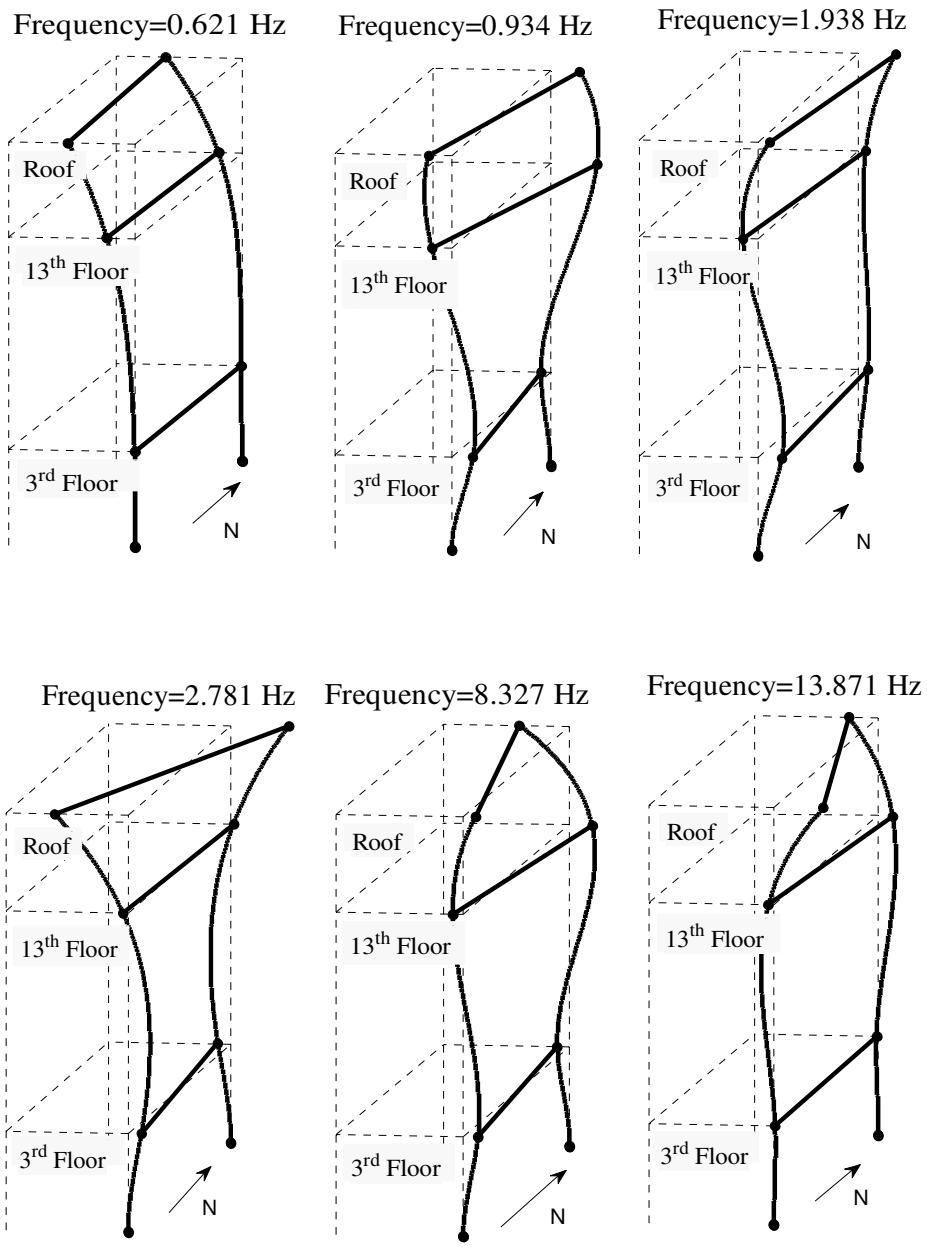

Figure 6.23. Identified modes of vibration

6.8. Summary and Conclusion of Field Deployment on the Building Structure

This chapter presented the integration and deployment of a comprehensive sensing system which is used for evaluation of a building's vibrations. The sensing system

included two networks of wired and wireless sensors providing an effective tool for capturing different types of structural responses. This integration of wireless and wired sensor networks represents the state of the art sensing for structural health monitoring. Integrated in the sensing system were accelerometers, strain gages, displacement sensors and anemometers. Utilizing different sensor types with relatively high spatial and temporal resolution enabled reliable evaluation of the building's performance.

It is shown that the application of the wireless accelerometer sensors significantly facilitates measurement of structural response from different locations. The ease of installation due to the absence of wiring was a major advantage in wireless sensors as valuable information about the structure's performance is obtained with minimal efforts. Deployment of the sensing system demonstrated that wireless mobile accelerometer networks are effective tools for forensic quantification of building vibrations. However, some challenges associated with the use of wireless sensors, such as limitation due to finite battery life and the communication problem in the presence of obstacles, make the application difficult for long term monitoring of building structures, requiring the deployment of wired sensors for this purpose. Complementing the sensing system by the traditional wired sensors further enhanced the capability of the sensing system in capturing the structural response. Wireless sensors were relocated multiple times for measuring acceleration response from various locations and the wired sensors were placed on the fixed locations and monitored the response for a long duration.

The wired sensors were programmed specifically for automatic data collection during different events such as the occurrence of a high speed wind or an aerobics class in the building. Reliable data characterizing the structure's response to different dynamic excitations provided the needed information for the assessment of the structure's performance.

The collected data was analysed with different data processing techniques (e.g., time- and frequency-domain data analysis, spectrum analysis, and modal identification) to extract different characteristics of the loads and the structural response. Dynamics of the floor vibrations, the structural demands under various loading conditions, the wind spectra and response spectra, and the modal parameters of the structure are important results obtained using collected data. The three-dimensional wind spectrum is developed to reflect the logarithmic power spectrum of the wind in different directions. The wind spectrum which is developed in this dissertation assisted in determination direction-dependent frequency contents of the wind and showed that the wind–induced vibration will overlap with fundamental vibration frequencies of the building. Transmissibility of the vibration in this particular structure is investigated and it is observed that the floor system damps the vibration more efficiently compared to the vertical system, as the level of vibration decreases with a higher rate in floors compared to height. Applying the results of data processing and available standards, along with engineering insights, the vibration performance of the building structure is evaluated. The evaluation showed that the performance of the structure under human induced vibration effects is not

satisfactory, in terms of serviceability, as the vibration amplitudes in some locations of the building exceed the maximum comfort limits. However, the strengths of structural components are well above the demands by the measured stresses. The evaluation of the structural response to wind showed that the lateral vibration performance of the building meets the limits in terms of strength demand as well as serviceability. Moreover, inspection of the response spectrum along with the results of modal identification showed that the torsional modes of vibration dominate the response, as compared to flexural modes.

The investigation indicates that the vibration-induced stresses are low under all conditions studied and are not a significant concern. The accelerations measured through the structure indicate that the aerobic activity does induce significant accelerations through the structure. During the period investigated the accelerations induced on the 16th floor down to the 12th floor were perceptible. While this activity will not result in any likely damage to the building the effect on human comfort is significant. To alleviate the exercise-induced vibration two options are proposed: (i) isolate the aerobics floor. The transmission of accelerations is due to the activity on the 16th floor slab. Floating slab systems are commercially available which allow for isolation of a floor from the rest of the building. These systems typically work through the use of a built up floor supported by springs connected to stiff regions of the existing floor. This can be accomplished easily; however, the additional load of the system would need to be compared to the strength of the existing floor system to ensure that the additional weight can be safely

supported. (ii) Re-locate the aerobics class. Moving the exercise area to a lower portion of the building where the floor framing is stiffer and heavier would reduce (but not eliminate!) the acceleration transmission to other portions of the structure.

Chapter 7

Field Deployment - Application of wireless sensors for vibration monitoring of a steel truss bridge structure

7. Application of wireless sensors for vibration monitoring of a steel truss bridge

7.1. Introduction

This chapter presents field deployment and structural identification of a wireless sensor network on a steel bridge. In this work, the vibration of a steel truss bridge is monitored throughout a year in different environmental and operational conditions. The objective of the project was to identify the dynamic characteristics of the bridge through modal testing, and also to observe the variability of results due to the changes in environmental and operating conditions of the bridge. For this purpose, the vibration of the bridge is measured multiple times in different seasons while the temperature and the number of vehicles passing the bridge were recorded at the time of each test. Having the modal parameters identified from separate data sets, a statistical study could be performed which provides the mean and standard deviation of the identified parameters. Besides, the possible dependency of the identified parameters on the mentioned variables can be assessed. Furthermore, this chapter presents an attempt towards constructing the Finite Element model of the bridge and updating the modelling parameters based on the estimated modal frequencies. For finite element model updating, sensitivity based algorithm is used.

7.2. History and Specification of the Bridge

The Northampton Street Bridge was open in October of 1806. The original bridge was a wooden structure and replaced the ferry, which crossed the Delaware River from

Easton, Pennsylvania to Phillipsburg, New Jersey, up until the nineteenth century. This original wooden design, built by Timothy Palmer, lasted until the late nineteenth century when the demand on the bridge changed from horse-drawn streetcars to trolley cars. In order to meet the demand of this new traffic pattern, a new steel cantilevered-truss bridge was designed by James Madison Porter III. In August of 1955, the Northampton Street Toll Supported Bridged sustained major damage during the floods following Hurricane Diane. Repairs were made over the next few years, but the flood damage left a noticeable sag in the center span of the bridge that can still be seen today. Most recently, the Northampton Street Bridge underwent renovation in the summer 2002. The improvements included a structural steel repair, painting, and the installation of a pedestrian sidewalk with railings.

Today the bridge has a three-ton weight limit, restricting traffic to only small vehicles. It is held up by two piers that support two 125 foot cantilevers. The bridge can facilitate traffic due to three lanes for motor vehicles as well as pedestrian walk ways on both the North and South side. Although not a toll bridge, the Northampton Street Bridge is maintained by the Delaware River Joint Toll Bridge Commission.

The current structure of the bridge, shown in Figure 7.1, has a total span of 550 (ft) supported by 2 piers. The span is divided into 25 (ft) sections such that each pier supports a 125ft cantilever on both sides and a 50 (ft) (two panels) section is suspended between them. The width of the bridge is 36 (ft) from center-to-center of the trusses, with a 9 (ft) sidewalk on either side.

Figure 7.1. A view of the Northampton St. Bridge

7.3. Wireless Sensor Network

A network of 20 Imote2 wireless sensors is used for this monitoring project. The sensor board which is utilized for measuring the acceleration is SHM-A. Specifications of both Imote2 and SHM-A sensor board are presented in previous chapters (Table 6.1 in Chapter 6). The sensors were installed across the bridge to capture its vibration under ambient loads during tests in vertical and transverse directions. The implementation plan for the sensor networks on this bridge is shown in Figure 7.2. The locations of sensors are

selected such that they capture enough information to provide the modal parameters of the bridge, including modeshapes, with a proper resolution. Seventeen sensors are located on the south-side of the bridge, along the main and the two short spans, and three sensors are selected to be on the opposite side (north-side) along the main span. This arrangement allows for extraction of different types of modeshapes including flexural bending and torsional modes.

To attach the sensors to different locations on the bridge a magnet bracket was assembled, as shown in Figure 7.3. This configuration made the installation of sensors very convenient. The vibration monitoring tests were conducted multiple times throughout a year. The magnet-bracket configuration allowed for quick installation of the sensors and therefore, the sensors were attached and detached before and after each testing trip. The locations of the sensor where determined and tried to be constant through the different tests. To assure the alignment of the sensors, a handy electronic level was used. The alignment is an important issue in installation as it can bring some random scaling in the amplitude of measured acceleration responses.

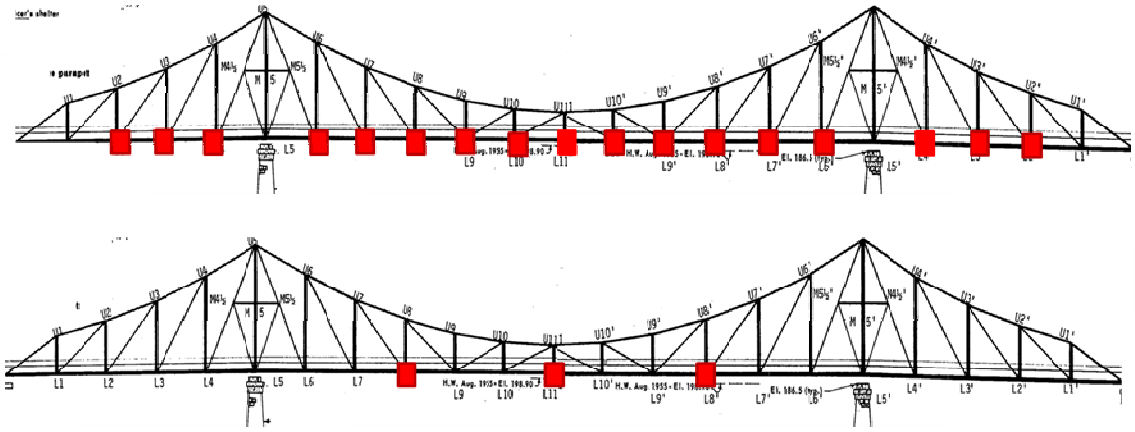

Figure 7.2. Sensor locations along the bridge

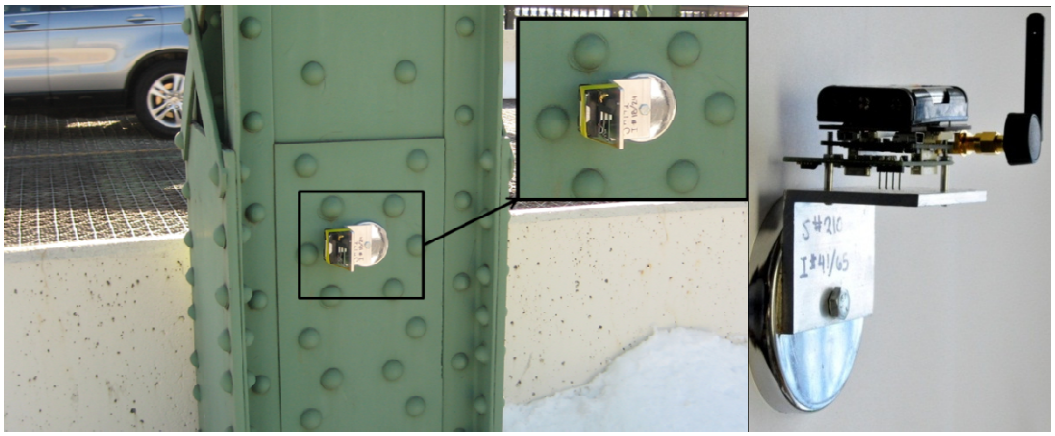

Figure 7.3. Sensor attachment using magnet connections

To have an estimate of the performance of the radio communication and to determine the sensor arrangement on the bridge, a set of radio tests (Linderman et al. 2010) are conducted on the network to indicate the strength of the radio signals, which transmit data between the base station and the remote nodes, in terms of the percentage of package loss during communication. Results of the test are shown in Figure 7.4. Since the sensor units were attached to the web of the columns, a number of sensors are not in line-of-sight with the base station. As it can be seen in Figure 7.4, for these sensors, the percentage of package loss in transmission is relatively high. However, incorporating

reliable data transfer protocol in data transmission permits having somewhat low signal strength in the network and still send and receive the data in the network.

For cross verification of results a network of wired sensors is also used during one of the field tests. The wired sensor network included seven accelerometers connected to a data acquisition system. The accelerometers are low noise Silicon Design 2210-002 with ±2g acceleration range. The data acquisition system was PDAQ Premium data acquisition system from DIGITEXX with 16 Channels for voltage input from different sensors types measuring acceleration, strain, wind speed/direction, temperature. This system integrates an analog filter with 24 bit resolution. The software which retrieves and converts data is Digitexx. Figure 7.5 shows the data acquisition system and a SD 2210 accelerometer.

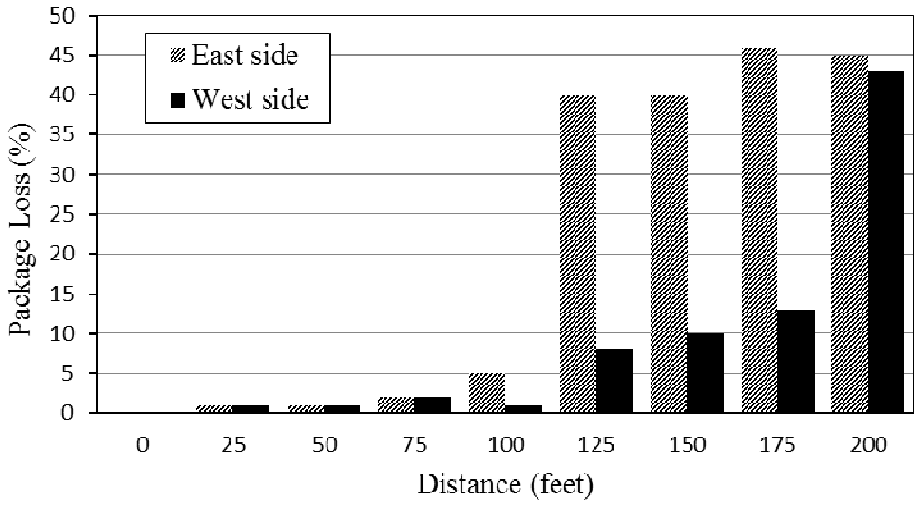

Figure 7.4. Package loss percentage vs. distance for the implemented wireless sensor configuration

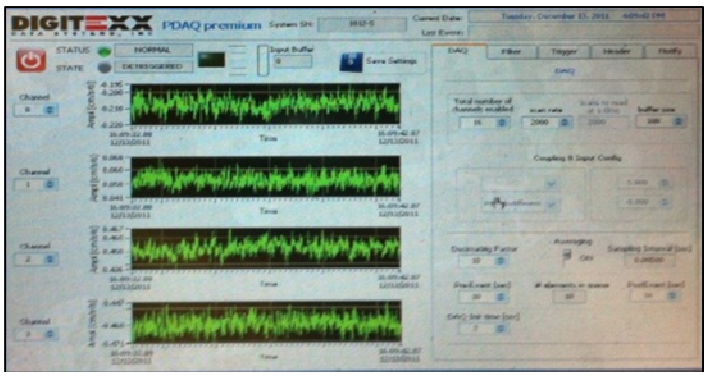

Figure 7.5. PDAQ data acquisition from Silicon Design 2210 accelerometer

7.4. Data Processing

Before performing modal identification, it is important to pass the data through a pre-processing. The main pre-processing tasks are filtering of the data and linearly de-trending the data. As the name suggests, the filtering step serves to filter out high frequency noise, such as those from unwanted environmental vibrations, so as to allow for the data to focus on the lower frequency content of the signals that correspond to the response of the structure to the excitation. Similarly, the data is de-trended to set the mean at zero.

The data are collected from wireless sensors by 280 Hz sampling rate (3.6 milli-sec. time intervals) and are passed through on-board analog and digital filters. The on-board digital filter has cut-off frequency of 140 Hz. The collected data is further filtered with cut-off frequency of 70Hz through a *cheby2* filter. The data from wired sensors are collected using 200 Hz sampling rate (5.00 milli sec. time interval) and are passed through the same filter as for wireless sensors. Figures 7.6 and 7.7 show the time-history

and power spectrum of an example acceleration data collected from the seven wired and the seven wireless sensors located along the main span. The collected data from the two sensor network are consistent and comparable. The different noise characteristics of the different utilized accelerometers in each sensing network make the frequency responses slightly different. This difference is basically negligible in identification of the modal properties. However, the identified modal properties may have different accuracy and purities. This topic is discussed with details in Chapter 4.

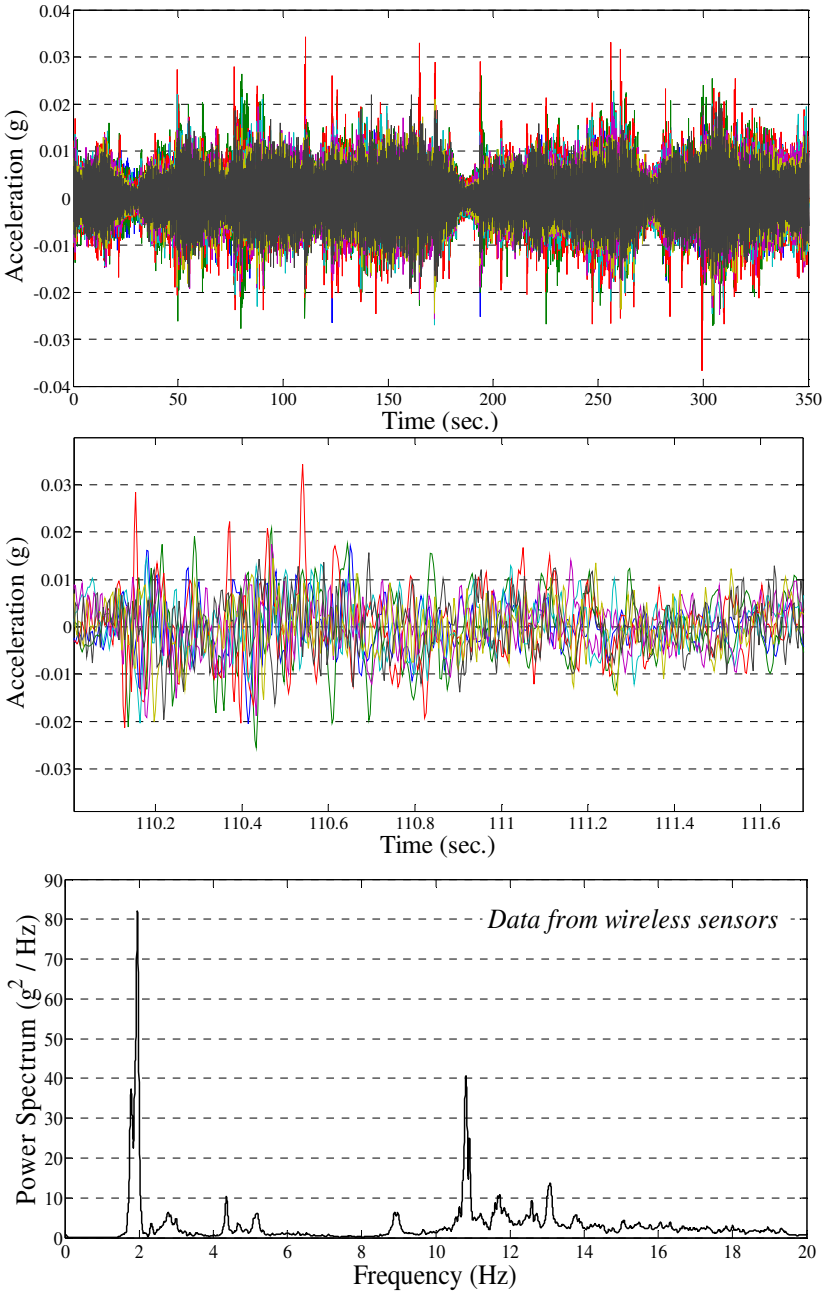

Figure 7.6. Acceleration data from wireless sensor data

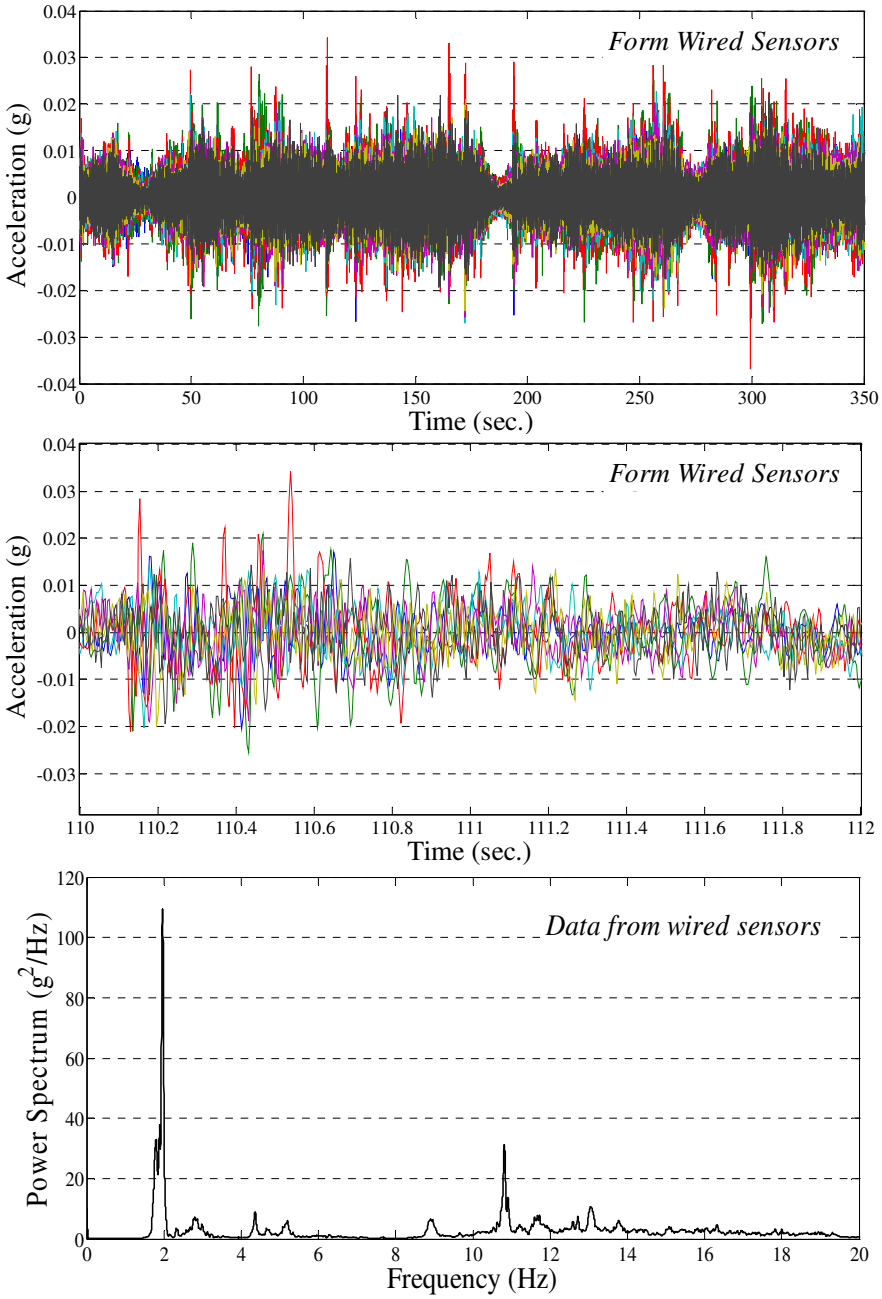

Figure 7.7. Acceleration data from wired sensors

7.5. Modal Parameter Identification

As the main objective of the dynamic testing of a structure, modal properties are aimed to be identified. In most of the civil infrastructure, the excitation is not measured and therefore, output-only system identification algorithms are the only applicable algorithms. The advantage of such algorithms in the bridge monitoring is that the data collection can take place anytime, when the bridge is under the random ambient and traffic loads.

Modal parameter identification of the bridge is performed using different time and frequency domain algorithms. The utilized algorithms are Frequency Domain Decomposition (FDD) algorithm, Eigen Realization Algorithm (ERA-NeXT, -OKID, and -Average) (for ERA-OKID and ERA-Avg, the reader is referred to Change et al. 2012), Auto Regressive (AR), and N4SID. Different algorithms have different time-efficiencies and accuracies. However, the different accuracy also depends on the characteristics of the data and the testing conditions (e.g. the length of data or the randomness of the ambient input). Except the FDD algorithm, the identification algorithms and corresponding results also depend on the selected model order as described in Chapter 2. Using the stabilization diagram, the optimum order can be found and from that the modal properties can be extracted. As an example, Figure 7.8 shows the stabilization diagram for the identification of the bridge modal properties in vertical direction using AR algorithm. Similar plots are extracted for other time-domain algorithms named above. As explained in Chapter 2, the stabilization diagram requires threshold values to determine the stable

order which is defined as the deviation of natural frequency, modeshape, and damping ratio in order *p* from the order *p-1*. In this work these values are selected as 5% and 20% for frequency and damping ratio, and 95% for MAC value of identified parameters in two consecutive orders.

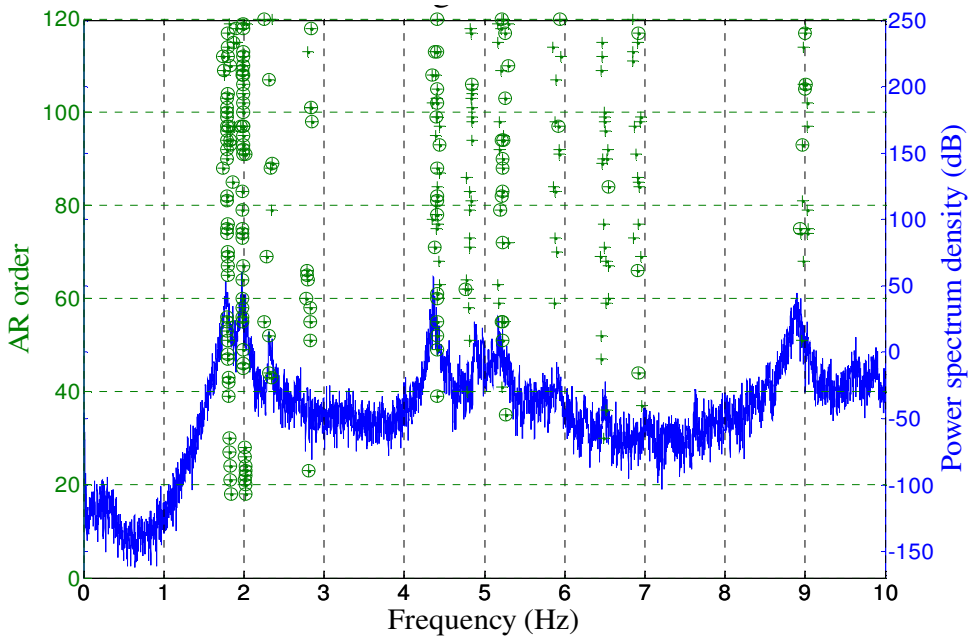

Figure 7.8. Stabilization diagram for model order selection for vertical direction in AR algorithm

For comparison of the results of modal parameter identification using different algorithms, the FDD is selected as the reference algorithm and the results of other methods are compared to the results of this method. FDD is selected as the basis of comparison as it does not need model order selection. Details of this method are explained in Chapter 2.

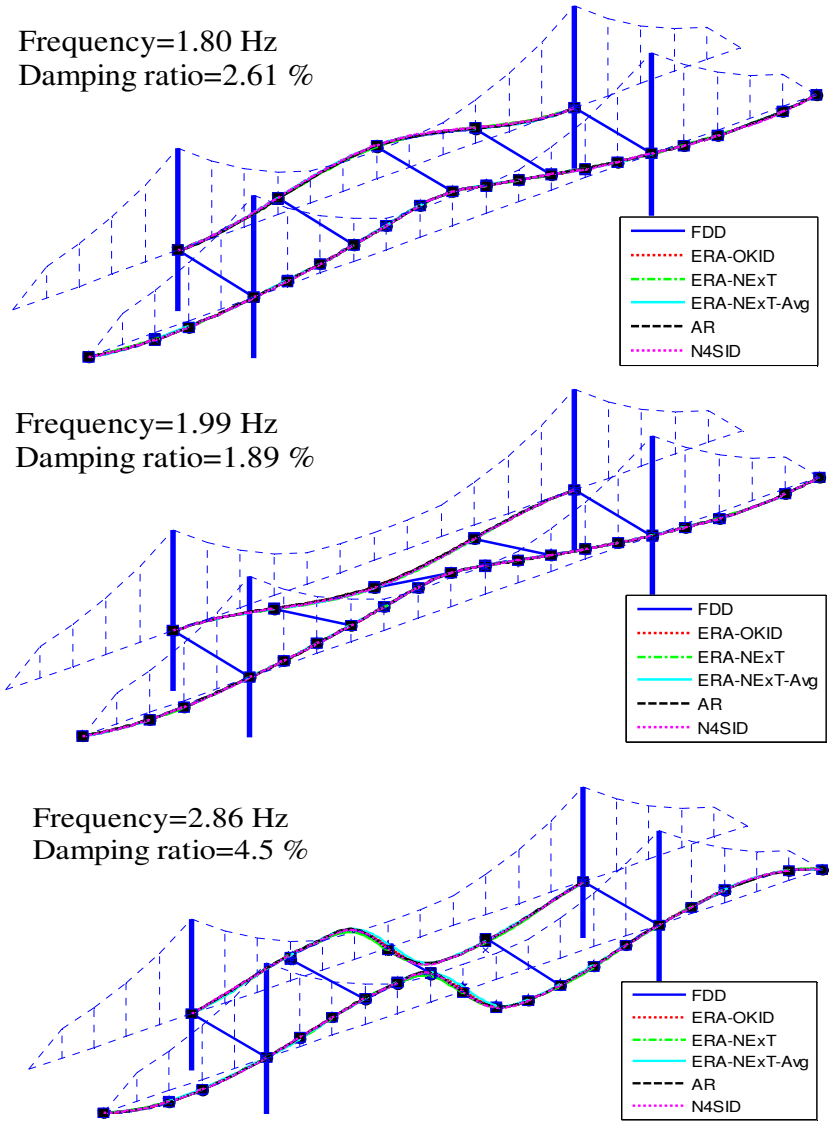

Figure 7.9. Estimated modeshapes using different algorithms

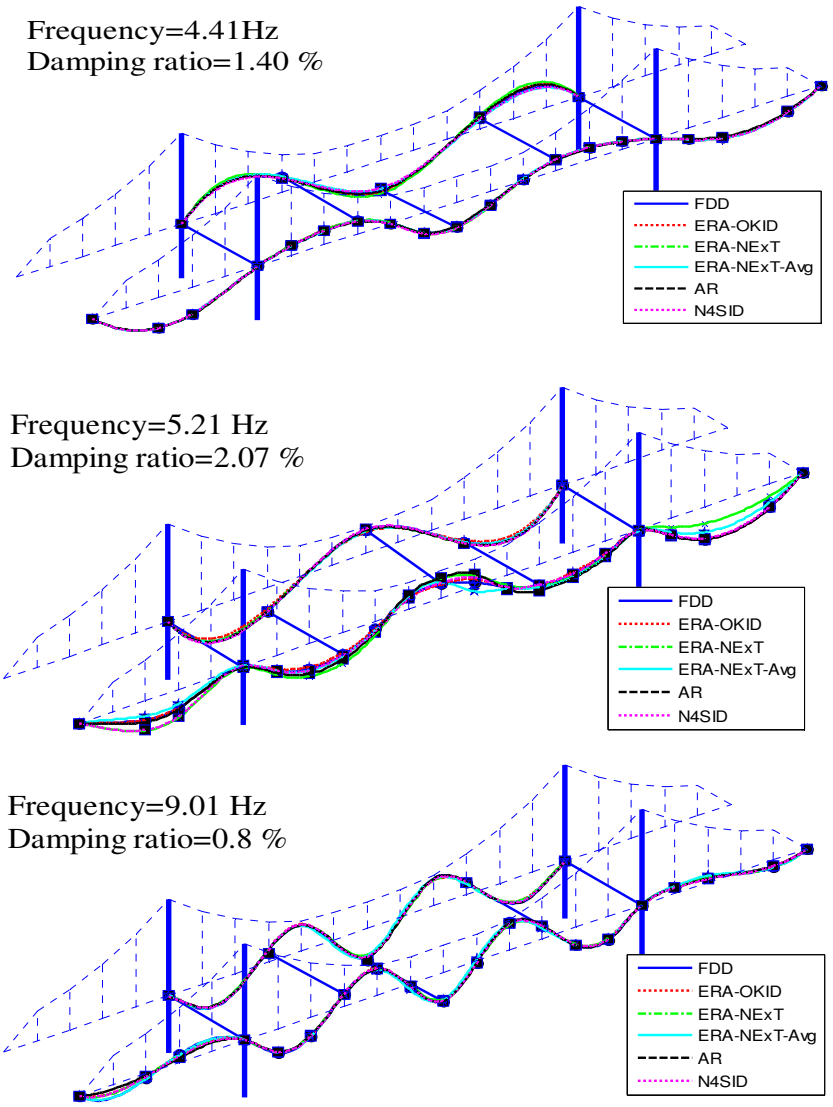

Figure 7.9 (Cont'd). Estimated modeshapes using different algorithms

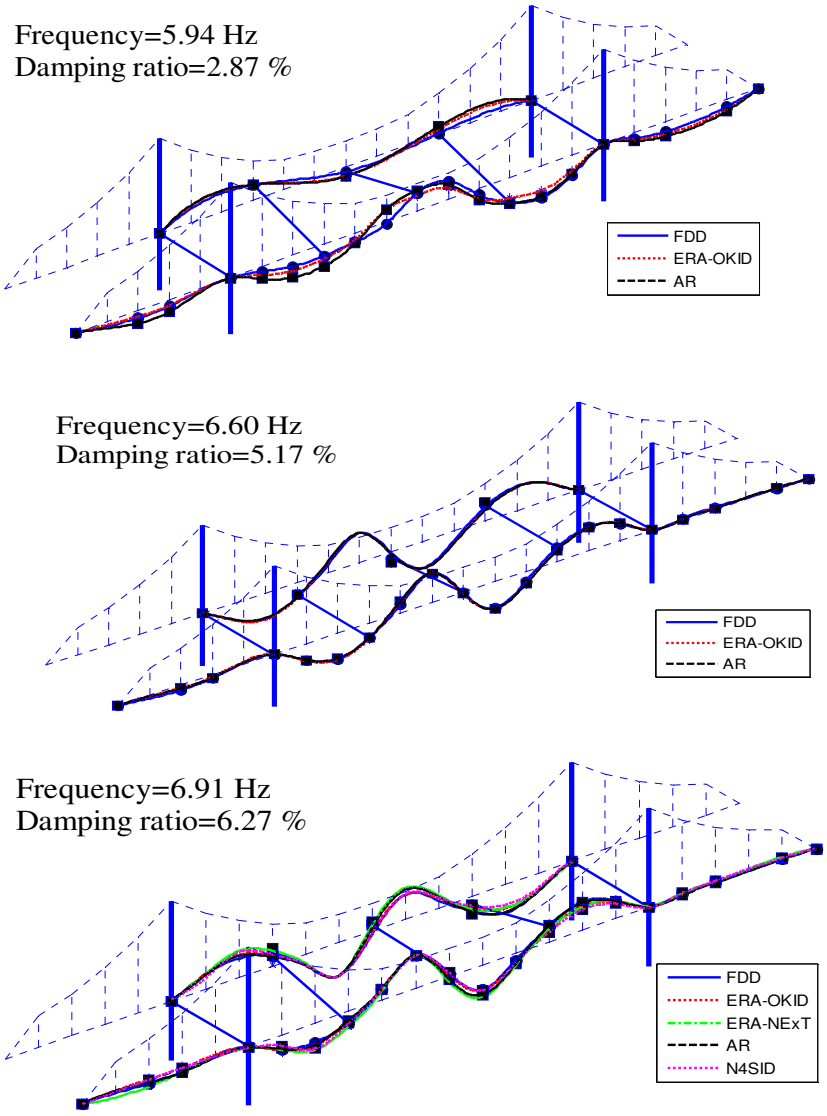

Figure 7.9 (Cont'd). Estimated modeshapes using different algorithms

Table 7.1. Frequencies estimated using different algorithms

Frequency (Hz)	Mode 1	Mode 2	Mode 3	Mode 4	Mode 5	Mode 6	Mode 7	Mode 8	Mode 9	Mode 10	Mode 11	Mode 12	Mode 13
FDD	1.801	1.993	2.856	4.407	4.742	5.208	5.360	5.939	6.597	6.906	7.680	9.008	9.414
AR	1.822	2.015	2.837	4.407	4.728	5.220	not id'ed.	5.993	6.533	6.968	not id'ed.	8.994	9.388
ERA-NExT	1.824	2.006	2.851	4.420	4.701	5.210	not id'ed.	not id'ed.	not id'ed.	6.937	not id'ed.	9.022	not id'ed.
ERA-NExT-Avg	1.796	1.990	2.887	4.407	4.731	5.247	5.355	not id'ed.	not id'ed.	not id'ed.	7.679	9.022	not id'ed.
ERA-NExT-OKID	1.791	2.018	2.815	4.411	4.721	5.215	5.395	6.004	6.474	6.932	7.724	9.004	9.372
N4SID	1.811	1.979	2.819	4.411	4.721	5.184	not id'ed.	not id'ed.	not id'ed.	6.975	not id'ed.	8.991	not id'ed.
Deviation (%)	0.68	0.70	0.86	0.10	0.26	0.36	0.33	0.48	0.76	0.36	0.27	0.14	0.19

Table 7.2. Damping ratios estimated using different algorithms

Damping ratio (%)	Mode 1	Mode 2	Mode 3	Mode 4	Mode 5	Mode 6	Mode 7	Mode 8	Mode 9	Mode 10	Mode 11	Mode 12	Mode 13
AR	2.609	1.891	4.513	1.400	2.269	2.066	not id'ed.	2.872	5.173	6.264	not id'ed.	0.796	1.141
ERA-NExT	3.742	1.398	5.500	1.049	1.039	2.118	not id'ed.	not id'ed.	not id'ed.	3.729	not id'ed.	0.737	not id'ed.
ERA-NExT-Avg	2.084	1.177	3.620	0.536	1.325	1.575	0.521	not id'ed.	not id'ed.	not id'ed.	0.139	0.329	not id'ed.
ERA-NExT-OKID	2.057	1.925	4.695	1.052	1.472	1.792	1.989	3.052	4.948	3.194	2.863	0.963	1.232
N4SID	3.194	1.190	6.731	1.248	1.682	3.217	not id'ed.	not id'ed.	not id'ed.	3.638	not id'ed.	0.875	not id'ed.
Deviation (%)	23.80	21.72	20.89	27.59	26.52	26.31	58.51	3.05	2.22	28.65	90.74	29.59	3.80

Table 7.3. MAC values of modeshapes (vs. FDD results), estimated using different algorithms

Modeshapes MAC value (vs. FDD)	Mode 1	Mode 2	Mode 3	Mode 4	Mode 5	Mode 6	Mode 7	Mode 8	Mode 9	Mode 10	Mode 11	Mode 12	Mode 13
Frequency (Hz)	1.808	2.000	2.844	4.410	4.724	5.214	5.370	5.979	6.535	6.944	7.694	9.007	9.391
AR	1.00	1.00	1.00	1.00	0.99	0.98	not id'ed.	0.82	0.99	0.98	not id'ed.	0.99	0.99
ERA-NExT	1.00	1.00	0.99	1.00	0.99	0.91	not id'ed.	not id'ed.	not id'ed.	0.93	not id'ed.	1.00	not id'ed.
ERA-NExT-Avg	1.00	1.00	0.99	1.00	1.00	0.97	0.94	not id'ed.	not id'ed.	not id'ed.	0.98	0.99	not id'ed.
ERA-NExT-OKID	1.00	1.00	1.00	1.00	1.00	1.00	0.81	0.78	0.99	0.97	0.96	1.00	0.99
N4SID	1.00	1.00	1.00	1.00	1.00	0.98	not id'ed.	not id'ed.	not id'ed.	0.91	not id'ed.	1.00	not id'ed.
Deviation (%)	0.02	0.01	0.47	0.07	0.30	3.31	7.11	2.34	0.11	3.07	1.35	0.11	0.04

Figure 7.9 shows the estimated modeshapes of the bridge, extracted from different algorithms. The first 6 modeshapes presented in Figure 7.9 show the modeshapes which are identified with all the applied algorithms. The rest of the modeshape plots however, show those modes which could be identified using only a few of the algorithms. In the other words, some of the algorithms have not been able to identify those modes with the consistency that the threshold level of the corresponding stabilization diagram requires. Table 7.1 through 7.3 also present the estimated modal parameters (frequencies, damping ratios, and modeshapes MAC values as compared to FDD modeshapes) using different algorithms. The results for the modes which are not identified through some of the methods are presented as "*not id'ed*". The last row in the tables presents the normalized standard deviation (σ/μ) of the estimated values. It can be realized that the identified frequencies and modeshapes are quite consistence (normalized standard deviation are less than 1%) whereas the damping ratios have significantly higher deviation (up to 30% for those that are estimated using all the algorithms).

The variation of results, shown in Tables 7.1 through 7.3, highlights the existence of an uncertainty in the identification of bridge's dynamic characteristics. Beside the effects of selection of identification algorithm, there are other sources that impose uncertainty to the results. The most important ones are the environmental and operational conditions (EOCs). In particular, the amount of traffic load and the ambient temperature are important EOC parameters for modal identification of the bridge structures. The effects of the two mentioned parameters are discussed in the next section.

7.6. Effects of Temperature and Traffic Loads

Dynamic characteristics reflect the global structural behavior of the system and therefore any change in their value can reflect the structural change and can be used in the performance evaluation and health assessment of the system. Modal parameters of constructed structures are estimated through vibration monitoring and applying system identification algorithms on the measured responses, and as mentioned in the previous section, there are uncertainties associated with this process. Some of the uncertainties are rooted in the natural randomness of testing (e.g. noise in measurement and randomness in the ambient vibrations) and some are rooted in the environmental and operational condition changes (e.g. temperature and traffic load changes). While the ultimate goal would be to eliminate or minimize the uncertainty in the estimation process, the fundamental step towards this goal is to study different sources of uncertainty and provide understanding about their impact on the results of modal parameter identification.

Table 7.4. Recorded temperature and number of vehicles during the ambient tests of Northampton Bridge

Test number	Temperature (F)	Number of Cars
1	58	168
2	59	135
3	59	153
4	59.7	149
5	60.4	154
6	63.7	154
7	70.9	162
8	67.5	177
9	61.9	174
10	50.9	126
11	52.3	131
12	53.2	103
13	43.2	97
14	43.2	91
15	44.4	86
16	51.5	122
17	50.2	117
18	48.6	146
19	44.6	112
20	43.3	112
21	43.3	120
22	46	132
23	46	157
24	45	150
25	58.1	91
26	59.5	116
27	57.6	88
28	62.1	60
29	57.9	49
30	58.5	52
31	56.3	128
32	55	107
33	79	62
34	79	94
35	77.5	100
36	92.3	114
37	91.8	118
38	92.3	132
39	74.5	42
40	72.3	42
41	70.9	38
42	71.2	21
43	85.1	119
44	77.4	114
45	77.9	84
46	79.7	113
47	58.6	84

Having the vibration data of the bridge in a wide range of temperature and traffic load in different ambient tests, the variation of modal parameters of the bridge can be observed and their correlation with the temperature and traffic load can be estimated. The range of temperature in which the data is collected from is from 43.2 to 92.3°F and the numbers of passing vehicles are from 21 to 171. Table 7.4 lists the temperature and the number of passing vehicles recorded throughout the vibration test in different tests.

To evaluate the effect of each of the two parameters on the modal parameters, the correlation between the identified frequencies and the two investigated parameters, temperature and traffic load, are estimated as:

$$R = \frac{E[(X-\bar{X})(Y-\bar{Y})]}{\sigma_X \sigma_Y} \tag{7.1}$$

where X and Y are the two parameters that their correlation is estimated (e.g. the first identified frequency and the ambient temperature), $\bar{X}$ and $\bar{Y}$ are the mean values, and σ_X and σ_Y are also their standard deviations.

Figure 7.10 shows dispersion of estimated frequencies as functions of temperature, along with the mean value and the standard deviation of the frequencies and the correlation with the temperature.

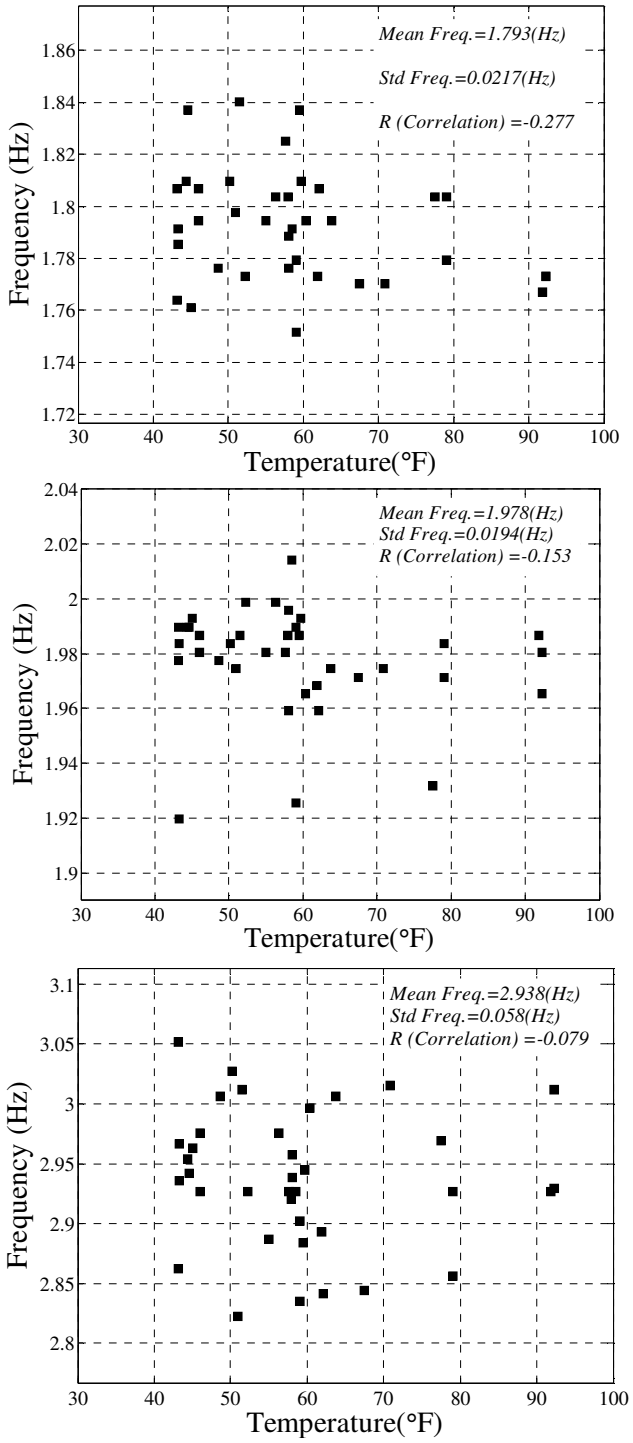

Figure 7.10. Estimated frequencies versus ambient temperature

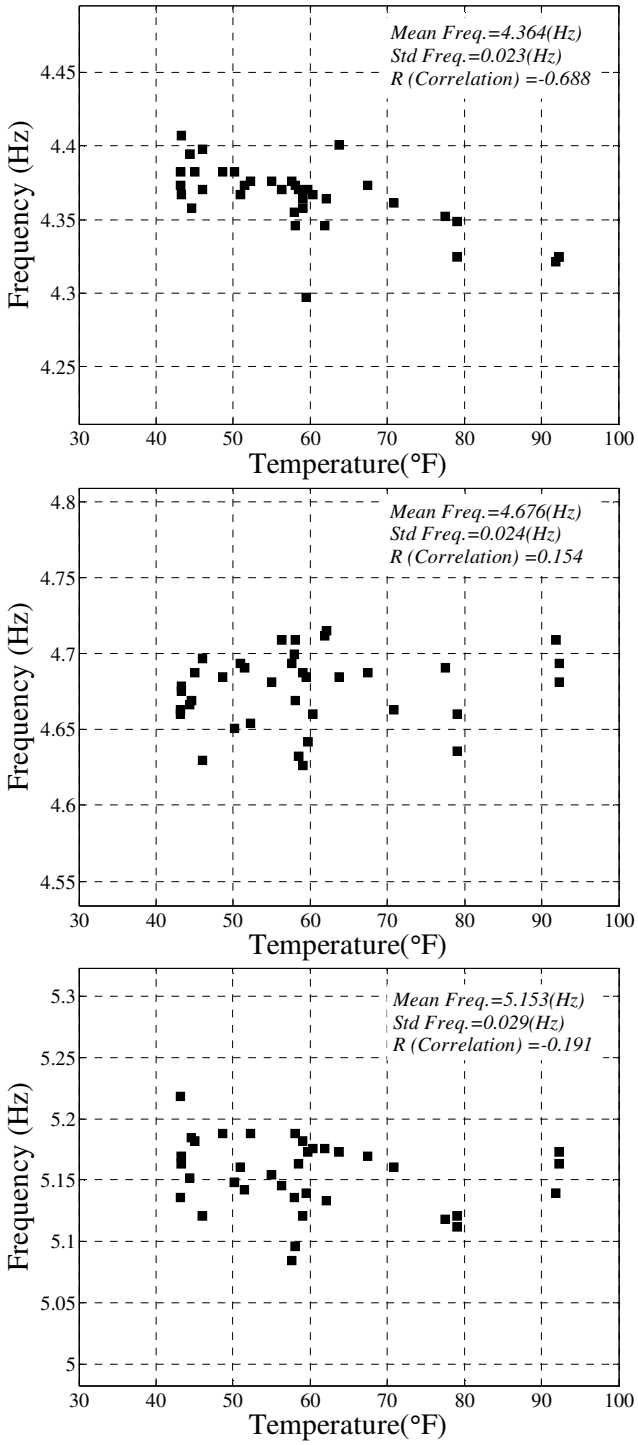

Figure 7.10 (Cont'd). Estimated frequencies versus ambient temperature

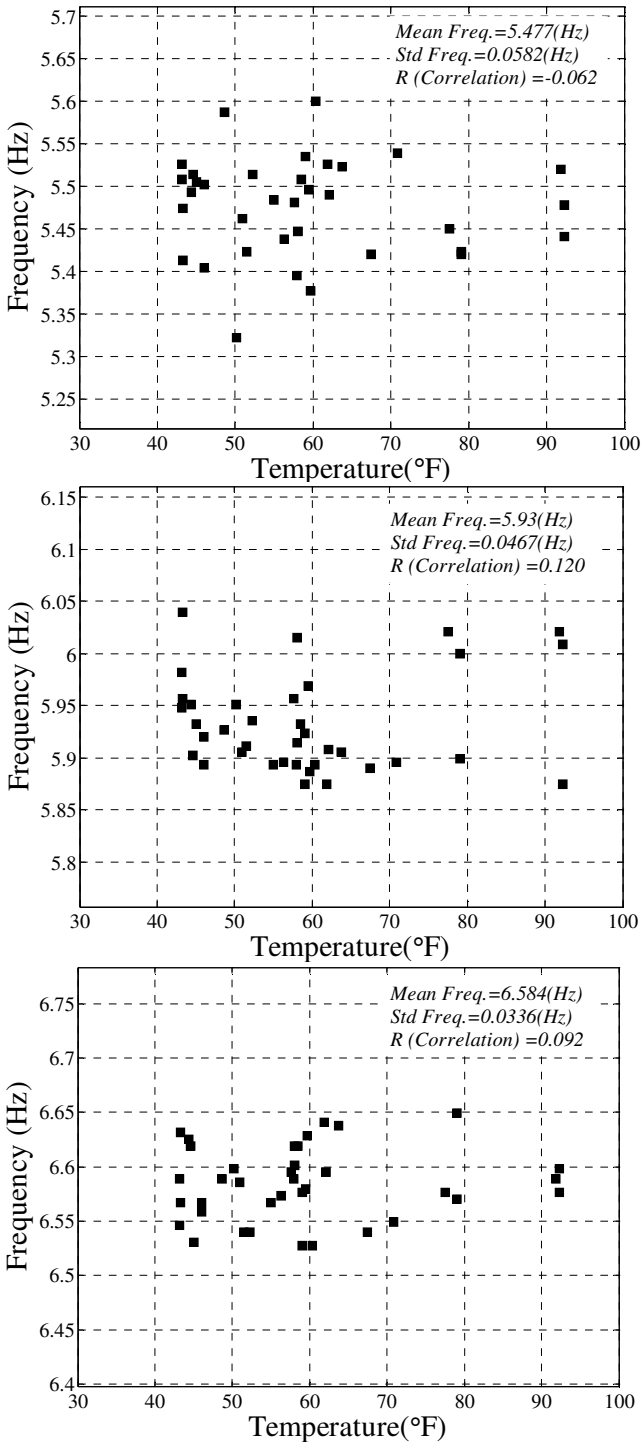

Figure 7.10 (Cont'd). Estimated frequencies versus ambient temperature

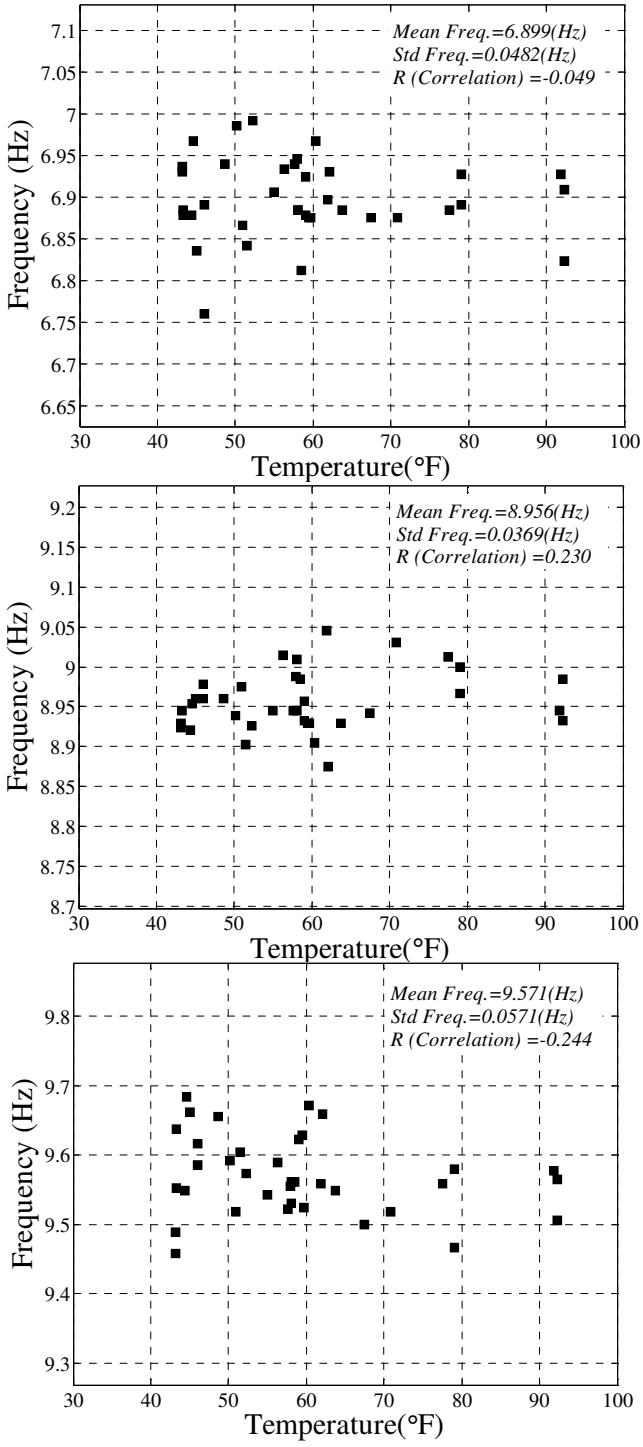

Figure 7.10 (Cont'd). Estimated frequencies versus ambient temperature

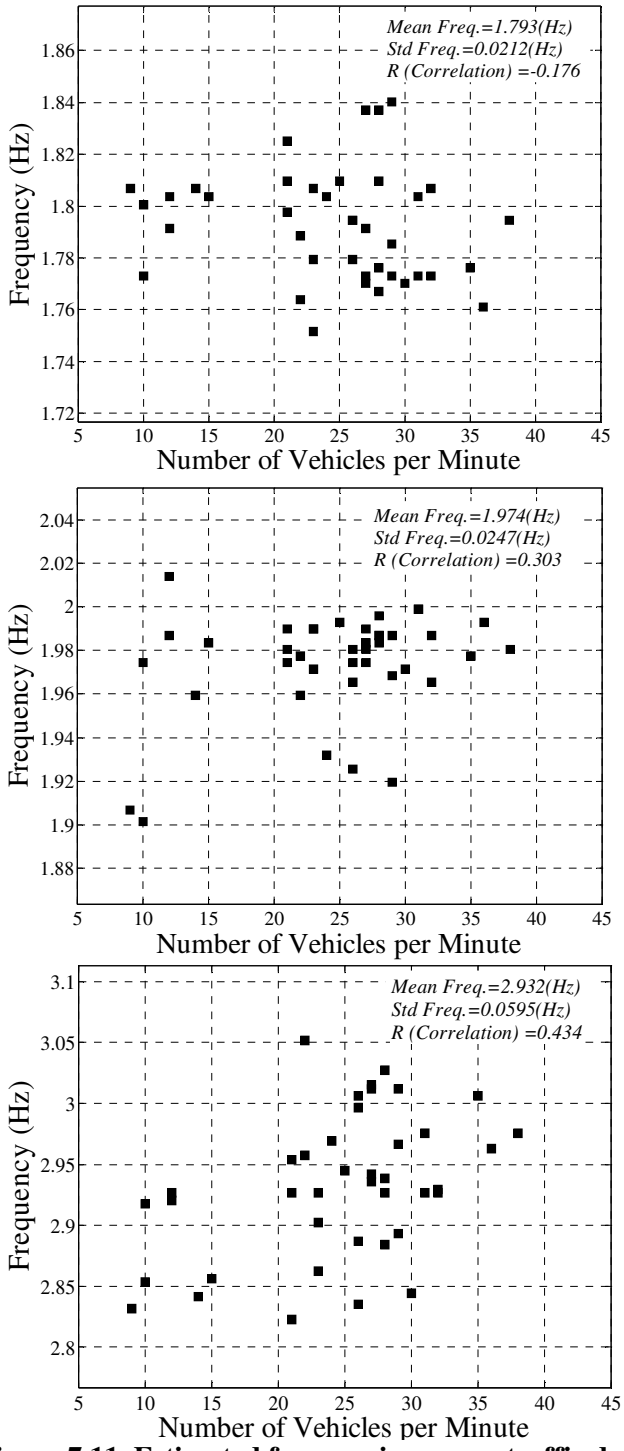

Figure 7.11. Estimated frequencies versus traffic density

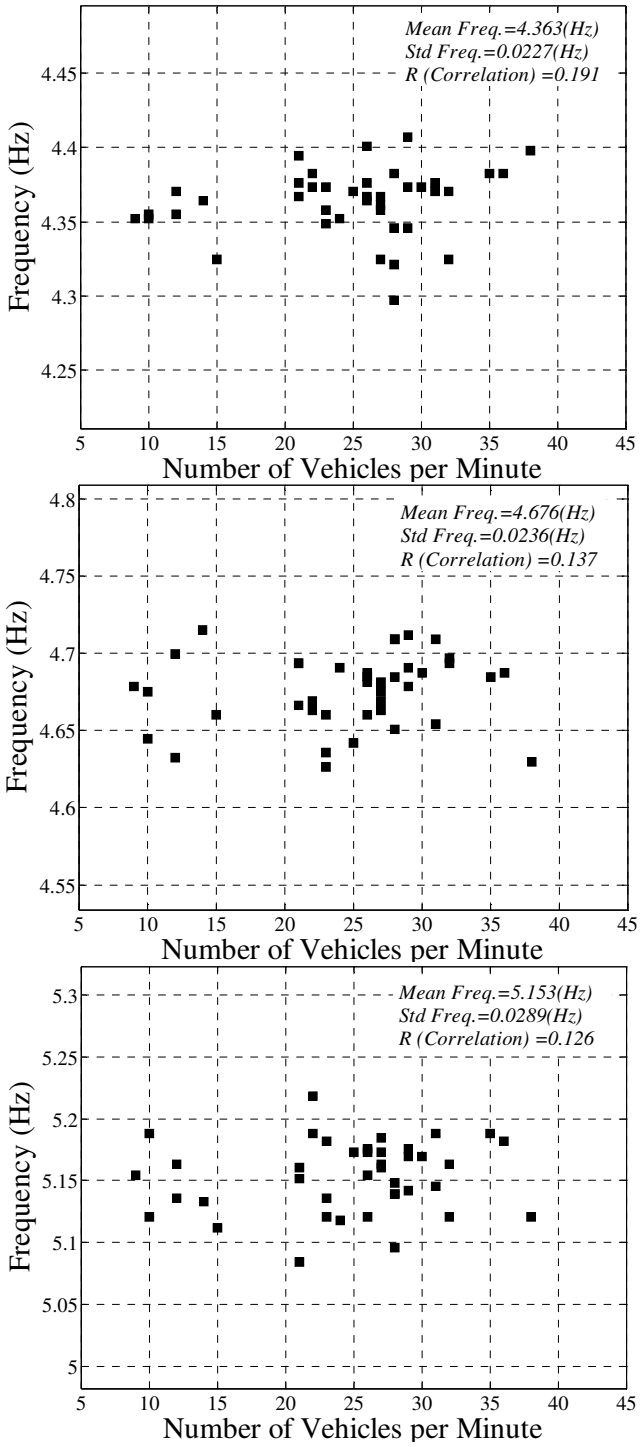

Figure 7.11 (Cont'd). Estimated frequencies versus traffic density

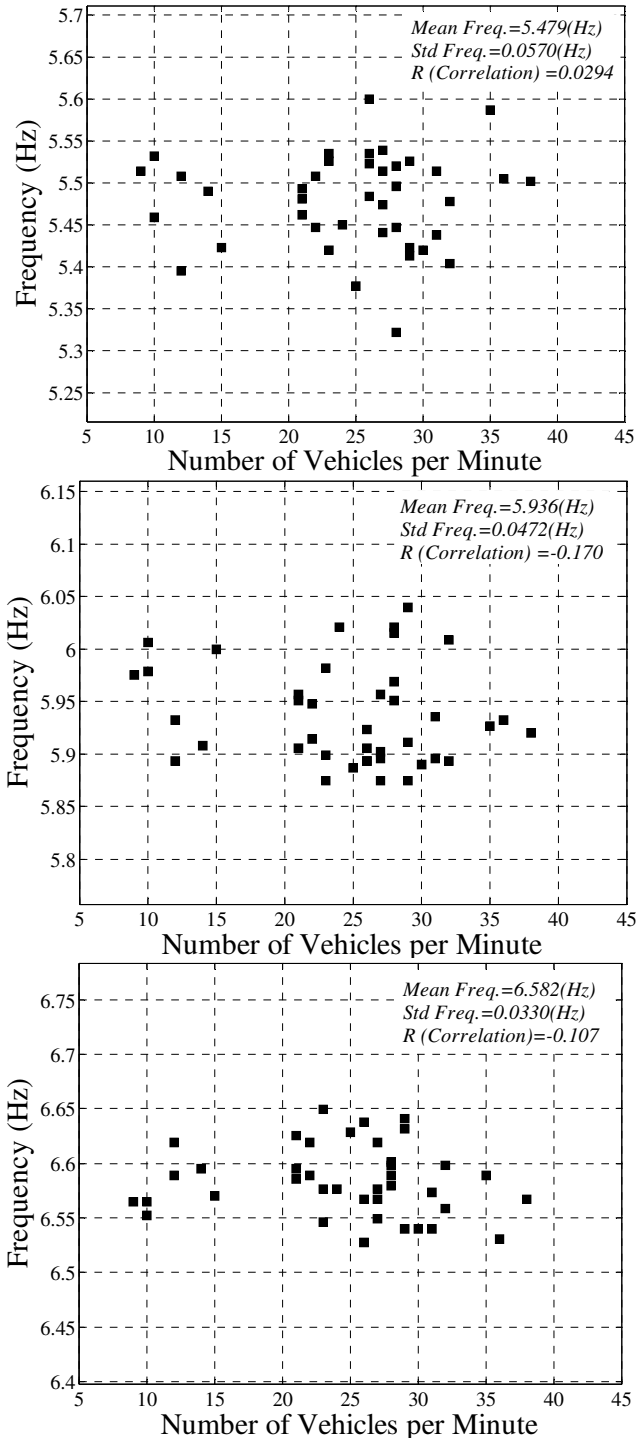

Figure 7.11 (Cont'd). Estimated frequencies versus traffic density

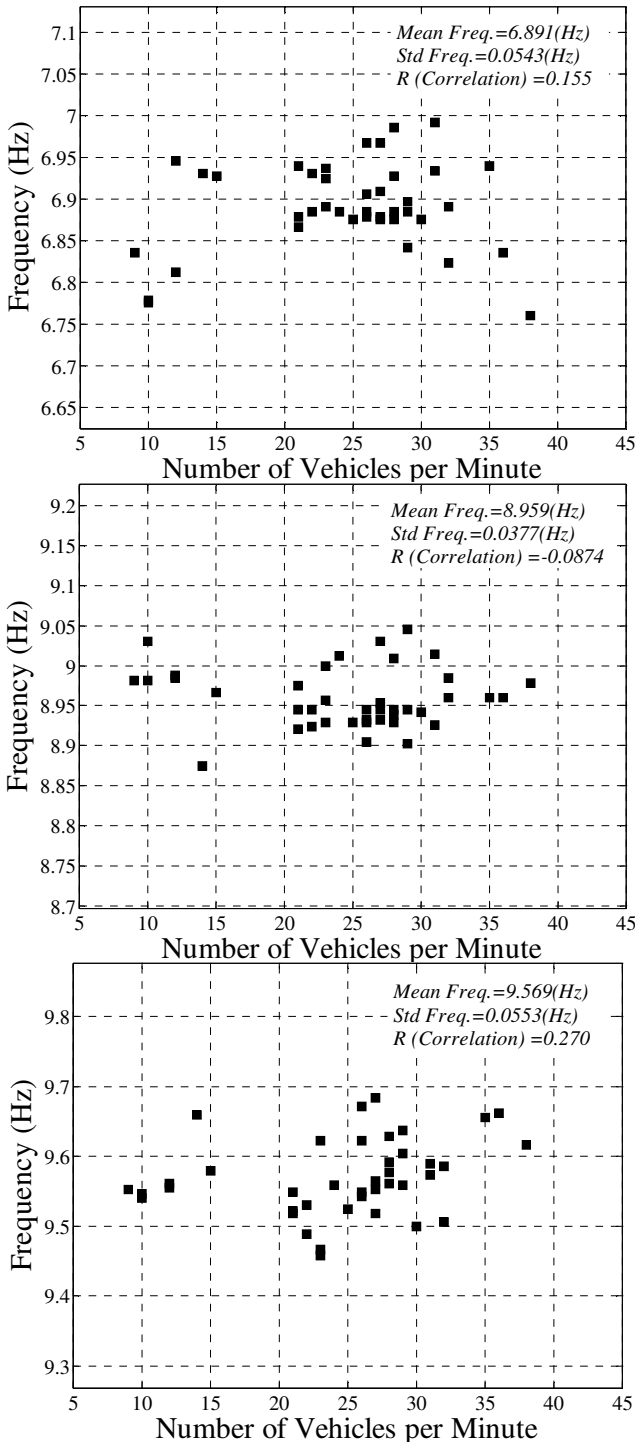

Figure 7.11 (Cont'd). Estimated frequencies versus traffic density

Figure 7.11 also presents the same information for evaluation of the correlation between identified natural frequencies and the number of vehicles passed over the bridge per minute during the vibration monitoring.

As can be seen in the presented plots, in contrary to the expectations, there is not a clear and strong correlation between the estimated frequencies and the two parameters. To better understand the range of correlations, the calculated correlations for different identified frequencies are shown in Figures 7.12 and 7.13. The weak correlation with both ambient temperature and the number of vehicle is observed for most of the frequencies. However, the deviation of the estimated frequencies in different tests shows the uncertainty associated with the results. The standard deviations for the selected identified frequencies are from 0.5% to 2% of the mean values (normalized with respect to the mean). This uncertainty is slightly higher than the uncertainty associated with the selection of the algorithm (Table 7.1).

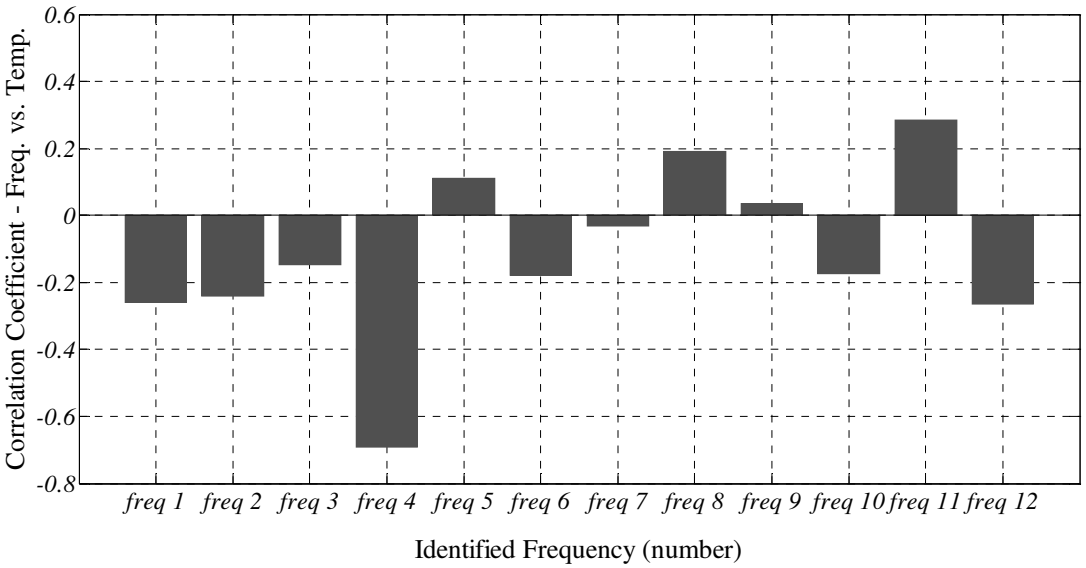

Figure 7.12. Estimated correlations between frequencies and the ambient temperature during the vibration monitoring

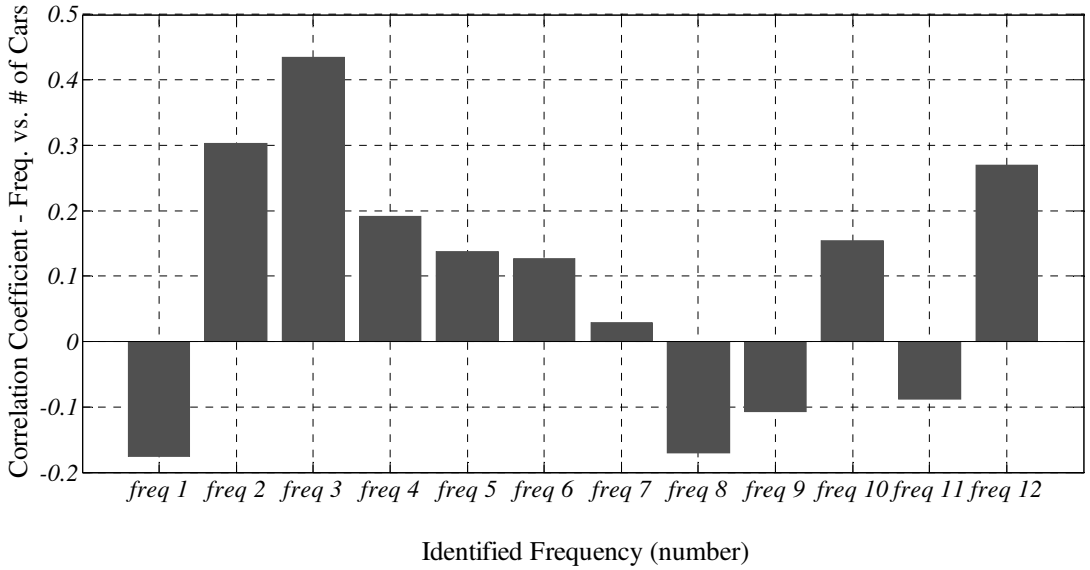

Figure 7.13. Estimated correlations between frequencies and the number of vehicles passed over the bridge during the vibration monitoring

7.7. Finite Element Model of the Bridge

This section presents the Finite Element (FE) modeling of the Northampton Bridge which is developed in SAP2000. The FE model is constructed based on information provided through the 1978 Bridge Inspection and Rating report (DRJTBC 1978). When converting these plans into a SAP model, simplifications are necessary, since modeling every piece of the structure is impractical. Furthermore, the plans, while detailed, are surveyed in 1978 and multiple changes have been made to the bridge since then. In 2002 a new railing and sidewalk system were added to the bridge (Bridge Information 2012). The mass from the additional components and un-modeled structural elements must be calculated, or in some cases estimated, and applied to the model separately. As a result, differences will exist between the modal frequencies given by the FE model and the actual bridge frequencies, estimated through vibration monitoring. Variations in these frequencies may also result from changes in material properties, such as elastic modulus, or boundary conditions (Jaishi and Ren 2007).

7.7.1 Constructed FE Model

The Bridge Inspection Plans (1978) contain section and connectivity information for the structural components of the bridge. Figure 7.14 shows one of the side views of the bridge. SAP2000's Section Designer feature is used to define the individual sections for each member. To simplify analysis, truss members are released only in the M33 direction. Though in reality the bridge experiences both lateral and vertical modes of vibration, the FE model which is used for updating only considers the vertical bending

modes (when releasing the truss members in only one direction, transverse modes are prevented).

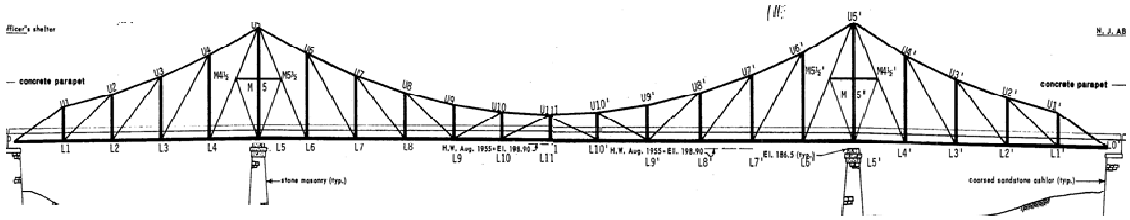

Figure 7.14. The side view of the Northampton Bridge provided by Bridge Inspection Plans report

Since the plans are more than 30 years old, it was necessary to have a visit to the bridge and investigate how closely the plans match the real structure. At the bridge the following modifications are noted:

- The concrete deck has been replaced with a steel deck
- The original railing (contained in the plans) has been replaced
- There is a concrete barrier, not included in the plans, between the road and the sidewalk
- The frame section for members has been modified.

To obtain a set of matching modal parameters from the FE model, it is critical to account for the mass as accurately as possible. While self-weights are automatically computed, the SAP model does not account for non-structural elements such as pins or plates. The dead load for each member, excluding self-weight, can be calculated using the Bridge Inspection report and applied to the joints as point loads. The mass due to the new railing and concrete barrier is also accounted for by applying point loads. Appendix

7-A contains the section information and dead loads (excluding self-weight) for each of the truss members.

The dead loads experienced by the bridge are divided into three categories:

1. Non-structural dead load described in the Bridge Inspection manual (pins and plates)
2. Non-structural dead load estimated from visiting the bridge (railing and concrete barrier)
3. Structural self-weight for members modeled in SAP2000

Each type of the dead load is applied as a separate load pattern as the certainty regarding accuracy of each one is different and the separation of load patterns allows for a better control over load cases and the updating process. To account for the entire mass of the bridge each load pattern is set as a mass source. A view form the final SAP model can be seen in Figure 7.15.

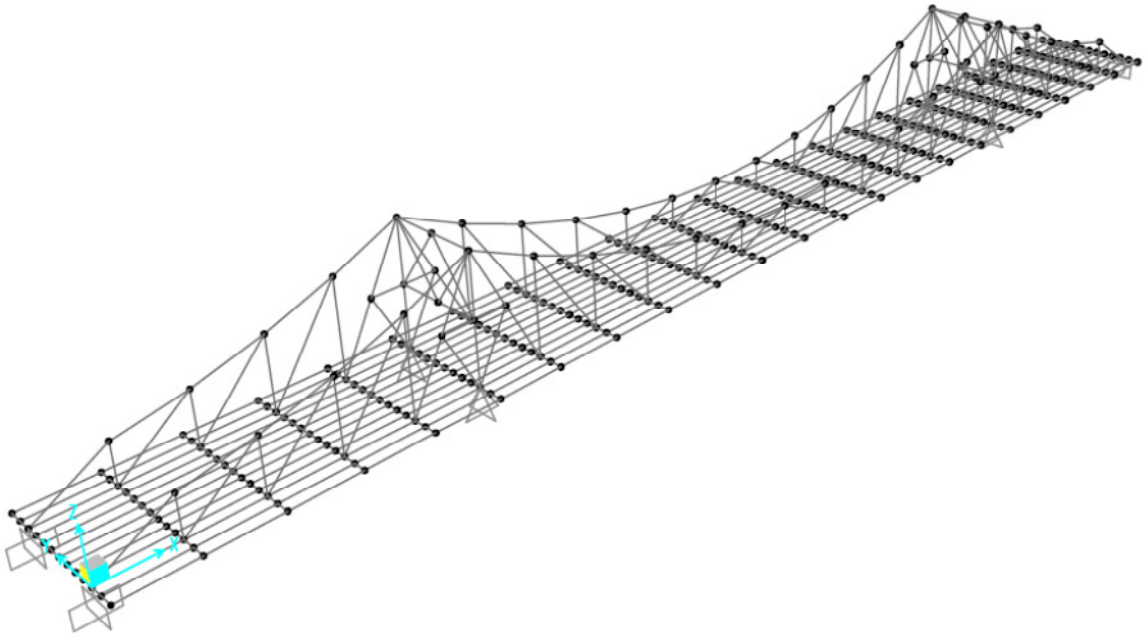

Figure 7.15. Finite Element Model of the Northampton Bridge developed in SAP2000

7.7.2 FE Model Updating Approach

Much work has been done to develop methods of updating FE models to more accurately reflect real structure. Two general approaches for model updating are: the direct method and the indirect (iterative) method. The iterative method, used in this study, is the more common method in structural systems with dynamic testing. This approach requires one to choose a set of updating parameters (Levin and Lieven 1998). The selection of the type and number of updating parameters is critical in the process of FE model updating. Sensitivity analysis is performed to determine which parameters will result in the most efficient model improvement.

Mottershead et al (2011) has identified elastic modulus and non-structural applied mass as valid parameters for model updating. Thus, elastic modulus and non-structural

applied mass are selected as the updating parameters in this study. The number of updating parameters is limited by the available information about the real structure which in this case is the identified modal parameters from the vibration data. Generally, a small number of parameters are used in order to maintain a well-conditioned problem (Brownjohn et al 2001). It is also important to pay attention to choose of modal parameters to match. Not all modes are able to be measured with an equal amount of accuracy, and these differences must be taken into account when updating (Zhang et al 2001).

As presented by Friswell and Mottershead (2001), the iterative updating process used in this study consists of minimizing the solution, (Equation 7.3) to the optimization equation (Equation 7.2):

$$\delta\theta^{\mathrm{T}}\mathbf{W}_{\theta\theta}\delta\theta \text{ subject to } \delta\mathbf{z} = \mathbf{S}\delta\theta \tag{7.2}$$

$$\delta\theta = [\mathbf{S}^{\mathrm{T}}\mathbf{W}_{\varepsilon\varepsilon}\mathbf{S} + \mathbf{W}_{\theta\theta}]^{-1}\left\{\mathbf{S}^{\mathrm{T}}\mathbf{W}_{\varepsilon\varepsilon}\delta\mathbf{z} - \mathbf{W}_{\theta\theta}\{\theta_j - \theta_0\}\right\} \tag{7.3}$$

where:

θ_j, θ_0 = current or initial parameter value

$\delta\mathbf{z}$, $\delta\theta$ = change in response or parameter

$\mathbf{S}$ =Sensitivity Matrix

$\mathbf{W}_{\varepsilon\varepsilon}, \mathbf{W}_{\theta\theta}$ =Weighting matrices for frequencies and parameters

Solving Equation 7.3 indicates how the parameter values must be changed to increase agreement between the model and the actual responses.

7.7.3 Model Updating Process

To update the FE model based on the identified parameters, Equations 7.2 and 7.3 are used. Basically Equation 7.3 minimizes the change in the parameter value from the initial estimate of the parameter.

The updating parameters chosen in this study are the elastic modulus of steel and estimated non-structural loads (ENSL). The ENSL consists of the railing, railing support, and concrete barrier. This load is applied equally at all deck joints except for the end joints (L0 and L0'). As mentioned before, Equation 7.3 minimizes the parameter's change from the initial estimate. Since the absolute value of the elastic modulus is much greater than the ENSL, parameter values are replaced by normalized factors in the MATLAB code. These factors are created by scaling each parameter to the initial estimate; ENSL is scaled to the load applied at the deck joints (the ENSL is updated in model by changing the mass multiplier for the corresponding load case).

The responses for FE model updating are chosen to be the natural frequencies, estimated from modal identification. The selected frequencies are limited to 5 of the identified modes. Model updating matches the analytical frequencies (from the FE model) to the average measured frequencies (Brownjohn et al 2001).

Sensitivity Matrix (S) is to be estimated as is required in Equation 7.2. The sensitivity matrix is calculated by taking the first derivative of the response with respect to the parameter (Mottershead 2011). This matrix accounts for the change in response (frequency) for a given change in parameter. In this work, the value of one parameter is changed by 1% in the SAP model, and the corresponding frequencies are extracted. The process is repeated with the second parameter, when the first parameter held at the initial value. In sensitivity based model updating, the sensitivity matrix may either be held constant throughout the updating process, or recalculated per iteration. Both approached are taken in this updating process and based on the results and recommendation by Friswell and Mottershead (1995), the recalculated method was chosen.

Since the value of the elastic modulus is known with greater confidence than the value of the estimated loads, a weighting matrix must be also considered for the parameters ($\mathbf{W}_{\theta\theta}$). Weighting matrix is a positive, diagonal matrix and its first row corresponds to the elastic modulus; the second row corresponds to the ENSL. To prevent the change in elastic modulus from exceeding ±5%, the elastic modulus is assumed to be known with 3,500 times more certainty than the ENSL.

Therefore,

$$\mathbf{W}_{\theta\theta} = \begin{bmatrix} 3500 & 0 \\ 0 & 1 \end{bmatrix}$$

is assumed.

Similarly, variation exists in the accuracy of the measured frequencies. The weighting matrix $W_{\varepsilon\varepsilon}$ accounts for these variations which is also a positive, diagonal matrix, whose entries correspond to the reciprocal of the variance for each average modal frequency. Table 7.5 shows the average of the selected frequencies (as responses) and corresponding standard deviations.

Table 7.5. Average and Standard Deviation of selected frequencies for updating

Average Frequency (Hz)	Standard Deviation
1.793	0.0212
4.363	0.0227
5.933	0.0472
8.959	0.0377

The FE model updating process consists of four main steps:

Step 1: Calculate the sensitivity matrix in MATLAB.

Step 2: Enter the current parameter values into SAP and run the modal analysis.

Step 3: Enter the modal frequencies generated by SAP2000 into the MATLAB code and calculate the updated parameter values and new sensitivity matrix.

Step 4: Modify the parameter values in SAP to the updated values and repeat the process until the system converges.

Tables 7.6 shows the change imposed to the modeling parameters through FE model updating. It can be seen that the elastic modulus increases by 4.8% and the ENSL increases 52.11%. The greater change in ENSL compared to elastic modulus indicates the effectiveness of using a parameter weighting matrix. Table 7.7 also contains the

frequencies that are identified, and also computed from the initial and the updated FE model. It can be seen that the updating process improves the consistency of the FE model and the measured response of the structure. It can also be seen the updated model has natural frequencies within 5% of the measured frequencies. Figure 7.16 also shows the modes of vibration in the selected frequencies, obtained from the updated SAP model.

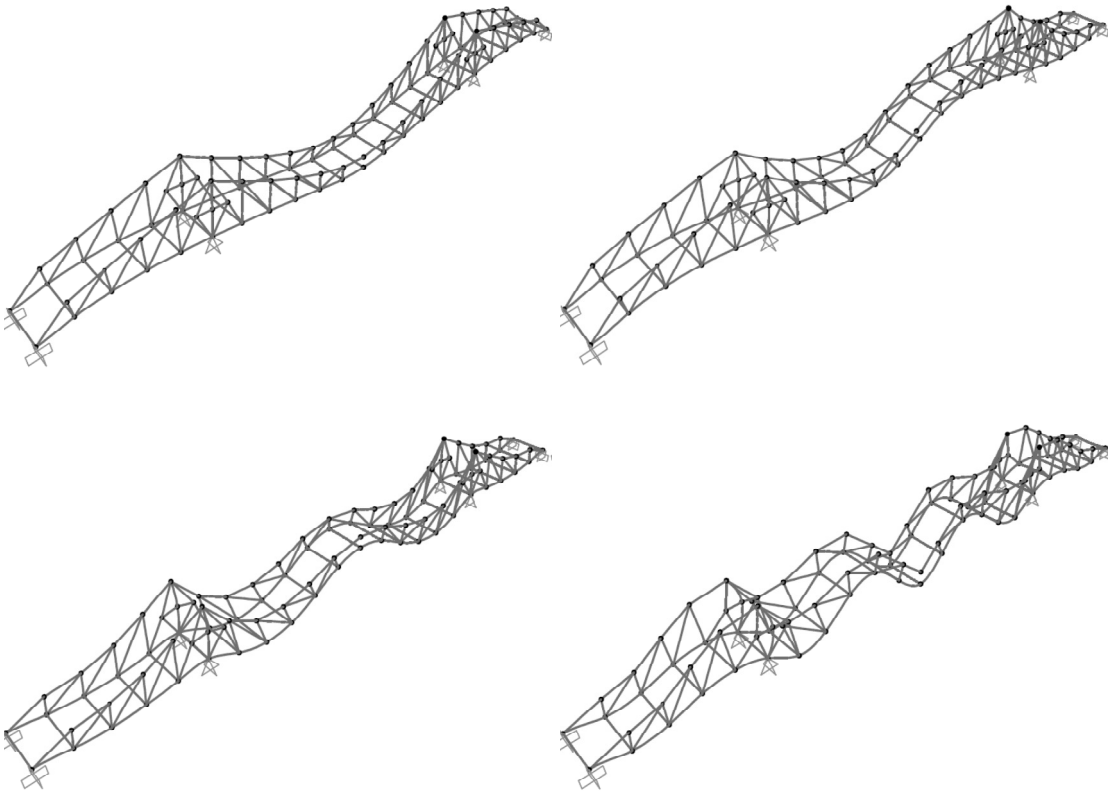

Figure 7.16. Modes of vibration in selected frequencies from FE Model in SAP2000

Table 7.6. The FE modelling parameters selected for updating

Initial parameter		Final parameter		% change	
Elastic modulus (kip/in^2)	Estimated non-structural load (kip)	Elastic modulus (kip/in^2)	Estimated non-structural load (kip)	Elastic modulus (kip/in^2)	Estimated non-structural load (kip)
29000	5.957	30,401	9.061	4.83	52.11

Table 7.7. Identified, initial, and updated frequencies

Identified Frequency (Hz)	Initial Frequency (Hz)	Difference (%) before Updating	Updated Frequency (Hz)	Difference (%) after Updating
1.793	1.847	3.035	1.816	1.302
4.363	4.463	2.282	4.416	1.210
5.933	5.665	4.511	5.780	2.585
8.956	8.001	10.659	8.599	3.986

7.8. Summary of the Bridge Monitoring

The semi-long term monitoring of Northampton Bridge is presented in this Chapter. The portability of the wireless sensors and the ease of installation facilitated the vibration monitoring of the bridge. The wireless sensor network deployed in this experiment consisted of 20 wireless sensors and in addition, 7 wired sensors (in one test only) for cross-verification of the obtained results. The modal parameters of the bridge structure are identified using different time- and frequency-domain identification approaches. It is observed that while the identified modal parameters are in general agreement, there exist

slight variations among the identified parameters. This is considered as the uncertainty due to the algorithm selection.

Having the measured data collected during different environmental and operational conditions (EOCs), the uncertainty of the results due to these parameters is investigated. It is attempted to find a correlation between the dynamic characteristics of the bridge and the mentioned parameters. The effects of the parameters (ambient temperature and number of vehicle passing the bridge during the monitoring) did not follow a uniform trend and the correlations were weak and inconsistent for different modes of vibration. This means that different vibration frequencies of the bridge structure react to the EOCs in different way. In addition to that, it can be realized that the effects of the extra mass due to the passing vehicles is insignificant and also different for different modes. Although no correlation could be established between the dynamic characteristics and the EOC parameters, the variation of results could be easily observed.

Along with the study on the identified modal parameter identification of the bridge, the Finite Element model of the bridge is also developed in SPA2000. The modeling is performed based on the information provided in the as-built drawings of the bridge given in the Bridge Inspection report. Some details are however obtained through the visit to the bridge. The objective for development of Finite Element model is to have a model that perfectly represents the real structure. Therefore, some uncertain initial modeling parameters are modified using iterative, sensitivity-based model updating approach. For simplicity, only the fundamental natural frequencies are selected as response for updating

process. Further study could be performed to include different responses such as modes of vibration and higher frequencies in the updating process.

Chapter 8

Summary of Contribution of the Research, Broader Impact, and Future Studies

8. Contribution of the Research, Broader Impact and Future Studies

8.1.Original Contribution of the Dissertation

This research contributes in enhancement and improvement of the current state of SHM and application of advanced sensing technology in the SHM practice. Some challenges in application of wireless sensor networks (WSNs) are addressed and new algorithms and approaches are developed. In following section, the existing challenges and the most recent efforts for addressing them are presented and then the original contribution of this dissertation is discussed.

Challenge and Existing Solutions in Modal Identification using WSNs

Latency in the data collection and prohibitive power consumption, as major drawbacks in application of WSN in SHM, need special considerations. Due to the limited bandwidth in wireless networks, transmitting large volumes of data can take a prohibitively long time. In addition to the latency, power consumption also limits the performance of WSNs in long term monitoring. Different components of a wireless sensor unit consume different amounts of energy when performing different tasks. From the power measurement, it is observed that the radio transceiver is the major power consumer in a unit of wireless sensor. The onboard processing techniques attempt to reduce the communication by pushing the computation into the network. Efforts in developing onboard processing algorithms for application of wireless sensors include: decentralized damage detection algorithm using transfer function and migration of its parameters by Swartz (2009); Coordinated Computing Strategy which divides the network into a number of sub-networks with cluster heads in a hierarchical topology by Nagayama and Spencer 2007 and its further improvement by deploying decentralized

Random Decrement function estimation (Sim, et al. 2010). Although these limited attempts reduce the amount of communication, they are restricted by the network topology and the underlying algorithms, and mostly developed for damage detection. The limited effort is devoted to onboard modal identification which is just partially onboard and still a significant portion of computation is assigned to a central computer. Additionally, the efficiency of the proposed algorithms is not high enough to alleviate the challenge (for example in the algorithm developed by Sim et al. 2010, the saving in communication is just 20~25%). Therefore more efficient algorithms are still needed to remedy the latency and power consumption issue which exist in the current WSN deployments.

Contribution in Addressing Limitations of WSNs for Modal Identification

This dissertation presents a novel approach for modal identification of structural systems in a distributed scheme, suitable to address challenges in application of WSN in SHM. The proposed algorithm, called Iterative Modal Identification (IMID), assigns the entire computational task of modal identification to remote nodes and limits the data communication to transmission of only modal analysis results. In this approach the communication burden is reduced and as a result, the time and the energy consumption of the monitoring system are minimized. The algorithm is developed such that each node estimates the system's parameter (θ) based on the measured data at the node (available observation, Y) plus the assumed responses in the other nodes, $\hat{Y}$. The estimation results are updated recursively by passing the results through the network in an iterative manner. Considering a structure instrumented by N sensor nodes, the first node uses the initial value of the parameters and makes a numerical simulation to obtain the response on other nodes. The simulated response and the measured data at this node are used to estimate

system's modal parameters and send them forward. These steps are taken in all of the nodes of the network one-by-one and each node updates the estimation by the measured data at its location until the estimated parameters are stabilized and converged. Note that the algorithm with this configuration is applicable to input-output systems. The algorithm is implemented on different input-output numerical models and a laboratory 5 DOF model (on shaking table) and its performance is validated.

IMID needs a starting point for iteration process. For cases where this is not available, another novel approach, called Cumulative System Formation, is developed which addresses this requirement. In this approach, the parameters for the first node are estimated using only measured data at its location (single output problem). The second node then receives parameters and with its locally measured data updates the estimated parameters (two outputs). The third node performs similar process with three outputs and the process continues up to the last node in the array, each time the number of outputs increases by one. As the estimation reaches the last node, one cycle of iteration is completed and the system parameters are formed from multiple outputs.

Challenge for Output-only Modal Identification Problems

The modal identifications for civil structures are mostly output-only problems because the input is not controllable and measurable. Therefore it is important to have the identification algorithm formulated for output-only systems as well.

Contribution in Addressing Output-only Problems:

The approach which is developed to address output-only modal identification is such that one node, as the reference, sends its measured time history data to the rest of the nodes in the network. The other nodes, then, calculate the cross-correlation functions (as

estimates of impulse responses) and send them to the base station for modal identification. IMID can utilize similar step to allow all the nodes to have the cross-correlation functions computed (between their measured data and the reference node data). As an alternative, the unscaled impulse response can be estimated through the use of Random Decrement (RD) technique, in which instead of transmission of time-history data from reference node to the rest, the trigger crossing information is sent for estimation of impulse response. While estimation of impulse response with correlation functions and random decrement function have been available in literature, the novelty of the developed algorithm is their adoption for use in the Iterative Modal Identification.

The performance of the algorithm is enhanced using developed AR-ARX analogy approach. AR-ARX is a two steps process which is an implementation of ARMA. An analogous strategy is utilized in the implementation of IMID. In this strategy, the first iteration cycle uses AR model and the later iterations use ARX model (using residuals of the AR model) for estimating the system parameters and predicting the response. The ARX models (second cycles of iteration) use residuals as the input. The available residual at the sensor location is the difference between the locally measured signal and the predicted one from simulation. The algorithm with all elements (for output-only systems) is also implemented on a numerical 10-DOF model, an experimental 3-D truss and the data collected from ambient vibration of Golden Gate Bridge.

Efficiency of the Algorithm and Comparison

The efficiency of the algorithm is investigated by assessing the reduction in the communication burden, compared to the centralized data processing scheme. For the input-output experimental model up to 95% reduction in communication is achieved. For the 3-D steel truss model 90% reduction and for the implementation on the ambient response data from Golden Gate

Bridge 83%~89% reduction in communication is achieved. This reduction is significantly higher than what is achieved through other state-of-the-art approaches which are introduced earlier (e.g. 20~25% reduction in communication through algorithm developed by Sim et.al. 2010). This reduction in communication, which is the result of novel approaches developed in this dissertation, clearly results in a reduction in energy consumption (e.g. the total energy is estimated to have up to 75% reduction) and also agility of the sensing network. An automated long-term monitoring system, which is time-efficient and energy-efficient, can be established based on use of this algorithm. The algorithm can be also considered as a basis for damage detection in long-term monitoring as it provides the updated modal parameters through the time.

Challenge in Assessing the Effects of Measurement Noise:

A challenge associated with the design of wireless sensor platforms is the trade-off between the functionality and the power consumption and attempts for minimizing the cost. These considerations usually cause limitations in the architecture and quality of wireless sensors. As the source of measurement noise, the selected sensors may introduce an epistemic uncertainty into the results of system identification. Despite the development of numerous system identification methods and many successful implementations on structural systems, relatively limited efforts have been devoted to evaluation of the results in terms of accuracy and credibility. The limited research is also mainly concerned about the uncertainties associated with environmental conditions (Peeters and DeRoeck 2001), excitation characteristics (Nagayama *et al* 2008) and data processing methodology (Reynolders *et al* 2007, Zhang *et al* 2010), and less attention is paid to the impact of measurement system and the possible uncertainties derived from measurement noises. Similarly, the measurement noise can have impacts on the results of damage detection and these effects need to be investigated.

Contribution in Quantifying the in Modal Identification Quality due to Noise

This PhD dissertation develops a parameter that quantifies the quality of estimated modal parameters in presence of measurement noise. The developed parameter, called Physical Contribution Ratio (PCR), reflects the contribution of system's response in the estimated impulse response from the measurement in presence of noise. Higher PCR translates into more accurate identified modal parameters. Therefore, the identified modal parameters can be passed through this assessment to be quantitatively assessed in terms of the quality. The performance of this developed approach is validated by a numerically simulated example. It is also used to investigate the accuracy of identified modal properties of Golden Gate Bridge using ambient data, collected by wireless sensors. The vibration monitoring tests of Golden Gate Bridge provided two synchronized data sets collected by two different sensor types. The influence of sensor's noise level on the accuracy of results is investigated throughout this work and it is shown that the high quality sensors provide more accurate results as the physical contribution of response in their measured data is significantly higher. Therefore, the developed parameter can be used for quantification of the modal identification results and also a basis for selection of sensor quality. Moreover, it can be a basis for selection of sensor location as it provides the physical contribution of response in terms of the location of sensor as well.

Development and Validation of a Damage Detection Algorithm and Assessing its Efficiency in Presence of Noise

Providing enhancements in the sensing and measurement systems, this research also looks into improvements in one of the fundamental applications of sensing and response monitoring which is damage detection. While providing a review on the current state of

the damage detection, the study contributes in validation of a developed damage detection algorithm which works with the correlation function of the measured responses at different locations of the structure. The damage detection algorithm is implemented on two small-scale and large-scale experimental models and its functionality and performance are validated. The small-scale experimental model is built to represent a beam-column connection and the implemented sensor network (including 9 sensors) is assumed to represent a portion of a dense array of sensor in a small portion of a structure. Through this implementation, two different sets of wired and wireless sensors are utilized and having the obtained results, the performance of each sensor network is evaluated. It is shown that though the wired sensor network, due to the higher sensing quality, provides slightly more accurate damage indicators, the results obtained from both networks are capable of reflecting the structural change in the instrumented model.

While the first implementation used the acceleration response form dynamic testing, the second implementation used the strain data from cyclic loading of a large-scale beam-column connection. Through the two implementations, the algorithm is shown to be effective in reflecting the damage, whether it is introduced suddenly or gradually throughout the time (or throughout the increase of the load). Along with the implementation and validation of the damage diagnosing algorithm, this research also explores the importance of statistical frameworks in this area. Several different statistical approaches are utilized to detect the change in the damage indicator and also to reflect the significance of the change. The statistical frameworks used for change point detection in

the validated damage detection are Bayesian Testing, Exponentially Weighted Moving Average, and Cumulative Sum. Equipping the damage detection approaches with such statistical framework is particularly important as there are always minor changes associated with non-structural changes which need to be differentiated form the structural ones.

Implementation of Wireless Sensors for Monitoring of Real-Life Structures

This dissertation is complemented by presenting two field-deployments for structural health monitoring. The first one is implementation of a state-of-the-art sensing system in monitoring of a tall building structure which is suffering from excessive vibration in vertical and lateral directions. The utilized sensing system consists of both wired and wireless sensors which are integrated to provide a cost-effective sensing system. The vast variety of sensors, including accelerometers, strain gauges, displacement sensors, and anemometer, are deployed and, along with different data processing techniques, facilitated the forensic quantification of the building. The performance of the building is evaluated in terms of serviceability and strength demand. Time- and frequency-domain analysis of response and comparison with the design guidelines, wind spectrum analysis, modal identification and extraction of excited modes of vibration are some data processing tasks performed in this study.

The second field deployment is utilization of a network of wireless sensors for vibration monitoring of a steel bridge structure. The monitoring task is performed in a one-year period during multiple tests in different seasons to identify the dynamic

characteristics of the bridge and also find the uncertainty introduced to the results due to the changes in environmental and operational condition of different tests. The parameters which their effects are studied are the ambient temperature and the volume of traffic load crossing the bridge during the vibration monitoring. Variation of results due to the variation of each of these factors and a general conclusion are studied and it is shown that the modal parameters do not have strong correlation with the studied parameters for this specific bridge.

8.2.Broader Impact of the Research

The goal of this research was to facilitate the application of wireless sensors, as advanced sensing and monitoring technology, in structural health monitoring to allow this practice fully benefit from the advantages of wireless sensing and onboard computing.

The approaches developed through this research may be further improved and adapted to be used in different scenarios in structural health monitoring. For example, the developed distributed modal identification can be utilized as a basis for development of distributed damage detection or the approach for quantification of the modal parameter quality can be used for sensor location selection. However, more importantly, this research can contribute in introducing a considerably superior monitoring approach for the civil infrastructure. As the application of wireless sensors in different elements of structural health monitoring (e.g. modal parameter identification and damage detection) is facilitated, many structural systems can benefit from their affordability and ease of utilization. Therefore, not only a broader range of structures will be considered for

monitoring, but a higher spatial resolution will be achieved in the monitoring. Distributed algorithms for onboard computations along with remote sensing technology can form a new avenue for establishing smart sensing systems and ultimately smart structures.

8.3.Future Studies

While this dissertation presented different approaches and techniques for enhancement of SHM, a wide range of research topics is also opened as a result, which can be explained and classified as the future studies. This Section also includes the studies that can be done as the continuation of the research presented in this presentation.

8.3.1 Distributed Data Processing

The iterative modal identification presented in Chapter 3 provided a significant enhancement in the efficiency of modal identification using WSNs. However, there is still a great potential for further improvement of the algorithm by examining different simulation and system identification approaches. The presented algorithm based its modal identification step on the Auto Regressive Exogenous (ARX) while it could use different time-domain or frequency domain algorithms. The same flexibility exists with the numerical simulation step. Using different approaches could make the algorithm more efficient in terms of computation which eventually helps with the energy-efficiency of the modal identification process. While ARX is selected among different algorithms, a broad study needs to be performed to find out the most efficient algorithms in terms of efficiency and also accuracy. Additionally, sensitivity analysis can be performed to find

out the dependency of the results (e.g. the convergence results) of the algorithm on the parameters such as the initial estimate of the system, and the window size or triggering criteria in estimation of impulse response using correlation function and random decrement.

While the performance of the iterative modal identification algorithm is validated through implementation on several numerical, experimental, and real-life vibration data in MATLAB, the approach still needs to be programmed and compiled on actual wireless sensor platforms and be examined in a real structural monitoring scenario. In addition to the modal identification algorithm which is developed for onboard computation, there are plenty of data processing approaches which can be adopted for installation on wireless sensors. An example of such algorithms is the damage detection algorithm presented in Chapter 5. An automated monitoring system can be developed having the damage detection approach programmed and compiled on the wireless sensors. Statistical frameworks can also be utilized along with the damage detection method to provide a basis for reliable decision making about the assurance of damage. Further automation can be achieved through defining thresholds for change point detection and deployment of alarming system.

8.3.2. Preemptive Sensing System

An important future research for the application of wireless sensors in structural health monitoring is to enable the monitoring system to capture the sudden and drastic events, such as earthquakes or high speed wind. The current state of the wireless sensors in

structural monitoring does not provide real-time triggering of the sensing system in reaction to high structural response levels. Additionally, an effective and responsive monitoring system should be able to capture the sudden events and also respond to the collected information. Solutions to this need can be either found in hardware development (or hardware adjustment) or algorithm development. The iterative modal identification can be considered as a step towards a responsive sensing system as it estimates the system parameters onboard in a time- and energy-efficient way. However, this area is still in its infancy stages. Providing real-time control on the wireless sensors needs more hardware development and ensuring the effective and the timely response from the monitoring system also needs more improvements in data processing algorithms and the corresponding hardware.

8.3.3. Uncertainty Assessment

While this research attempted to provide an understanding about different types of uncertainty, further investigation on different sources of uncertainty is still needed. Chapter 4 provided a metric which quantifies the accuracy of the modal parameters identified through vibration monitoring with existence of measurement noise. However, measurement noise is not the only root of the uncertainty in modal identification. Environmental and operational conditions (e.g. temperature and randomness of traffic) also have significant impacts on the results. Literature shows some efforts towards this investigation and Chapter 7 also presents some studies regarding the variation of modal parameters due to temperature and traffic loads. Further investigation, however, would

improve the current state of this area and can assist with minimizing the uncertainty in the process of modal parameters identification. A complementary study that could be done on in conjunction with the performed research is to incorporate the assistance of Finite Element models in modeling the effects of different sources of uncertainty. For example, the emperature gradient and also the random traffic loads could be modeled in the developed FE model and their effects on the dynamic characteristics of the structure could be investigated theoretically. These results could be then compared to the observations of the experimental study, presented in Chapter 7.

Additionally, extracting the effects of environmental and operational conditions can provide a basis for developing some approaches for excluding their effects from the results. In the other words, knowing the dependency of the identified modal properties on the testing parameters assists in removing the unwanted effects and more reliable identification. Although literature presents some efforts in this area, the approaches are not commonly utilized and there is still a significant need for more studies.

Also, the knowledge of uncertainty in the results of modal identification does not help in assessing the reliability of the monitoring process until their effects are also studied in the following application of the modal identification practice. As discussed in Chapter 1 and 2, typical applications of the modal identification are in damage detection and finite element model updating. Investigating the uncertainty in the identified modal parameters would be more helpful when it is continued to the assessment of their effects on each of

the mentioned applications (damage detection and finite element model updating). Thus, this topic should be an important focus for the future studies.

Appendices

Appendix 6-A

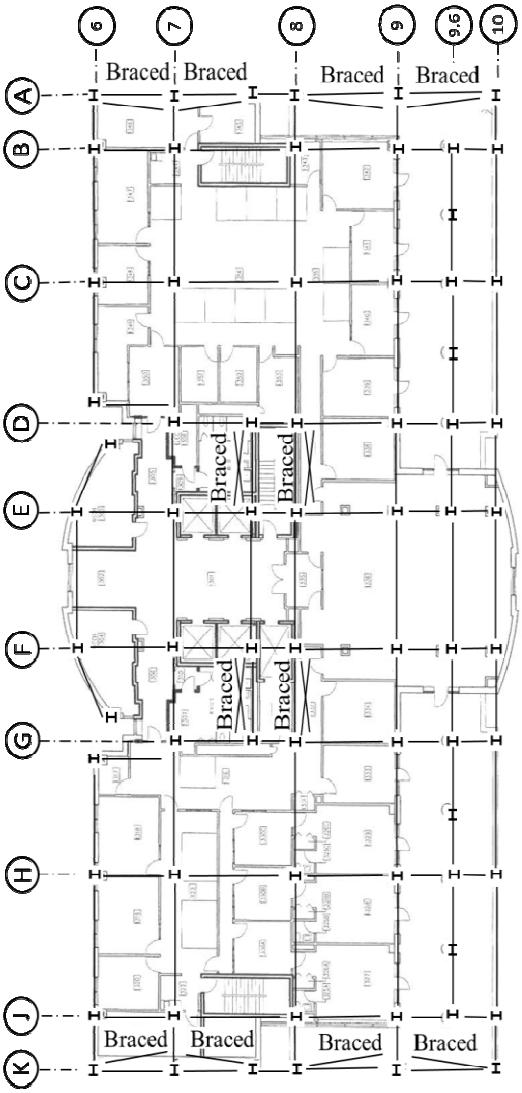

Figure A8.1. Typical plan of the building

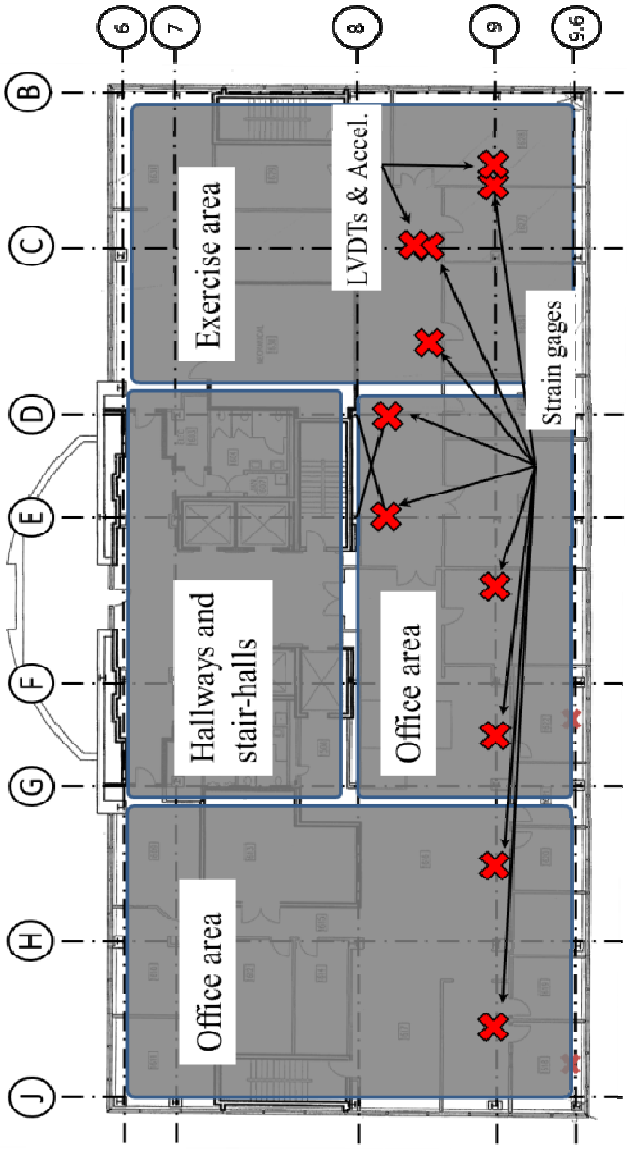

Figure A8.2. 16th floor plan, different occupancies and wired sensor locations

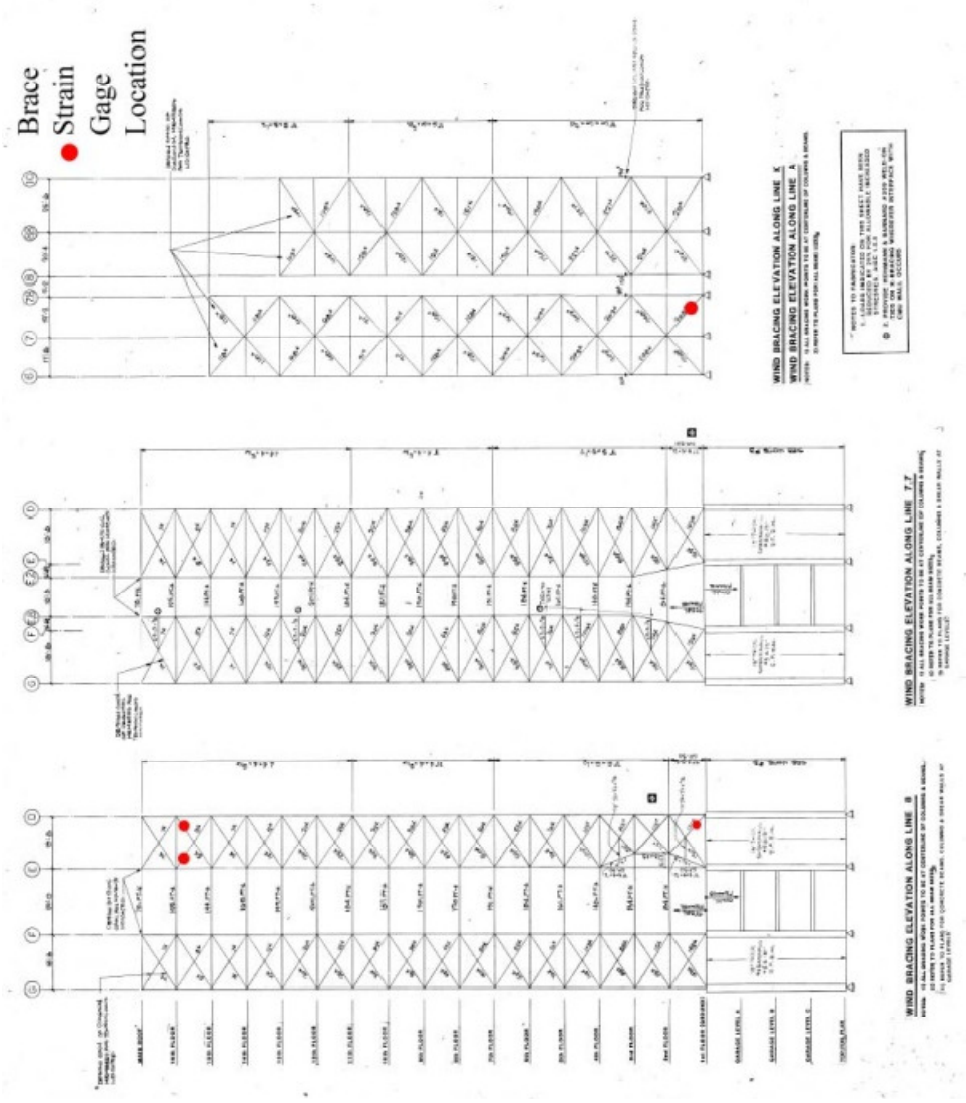

Figure A8.3. Lateral bracing frames of the building and location of strain gauges

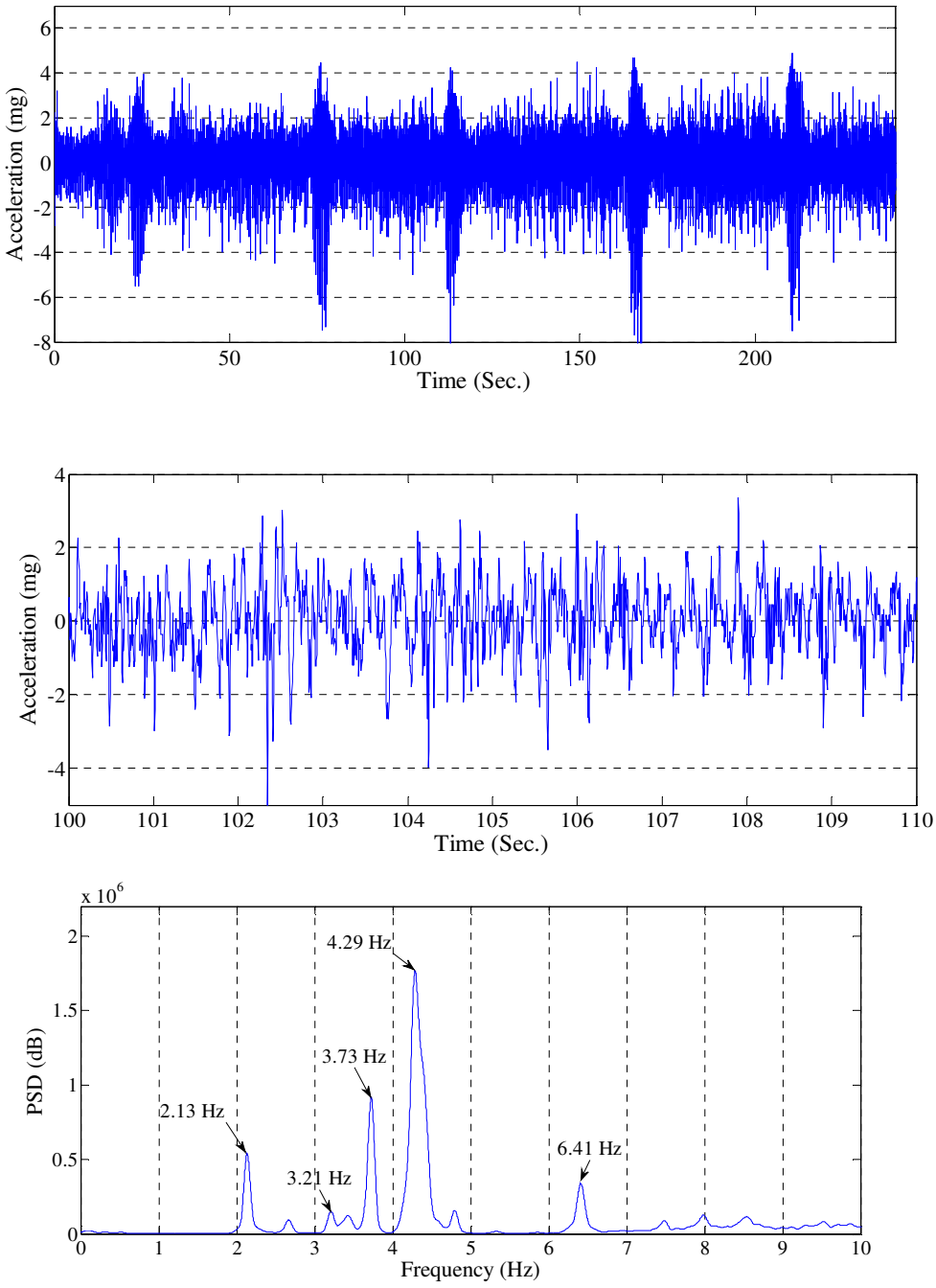

Figure A8.4. Time-history plot and Power Spectrum Density of acceleration from 15th floor between C-9 & D-9 during aerobics class

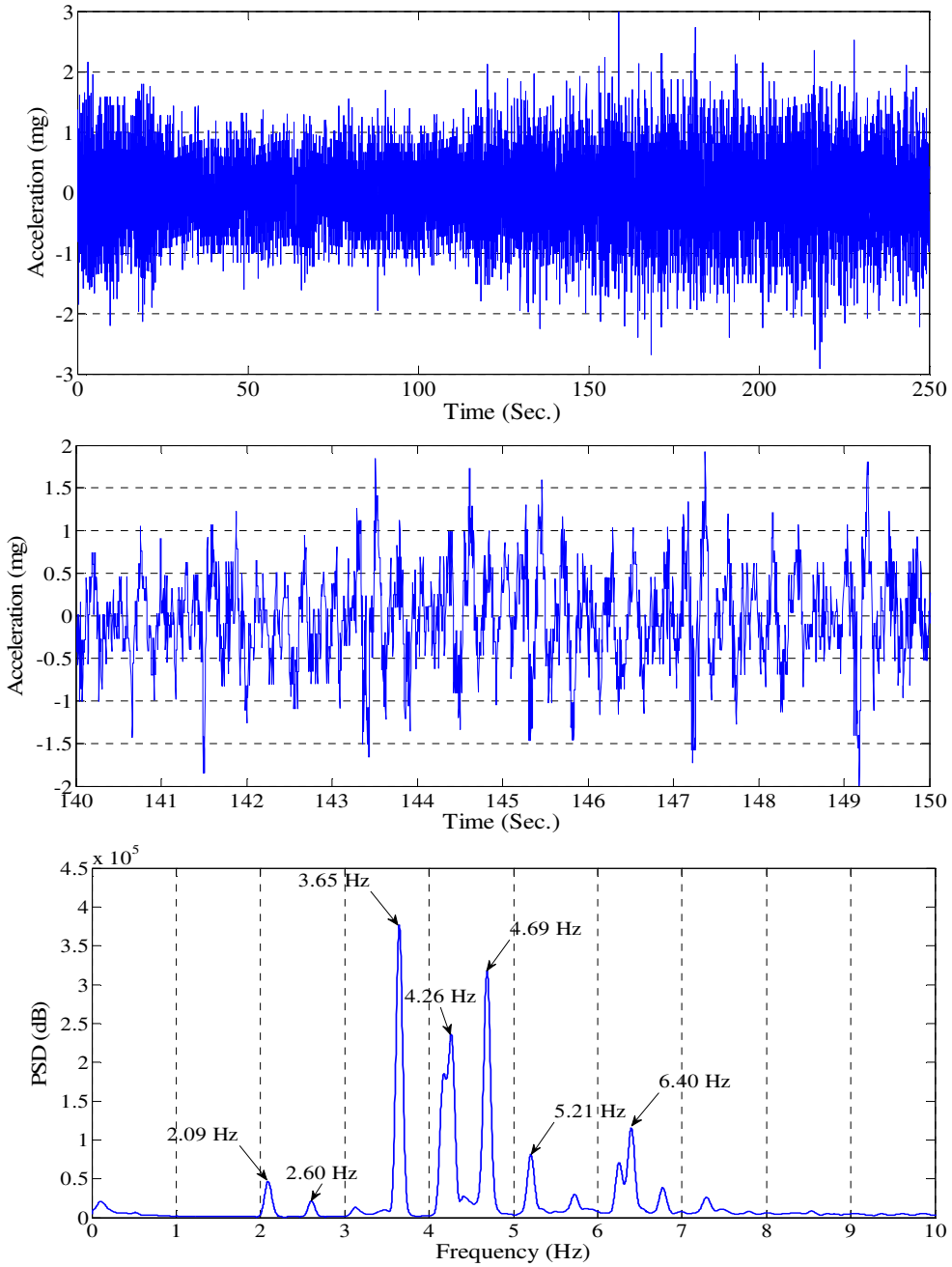

Figure A8.5. Time-history plot and Power Spectrum Density of acceleration from 13th floor on location of C-10, during aerobics

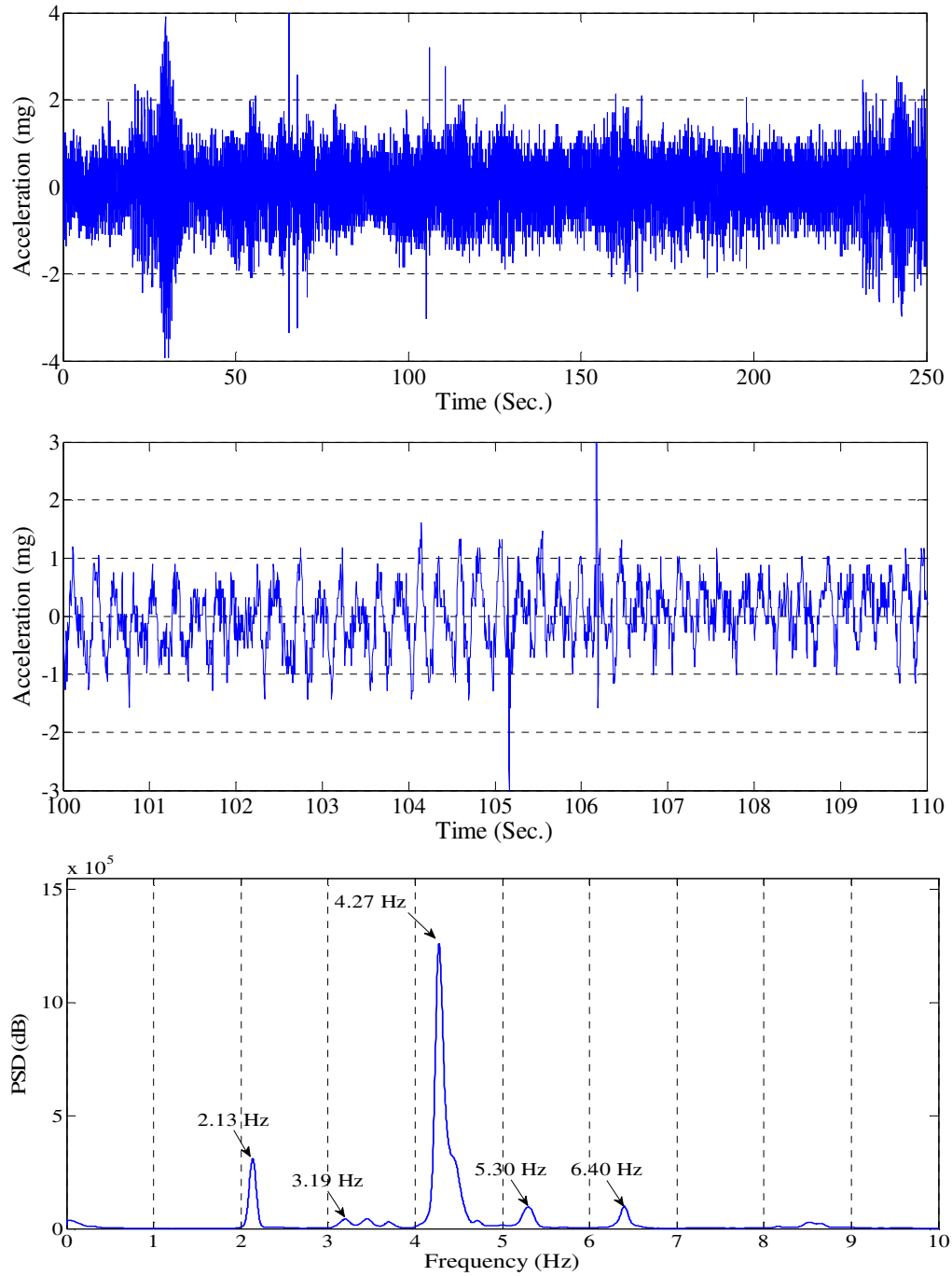

Figure A8.6. Time-history plot and Power Spectrum Density of acceleration from 12th floor between C-9 & C-10 during aerobics class

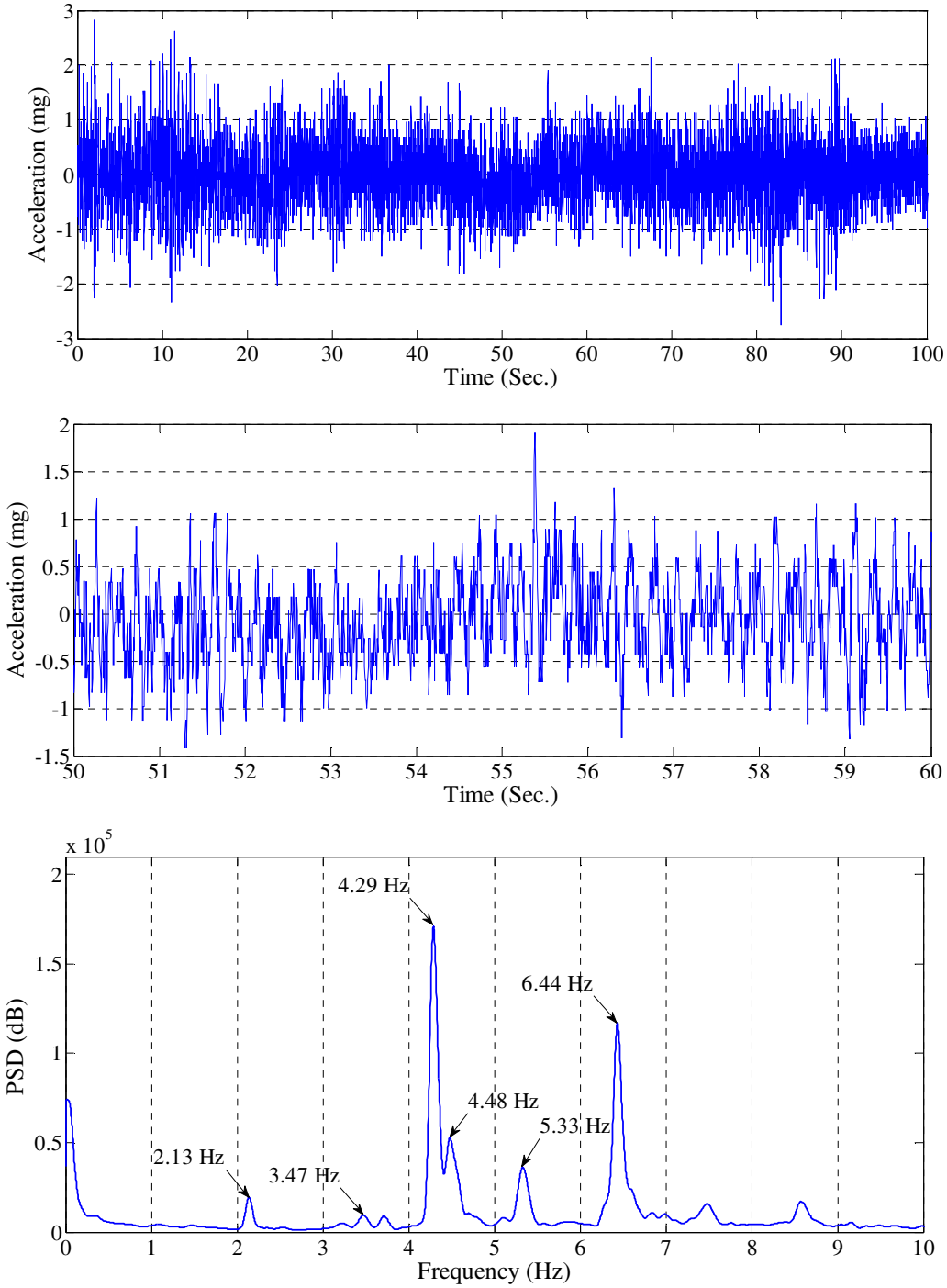

Figure A8.7. Time-history plot and Power Spectrum Density of acceleration from 7th floor between C-9 & C-10 during aerobics class

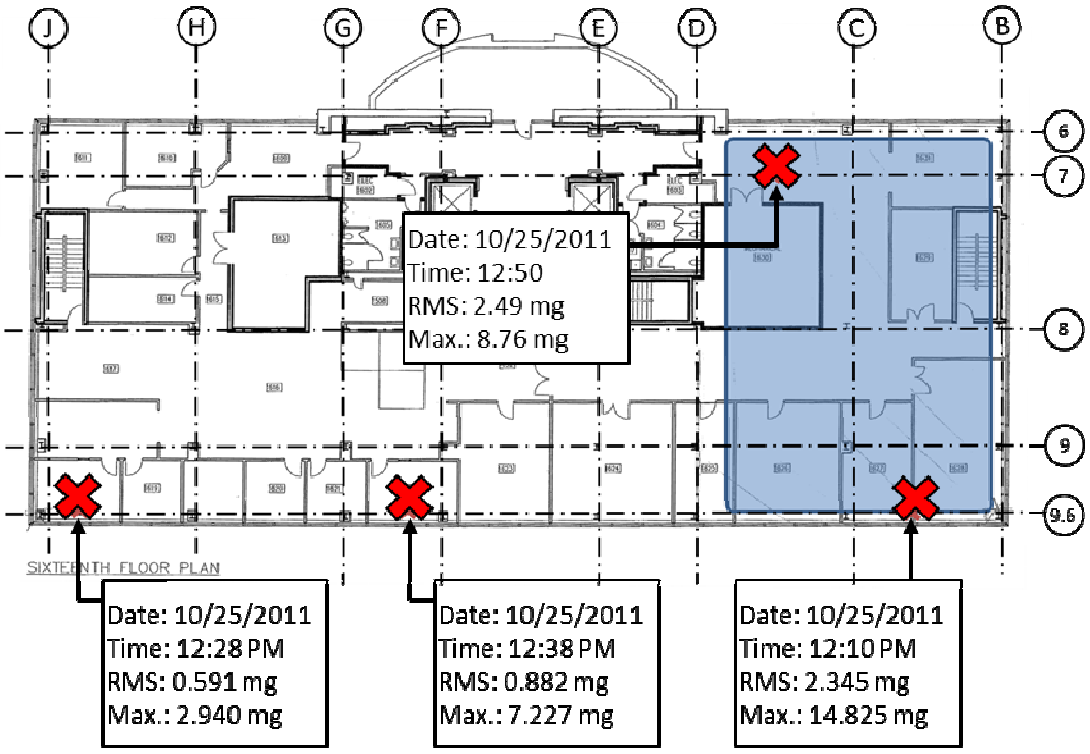

Figure A8.8. Peak measured accelerations and RMS accelerations obtained from wireless sensors on the 16th floor during aerobics class

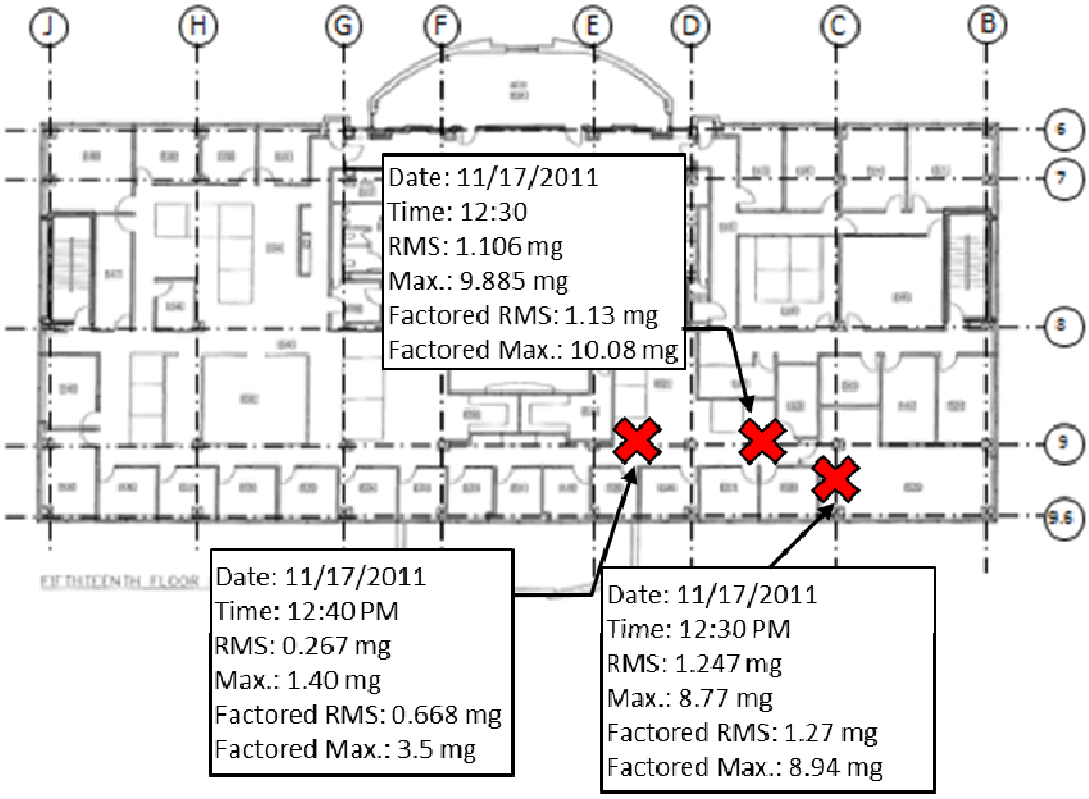

Figure A8.9. Peak measured accelerations and RMS accelerations and corresponding factored values obtained from wireless sensors on the 15th floor during aerobics class

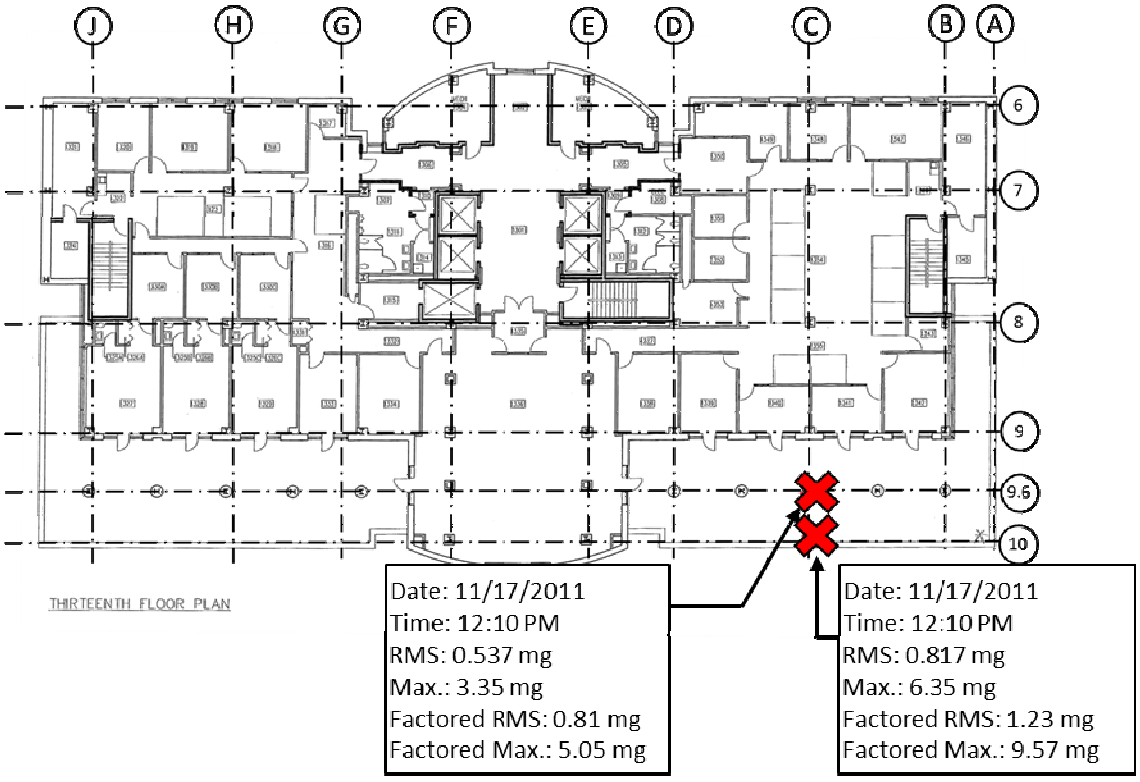

Figure A8.10. Peak measured accelerations and RMS accelerations and corresponding factored values obtained from wireless sensors on the 13th floor during aerobics class

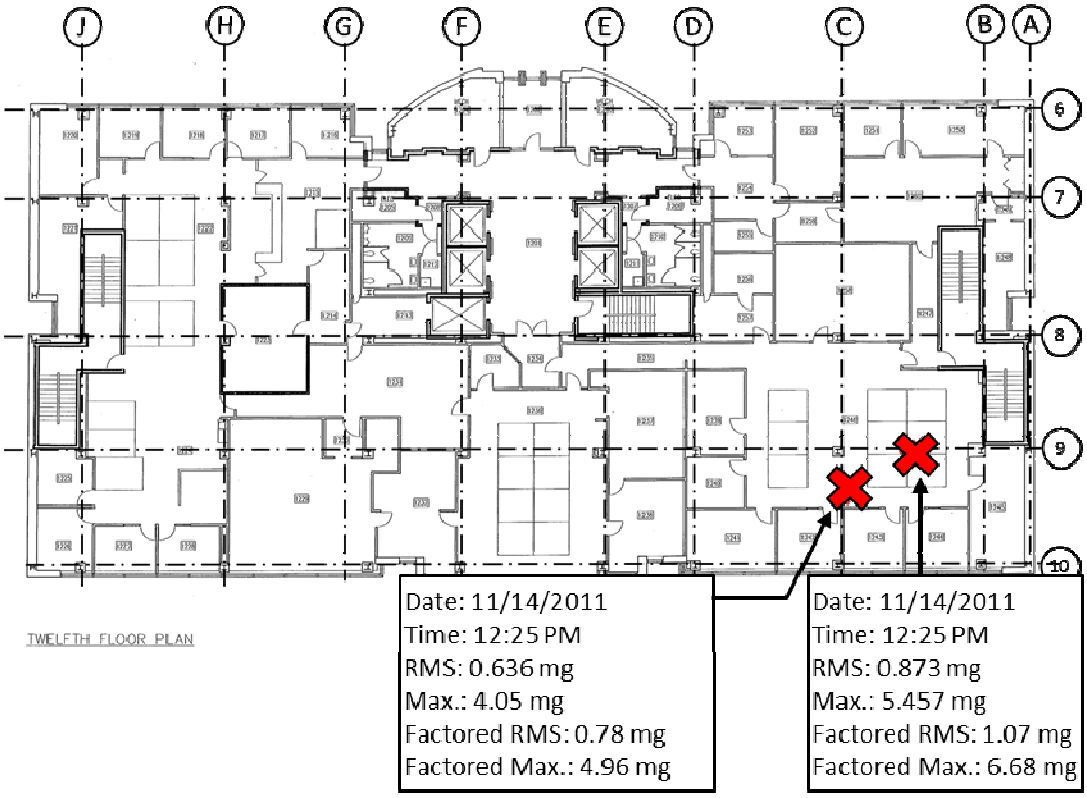

Figure A8.11. Peak measured accelerations and RMS accelerations and corresponding factored values obtained from wireless sensors on the 12th floor during aerobics class

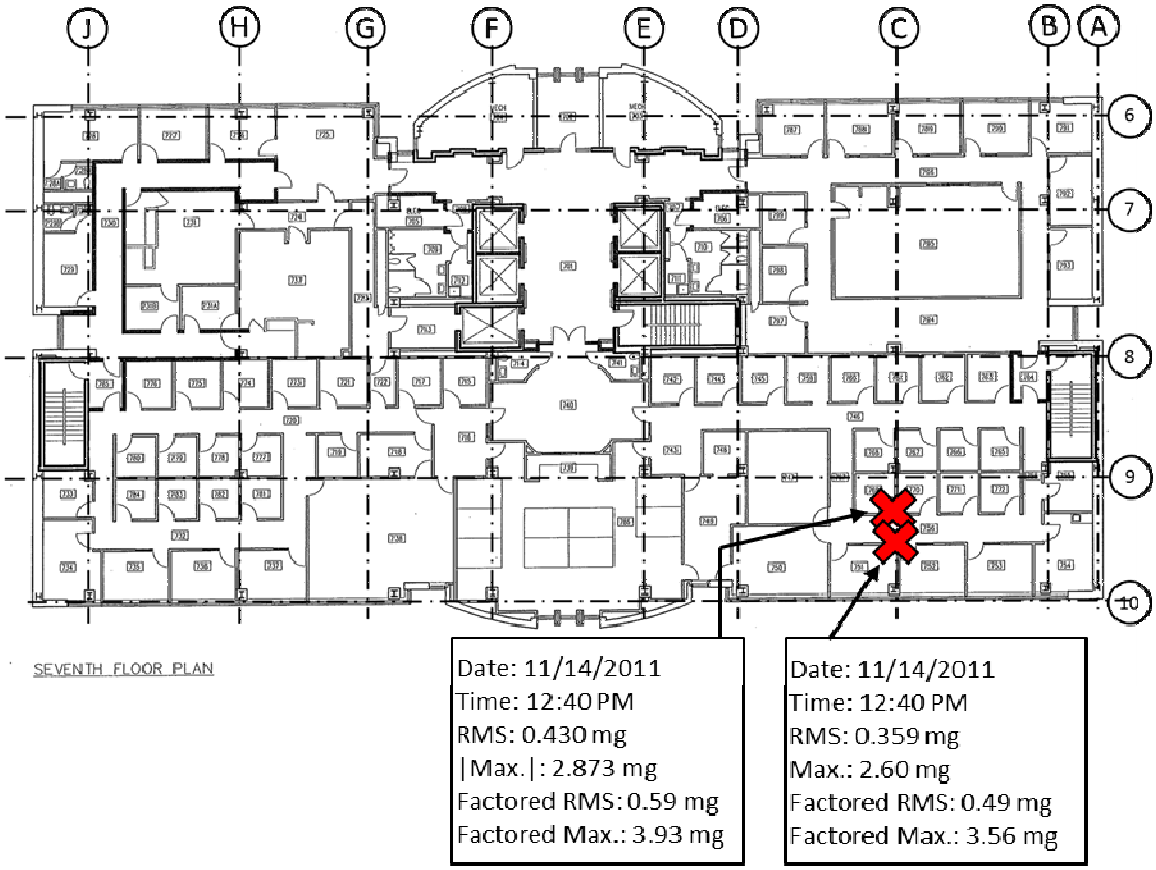

Figure A8.12. Peak measured accelerations and RMS accelerations and corresponding factored values obtained from wireless sensors on the 7th floor during aerobics class

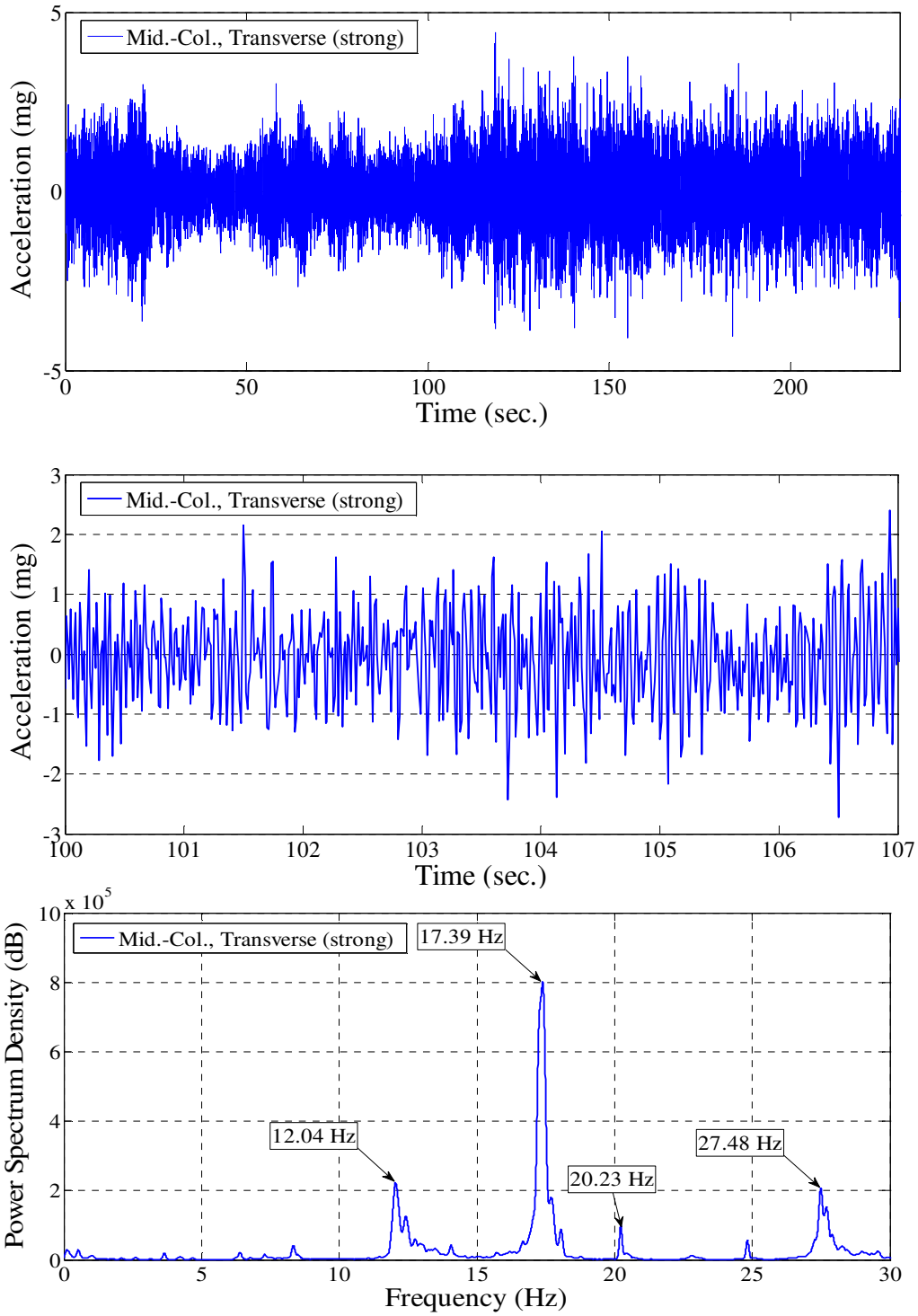

Figure A8.13. Time-history plot and Power Spectrum Density of acceleration from the column from middle of column C-9.6 on 13th floor in transverse direction during aerobics class

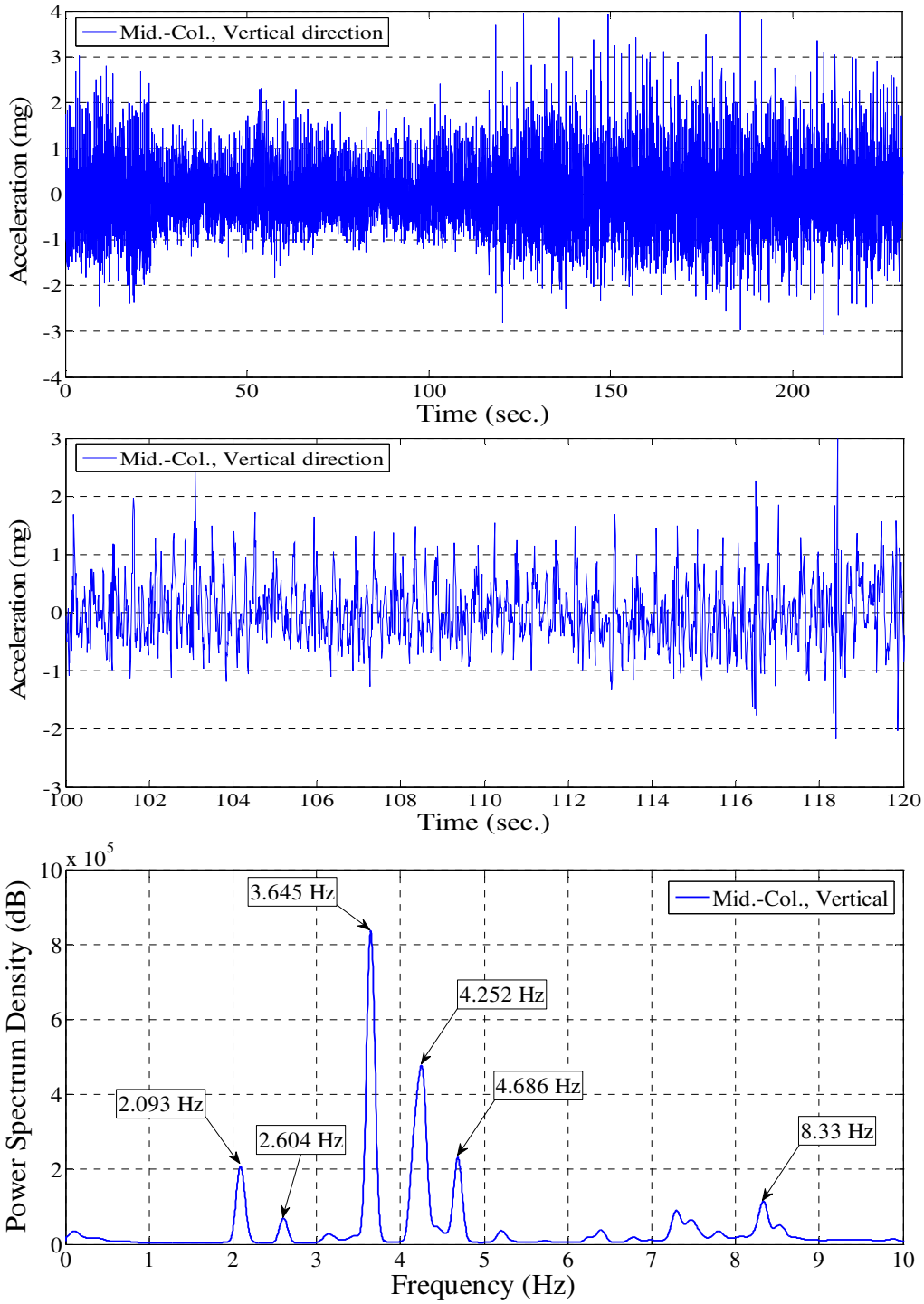

Figure A8.14. Time-history plot and Power Spectrum Density of acceleration from the column from middle of column C-9.6 on 13th floor in transverse direction during aerobics class

Appendix 7-A

Section information and dead loads for bridge members

Member		Section	Included Loads (lbs)	
Upper Truss Members	L0U1	TC: 4x6x1-5/16	eyes	37.145
	U1U2	TC: 4x6x1-1/8	eyes	63.8
	U2U3	TC: 4x7x1-9/16	eyes	88.47
	U3U4	TC: 4x8x1-11/16	eyes	95.845
	U4U5	TC: 4x9x1-11/16	eyes	95.845
	U5U6	TC: 4x9x1-1/2	eyes	86.771
	U6U7	TC: 4x8x1-3/8	eyes	79.965
	U7U8	TC: 4x6x1-3/8	eyes	75.995
	U8U9	TC: 2x6x1-5/16	eyes	37.147
	U9U10	TC: 2x6x1-5/16	eyes	37.147
	U10U11	TC: 2x5x3/4	eyes	21.267
Lower Truss Members	L0L1	L0L1	lacing bars stay plates splicer plates total	530 310 40 880
	L1L2	L1L2	lacing bars stay plates splicer plates total	570 310 40 920
	L2L3	L2L3, L6L7	lacing bars, stay plates, splicer plates	920
	L3L4	L3L4	lacing bars, stay plates, splicer plates	920
	L4L5	L4L5, L5L6	lacing bars stay plates total	530 310 840
	L5L6	L4L5, L5L6	lacing bars stay plates splicer plates total	530 310 40 880
	L6L7	L2L3, L6L7	lacing bars, stay plates, splicer plates	920

Member		Section	Included Loads (lbs)	
Lower Truss Members	L7L8	L7L8	lacing bars, stay plates, splicer plates	920
	L8L9	L8L9	lacing bars, stay plates, splicer plates	920
	L9L10	L9L10	lacing bars, stay plates	880
			splicer plates	100
			total	980
	L10L11	L10L11	lacing bars, stay plates	880
Vertical Truss Members	U1L1	Typ Vertical	lacing bars	150
			angles and plates	730
			pin plates	260
			total	1140
	U2L2	Typ Vertical	lacing bars	200
			angles and plates	320
			pin plates	200
			stay plates	120
			total	840
	U3L3	Typ Vertical	lacing bars	320
			angles and plates	320
			pin plates	250
			stay plates	90
			total	980
	U4L4	Typ Vertical	lacing bars	470
			stay plates, misc plates	170
			pin plates	250
			total	890
	U5L5	Vertical 5	lacing bars	670
			diaphragms	350
			stay plates	1290
			pin plates, misc plates	1130
			total	3440
	U6L6	Typ Vertical	stay plates, misc plates/angles	820
			pin plates	230
			total	1520

Member		Section	Included Loads (lbs)	
Vertical Truss Members	U7L7	Typ Vertical	lacing bars	320
			stay plates, misc plates/angles	350
			pin plates	250
			total	920
	U8L8	Typ Vertical	lacing bars	200
			stay plates, misc plates/angles	350
			pin plates	210
			total	760
	U9L9	Typ Vertical	lacing bars	130
			stay plates, misc plates/angles	230
			pin plates	340
			total	700
	U10L10	Vertical 10/11	lacing bars	80
			stay plates, misc plates/angles	230
			pin plates	220
			total	530
	U11L11	Vertical 10/11	lacing bars	30
			stay plates, misc plates/angles	360
			gusset plates	310
			total	700

Member		Section	Included Loads (lbs)	
Horizontal M-bars	M4.5M5	M bars	lacing bars misc plates total	100 180 280
	M5M5.5	M bars	lacing bars misc plates total	100 180 280
Diagonal M-bars	M4.5L5	rod	only self-weight	NA
	L5M5.5	rod	only self-weight	NA
Half- Tower	Top Strut	Portal: Top Horizontal	lacing bars	344.53
	Bottom Strut	Portal: Bottom Horizontal	lacing bars	516.8
	Diagonals	Portal: Outside Diagonal, Portal: Inside Diagonal	lacing bars	430.66
			filials misc steel total	770 400 2461.99
Sidewalk (load per panel)	366:565	Edge Stringers Floor Beams FSEC1 (at ends)	connections buckle plates concrete checkered plates total	330 1790 12030 1280 15430
Deck (load per panel)	Panels L0-L8	Interior Stringers Floor Beams FSEC1 (at ends)	connections buckle plates lateral bracing total	1970 10210 630 12810
	Panels L8-L11	Interior Stringers Floor Beams FSEC1 (at ends)	connections lateral bracing total	1970 630 2600

Member		Section	Included Loads (lbs)	
Diagonal Truss Members	L1U2	Diag: 4x1/16	eyes	60.116
	L2U3	Diag: 2x7/16	eyes	40.833
	L3U4	Diag: 2x1/4	eyes	35.446
	L4U5	Diag: 2x5/16	eyes	37.147
	U5L6	Diag: 2x1/16	eyes	30.058
	U6L7	Diag: 2x1/4	eyes	55.295
	U7L8	Diag: 2x7/16	eyes	40.833
	U8L9	Diag: 2x5/8	eyes	46.221
	L9U10	BU L9-U10	lacing bars	330
			stay plates	130
			pin plates	390
			total	850
	L10U11	BU L10-U11	lacing bars	310
			stay plates	130
			pin plates	180
			total	620

Member	Section	Included Loads (lbs)
Pins	Not Drawn	180
Anchorage	Not Drawn	1010
Railing (load per panel)	Not Drawn	1170
Railing Support (load per panel)	Not Drawn	870
Concrete Barrier (load per panel)	Not Drawn	3898

References

References

American Institute of Aeronautics and Astronautics. (1968). “Bridge Information: Easton-Phillipsburg Bridge (Northampton St)”. Delaware River Joint Toll, 28 Cole, H. A. On-the-line analysis of random vibrations. , Paper No. 68–288.

Alampalli, S, (1998). Influence of In-Service Environment on Modal Parameters. In Proceedings of the 16th International Modal Analysis Conference (IMAC 16), Santa Barbara, CA, 111–16.

Allemang, R.J., (2003). The Modal Assurance Criterion - Twenty Years of Use and Abuse. *Sound and Vibration*, pp.14-21.

Allen, D. E. & Murray, T. M. (1993). Design criterion for vibrations due to walking. Engineering Journal - American Institute of Steel Construction, 30 (4), pp. 117-129.

Alvandi, A., and Cremona, C. (2006) “Assessment of vibration-based damage.” Journal of Sound and Vibration **292,** 179–202.

American Institute of Steel Construction (1986). Steel Construction Manual, Chapter 6: Commentary on the AISC LRFD Specification, pp. 6-198.

Analog Devices. 1999 ADXL202 low cost ±2g dual axis iMEMS® accelerometer with duty cycle output. http://www.analog.com/ UploadedFiles/Data_Sheets/ADXL202E.pdf.

Anon., (1992), “ASM Handbook, Volume 17, Nondestructive Evaluation and Quality Control”, *ASM International*.

Asmussen, J. C. (1997). Modal analysis based on the random decrement technique-application to civil engineering structures. Doctoral dissertation, University of Aalborg, Aalborg, Denmark.

Asmussen, J. C., Ibrahim, S. R., and Brincker, R. (1996). Random decrement and regression analysis of traffic responses of bridges. *In Proceeding of 14th Int. Modal Analysis Conf.*, SEM, Dearborn, Mich., 453–458.

Ball, R. J. and Almond, D. P., (1998), “Detection and measurement of impact damage in thick carbon fibre reinforced laminates by transient thermography”, NDT *and E International*, **31**(3), 165-173.

Banks, H. T., Joyner, M. L., Wincheski, B. and Winfree, W. P., (2002), “Real time computational algorithms for eddy-current based damage detection”, *CRSC-TR01-16, NCSU Inverse Problems* 18 795-823

Beck, J L, Vanik, M W, and Katafygiotis, L S (1994). Determination of model parameters from ambient vibration data for structural health monitoring. in Proceeding of the 1st World Conf. on Structural Control, Pasadena, Calif., 3–12.

Bennett, R., Hayes-Gill, B., Crowe, J. A., Armitage, R., Rodgers, D., and Hendroff, A., (1999). Wireless Monitoring of Highways. *In Proceeding of SPIE, Smart Systems for Bridges, Structures, and Highways*, Newport Beach, CA, Vol. 3671, 173–182.

Bernal, D., M.ASCE (2002). "Load Vectors for Damage Localization." *Journal of Engineering Mechanics*, **7**(14).

Boggs D. (1997). Acceleration Indexes for Human Comfort in Tall Buildings - Peak or RMS?. CTBUH Monograph Chapter 13: Motion Perception Tolerance and Mitigation. Retrived from: http://www.cppwind.com/support/papers/papers/structural/PEAKvsRMS.pdf

Box, G., Jenkins, G., Reinsel, G., (1994). Time Series Analysis: Forecasting and Control, 3rd edition. *Englewood Cliffs*, 1994, NJ: Prentice-Hall.

Bridge Commission. <http://www.drjtbc.org/default.aspx?pageid=101>. 2012.

Brinker, R. Zhang, L. and Anderson, P. 2001, Modal identification of output only systems using frequency domain decomposition. *Smart Mater. Struc., 10, 441-445*

Brockwell, P. J., Davis, R.A., 2002. *Introduction to Time Series and Forecasting*, Springer, NY, 2nd edition.

Brownjohn, J. M. W. et al. (2001). "Civil structure condition assessment by finite element model updating." *Finite Elements in Analysis and Design,* 37(10), 761-775.

Brownjohn, J. M. W., Xia, P. Q., (2000). Dynamic Assessment of Curved Cable-Stayed Bridge by Model Updating, *ASCE, Journal of Structural Engineering*, Vol.126, Issue 2.

Caffrey, J., Govindan, R., Johnson, E., Krishnamachari, B., Masri, S., Sukhatme, G., Chintalapudi, K., Dantu, K., Rangwala, S., Sridharan, A., Xu, N., and Zuniga, M., (2004). Networked Sensing for Structural Health Monitoring, in *Proceedings of the 4th International Workshop on Structural Control*, New York, NY, June 10–11, 57–66.

Caicedo, J M, Dyke, S J, and Johnson, E A (2004). Natural excitation technique and eigensystem realization algorithm for phase I of the IASC-ASCE benchmark problem: Simulated data. Journal of Engineering. Mechanics., 130(1), 49–60.

Campbell Scientific Inc. (1995), CR9000X measurement and Control System. Logan, UT, USA.

Casciati, F. and Rossi, R. A power harvester for wireless sensing applications. *Structural Control and Health Monitoring*, 2007, 14: 649–659. DOI: 10.1002/stc.179

Chang, M. (2010), "Damage detection and modal identification of structural systems using sensor data." *MS thesis*, Lehigh University, Bethlehem, PA.

Chang, M., Pakzad, S. N. (2011) Modified Natural Excitation Technique for Stochastic Modal Identification. ASCE Journal of Structural Engineering, (doi http://dx.doi.org/10.1061/(ASCE)ST.1943-541X.0000559).

Chang, P. C., Flatau, A., and Liu, S. C. (2003). "Review paper: health monitoring of civil infrastructure." *Structural Health Monitoring,* **2**, 257-267.

Chen, J., and Gupta, A.K. (2000), *Parametric statistical change point analysis* Birkhäuser, Boston

Chipcon AS SmartRF®, 2004. CC2420 Preliminary Datasheet, rev 1.2.

Cho, S., Jo, H., Jang, S., Park, J., Jung, H.J., Yun, C.B., Spencer, Jr., B.F. and Seo, J., (2010). Structural health monitoring of a cable-stayed bridge using smart sensor technology: data analysis, *Smart Structures and Systems*, 6(5-6), 461-480.

Chung, H C, Enotomo, T, Loh, K, and Shinozuka, M, (2004). Real-time Visualization of Bridge Structural Response Through Wireless MEMS Sensors, in Proceedings of SPIE, Testing, Reliability, and Application of Micro- and Nano-Material Systems II, San Diego, CA, Vol. 5392, 239–246.

Crossbow Technology, Inc. (2007). *MICAz Wireless Measurement System,* San Jose, CA.

Crossbow Technology, Inc. (2007). Imote2, high-performance wireless sensor network node, *Product Datasheet* (http://www.xbow.com).

Das, N. K., Khorrami, F., and Nourbakhsh, S., (1998). A New Integrated Piezoelectric–Dielectric Microstrip Antenna for Dual Wireless Actuation and Sensing Functions*,* in *Proceedings of the SPIE, Smart Electronics and MEMS*, San Diego, CA, Vol. 3328, 133–146.

Davenport, A. G. & Novak, M. (2002). Chapter 29: Vibration of Structures Induced By Wind. In Harris, C. M. & Piersol, A. G. (Ed.) Harris' Shock and Vibration Handbook (pp. 29.1-29.67), 5th Edition. McGraw-Hill, New york, NY.

Delaware River Joint Toll Bridge Commission (DRJTBC) (Mar. 14, 1978). *Bridge Inspection and Rating: Northampton Street Tax-Supported Bridge*, Edwards and Kelcey, INC.

Delaware River Joint Toll Bridge Commission (DRJTBC) (1993). Easton-Phillipsburg Non-Toll Bridge (Northampton Street Bridge) Structure No. 280, Ep1-Ep24.

Dempster, A. P., Laird, N. M. and Rubin, D. B., (1997). Maximum Likelihood from Incomplete Data via the EM Algorithm, *Journal of Royal Statistical Society*, Series R, vol. 39, no.1, pp.1-38.

Deutsch, S., (1979), "A Preliminary Study of the Fluid Mechanics of Liquid Penetrant Testing", *Journal of Research of the National Bureau of Standards*, **84** (4), 287-292

Doebling, S.W., Farrar, C.R., and Prime, M.B. (1998). "A Summary Review of Vibration-Based Damage Identification Methods," *The Shock and Vibration Digest,* **30**, 91-105.

Dorvash S., Pakzad, S.N., 2012. Iterative Modal Identification Algorithm; Implementation and Evaluation, in *Proceedings of the 30th International Modal Analysis Conference (IMAC XXX),* Jacksonville, FL, January 30-February 2.

Dorvash, S., Pakzad, (2012) "Effects of Measurement Noise on Modal Parameter Identification", Smart Mater. Struct. 21(6) 065008

Dorvash, S., Pakzad, S. N., Labuz, E., Chang, M., Li, X. and Cheng, L. (2010). Validation of a Wireless Sensor Network using Local Damage Detection algorithm for Beam-Column Connections. *in Smart Structures and Materials, San Diego, CA.*

Dorvash, S., Pakzad, S.N., Cheng, L. An Iterative Modal Identification Algorithm for Structural Health Monitoring using Wireless Sensor Networks. *Earthquake and Spectra, Journal of Earthquake Engineering Research Institute*, 2012 (In Press).

Dorvash, S., Pakzad, S.N., Naito, C.J., Yen, B., Hodgson, I.C., (2012). "Application of state of the art in measurement and data analysis techniques for vibration evaluation of a tall building" *Journal of Structure and Infrastructure Engineering* (In Press).

Farrar, C R, and James, G H, (1997). System identification from ambient vibration measurements on a bridge. Journal of Sound and Vibration, 205, 1–18.

Farrar, C.R., Allen, D.W., Ball, S., Masquelier, M.P., and Park. G. (2005), "Coupling Sensing Hardware with Data Interrogation Software for Structural Health Monitoring" *In Proceeding of 6th International Symposium, Dynamic Problems of Mechanics,* Ouro Preto, Brazil.

Farrar, C.R., Baker, W.E., Bell, T.M., Cone, K.M., Darling, T.W., Duffey, T.A., Eklund, A., and Migliori, A. (1994), "Dynamic characterization and damage detection in the I-40 bridge over the Rio Grande." *Los Alamos National Laboratory Report*, LA 12767-MS.

Friswell, M., and Mottershead, J.E. (1995) "Iterative Methods using Modal Data". Finite element model updating in structural dynamics, 1st Ed., pp. 159-226.

Ganeriwal, S.; Kumar, R. and Srivastava, M. B., (2003). Timing-sync Protocol for Sensor Networks. *UC Los Angeles: Center for Embedded Network Sensing*. http://escholarship.org/uc/item/5mh7m01j

Gangone, M.V., Whelan, M.J. and Janoyan, K.D. (2011), "Diagnostic Load Testing and System Identification Using Wireless Sensors, " *Computer-Aided Civil and Environmental Engineering* (CACAIE), **26**(7), 560-579.

Gao, Y., Spencer, Jr., B. F., and Ruiz-Sandoval, M., (2006). Distributed Computing Strategy for Structural Health Monitoring, *Journal of Structural Control and Health Monitoring*, 13(1), 488-507.

Gibson, E. J. (1982). Working with the Performance Approach in Building. Cib Report, Publication #64.

Grimmelsman K A, and Aktan A E, (2005). Impacts and mitigation of uncertainty for improving the reliability of field measurements. Proceedings of the 2nd International Conference on Structural Health Monitoring of Intelligent Infrastructure (SHMII–2), Shenzhen, China.

Grisso, B. L., Martin, L. A., and Inman, D. J., (2005). A Wireless Active Sensing System for Impedance-based Structural Health Monitoring. *In Proceedings of the 23rd International Modal Analysis Conference*, Orlando, FL.

Gul, M. and Catbas, F.N. (2008). Ambient Vibration Data Analysis for Structural Identification and Global Condition Assessment. *Journal of Engineering Mechanics,* 134(8), p.650.

Hackmann, G., Sun, F., Castaneda, N., Chenyang Lu, Dyke, S.,(2008). A Holistic Approach to Decentralized Structural Damage Localization Using Wireless Sensor Networks*, Real-Time Systems Symposium,* vol., no., pp.35-46.

Hodgson, I. C, and Ricles, J. M., "Cyclic Testing of Beam-Column Subassemblages Connected with SidePlateTM Steel Moment Frame Connections." (2010).

Intel Corporation Research 2005. Intel Mote2 Overview, Version 3.0, Santa Clara, CA, Unite State.

International Standard Organization (1989). Evaluation of Human Exposure to Whole-Body Vibration-Part 2: Human Exposure to Continuous and Shock-Induced Vibrations in Buildings (1 to 80 Hz). ISO 2631-2.

Irwin, A.W. (1978). Human Response to Dynamic Motion of Structures. The Structural Engineering, Vol. 56A(9), pp. 237–244.

ISHMP (2009). http://shm.cs.uiuc.edu/software.html

Jaishi, Bijaya, and Ren, Wei-Xin. (2007). "Finite element model updating based on eigenvalue and strain energy residuals using multiobjective optimization technique." *Mechanical Systems and Signal Processing* (21), 2295-2317.

James, G H, Carne, T G, and Lauffer, J P, (1993). The natural excitation technique for modal parameter extraction from operating wind turbines. Rep. No. SAND92-1666, UC-261, Sandia National Laboratories, Sandia, N M

James, G H, Carne, T G, Lauffer, J P, and Nord, A. R. (1992). Modal testing using natural excitation. in Proceeding of the 10th Int. Modal Analysis Conf., San Diego.

Jang, S., Jo, H., Cho, S., Mechitov, K., Rice, J. A., Sim, S. H., Jung, H. J., Yun, C. B., Spencer, Jr., B. F. and Agha, G., (2010), "Structural Health Monitoring of a Cable Stayed Bridge using Smart Sensor Technology: Deployment and Evaluation", *Smart Structures and Systems*, **6**(5-6), 439-459.

Juang, J N and Pappa, R S, (1985). An Eigensystem Realization Algorithm for Modal Parameter Identification and Model Reduction. Journal of Guidance, Control and Dynamics, Vol. 8, No. 5, pp. 620-627.

Juang, J. N., and Phan, M. Q. (2001). Identification and control of mechanical systems, Cambridge University Press, 2001, Cambridge, U.K.

Juang, J-N, & Pappa, R S (1986). Effect of Noise on Modal Parameters Identified by the Eigensystem Realization Algorithm. Journal of Guidance, Control, and Dynamics, 9(3), 294-303.

Kim, J, Swartz, R A, Lynch, J P, Lee, J J and Lee, C G, (2010). Rapid-to-Deploy Reconfigurable Wireless Structural Monitoring Systems using Extended-Range Wireless Sensors, Smart Structures and Systems, Vol. 6, No. 5-6, 505-524 505.

Ko, J. M, and Ni, Y. Q. (2005). "Technology Developments in Structural Health Monitoring of Large-Scale Bridges." Engineering Structures, (27),1715-1725.

Koh, C.G., See, L.M., and Balendra, T. (1995). "Damage Detection of Buildings: Numerical and Experimental Studies." *J. Struct. Engrg*. **121**(8), 1155-1160.

Labuz, E. L., Chang, M., Pakzad, S., (2010). "Local Damage Detection in Beam-Column Connections Using a Dense Sensor Network," Proc. of Structures Congress, Orlando, FL.

Lenett, S M, (1998). Global Condition Assessment Using Modal Analysis and Flexibility. PhD Dissertation, University of Cincinnati, OH.

Levin, R.I, and Lieven, N. A. J. (1998). "Dynamic Finite Element Model Updating Using Simulated Annealing and Genetic Algorithms." *Mechanical Systems and Signal Processing*, (12), 91-120.

Linderman, L. E., Rice, J., Barot, S., Spencer, B. F., Bernhard, J. T. (2010). Characterization of Wireless Smart Sensor Performance. Journal of Engineering Mechanics, 136(12), pp.14-35.

Liu, S. C. and Tomizuka, M., 2003. Strategic Research for Sensors and Smart Structures Technology, in *Proceedings of the International Conference on Structural Health Monitoring and Intelligent Infrastructure*, Tokyo, Japan, November 13–15, Vol. 1, 113–117.

Ljung, L. (1999). System Identification, Theory for the User. Prentice Hall, Upper Saddle River, NJ.

Lynch J. P., Loh K. J., (2006), "A summary review of wireless sensors and sensor networks for structural health monitoring," *The Shock and Vibration Digest* ISSN 0583-1024, **38**, 91-128.

Lynch, J P, Law, K H, Kiremidjian, A S, Carryer, E, Farrar, C R, Sohn, H, Allen, D W, Nadler, B and Wait, J R, (2004). Design and performance validation of a wireless sensing unit for structural monitoring application, Structural Engineering and Mechanics, Vol. 17, No. 3-4, 393-408.

Lynch, J P, Partridge, A, Law, K H, Kenny, T W, & Kiremidjian, A. S. (2003). Design of Piezoresistive MEMS-Based Accelerometer for Integration with Wireless Sensing Unit for Structural Monitoring. Aerospace Engineering, DOI:10.1061/(ASCE)0893-1321

Lynch, J P, Wang, Y, Law, K H, Yi, J H, Lee, C G, and Yun, C B, (2005). Validation of a Large-scale Wireless Structural Monitoring System on the Geumdang Bridge, in Proceedings of the International Conference on Safety and Structural Reliability (ICOSSAR), Rome, Italy, June 19–23.

Lynch, J. P., Sundararajan, A., Law, K. H., Kiremidjian, A. S., and Carryer, E., (2004). Embedding Damage Detection Algorithms in a Wireless Sensing Unit for Operational Power Efficiency*, Smart Materials and Structures*, Vol. 13, No. 4, 800–810.

Lynch, J. P. & Loh, K. J. (2006). A Summary Review of Wireless Sensors and Sensor Networks for Structural Health Monitoring. The Shock and Vibration Digest, 38(2), pp. 91-128. DOI:10.1177/0583102406061499

Lynch, J. P., Law, K. H., Kiremidjian, A. S., Kenny, T. W., Carryer, E., and Partridge, A. The Design of a Wireless Sensing Unit for Structural Health Monitoring. *In Proceedings of the 3rd Interna- tional Workshop on Structural Health Monitoring,* 2001, Stanford, CA.

Lynch, J. P., Parra-Montesinos, G., Canbolat, B. A., and Hou, T.C. (2004). Real-time Damage Prognosis of High-performance Fiber Reinforced Cementitious Composite Structures. *In Proceedings of Advances in Structural Engineering and Mechanics (ASEM'04)*, Seoul, Korea.

Lynch, J. P., Sundararajan, A., Law, K. H., Kiremidjian, A. S. and Carryer, E., (2003). Power-efficient Data Management for a Wireless Structural Monitoring System, in *Proceedings of the 4th International Workshop on Structural Health Monitoring*, Stanford, CA, September 15–17, 1177–1184.

Lynch, J. P., Wang, Y., Law, K. H., Yi, J-H., Lee, C. G., and Yun, C. B., (2005). Validation of a Large-scale Wireless Structural Monitoring System on the Geumdang Bridge, in *Proceedings of the International Conference on Safety and Structural Reliability (ICOSSAR)*, Rome, Italy, June 19–23.

Lynch, J.P., Law, K.H., Kiremidjian, A.S., Carryer, E., Farrar, C.R., Sohn, H., Allen, D.W., Nadler, B. and Wait, J.R., (2004), "Design and performance validation of a wireless sensing unit for structural monitoring application", *Structural Engineering and Mechanics*, **17** (3-4), 393-408.

Lynch, J.P., Law, K.H., Kiremidjian, A.S., Carryer, E., Farrar, C.R., Sohn, H., Allen, D.W., Nadler, B. and Wait, J.R., (2004), "Design and performance validation of a wireless sensing unit for structural monitoring application", *Structural Engineering and Mechanics*, **17** (3-4), 393-408.

Mallet, L., Staszewski, W.J., Scarpa, F. (2004), "Structural health monitoring using scanning laser vibrometry: II. Lamb waves for damage detection" Smart Materials and Structures, **13**, 261-269.

Moon, F L (2006). Impacts of Epistemic (Bias) Uncertainty on Structural Identification of Constructed (Civil) Systems. The Shock and Vibration Digest, 38(5), 399-420. doi:10.1177/0583102406068068

Morassi, A., and Rovere, N. (1997), "Localizing a Notch in a Steel Frame from Frequency Measurements," *J. Engrg. Mech.* **123**(5), 422-432.

Mottershead, John E. et al. (2011). "The sensitivity method in finite element model updating: A tutorial." Mechanical Systems and Signal Processing,(25), 2275-2296.

Murray, T. M. (1991). Building floor vibrations. AISC Engineering Journal, Vol. 28(3), pp. 102–109.

Murray, T. M., Allen, D. E., & Ungar, E. E. (1997). Steel design guide series #11: Floor vibrations due to human activity. American Institute of Steel Construction, Chicago, USA.

Nagayama, T. and Spencer Jr., B. F., (2007). Structural Health Monitoring using Smart Sensors, *Newmark Structural Engineering Laboratory (NSEL)* Report Series, No. 1, University of Illinois at Urbana-Champaign, Urbana, Illinois (http://hdl.handle.net/2142/3521).

Nagayama, T., Abe, M., Fujino, Y., and Ikeda, K. (2005). Structural identification of a non-proportionally damped system and its application to a full-scale suspension bridge. *J. of Structural Engineering-ASCE, 2005; 131(10): 1536-1545.*

Nagayama, T., Moinzadeh, P., Mechitov, K., Ushita, M., Makihata, N., Ieiri, M., Agha, G., Spencer, Jr. B. F., Fujino, Y., Seo, J. W., (2010). Reliable Multi-Hop Communication for Structural Health Monitoring, *Smart Structures and Systems*, Vol. 6, No. 5-6, 481-504.

Nayeri, R D, Tasbihgoo, F, Wahbeh, M., Caffrey, J P, Masri, S F, Conte, J P, & Elgamal, A., (2009). Study of Time-Domain Techniques for Modal Parameter Identification of a Long Suspension Bridge with Dense Sensor Arrays. Journal of Engineering Mechanics, 135(7), 669. doi:10.1061/(ASCE)0733-9399(2009)135:7(669)

Overschee, P V Moor, B D, (1994) N4SID: Subspace Algorithms for the Identification of Combined Deterministic-Stochastic Systems, Automatica ISSN 0005-1098 CODEN ATCAA9, Vol. 30, No. 1, pp. 75-93.

Pakzad, S N and Fenves, G L, (2009) Statistical analysis of vibration modes of a suspension bridge using spatially dense wireless sensor network. Journal of Structural Engineering, 135(7), 863-872.

Pakzad, S N, (2010). Development and Deployment of Large Scale Wireless Sensor Network on a Long-span Bridge, Smart Structures and Systems, 6, 525–543.

Pakzad, S. N., Fenves, G. L., Kim, S, and Culler, D E, (2008). Design and Implementation of Scalable Wireless Sensor Network for Structural Monitoring, ASCE Journal of Infrastructure Engineering, 14(1):89-101.

Pakzad, S. N., Rocha, G. V. and Yu, B., (2011). Distributed modal identification using restricted auto regressive models, *International Journal of Systems Science*, DOI: 10.1080/00207721.2011.563875.

Pakzad, S.N. (2008), "Statistical approach to structural monitoring using scalable wireless sensor networks." *PhD dissertation,* University of California, Berkeley.

Pandit, S M 1991 Modal and Spectrum Analysis: Data Dependent Systems in State Space. John Wiley and Sons.

Pappa, R S, Elliott, K B, & Schenk, A (1993). Consistent-mode indicator for the eigensystem realization algorithm. Journal of Guidance, Control, and Dynamics. doi:10.2514/3.21092

Pappa, R. S., James, G. H., and Zimmerman, D. C., (1998). Autonomous modal identification of the space shuttle tail rudder*,* *Journal of Guidance, Control, and Dynamics*, 35(2), 163–169.

PCB Piezotronics Inc. (2005). Single axis capacitive accelerometer, series 3701, NY, http://www.pcb.com/Linked_Documents/Vibration/VIB300E_1204.pdf

Peeters B, and Roeck G, (2001). One-year monitoring of the Z24-Bridge: environmental effects versus damage events. Earthquake Engineering and Structural Dynamics, 30, 149-171.

Ratcliffe, C.P. (1997). "Damage Detection Using a Modified Laplacian Operator on Mode Shape Data." *Journal of Sound and Vibration* **204**(3), 5-517.

Reynders, E, Pintelon, R, & Deroeck, G (2007). Uncertainty bounds on modal parameters obtained from stochastic subspace identification. Mechanical Systems and Signal Processing, 22, 948-969. doi:10.1016/j.ymssp.2007.10.009

Reynolds, P, Pavic, A., Ibrahim, Z, & Street, M (2004). Changes of modal properties of a stadium structure occupied by a crowd Department of Civil and Structural Engineering Sir Frederick Mappin Building. IMAC XXII.

Rice, J. A. and Spencer Jr., B. F., (2008), "Structural health monitoring sensor development for the Imote2 platform," *Proceeding of SPIE Smart Structures/NDE,* San Diego, CA.

Rice, J.A. & Spencer, B.F. (2009). Flexible Smart Sensor Framework for Autonomous Full-scale Structural Health Monitoring. NSEL Report Series, No. 18, University of Illinois at Urbana-Champaign. Retrieved from: http://hdl.handle.net/2142/13635

Roeck, G D, Claesen, W and Broeck. P V D, (1995). DDS-Methodology Applied to Parameter Identification in Civil Engineering Structures. in Proceeding of Vibration and Noise, Venice, Italy, pp. 341–353.

Sen, A. and Srivastava, M.S. (1975), "On tests for detecting change in mean." *The Annals of Statistics*, **3**, 98-108.

Silicon Design (2007). Model 1221, low noise analog accelerometer. http://www.silicondesign.com/pd.

Sim, S. H., and Spencer, B. F. (2009). Decentralized Strategies for Monitoring Structures using Wireless Smart Sensor Networks. *Newmark Structural Engineering Laboratory (NSEL)*, ISSN: 1940-9826.

Sim, S.H., Carbonell-Marquez, J., Spencer, Jr., B.F. and Jo, H., (2010). Decentralized Random Decrement Technique for Efficient Data Aggregation and System Identification in Wireless Smart Sensor Networks. *Probabilistic Engineering Mechanics,* 2010, 26(1), pp. 81-91.

Sim, S.H., Jang, S.A., Spencer, Jr., B.F., and Song, J. (2008), "Reliability-based Evaluation of the Performance of the Damage Locating Vector Method," *Probabilistic Engineering Mechanics*, **23**, 489-495

Sim, S.H., Spencer, Jr., B.F., and Nagayama, T. (2011), "Multimetric Sensing for Structural Damage Detection," *Journal of Engineering Mechanics, ASCE*, **137**(1), 22-30.

Simulated Annealing and Genetic Algorithms." Mechanical Systems and Signal Processing, (12), 91-120.

Sohn, H, (2007) Effects of Environmental and Operational Variability on Structural Health Monitoring Journal of Philosophical Transactions of the Royal Society, Series A, Mathematical, physical, and engineering sciences, pp.539-560, DOI: 10.1098/rsta.2006.1935.

Sohn, H., and Farrar, C.R. (2001). Damage diagnosis using time series analysis of vibration signals. *Smart Materials and Structures*, 10(3), 446-451.

Sohn, H., and Law, K.H. (1997), "A Bayesian Probabilistic Approach for Structure Damage Detection." *Earthquake Engineering and Structural Dynamics* **26**, 1259-1281.

STMicroelectronics (2005), *LIS3L02AS4 MEMS Inertial Sensor* Geneva, Switzerland.

Straser, E. G. & Kiremidjian, A. S. (1998). A Modular, Wireless Damage Monitoring System for Structures. Technical Report 128, John A. Blume Earthquake Engineering Center, Stanford University, Stanford, CA.

Swartz, R. A., Jung, D., Lynch, J. P., Wang, Y., Shi, D., Flynn, M. P., (2005). Design of a Wireless Sensor for Scalable Distributed In-Network Computation in a Structural Health Monitoring System, In *Proceedings of the 5th International Workshop on Structural Health Monitoring*, Stanford, CA, USA.

Swartz, R.A., Lynch, P. & Loh, C., (2009). Decentralized Damage Detection by Transfer Function Pole Migration in Dense Sensor Networks. *In Proceeding of International Workshop on Structural Health Monitoring*, Stanford, CA.

Moon. T.K. (1996). The Expectation-Maximization Algorithm in Signal Processing. *IEEE Signal Processing Magazine*, 1996, V. 13, No. 6, pp. 47–60. DOI 10.1109/79.543975. URL

Tanner, N A., Wait, J R, Farrar, C R, and Sohn, H, (2003). Structural Health Monitoring Using Modular Wireless Sensors, Journal of Intelligent Material Systems and Structures, Vol. 14, No. 1, 43–56.

Trimm, M., (2003). "An overview of nondestructive evaluation methods" *Journal of Failure Analysis and Prevention*, **3**(3), 17-31

Vandiver, J. K., Dunwoody, A. B., Campbell, R. B. and Cook, M. F. A (1982). Mathematical Basis for the Random Decrement Vibration Signature Analysis Technique. Journal of Mechanical Design, 104: 307-13.

Void H and Rocklin G F (1982). The Numerical Implementation of a Multi-Input Modal Estimation Method for Mini-Computers, International Modal Analysis Conference Proceeding.

Wang, Y., Lynch, J. P., Law, K. H. (2007). A wireless structural health monitoring system with multithreaded sensing devices: design and validation. Structure and Infrastructure Engineering , Taylor & Francis, Vol. 3, pp. 103-120, DOI: 10.1080/15732470600590820

Whelan, M J, Janoyan, K D (2009). Design of a Robust, High-rate Wireless Sensor Network for Static and Dynamic Structural Monitoring, Journal of Intelligent Material Systems and Structures, Vol. 20, No. 7, 849-863.

Wong, K. Y. (2007). Design of a structural health monitoring system for long-span bridges. Structure and Infrastructure Engineering, Taylor & Francis Vol. 3, Iss. 2, pp. 169-185. DOI: 10.1080/15732470600591117

Yoon, M.K., Heider, D., Gillespie Jr., J.W., Ratcliffe, C.P., and Crane, R.M. (2005), "Local damage detection using the two-dimensional gapped smoothing method." *Journal of Sound and Vibration* **279**, 119-139.

Zhang, Q. W., Chang, T. Y. P., & Chang, C. C. (2001). Finite-Element Model Updating for the Kap Shui Mun Cable-Stayed Bridge. *Journal of Bridge Engineering*, Vol. 6, No. 4, 285-293.

Zhang, Q. W., et al. (2001). "Finite-Element Model Updating for the Kap Shui Mun Cable- Stayed Bridge." Journal of Bridge Engineering, 6(4), 285-293.

Zilberstein V., Walrath K., Grundy D., Grundya, D., Schlickera, D., Goldfinea, N., Abramovicib, E., Yentzerc, T., (2003), "MWM eddy-current arrays for crack initiation and growth monitoring*", International Journal Of Fatigue,* **25**, 1147-1155.

Zimmerman, A.T., Shiraishi, M., Swartz, A., Lynch, J.P. Automated Modal Parameter Estimation by Parallel Processing within Wireless Monitoring Systems. *Journal of Infrastructure Systems*, 2008, 14(1), p.102. Available at: http://link.aip.org/link/JITSE4/v14/i1/p102/s1&Agg=doi.

Author's Biography

Siavash Dorvash was born in Ehfahan, Iran on December 27, 1980. He graduated from Isfahan University of Technology, Esfahan, Iran, in 2003 with a B.Sc. in Civil Engineering. In 2006 he completed his M.Sc. in Earthquake Engineering at K.N.Toosi University of Technology, Tehran, Iran. Siavash entered Lehigh University in the fall of 2008. He will receive his PhD in Structural Engineering in May 2013.